Aalborg Universitet

![Aalborg University Denmark logo]

AALBORG UNIVERSITY
DENMARK

Dynamic Study on the 400 kV 60 km Kyndbyværket – Asnæsværket Line

Ohno, Teruo

Publication date:
2012

Document Version
Early version, also known as pre-print

[Link to publication from Aalborg University](#)

Citation for published version (APA):
Ohno, T. (2012). *Dynamic Study on the 400 kV 60 km Kyndbyværket – Asnæsværket Line*. Department of Energy Technology, Aalborg University.

PhD Thesis

Dynamic Study on the 400 kV 60 km Kyndbyværket – Asnæsværket Line

PhD student Teruo Ohno

Supervisor: Claus Leth Bak

Co-supervisors: Thomas Kjærsgaard Sørensen, Wojciech Tomasz Wiechowski and Akihiro Ametani

Period: December 1st 2009 - December 1st 2012

Preface

This thesis is submitted to the Faculty of Engineering, Science and Medicine at Aalborg University in the partial fulfilment of the requirements for the PhD degree in Electrical Engineering. The research was conducted at the Department of Energy Technology for Energinet.dk.

The research has been followed full time by Professor Claus Leth Bak (Department of Energy Technology), Professor Akihiro Ametani (Doshisha University), Dr. Thomas Kjærsgaard Sørensen (Energinet.dk), and Dr. Wojciech Wiechowski (RWE Innogy).

The research has been conducted while the PhD student is working full-time for Tokyo Electric Power Company (TEPCO), one of major users of EHV cables. The work in TEPCO, including international consultancy projects on EHV cables, has contributed to the research.

This thesis is divided into seven chapters. A list of all authored and co-authored publications written by the author is presented in Section 7.2. Literature references are shown as [j], where j is the number of the literature in the reference list. References to figures, tables, and equations are shown as Fig. C.F, Table C.F, or Eqn. C.F, where C is the chapter number and F indicates the figure, table or equation number.

Acknowledgments

I owe gratitude to many people that have helped me in various ways. In particular, I would like to thank:

Abstract

Until recently, the use of HVAC underground cable systems has been mainly limited to densely populated area. As such, HVAC underground cable systems are limited both in length and numbers to date. This tendency has been changing over the past ten years as the service experience of HVAC, cable systems have shown to be satisfactory. The applications of HVAC cable systems are proposed more often for transmission projects, and recently proposed HVAC underground cable systems are longer compared to existing cable systems. Due to this historical background, HVAC underground cable systems have been studied and tested primarily with short cable lengths. Some knowledge from short cable lines can be directly applied to long cable lines, but there are several phenomena which are peculiar to long cable lines.

The main objectives of the PhD project are to shed light on the phenomena peculiar to long cable lines. The PhD project focuses on the 400 kV 60 km Kyndbyværket – Asnæsværket line, which will feed power to Copenhagen, the Danish capital. The PhD project addresses major problems and potential countermeasures related to the installation and operation of a long cable line, through:

(1) Insulation coordination study

(2) Derivation of theoretical formulas of sequence currents

(3) Identification of dominant frequency components contained in the overvoltage

(4) Analysis on the statistical distribution of energization overvoltages

(5) Protection study

First, the insulation coordination study have found that it is feasible to build and operate the 400 kV 60 km Kyndbyværket – Asnæsværket line and have identified necessary considerations in the equipment specification and required countermeasures against possible problems. Especially, severe temporary overvoltages caused by parallel resonance and system islanding are observed, which requires a consideration in the selection of surge arresters.

Second, the PhD project has derived theoretical formulas of sequence currents of a cross-bonded cable and a solidly-bonded cable. These formulas are obtained by solving equations which are derived from the setups for measuring sequence currents of cross-bonded and solidly-bonded cables. For a cross-bonded cable, the equations are solved utilizing the known impedance matrix reduction technique. The derived formulas consider the cable as a cable system; they can thus consider sheath bonding and sheath grounding resistance. An accuracy of proposed formulas is verified through a

comparison with EMTP simulation results. The verified accuracy of the proposed formulas shows sequence impedance / current can be obtained before the installation without making measurements for a majority of cables. This gives an important advantage in setting up transient overvoltage studies as well as planning studies.

Third, as the switching of EHV cables can trigger temporary overvoltages, it is important to find the dominant frequency component contained in the switching overvoltages of these cables. Since there are no theoretical formulas to find the dominant frequency, it is generally found by means of time domain simulations or frequency scans. The derivation of theoretical formulas has been desired as the formulas would be useful in verifying the results of time domain simulations or frequency scans. Additionally, the formulas could eliminate the necessity of building simulation models of some network components.

The PhD project has derived the simple theoretical formulas for estimating the propagation velocity and dominant frequency from impedance and admittance calculations. The comparison between the proposed formulas and the simulation results is performed using the Kyndbyværket – Asnæsværket line. From the comparison, the derived formulas are found to be sufficiently accurate to be used for efficient analysis of resonance overvoltages. In addition, the accuracy of the formulas derived demonstrates that the propagation velocity and the dominant frequency are determined by two inter-phase modes for long cables.

Forth, the statistical distribution of energization overvoltages of EHV cables is derived in the PhD project from a number of simulations. Through the comparison with the statistical distributions of energization overvoltages of overhead lines, the main characteristics of the statistical distribution for cables are identified. In particular, it has been found that line energization overvoltages of cables are lower than those of overhead lines with respect to maximum, 2 %, and mean values. The standard deviation has been found to be smaller for cables.

The main characteristics of the statistical distribution are found to be caused not by random switching by accident, rather there are contributing factors and physical meanings behind the characteristics. These contributing factors and physical meanings are identified from the theoretical analysis of voltage waveforms of energization overvoltages. These findings are useful not only for the determination of insulation levels of cable systems, but also for insulation coordination studies of cable systems.

Finally, through the calculation of the ground loop impedance for cable lines, it has been found that, for long EHV cable lines, the reliable operation of the ground distance relay is possible with a typical relay setting. It is known that the ground loop impedance of EHV cable lines does not have a linear relationship to the distance. There is a discontinuity in the ground loop impedance at cross-bonding points, which may have an ill effect on the reliable operation of the ground distance relay. However, the discontinuity of the ground loop reactance of the long EHV cable lines is small enough for the ground distance relay to operate satisfactory with a typical relay setting. Effects of parameters, such as substation grounding, cable layouts and transposition, are also found through the analysis.

Table of contents

Chapter 1 Introduction

1.1 Background

In order to mitigate climate change, many countries have set a target to reduce their greenhouse gasses. Due to its abundant natural resources (wind) and green minded people, Denmark is one of the leading countries in this effort of the world to tackle global warming. As of the year 2011, the wind energy accounted for 29.1 % in generation capacity and 28.1 % of the electrical production [1].

This change of the generation profile has led to and will continue to lead to the necessity of major upgrades in the Danish transmission grid. Especially, the expansion of Horns Rev, the world largest offshore wind farm, will require the ability of the Danish transmission grid to transmit increased power from west to east where the electricity is consumed.

As in Denmark, transmission system operators (TSOs) in the world have been seeing growing numbers of transmission line projects in the recent years, due to different reasons, which include the increase of cross-border trades, renewable energy sources, smart grid projects, the replacement of aging facilities, and in some countries due to growing demand.

Until recently, TSOs in the world have responded to these necessary transmission upgrades mostly by the introduction of overhead lines (OHLs). HVAC underground cable systems have been used, but their applications have been mainly limited to densely populated area. As such, HVAC underground cable systems are limited both in length and numbers to date.

This tendency has been changing over the past ten years as the service experience of HVAC, especially EHV AC, cable systems have become satisfactory [2]. The applications of HVAC cable systems are proposed more often in order to protect the beautiful landscape and also public health, e.g. EMF.

In Denmark, receiving public and political pressures to underground its OHLs, Energinet.dk published a report on the future expansion and undergrounding of its transmission grid on the 3rd of April 2008 [3]. The report proposed and compared five principles (A – E in Fig. 1.1). From the five principles, the Danish government has selected Principle C in which all new 400 kV lines will basically be undergrounded.

A	B	C	D	E	F
Complete undergrounding	New power lines in underground cables	New power lines in underground cables and new towers in an existing line route	New overhead lines in areas where overhead lines have already been constructed	New overhead lines	No grid expansion

Improvement of the visual appearance of the existing 400 kV grid using lower towers in a new design and undergrounding of specifically chosen sections

400 kV

132 kV and 150 kV

Undergrounding of existing 132 kV and 150 kV grids in accordance with separate cable action plan

Fig. 1.1 Five principles for the future grid expansion (from [3]).
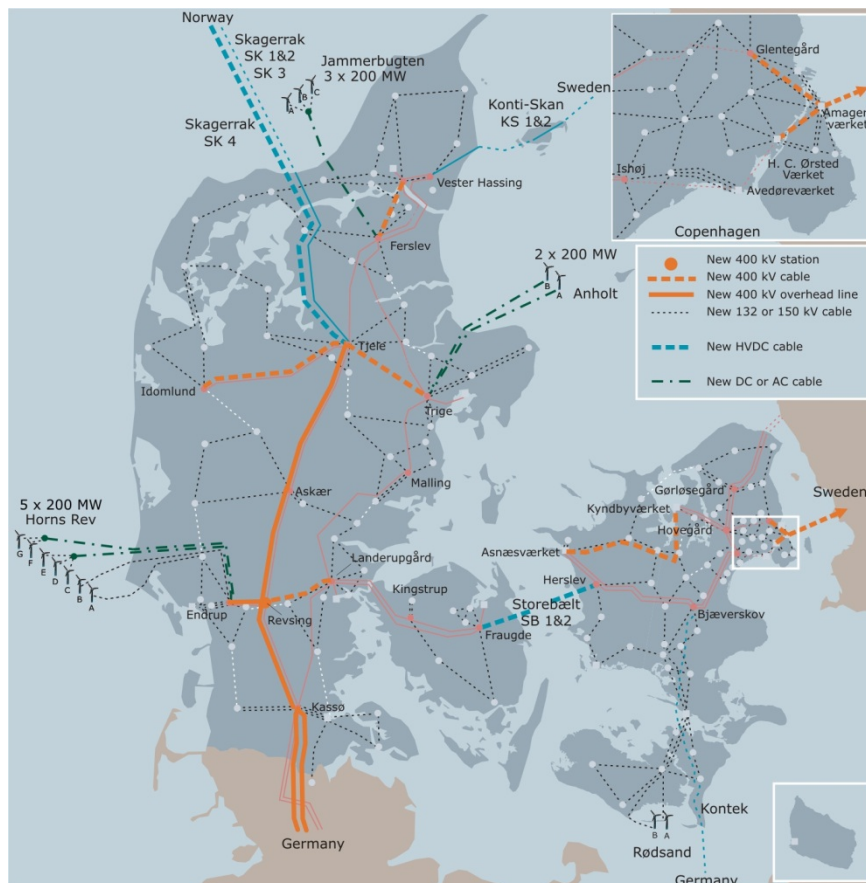
Fig. 1.2 Grid expansion plan based on Principle C (from [3]).

Due to the historical background, HVAC underground cable systems have been studied and tested primarily with short cable lengths. Because of this shift in trend, however, the recently proposed HVAC underground cable systems are longer compared with existing cable systems. As a result, when TSOs face increased number of recent transmission projects with HVAC underground cables, there is a lack of knowledge and expertise in long underground cables. Some knowledge and expertise from short cable lines can be directly applied to long cable lines. However, there are several phenomena which are peculiar to long cable lines [4] – [10].

The objectives of this PhD thesis are to shed light on the phenomena peculiar to long cable lines. The PhD thesis will focus on the 400 kV 60 km Kyndbyværket – Asnæsværket line, which is the longest 400 kV line in the grid expansion plan based on Principle C and will help to ensure the supply to Copenhagen. The thesis will address major problems and potential countermeasures related to the installation of this long cable line.

1.2 Problem Formulation

One of the biggest problems in the EMT (electromagnetic transient) analysis of long cable lines is a lack of understanding in frequency components contained in the overvoltages. Although an extensive study was performed upon the installation of the 500 kV Shin-Toyosu line, there was a lack of understanding in frequency components contained in the overvoltages associated with long cable lines. More importantly, the significance of the frequency components was not well understood.

Thanks to the recent progress in the modelling technique and computational limitations [11] – [22], the EMT analysis with EHV cables is considered to have a reasonable accuracy whose typical error can be less than 10% in magnitude. However, the typical error is expected to increase to around 30% when the waveform of the overvoltage is considered. This implies that some frequency components are not accurately reproduced in the EMT analysis for some reason.

It has to be noted that one of the most worrying problems for long cable lines is the resonance overvoltage, which shows significant nonlinearity around the resonance frequencies. From this point of view, frequency components in the overvoltages have to be found with greater accuracy, compared with other EMT analyses. Reasonable accuracy may not be good enough for the analysis of long cable lines.

Objectives of the PhD project include the following items:

(1) Insulation coordination study for the 400 kV Kyndbyværket – Asnæsværket line
    The PhD project intends to address major problems and potential countermeasures related to the installation of the 400 kV Kyndbyværket – Asnæsværket line.

(2) Identification of dominant frequency components contained in the overvoltage
    In relation to the study of the 400 kV Kyndbyværket – Asnæsværket line, the PhD project intends to explore ways to find dominant frequency components contained in the overvoltage. As discussed above, it is crucial especially in the resonance overvoltage study.

(3) Finding probabilistic distribution of the overvoltage
    Probabilistic distribution of the overvoltages [23][24] is another research interest of the PhD project. Because of the low frequency components in the overvoltages, the probabilistic distribution of the overvoltages can be very different from the one assumed for OHLs. An effect of the frequency components on the probabilistic distribution will be explored in order to

find the meaning of well-known 2 % overvoltage and the conversion factor for long cable lines.

(4) Protection studies for the long EHV cable

The PhD project also covers protection studies. Especially, effects of cable layouts and transposition on the ground loop impedance of cross-bonded cables are studied.

1.3 Thesis Outline

This thesis is composed of seven chapters. This section gives the short descriptions of these chapters:

Chapter 1   Introduction

This chapter first presents background of this PhD project. It explains the current situation in which more and more long cable lines are planned and installed. Problems and challenges the PhD project tackles are then described in this chapter.

Chapter 2   Reactive Power Compensation

The charging capacity of a long EHV AC cable line needs to be compensated in order to suppress the steady-state overvoltage of the network around the cable line or at the cable open terminal and to mitigate the reduction of the effective transmission capacity due to the charging current. This chapter finds the optimal reactive power compensation for the Kyndbyværket – Asnæsværket line.

Chapter 3   Model Setup

This chapter describes how transient simulation models were created. The derivation of input data is explained for each type of equipment. Considerations in the cable model setup are discussed in detail.

Chapter 4   Temporary Overvoltage Analysis

Temporary overvoltages are the highest concerns when studying long EHV AC cable lines. This chapter analyses the temporary overvoltages – the resonance overvoltage and the overvoltage caused by the system islanding.

Chapter 5   Slow-front Overvoltage Analysis

The slow-front overvoltages caused by line energization, ground fault and fault clearing are studied in this chapter in order to compare those in cables and in overhead lines. The statistical distributions of the slow-front overvoltages are also derived and compared between cables and overhead lines.

Chapter 6   Other Studies

This chapter discusses other studies related to the installation of long EHV AC cable lines, such as protection studies, leading current interruption and zero-missing phenomenon. Countermeasures are proposed to these problems.

Chapter 7   Conclusion

The final chapter summarizes the results of the insulation coordination study of the Kyndbyværket – Asnæsværket line and new contributions of the PhD project to the future cable studies.

References

[1]   *Danish Annual Energy Statistics 2011*, (available on the web) Danish Energy Authority, October 2008, http://www.ens.dk/en-US/Info/FactsAndFigures/Energy_statistics_and_indicators/Annual%20 Statistics/Documents/Energy%20in%20Denmark%202010.pdf.

[2]   *Update of Service Experience of HV Underground and Cable Systems*, CIGRE Technical Brochure 379, April 2009

[3]   *Technical report on the future expansion and undergrounding of the electricity transmission grid*, (available on the web) Energinet.dk, April 2008, https://selvbetjening.preprod.energinet.dk/NR/rdonlyres/CC966C3A-FE78-41D8-9DC7-6B45 5210B502/0/TechnicalReportSummary.pdf.

[4]   *Joint Feasibility Study on the 400kV Cable Line Endrup-Idomlund: Final Report*, Tokyo Electric Power Company, April 2008,

[5]   *Assessment of the Technical Issues relating to Significant Amounts of EHV Underground Cable in the All-island Electricity Transmission System*, (available on the web) Tokyo Electric Power Company, November 2009, http://www.eirgrid.com/media/Tepco%20Report.pdf.

[6]   V. Akhmatov. "Excessive over-voltage in long cables of large offshore windfarms," *Wind Engineering*, vol. 30, no. 5, pp. 375-383, 2006

[7]   N. Momose, H. Suzuki, S. Tsuchiya, T. Watanabe, "Planning and Development of 500 kV Underground Transmission System in Tokyo Metropolitan Area," *CIGRE Session 1998*, 37-202

[8]   T. Kawamura, T. Kouno, S. Sasaki, E. Zaima, T. Ueda, Y. Kato, "Principles and Recent Practices of Insulation Coordination in Japan," *CIGRE Session 2000*, 33-109

[9]   L. Colla, S. Lauria, F. M. Gatta, "Temporary Overvoltages due to Harmonic Resonance in Long EHV Cables," *IPST 2007*, http://www.ipst.org/techpapers/2007/ipst_2007/papers_IPST2007/Session16/233. pdf.

[10]   M. Rebolini, L. Colla, F. Iliceto, "400 kV AC new submarine cable links between Sicily and the Italian mainland. Outline of project and special electrical studies," *CIGRE Session 2008*, C4-116

[11]   Atef Morched, Bjørn Gustavsen, Manoocher TartibiA, "Universal Model for Accurate Calculation of Electromagnetic Transients on Overhead Lines and Underground Cables," *IEEE Trans. on Power Delivery*, vol. 14, no.3, July 1999

[12]   Bjørn Gustavsen, Adam Semlyen, "Simulation of Transmission Line Transients Using Vector Fitting and Modal Decomposition," *IEEE Trans. on Power Delivery*, vol. 13, no. 2, April 1998

[13] B. Gustavsen, J. Sletbak, T. Henriksen, "Calculation of Electromagnetic Transients in Transmission Cables and Lines Taking Frequency Dependent Effects Accurately into Account," IEEE Trans. on Power Delivery, vol. 10, no. 2, April 2005

[14] T.Noda, N.Nagaoka, A.Ametani, "Phase Domain Modeling of Frequency-Dependent Transmission Lines by Means of an ARMA Model," *IEEE Trans. on Power Delivery*, vol. 11, no. 1, January 1996

[15] T.Noda, N.Nagaoka, A.Ametani, "Further Improvements to a Phase-Domain ARMA Line Model in Terms of Convolution, Steady-State Initialization, and Stability," *IEEE Trans. on Power Delivery*, vol. 12, no. 3, July 1997

[16] N. Amekawa, N. Nagaoka, V. Baba and A. Ametani, "Derivation of a semiconducting layer impedance and its effect on wave propagation characteristics on a cable," *IEE Proceedings*, Generation, Transmission and Distribution, vol. 150, issue 4, page(s): 434 – 440, July 2003

[17] A. Ametani, Y. Miyamoto, N. Nagaoka, "Semiconducting Layer Impedance and its Effect on Cable Wave-Propagation and Transient Characteristics," *IEEE Trans. on Power Delivery*, vol. 19, no. 4, October 2004

[18] N. Amekawa, N. Nagaoka and A. Ametani, "Impedance Derivation and Wave Propagation Characteristics of Pipe-Enclosed and Tunnel-Installed Cables," *IEEE Trans. on Power Delivery*, vol. 19, no. 1, January 2004

[19] H. V. Nguyen, H. W. Dommel, J. R. Marti, "Direct Phase-Domain Modelling of Frequency-Dependent Overhead Transmission Lines," *IEEE Trans. on Power Delivery*, vol. 12, no. 3, July 1997

[20] F. Castellanos, J. R. Marti, "Full Frequency-dependent Phase-domain Transmission Line Model," *IEEE Trans on Power Systems*, vol. 12, no. 3, August 1997

[21] Ting-Chung Yu, J. R. Marti, "A Robust Phase-Coordinates Frequency-Dependent Underground Cable Model (zCable) for the EMTP," *IEEE Trans. on Power Delivery*, vol. 18, no. 1, January 2003

[22] Abner Ramirez, J. Luis Naredo, Pablo Moreno, "Full Frequency-Dependent Line Model for Electromagnetic Transient Simulation Including Lumped and Distributed Sources," *IEEE Trans. on Power Delivery*, vol. 20, no. 1, January 2005

[23] *Insulation Coordination for Power Systems*, Andrew R. Hileman, published by Marcel Dekker Inc., June 1999

[24] CIGRE WG 13.02, "Switching Overvoltages in EHV and UHV Systems with Special Reference to Closing and Reclosing Transmission Lines," *ELECTRA*, Oct. 1973, pp. 70-122

Chapter 2 Reactive Power Compensation

2.1 Kyndbyværket – Asnæsværket Line

This section briefly introduces the Kyndbyværket – Asnæsværket line, which is being planned by Energinet.dk.

The 400 kV network in Zealand is shown by red lines in Fig. 2.1. Solid lines are overhead lines, and dotted lines are cable lines. The Kyndbyværket – Asnæsværket line will complete the loop configuration of the 400 kV network, which will improve the overall reliability of the Danish power system.

Fig. 2.1 Danish power system and Kyndbyværket – Asnæsværket line.

As the length of the Kyndbyværket – Asnæsværket line is expected to be 60 km, the cable line will definitely require reactive power compensation as discussed in this chapter. It has not been determined yet if a switching station or a substation will be built at Torslunde, but it will not change the necessity of the reactive power compensation.

2.2 Considerations in Reactive Power Compensation

Cable lines become sources of reactive power like shunt capacitors. Especially, long EHV cable lines produce large reactive power and usually require reactive power compensation for the following reasons:

- Suppress the steady-state overvoltage around the cable line
- Suppress the steady-state overvoltage at the cable open terminal
- Prevent the reduction of the active power transmission capacity due to the large charging current
- Reduce the leading current that flows through the line breaker so that it becomes lower than the leading current interruption capability of the line breaker

When the compensation rate 100 % is adopted, the installation of the cable line does not affect the reactive power balance around the cable line. Because of this, the compensation rate of 100 % is usually preferred in the planning of the cable line.

However, the compensation rate near 100 % cannot be achieved in some cases due to the unit size of shunt reactors for the compensation. For example, when a cable line has a charging capacity 250 MVar, two units of 100 MVar shunt reactors may be installed for the compensation, which results in the compensation rate of 80 %. In order to raise the compensation rate, the unit size needs to be increased to, for example, 120 MVar, but it is sometimes not a cost effective selection depending on manufacturers.

When the compensation rate, as a result, becomes low, it leads to steady-state overvoltage on the cable line. In addition, the compensation rate becomes low when the cable line needs to be operated even if one unit of the shunt reactor is out of service. It is not a focus of this PhD project, but it requires a careful consideration in the planning process.

The low compensation rate also leads to higher temporary overvoltages. It is highly recommended to study the temporary overvoltage in the feasibility study or at an earlier stage as it may affect the decision on the reactive power compensation in the planning process.

2.3 Impedance and Admittance Calculations

In order to perform the reactive power compensation analysis, the impedance and admittance of the 400 kV Kyndbyværket – Asnæsværket line are calculated in this section. The cable type assumed for the Kyndbyværket – Asnæsværket line is Al 1600 mm^2 XLPE cable (Al sheath). Physical and electrical parameters of the cable are given in Section 3.3.1.

2.3.1   Impedance Calculation in IEC 60909-2

The impedance of a cable is often measured after the installation by a cable supplier. Before the cable is installed, it has to be calculated by theoretical formulas.

In IEC/TR 60909-2 ed2.0 (2008) "Short-circuit currents in three-phase a.c. systems - Part 2: Data of electrical equipment for short-circuit current calculations", impedance formulas are given as follows [2]:

$$Z_1 = R_L + j\omega\frac{\mu_0}{2\pi}\left(\frac{1}{4} + \ln\frac{d}{r_L}\right) + \frac{\left(\omega\frac{\mu_0}{2\pi}\ln\frac{d}{r_{Sm}}\right)^2}{R_S + j\omega\frac{\mu_0}{2\pi}\ln\frac{d}{r_{Sm}}} \qquad \text{Eqn. 2.1}$$

$$Z_0 = R_L + 3\omega\frac{\mu_0}{8} + j\omega\frac{\mu_0}{2\pi}\left(\frac{1}{4} + 3\ln\frac{\delta}{\sqrt[3]{r_L d^2}}\right) - \frac{\left(3\omega\frac{\mu_0}{8} + j3\omega\frac{\mu_0}{2\pi}\ln\frac{\delta}{\sqrt[3]{r_{Sm}d^2}}\right)^2}{R_S + 3\omega\frac{\mu_0}{8} + j3\omega\frac{\mu_0}{2\pi}\ln\frac{\delta}{\sqrt[3]{r_{Sm}d^2}}} \qquad \text{Eqn. 2.2}$$

Here, Z_1 : positive sequence impedance

Z_0 : zero sequence impedance

R_L : conductor resistance

R_S : metallic sheath resistance

d : geometric mean distance between phases

r_L : core radius

r_{Sm} : cable outer radius

$\delta = \dfrac{1.85}{\sqrt{\dfrac{\omega\mu_0}{\rho}}}$: equivalent penetration depth

ρ : soil resistivity

We now show how the positive sequence impedance is derived in IEC 60909-2. Only the positive sequence impedance is necessary for the reactive compensation analysis.

The voltage drop caused by the current in the conductor can be calculated by

$$V = Z_c I_c - Z_m I_s$$ 　　　　　　　　　　Eqn. 2.3

where I_c and I_s are conductor and sheath currents, and Z_c and Z_m are conductor self and mutual impedances between the core and the metallic sheath.

Assuming the sheath is solidly-bonded and earthed at both ends, the following equation is satisfied:

$$0 = Z_m I_c - Z_s I_s$$ 　　　　　　　　　　Eqn. 2.4

Here, $Z_s = R_S + Z_m = R_S + jX_m$ is the sheath self impedance.

Eliminating I_s from Eqn. 2.3 using Eqn. 2.4,

$$
\begin{aligned}
V &= Z_c I_c - \frac{Z_m{}^2}{Z_s} I_c \\[2mm]
&= \left(Z_c - \frac{Z_m{}^2}{Z_s} \right) I_c \\[2mm]
&= \left(Z_c + \frac{X_m{}^2}{R_S + jX_m} \right) I_c
\end{aligned}
$$ 　　　Eqn. 2.5

Therefore,

$$
\begin{aligned}
Z_1 &= Z_c + \frac{X_m{}^2}{R_S + jX_m} \\[3mm]
&= R_L + j\omega \frac{\mu_0}{2\pi} \left(\frac{1}{4} + \ln \frac{d}{r_L} \right) + \frac{\left(\omega \frac{\mu_0}{2\pi} \ln \frac{d}{r_{Sm}} \right)^2}{R_S + j\omega \frac{\mu_0}{2\pi} \ln \frac{d}{r_{Sm}}}
\end{aligned}
$$ 　　　Eqn. 2.6

It is verified that the impedance formulas in IEC 60909-2 are derived assuming solidly-bonded cables and ignoring a grounding resistance of the sheath at substations.

2.3.2   Derivation of Theoretical Formulas of Sequence Currents

The sequence impedance / current calculation of overhead lines is well known and introduced in textbooks [1]. For underground cables, theoretical formulas are proposed for the cable itself [2]-[5] as described in the previous section. In order to derive accurate theoretical formulas, however, it is necessary to consider the whole cable system, including sheath bonding, since the return current of an underground cable flows through both metallic sheath and ground. Until now, there has existed no formula of the sequence impedances / currents which can consider sheath bonding and sheath grounding resistance at substations and normal joints. As a result, it has been a common practice that those sequence impedances or currents are measured after the installation, and it is considered difficult to predict those values beforehand.

For underground cable systems which are longer than about 2 km, it is a common practice to cross-bond the metallic sheaths of three phase cables to reduce sheath currents and to suppress sheath voltages at the same time [6]. Submarine cables, which are generally solidly-bonded, are now becoming a popular type of cable due to the increase of off-shore wind farms and cross-border transactions.

Therefore, this section derives theoretical formulas of the sequence currents for a majority of underground cable systems, that is, a cross-bonded cable which has more than a couple of major sections. It also derives theoretical formulas for a solidly-bonded cable, considering the increased use of submarine cables.

2.3.2.1   Cross-bonded Cable

(a) 6×6 impedance matrix

One cable system corresponds to 6 conductor system composed of 3 cores and 3 metallic sheaths. The 6×6 impedance matrix of the cable system is given by the following equation [1].

$$[Z] = \begin{bmatrix} [Zc] & [Zm] \\ [Zm]^t & [Zs] \end{bmatrix} = \begin{bmatrix} [Zc] & [Zm] \\ [Zm] & [Zs] \end{bmatrix} \qquad \text{Eqn. 2.7}$$

$$[Zc] = \begin{bmatrix} Zaa & Zab & Zac \\ Zab & Zbb & Zab \\ Zac & Zab & Zcc \end{bmatrix}_c, \quad [Zs] = \begin{bmatrix} Zaa & Zab & Zac \\ Zab & Zbb & Zab \\ Zac & Zab & Zcc \end{bmatrix}_s$$

$$[Zm] = \begin{bmatrix} Zaa & Zab & Zac \\ Zab & Zbb & Zab \\ Zac & Zab & Zcc \end{bmatrix}_m$$

where c: core,   s: sheath,   m: mutual coupling between core and sheath, t: transpose

In Eqn. 2.7, cable phase a is assumed to be laid symmetrical to phase c against phase b. The flat configuration and the trefoil configuration, which are typically adopted, satisfy this assumption.

(b) 4 × 4 reduced impedance matrix [7][8]

The lengths of minor sections can have imbalances due to the constraint on the location of joints. The imbalances are designed to be as small as possible since they increases sheath currents and raises sheath voltages. When a cable system has multiple major sections, the overall balance is considered to minimize sheath currents. As a result, when a cable system has more than a couple of major sections, sheath currents are generally balanced among 3 conductors, which allows us to reduce 3 metallic sheaths to one conductor.

Reducing the sheath conductors, the 6 conductor system is reduced to the 4 conductor system composed of 3 cores and 1 equivalent metallic sheath as shown in Fig. 2.2. The 4 × 4 reduced impedance matrix can be expressed as

$$[Z'] = \begin{bmatrix} Zaa & Zab & Zac & Zsa \\ Zab & Zbb & Zab & Zsb \\ Zac & Zab & Zaa & Zsa \\ Zsa & Zsb & Zsa & Zss \end{bmatrix}$$

Eqn. 2.8

Here, $Z'(4, j) = Z'(j, 4)$ can be calculated from the 6 × 6 impedance matrix Z as

$$Z'(4, j) = \frac{1}{3} \sum_{i=4}^{6} Z(i, j); \quad j = 1 \cdots 4$$

Eqn. 2.9

(a) Cross-bonded cable system with m-major sections

(b) Equivalent 4 conductor system
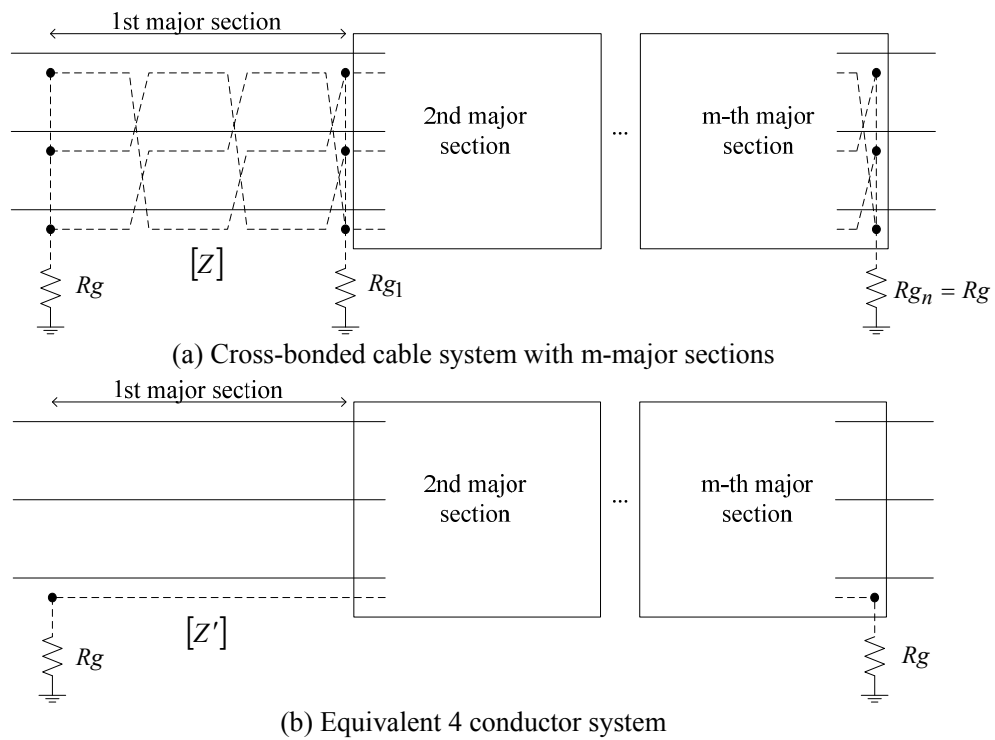
Fig. 2.2 Cross-bonded cable and its equivalent model.

(c) Zero sequence current

The following equations are derived from Fig. 2.3. Here, sheath grounding at normal joints is ignored, but sheath grounding at substations can be considered through *Vs*.

$$(V_1) = [Z'](I_1)$$ Eqn. 2.10

where
$$(V_1) = (E \quad E \quad E \quad Vs)^t$$
$$(I_1) = (Ia \quad Ib \quad Ic \quad Is)^t$$

Fig. 2.3(a) shows the setup for measuring the zero-sequence current for a cross-bonded cable
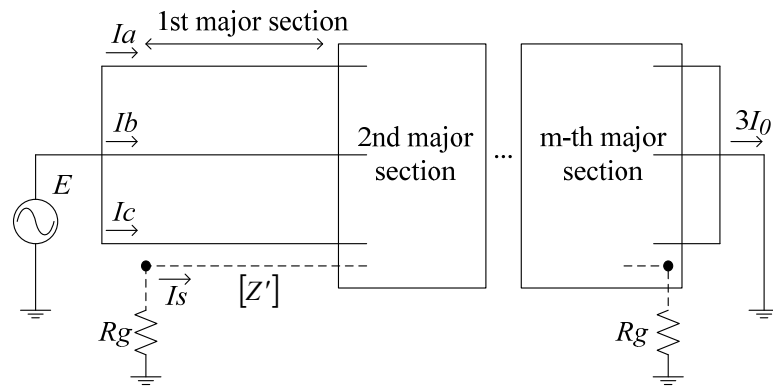
(a) Zero-sequence current
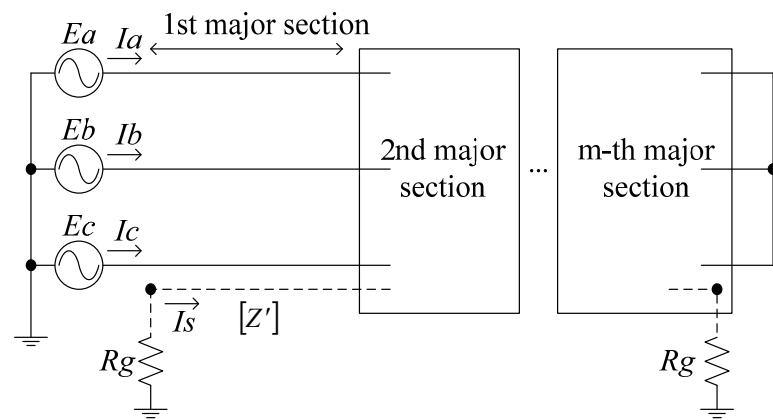
(b) Positive-sequence current

Fig. 2.3 Setup for measuring sequence currents for a cross-bonded cable.

Assuming the grounding resistance at substations Rg, the sheath voltage Vs can be found by

$$Vs = -2RgIs \qquad \text{Eqn. 2.11}$$

Since $Zsa = Zsc$ stands in the flat configuration and the trefoil configuration, the following equations can be obtained by solving Eqn. 2.10 and Eqn. 2.11.

$$Ia = Ic = (Z_{22} - Z_{12})E/\Delta_0$$
$$Ib = (Z_{11} - Z_{21})E/\Delta_0 \qquad \text{Eqn. 2.12}$$

where

$$\Delta_0 = Z_{11}Z_{22} - Z_{12}Z_{21}$$

$$Z_{11} = Zaa + Zac - 2Zsa^2/Z'ss$$

$$Z_{22} = Zbb - Zsb^2/Z'ss$$

$$Z_{12} = Zab - Zsa\,Zsb/Z'ss, \quad Z_{21} = 2Z_{12}$$

$$Z'ss = Zss + 2Rg$$

The zero-sequence current can be found from Eqn. 2.12 in the following equation.

$$I_0 = (2Ia + Ib)/3$$
$$= \frac{E}{3\Delta_0}(Z_{11} + 2Z_{22} - 2Z_{12} - Z_{21}) \qquad \text{Eqn. 2.13}$$

When three phase cables are laid symmetrical to each other, the following equations are satisfied.

$$Zaa_c = Zbb_c = Zc, \quad Zaa_s = Zbb_s = Zs$$
$$Zab_c = Zac_c = Zm, \quad Zsa = Zsb = Zn \qquad \text{Eqn. 2.14}$$

Using symmetrical impedances Zc, Zm, and Zn in Eqn. 2.14, Z_{11}, Z_{22}, and Z_{12} can be expressed as

$$Z_{11} = Zc + Zm - 2Zn^2/Z'ss$$

$$Z_{22} = Zc - Zn^2/Z'ss \qquad \text{Eqn. 2.15}$$

$$Z_{12} = Zm - Zn^2/Z'ss$$

Substituting Z_{11}, Z_{22}, and Z_{12} in Eqn. 2.12 and Eqn. 2.13 by the symmetrical impedances,

$$Ia = Ib = Ic \approx E / \Delta_1 , \quad Is \approx -3ZnE / Z'ss\Delta_1$$

$$I_0 \approx E / \Delta_1$$

<div align="right">Eqn. 2.16</div>

where $\Delta_1 = Zc + 2Zm - 3Zn^2 / Z'ss$

(d) Positive sequence current

In Fig. 2.3(b), the equation $Isa + Isb + Isc = 0$ is satisfied at the end of the cable line. The following equations are obtained since $Vs = 0$.

$$(V_1) = \begin{bmatrix} E & \alpha^2 E & \alpha E & 0 \end{bmatrix}^t$$

$$(I_1) = \begin{bmatrix} Ia & Ib & Ic & Is \end{bmatrix}^t$$

<div align="right">Eqn. 2.17</div>

where $\alpha = \exp(j2\pi/3)$

Solving Eqn. 2.17 for *Ia*, *Ib*, and *Ic* yields Eqn. 2.18.

$$\begin{pmatrix} E \\ \alpha^2 E \\ \alpha E \end{pmatrix} = \begin{bmatrix} Z_{11} & Z_{12} & Z_{13} \\ Z_{12} & Z_{22} & Z_{12} \\ Z_{13} & Z_{12} & Z_{11} \end{bmatrix} \begin{pmatrix} Ia \\ Ib \\ Ic \end{pmatrix}$$

$$\therefore \begin{pmatrix} Ia \\ Ib \\ Ic \end{pmatrix} = \begin{bmatrix} Z_{11} & Z_{12} & Z_{13} \\ Z_{12} & Z_{22} & Z_{12} \\ Z_{13} & Z_{12} & Z_{11} \end{bmatrix}^{-1} \begin{pmatrix} E \\ \alpha^2 E \\ \alpha E \end{pmatrix}$$

$$= \frac{1}{\Delta} \begin{bmatrix} Z_{11}Z_{22} - Z_{12}^2 & Z_{12}(Z_{13} - Z_{11}) & Z_{12}^2 - Z_{13}Z_{22} \\ Z_{12}(Z_{13} - Z_{11}) & Z_{11}^2 - Z_{13}^2 & Z_{12}(Z_{13} - Z_{11}) \\ Z_{12}^2 - Z_{13}Z_{22} & Z_{12}(Z_{13} - Z_{11}) & Z_{11}Z_{22} - Z_{12}^2 \end{bmatrix} \begin{pmatrix} E \\ \alpha^2 E \\ \alpha E \end{pmatrix}$$

<div align="right">Eqn. 2.18</div>

Here,

$$Z_{11} = Zaa - Zsa^2 / Zss$$

$$Z_{22} = Zbb - Zsb^2 / Zss$$

$$Z_{12} = Zab - Zsa\, Zsb / Zss$$

$$Z_{13} = Zab - Zsa\, Zsc / Zss$$

The positive sequence current is derived from Eqn. 2.18.

$$I_1 = \frac{1}{3}(Ia + \alpha Ib + \alpha^2 Ic)$$

$$= \frac{E}{3\Delta_2}\{(Z_{11} - Z_{13})(Z_{11} + Z_{13} + 2Z_{12})$$

$$+ Z_{22}(2Z_{11} + Z_{13}) - 3Z_{12}^2\}$$

Eqn. 2.19

where $\Delta_2 = (Z_{11} - Z_{13})\{Z_{22}(Z_{11} + Z_{13}) - 2Z_{12}^2\}$

When three phase cables are laid symmetrical to each other, Eqn. 2.19 can be further simplified using Eqn. 2.14.

$$I_1 = \frac{E}{Zc - Zm}$$

Eqn. 2.20

2.3.2.2 Solidly-bonded Cable

(a) 6 × 6 impedance matrix

Fig. 2.4 shows a sequence current measurement circuit for a solidly-bonded cable. The following equations are given from the 6 × 6 impedance matrix in Eqn. 2.7 and Fig. 2.4.

$$(E) = [Zc](I) + [Zm](Is)$$

Eqn. 2.21

$$(Vs) = [Zm](I) + [Zs](Is) = -2[Rg](Is)$$

Eqn. 2.22

Here, $(I) = (Ia \quad Ib \quad Ia)^t$:   core current

$(Is) = (Isa \quad Isb \quad Isa)^t$:   sheath current

$$[Rg] = Rg\begin{bmatrix} 1 & 1 & 1 \\ 1 & 1 & 1 \\ 1 & 1 & 1 \end{bmatrix}$$

From Eqn. 2.22, sheath current (Is) is found by

$$(Is) = -([Zs] + 2[Rg])^{-1}[Zm](I)$$

Eqn. 2.23

Eliminating sheath current (Is) in Eqn. 2.21, core current (I) can be derived as

$$(I) = \left([Zc] - [Zm]([Zs] + 2[Rg])^{-1}[Zm]\right)^{-1}(E) \qquad \text{Eqn. 2.24}$$
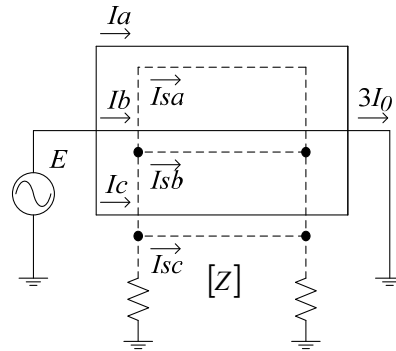
(a) Zero-sequence current
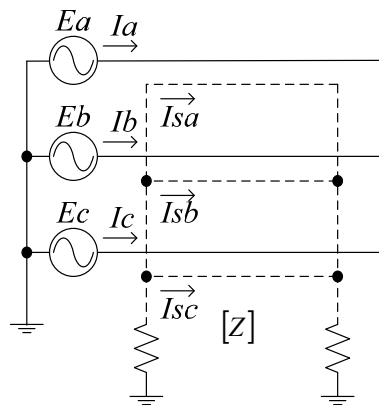
(b) Positive-sequence current

Fig. 2.4 Setup for measuring sequence currents for a solidly-bonded cable.

(b) Zero sequence current

From Fig. 2.4(a), (E) and (I) are expressed as

$$(E) = [E \ E \ E]^t, \ (I) = [Ia \ Ib \ Ia]^t \qquad \text{Eqn. 2.25}$$

Core current (I) is obtained from Eqn. 2.24 and Eqn. 2.25, and then the zero sequence current is calculated as $I_0 = (Ia + Ib + Ic)/3$.

Since the relationship $[Zm] \approx [Zs]$ generally stands, Eqn. 2.21 and Eqn. 2.22 can be simplified to Eqn. 2.26 using Eqn. 2.14.

$$
\begin{aligned}
((E) - (Vs)) &= ([Zc] - [Zs])(I) \\
&= (Zc - Zs)[U](I)
\end{aligned}
$$

Eqn. 2.26

where $[U]$: 3 $\times$ 3 unit (identity) matrix

Hence,

$$
\begin{aligned}
I_0 &= Ia = Ib = Ic \\
&= \frac{1}{Zc - Zs}(E - Vs)
\end{aligned}
$$

Eqn. 2.27

Using Eqn. 2.27, core current (I) in Eqn. 2.22 can be eliminated, which yields Eqn. 2.28.

$$
(Vs) = \frac{1}{Zc - Zs}[Zm]((E) - (Vs)) - [Zm](Is)
$$

Eqn. 2.28

Adding all three rows in Eqn. 2.28,

$$
3Vs = 3\frac{Zs + 2Zm}{Zc - Zs}(E - Vs) - \frac{Zs + 2Zm}{2Rg}Vs
$$

Eqn. 2.29

Solving Eqn. 2.29 for *Vs* and eliminating *Vs* from Eqn. 2.27, the zero sequence current is found as

$$
I_0 = \frac{6Rg + Zs + 2Zm}{6Rg(Zc + 2Zm) + (Zc - Zs)(Zs + 2Zm)}E
$$

Eqn. 2.30

(c)   Positive sequence current

From Fig. 2.4(b), (E) and (I) are expressed as

$$
(E) = \begin{bmatrix} E & \alpha^2 E & \alpha E \end{bmatrix}^t, \quad (I) = \begin{bmatrix} Ia & Ib & Ia \end{bmatrix}^t
$$

Eqn. 2.31

Core current (I) is obtained from Eqn. 2.24 and Eqn. 2.31. Once the core current is found, the

positive sequence current can be calculated as $I_1 = (Ia + \alpha Ib + \alpha^2 Ic)/3$.

The theoretical formula of the positive sequence current can also be simplified using Eqn. 2.26.

$$I_1 = \frac{1}{3(Zc - Zs)} \left\{ (E - Vs) + \alpha (\alpha^2 E - Vs) + \alpha^2 (\alpha E - Vs) \right\}$$

$$= \frac{E}{Zc - Zs} \qquad \text{Eqn. 2.32}$$

Eqn. 2.32 shows that the positive sequence current can be approximated by the coaxial mode current. It also shows that, similarly to a cross-bonded cable, the positive sequence current is not affected by substation grounding resistance *Rg*.

2.3.3 Comparison with EMTP Simulations

A comparison with EMTP simulations are conducted in order to verify the accuracy of theoretical formulas derived in the previous chapter.

Fig. 2.5 shows physical and electrical data of the 400 kV cable used for the comparison. An existence of semi-conducting layers introduces an error in the charging capacity of the cable. Relative permittivity of the insulation (XLPE) is converted from 2.4 to 2.729 according to Eqn. 2.33 in order to correct the error and have a reasonable cable model [9].
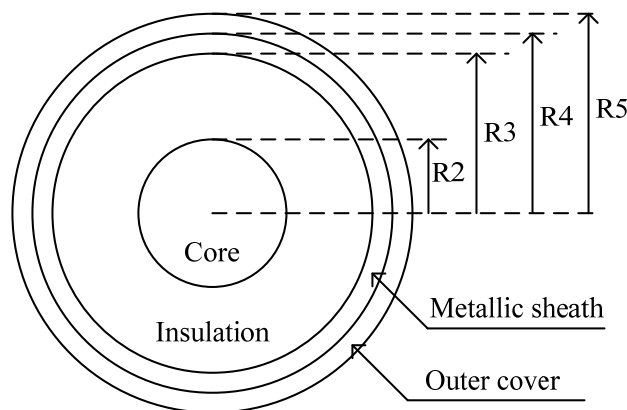
Core inner radius: 0.0 cm, R2 = 3.26 cm, R3 = 6.14 cm, R4 = 6.26 cm, R5 = 6.73 cm

Core resistivity: 1.724×10^{-8} Ωm, Metallic sheath resistivity: 2.840×10^{-8} Ωm,

Relative permittivity (XLPE, PE): 2.4

Fig. 2.5 Physical and electrical data of the cable.

$$\varepsilon_r' = \frac{\ln(R3/R2)}{\ln(Rso/Rsi)}\varepsilon_r = \frac{\ln(61.40/32.60)}{\ln(59.50/34.10)} \cdot 2.4 = 2.729 \qquad \text{Eqn. 2.33}$$

where Rsi: inner radius of the insulation, Rso: outer radius of the insulation

Fig. 2.6 shows the layout of the cables. It is assumed that the cables are directly buried at the depth of 1.3 m with the separation of 0.5 m between phases.
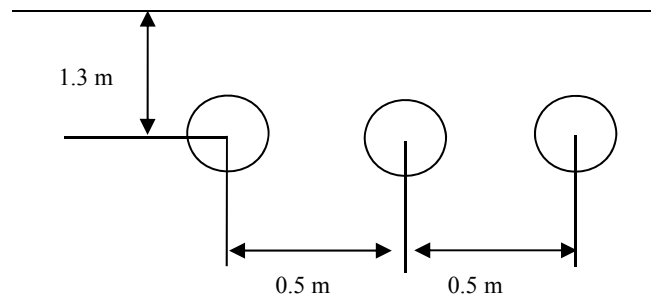
Fig. 2.6 Layout of the cable.

The lengths of a minor section and a major section are respectively set to 400 m and 1200 m. The total length of the cable is set as 12 km with 10 major sections.

Calculation process in case of a cross-bonded cable using proposed formulas is shown below. The 6 × 6 impedance matrix Z is found by CABLE CONSTANTS [10]-[12]:

[Z'] (unit: Ω)

$0.716463 + j8.449867 \quad 0.591366 + j6.285238 \quad 0.591366 + j5.762618 \quad 0.591371 + j6.635667$
$0.591366 + j6.285238 \quad 0.716463 + j8.449867 \quad 0.591366 + j6.285238 \quad 0.591371 + j6.809874$
$0.591366 + j5.762618 \quad 0.591366 + j6.285238 \quad 0.716463 + j8.449867 \quad 0.591371 + j6.635667$
$0.591371 + j6.635667 \quad 0.591371 + j6.809874 \quad 0.591371 + j6.635667 \quad 0.834382 + j6.634853$

Zero Sequence Current

$\Delta_0 = -3.9605900 + j12.489448$

$Z_{11} = 4.0641578 + j2.2224336$

$Z_{22} = 2.1959039 + j2.1450759$

$Z_{12} = 2.0193420 + j0.1372637$

$Z_{21} = 4.0386840 + j0.2745275$

$I_0(\text{rms}) = 81.814700 - j31.778479$

Positive Sequence Current

$\Delta_2 = -4.8574998 - j1.8394591$

$Z_{11} = 0.3670612 + j1.8221556$

$Z_{22} = 0.3801952 + j1.4707768$

$Z_{12} = 0.2482475 - j0.5159115$

$Z_{13} = 0.2419636 - j0.8650940$

$I_1(\text{rms}) = 14.118637 - j251.86277$

Table 2-1 shows zero and positive sequence currents derived by proposed formulas and EMTP simulations. In the calculations, the applied voltage is set to E = 1 kV / $\sqrt{3}$ (angle: 0 degree) and the source impedance is not considered. In this thesis, sequence currents are derived in accordance with the setups for measuring sequence currents in Fig. 2.3 and Fig. 2.4. The assumptions on the applied voltage and the source impedance match a condition in actual setups for measuring sequence currents since testing sets are generally used in the measurements. Grounding resistances at substations and normal joints are set to 1Ω and 10Ω, respectively

Table 2-1 Comparison of Proposed Formulas with EMTP Simulations

(a) Cross-bonded cable

	Zero Sequence		Positive Sequence	
	Amplitude [A]	Angle [deg]	Amplitude [A]	Angle [deg]
EMTP Simulation	133.8	-21.42	356.4	-86.35
Proposed formulas, eq. (8)/(14)	124.1	-21.23	356.7	-86.79

(b) Solidly-bonded cable

	Zero Sequence		Positive Sequence	
	Amplitude [A]	Angle [deg]	Amplitude [A]	Angle [deg]
EMTP Simulation	121.6	-21.80	694.9	-50.40
Proposed formulas, eq. (19), (20)/(26)	124.8	-22.50	722.7	-49.08

From the results in Table 2-1, it is confirmed that the proposed formulas have satisfactory accuracy for planning and implementation studies, compared to the results of EMTP simulations. An error of 7 % is observed in the zero sequence current of a cross-bonded cable. It is caused by the impedance matrix reduction discussed in Section 2.3.2. Due to the matrix reduction, unbalanced sheath currents that flow into earth at normal joints are not considered in proposed formulas.

Table 2-1 shows that the positive sequence impedance is smaller for a solidly-bonded cable than for a cross-bonded cable as the positive sequence current is larger for a solidly-bonded cable. This is because the return current flows only through the metallic sheath of the same cable and earth in the solidly-bonded cable whereas the return current flows through the metallic sheath of all the three phase cables in a cross-bonded cable ($Zc - Zm > Zc - Zs$).

The impedance calculation in IEC 60909-2 assumes solidly-bonding as discussed in Section 2.3.1. As a result, if the positive sequence impedance of a cross-bonded cable is derived based on IEC 60909-2, it might be smaller than the actual positive sequence impedance.

The phase angle of the zero sequence current in Table 2-1 demonstrates that the zero sequence current is significantly affected by a grounding resistance at substations in both cross-bonded and solidly-bonded cables. As a result, there is little difference in the zero sequence impedance between the cross-bonded cable and the solidly-bonded cable. The result has indicated an importance of obtaining an accurate grounding resistance at substations to derive an accurate zero sequence impedances of cable systems.

2.3.4 Application to the Kyndbyværket – Asnæsværket Line

According to the proposed formulas, when $E = Ea = 1$ kV (rms) is applied, the sequence current in the Asnæsværket – Torslunde line can be calculated as:

Table 2-2 Sequence Current in the Asnæsværket – Torslunde Line

	Zero Sequence		Positive Sequence	
	Amplitude [A]	Angle [deg]	Amplitude [A]	Angle [deg]
EMTP Simulation	99.6	-21.0	164.1	-83.2
Proposed formulas	95.7	-18.5	164.3	-84.1

The Torslunde – Kyndbyværket line is composed of a land part (22 km) and a submarine part (10 km). The sequence current in the line is calculated as:

Table 2-3 Sequence Current in the Torslunde – Kyndbyværket Line

	Zero Sequence		Positive Sequence	
	Amplitude [A]	Angle [deg]	Amplitude [A]	Angle [deg]
EMTP Simulation	57.9	-22.8	165.1	-77.7
Proposed formulas	57.3	-22.3	166.1	-77.5

Table 2-2 and Table 2-3 show sequence currents in the Asnæsværket – Torslunde – Kyndbyværket line is calculated accurately by the proposed formulas.

2.3.5 Impedance and Admittance of the Kyndbyværket – Asnæsværket Line

Table 2-2 and Table 2-3 give us the impedances of the Asnæsværket – Torslunde line and the Torslunde – Kyndbyværket as shown in Table 2-4. In the table, the admittance of the line was calculated using Eqn. 2.34. Per unit values were calculated on a system base 100 MVA.

$$B_p = \omega \frac{2\pi \varepsilon_r \varepsilon_0}{\ln\left(\dfrac{Rso}{Rsi}\right)}$$
$$= 2\pi \cdot 50 \cdot \frac{2\pi \cdot 2.4 \cdot 0.008854}{\ln\left(\dfrac{55.0}{28.0}\right)} \times 10^{-6} \qquad \text{Eqn. 2.34}$$
$$= 6.213 \times 10^{-5} \quad [\text{mho/km}]$$

where ε_0 is permittivity of free space (0.008854 μF/km).

Table 2-4 Impedances and Admittances of the Kyndbyværket – Asnæsværket Line

	R	X	Y
Asnæsværket – Torslunde	0.515 ohm 0.000322 pu	4.943 ohm 0.00309 pu	0.001740 mho 2.783 pu
Torslunde – Kyndbyværket	1.066 ohm 0.000666 pu	4.800 ohm 0.00300 pu	0.001988 mho 3.181 pu

Table 2-4 shows the impedance and admittance of the Torslunde – Kyndbyværket line including both the land part (cross-bonded) and the submarine part (solidly-bonded). Table 2-5 calculates them separately.

Table 2-5 Impedance and Admittance of the Torslunde – Kyndbyværket Line

	R	X	Y
Land part (22 km)	0.405 ohm 0.000253 pu	3.884 ohm 0.00243 pu	0.001367 mho 2.187 pu
Submarine part (10 km)	0.661 ohm 0.000413 pu	0.916 ohm 0.000573 pu	0.0006213 mho 0.994 pu

2.4 Maximum Unit Size of 400 kV Shunt Reactors

Maximum unit size can be determined from the allowable voltage variation in switching operations. The Danish Grid Code specifies the following allowable voltage variations [13]:

- In the normal operating condition: 4 %

Generally, shunt reactors connected to the 400 kV buses are switched in the normal operating condition for the voltage control. In this case, the switching of the shunt reactor should not cause the voltage variation exceeding 4 %. In contrast, shunt reactors connected directly to the cable line are generally not switched for the voltage control since they are installed to meet leading current interruption or to suppress temporary overvoltage.

The following severe assumptions were applied in the analysis:
- The switching can be performed in the off-peak condition.
- There can be a shunt reactor station at Torslunde, but it is not a switching station or a substation.
- All generators at Asnæsværket and Kyndbyværket are out of operation.

Fig. 2.7, Fig. 2.8, and Fig. 2.9 respectively show the voltage variation caused by the shunt reactor switching at the Asnæsværket, Torslunde, and Kyndbyværket 400 kV buses. The figures show that the maximum unit size of the shunt reactor can be much higher than 300 MVar, even though 300 MVar is much larger than existing shunt reactors. Considering the charging capacity of the Kyndbyværket – Asnæsværket line, it is enough to confirm that 300 MVar shunt reactor can be adopted.
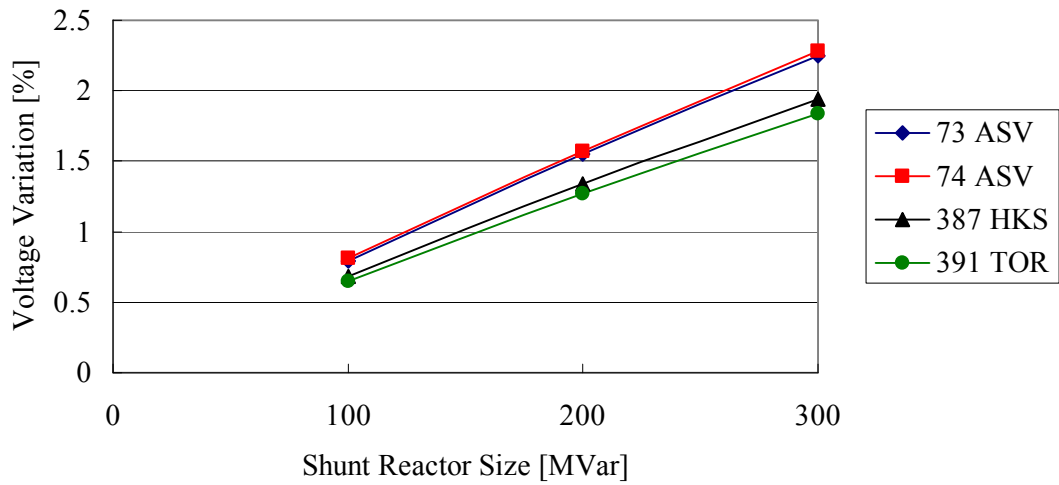
Fig. 2.7 Voltage variation caused by the shunt reactor switching at ASV 400 kV.
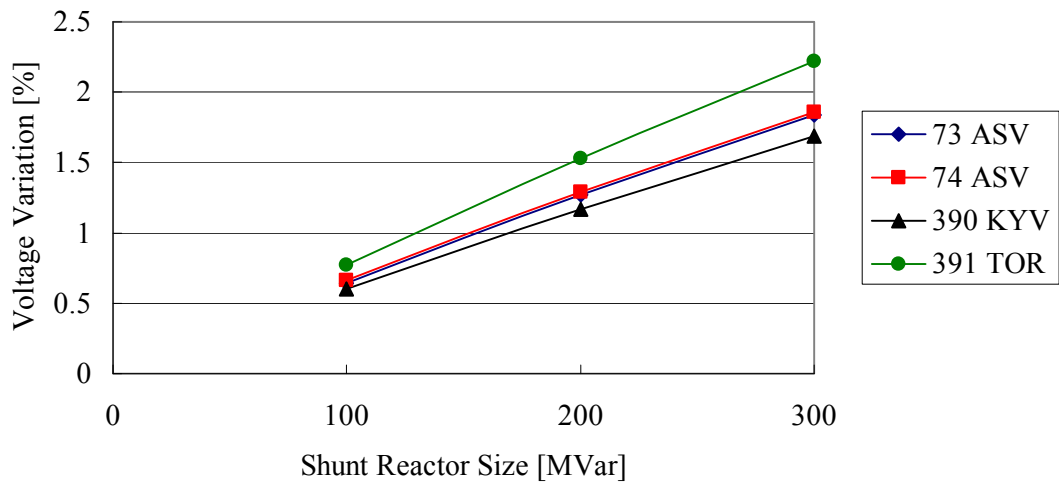
Fig. 2.8 Voltage variation caused by the shunt reactor switching at TOR 400 kV.
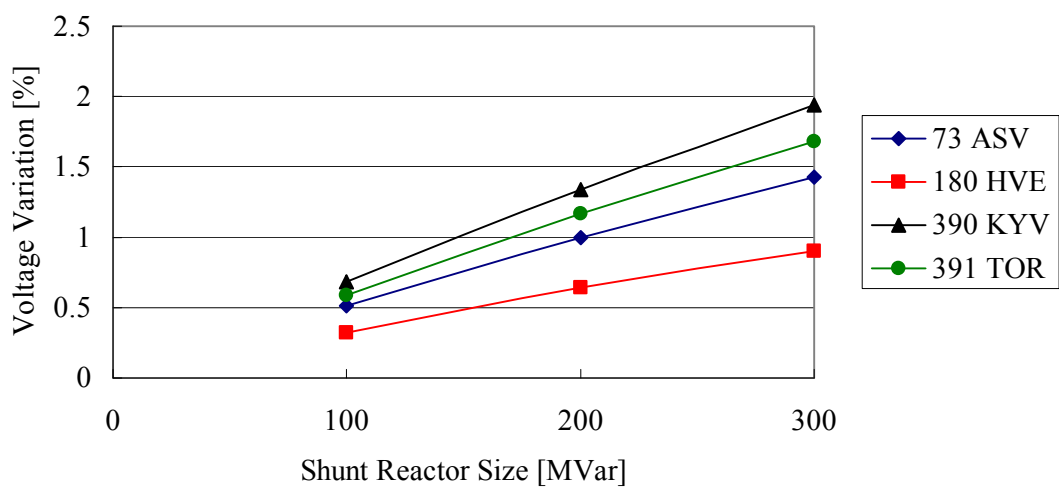
Fig. 2.9 Voltage variation caused by the shunt reactor switching at KYV 400 kV.

2.5 Compensation Patterns

In addition to the unit size limitation in the previous section, the switching of the cable with the shunt reactors should not cause the voltage variation exceeding 4 %. This requirement can set the restriction on the compensation rate. However, it is not an issue for most 400 / 500 kV cables. As their charging capacity is generally compensated line by line, the compensation rate near 100 % is often selected.

An area compensation is often adopted for 275 / 220 kV or lower voltages. In that case, shunt reactors are connected to the bus, not to the line, in many cases, and compensation rates range widely depending on the system requirements for the voltage control. Then, the voltage variation caused by the cable line switching becomes an important issue.

The following items are considered to determine compensation patterns and they suggest the compensation rate near 100 % is preferred:
- Voltage variation when switching the cable with shunt reactors
- Leading current interruption
- Ferranti phenomenon (sustained temporary overvoltage)

Considering the zero-miss phenomenon, lower compensation rates are preferred since the DC component of zero-miss current is smaller for lower compensation rates. However, it is not considered here as there are countermeasures that can be taken against the zero-miss phenomenon as discussed in Section 6.3.

The following items are not considered since they are not the scope of the PhD project:
- Voltage and reactive power control
- Transmission capacity

Charging capacity of the Kyndbyværket – Asnæsværket line is:
- Asnæsværket – Torslunde: 278.3 MVar at 400 kV
- Torslunde – Kyndbyværket: 318.1 MVar at 400 kV

The following compensation patterns are considered to compensate the charging capacity. It is assumed that these shunt reactors are connected directly to the line.

Table 2-6 Studied Compensation Patterns of the Kyndbyværket – Asnæsværket Line

	Pattern 1	Pattern 2	Pattern 3	Pattern 4
Asnæsværket	300 MVar	250 MVar	150 MVar	150 MVar
Torslunde	–	–	300 MVar	250 MVar
Kyndbyværket	300 MVar	300 MVar	150 MVar	150 MVar
Compensation Rate	100.7 %	92.2 %	100.7 %	92.2 %

Unit size will be considered after the voltage profile under the normal operating condition and active power loss are studied.

2.6 Voltage Profile under Normal Operating Conditions

The Kyndbyværket – Asnæsværket line was split into twelve sections:

Asnæsværket – Torslunde Line: 4.67 (= 28 / 6) km × 6 sections

Torslunde – Kyndbyværket Line: 5.5 (= 22 / 4) km × 4 sections (land section)

                                                 5 (= 10 / 2) km × 2 sections (submarine section)

Table 2-7 shows the impedance and admittance of these sections set to PSS/E data, and Fig. 2.10 shows the power flow in the Kyndbyværket – Asnæsværket line in the no load condition with the compensation Pattern 3.

The voltages at the Asnæsværket and Kyndbyværket 400 kV buses are fixed at 410 kV as a severe assumption.

Table 2-7 Impedances and Admittances of the Kyndbyværket – Asnæsværket Line

	R	X	Y
ASV – TOR (4.67 km)	0.0000537 pu	0.000515 pu	0.464 pu
TOR – KYV (5.5 km, land)	0.0000633 pu	0.000608 pu	0.547 pu
TOR – KYV (5.0 km, submarine)	0.000207 pu	0.000287 pu	0.497 pu
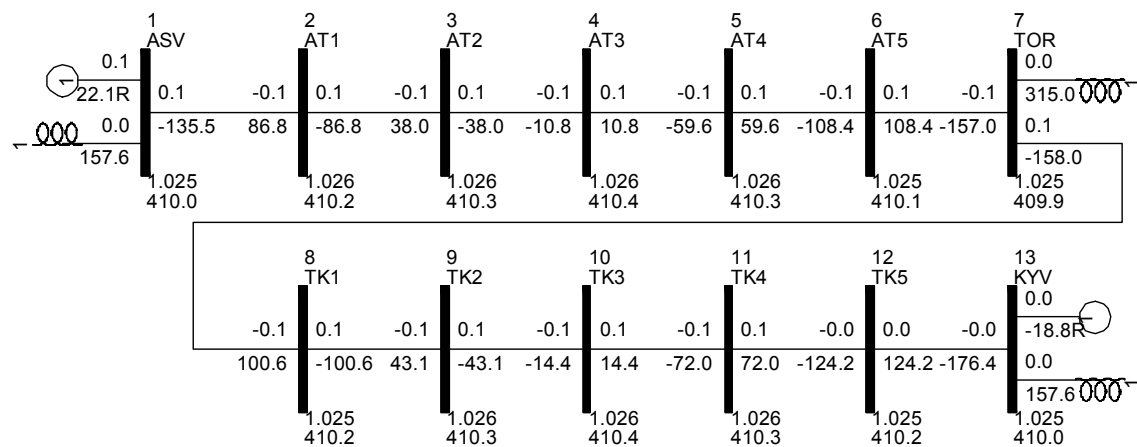
Fig. 2.10 Power flow in the Kyndbyværket – Asnæsværket line in the no load condition.

2.6.1 No Load Condition

Fig. 2.11 shows the voltage variation in the Kyndbyværket – Asnæsværket line in the no load condition. For the analysis, the active power output from the generator model at the Asnæsværket and Kyndbyværket 400 kV buses are set to nearly zero. Since the Asnæsværket 400 kV bus is the swing bus, there is small active power output 0.1 MW from the generator model.

From the result of the above analysis, the highest voltage along the Kyndbyværket – Asnæsværket line becomes greater than the both ends by 1.8 kV with the compensation Patterns 1 and 2. These two compensation patterns yield the same voltage profile as their difference is only the shunt reactor size at the Asnæsværket 400 kV bus where the bus voltage is fixed at 410 kV.

The compensation Patterns 3 and 4 yield even flatter voltage profile because of the shunt reactor at Torslunde. Most power systems do not require the flatness at this level; voltage profiles of all patterns are acceptable.

In Fig. 2.11, there is a discontinuity in the slope of the voltage profiles at the connection between land part and submarine part. It is caused by the difference of reactance per length between the cross-bonded cable and the solidly-bonded cable.

Fig. 2.11 Voltage variation in the Kyndbyværket – Asnæsværket line in the no load condition.

Table 2-8 shows the reactive power supplied into the Kyndbyværket – Asnæsværket line. Since Patterns 1 and 3 are over-compensation by 0.7 %, small reactive power 2 – 4 MVar has to be supplied from the outside. Patterns 2 and 4 are under-compensation by 7.8 %. It is reasonable that reactive power approximately 50 MVar flows out from the cable line to the outside.

This imbalance will not have a noticeable impact on the overall voltage and reactive power control of the network. The reactive power loss in the cable line is negligible because of the assumed no load condition.

Table 2-8 Reactive Power Supplied to the Kyndbyværket – Asnæsværket Line in the No Load Condition

	Asnæsværket [MVar]	Kyndbyværket [MVar]	Imbalance [MVar]
Pattern 1	23.8	-21.7	2.1
Pattern 2	-28.8	-21.7	-50.5
Pattern 3	22.1	-18.8	3.3
Pattern 4	-3.8	-45.4	-49.2

2.6.2　Maximum Power Flow Condition

The voltage profile can change in the maximum power flow condition. Al 1600 mm^2 XLPE cable is assumed for the Kyndbyværket – Asnæsværket line, and typical transmission capacity for this type of cable is around 800 – 900 MVA.

Fig. 2.12 shows the voltage variation with 800 MW power flow. The active power output from the generator model at Kyndbyværket is changed from 0 MW to – 800 MW. The negative sign means the power flow from Asnæsværket to Kyndbyværket.

The voltage variation becomes larger with 800 MW power flow, but it is still small enough. All compensation patterns are considered satisfactory.
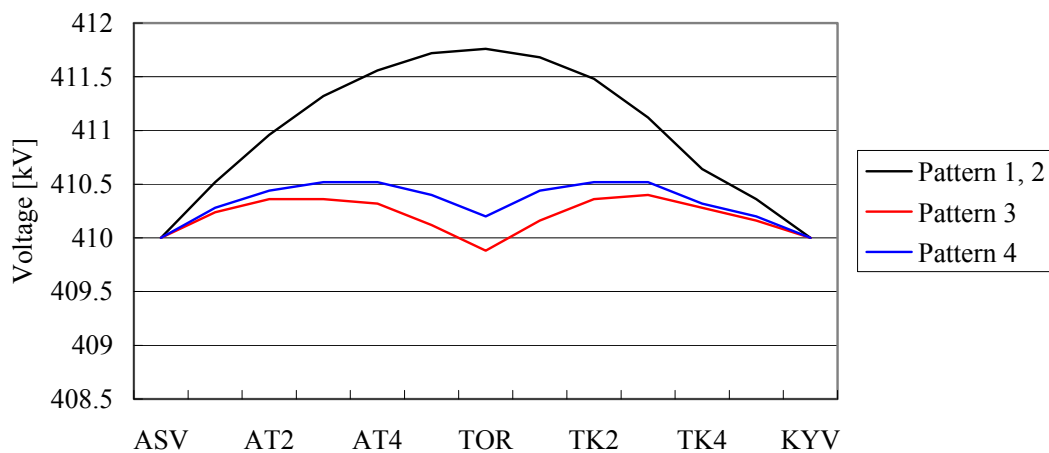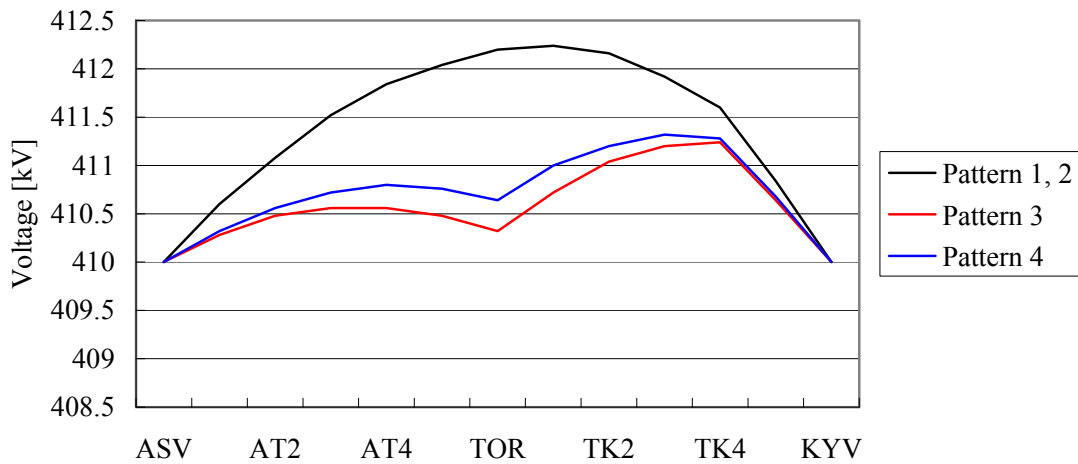
Fig. 2.12 Voltage variation in the Kyndbyværket – Asnæsværket line with 800 MW power flow.

Table 2-9 shows the reactive power supplied to the Kyndbyværket – Asnæsværket line in the maximum power flow condition. In Patterns 1 and 3, larger reactive power is supplied to the cable line, compared to the results in the no load condition. Comparing these two results, reactive power 35 – 40 MVar is lost in the line due to the large power flow in the line.

Due to the same reason, the reactive power supplied from the cable line to the outside is reduced by 35 – 40 MVar in Patterns 2 and 4. The amount of imbalance and reactive power loss should be acceptable in the Danish network.

Table 2-9 Reactive Power Supplied to the Kyndbyværket – Asnæsværket Line in the Maximum Power Flow Condition

	Asnæsværket [MVar]	Kyndbyværket [MVar]	Imbalance [MVar]
Pattern 1	-87.3	126.1	38.8
Pattern 2	-139.8	126.1	-13.7
Pattern 3	-89.1	130.1	41.0
Pattern 4	-114.9	103.3	-11.6

2.7 Active Power Loss

Active power loss in the cable line under the maximum power flow condition is found as below. It is confirmed that the reactive power compensation does not have meaningful impact on the active power loss.

Patterns 1, 2	6.4 MW
Patterns 3, 4	6.2 MW

2.8 Effect on the Transmission Capacity

Large reactive power flow can affect the active power transmission capacity of the cable line. Reactive power flow changes along the cable line, and Table 2-10 shows the largest reactive power flow in the Kyndbyværket – Asnæsværket line.

Table 2-10 Reactive Power Flow in the Kyndbyværket – Asnæsværket Line

	No load condition [MVar]	800 MW active power flow [MVar]
Pattern 1, 2	336.8	402.5
Pattern 3	176.4	288.9
Pattern 4	203.0	272.5
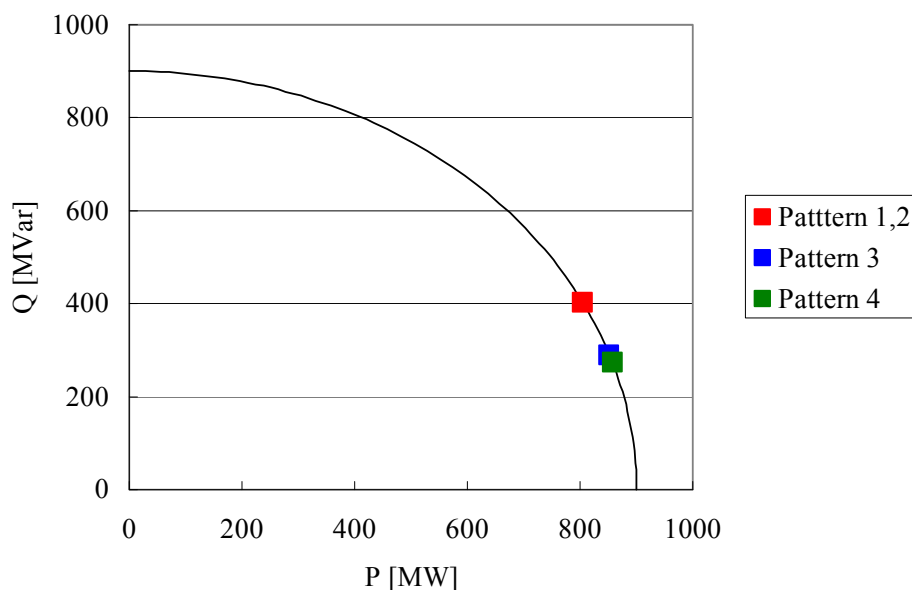
Fig. 2.13 Transmission Capacity of the Kyndbyværket – Asnæsværket line.

Fig. 2.13 illustrates the effect of this reactive power flow on the transmission capacity. Since the PhD project does not include the transmission capacity calculation, it assumes the transmission capacity 900 MVA.

According to the figure, Patterns 1 and 2 have lower active power transmission capacity by approximately 50 MW, compared to Patterns 3 and 4. Thus, it should be considered how much transmission capacity is necessary for the cable line. In addition, actual reactive power flow might

be affected by the network outside the cable line. As such, the analysis acts only as a relative comparison between the four compensation patterns.

For example, when the reactive power flow injection of 200 MVar is assumed from the network outside the cable line, Fig. 2.13 changes to Fig. 2.14. The effect of the compensation patterns on the transmission capacity increases for larger reactive power injection. In Fig. 2.14, the difference of transmission capacity with Pattern 1 and Pattern 4 increases to 90 MW.
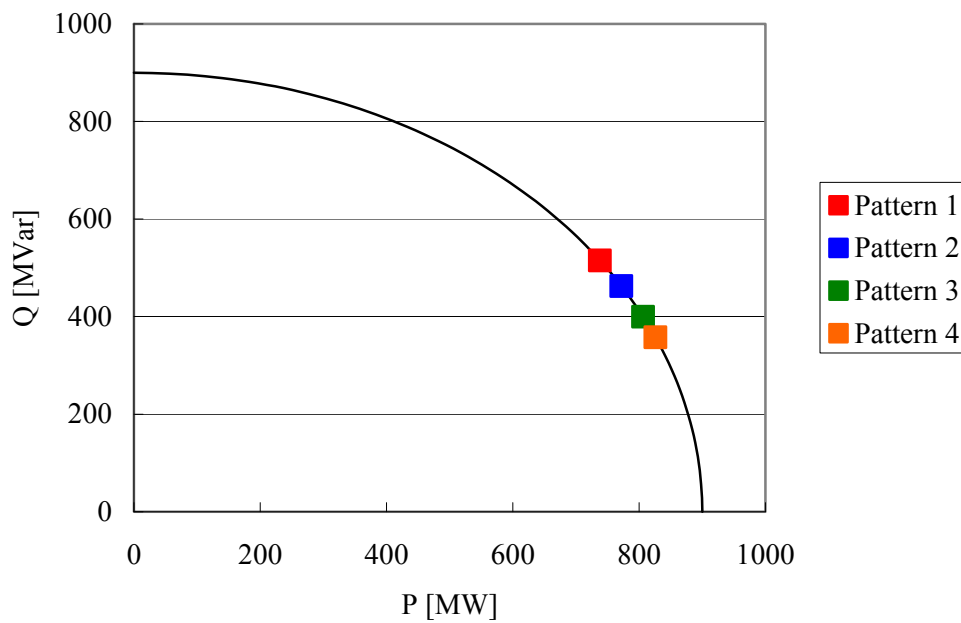
Fig. 2.14 Transmission Capacity of the Kyndbyværket – Asnæsværket line.

2.9 Ferranti Phenomenon

The voltage profile under the normal operating condition was studied in previous sections. In the normal operating condition, there is no technical reason to choose one proposed pattern over the others.

In the selection of the reactive power compensation, however, the following condition should additionally be considered:

- One shunt reactor out of service
- One end of the cable line is opened

Adopting large shunt reactors is a cheaper solution, but an effect of the shunt reactor outage becomes significant. Table 2-11 shows the compensation rate and leading current interruption capability when the largest shunt reactor is out of service.

Table 2-11 Leading Current Interruption with One Shunt Reactor out of Service

	Pattern 1	Pattern 2	Pattern 3	Pattern 4
Asnæsværket	300 MVar	250 MVar	150 MVar	150 MVar
Torslunde	–	–	~~300 MVar~~	~~250 MVar~~
Kyndbyværket	~~300 MVar~~	~~300 MVar~~	150 MVar	150 MVar
Compensation Rate	50.3 %	41.9 %	50.3 %	50.3 %
Leading Current	427.8 A	500.0 A	427.8 A	427.8 A

In the calculation of the required leading current interruption capability, it is assumed that both ends of the cable line are not opened at the same timing. As is sometimes the case in reality, one side is assumed to be opened earlier than the other, and the latter circuit breaker needs to open the charging (leading) current of the whole cable line.

The required leading current interruption capability is higher than the rated capacitive switching current specified in IEC 622271-100, which is 400 A for 420 kV equipment. The rated capacitive switching current is specified at the voltage factor 1.4 pu, and actual capability of circuit breakers are higher than the IEC rating for the lower voltage factor. If the expected voltage in the leading current interruption is lower than this, leading current interruption in Table 2-11 can be acceptable. However, actual capability of the circuit breaker has to be tested and verified in a factory for the cable line.

Additional discussions with regard to the leading current interruption are given in Sections 6.2 and 6.3.

Considering the required leading current interruption capability, it is recommended to adopt smaller unit size if the cable line has to be in-service even when the shunt reactor is out of service. Table 2-12 shows the proposed compensation pattern with smaller unit sizes. With the proposed compensation pattern in Table 2-12, there will be no problem in the leading current interruption capability even when one shunt reactor is out of service.

Table 2-12 Proposed Compensation Patterns with Smaller Unit Sizes

	Pattern 1'	Pattern 2'	Pattern 3'	Pattern 4'
Asnæsværket	150 MVar × 2	100 MVar × 1 150 MVar × 1	150 MVar × 1	150 MVar × 1
Torslunde	–	–	150 MVar × 2	100 MVar × 1 150 MVar × 1
Kyndbyværket	150 MVar × 2	150 MVar × 2	150 MVar × 1	150 MVar × 1
Compensation Rate	100.6 %	92.2 %	100.6 %	92.2 %

Now, we consider the voltage profile when one end of the cable line is opened. One end of the cable line is opened when:

- the cable line is energized from one end, or
- a bus fault is cleared by opening one end of the cable line.

In both occasions, system operators cannot monitor the voltage at the opened terminal. It is therefore recommended to limit the voltage at the open terminal to the critical maximum voltage 420 kV.

Fig. 2.15 shows the voltage profile in the Kyndbyværket – Asnæsværket line when the Kyndbyværket side is opened. The figure shows that there will be no problem in the voltage profile even when one side of the cable line is opened.
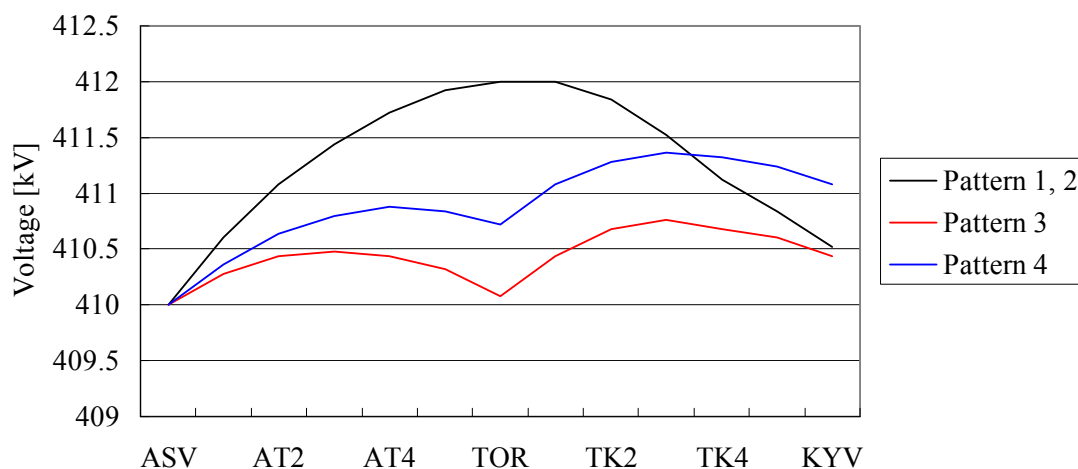
Fig. 2.15 Voltage variation in the Kyndbyværket – Asnæsværket line when the KYV side is opened.

When smaller shunt reactor sizes are adopted, the voltage profile will become severest when one shunt reactor is out of service and one end of the cable line is opened. Table 2-13 shows the severest condition.

Table 2-13 Severest Condition for the Voltage Profile with Smaller Unit Sizes

	Pattern 1'	Pattern 2'	Pattern 3'	Pattern 4'
Asnæsværket	150 MVar × 2	100 MVar × 1 150 MVar × 1	150 MVar × 1	150 MVar × 1
Torslunde	–	–	150 MVar × 2	100 MVar × 1 150 MVar × 1
Kyndbyværket (Open Terminal)	150 MVar × 1 ~~150 MVar × 1~~	150 MVar × 1 ~~150 MVar × 1~~	~~150 MVar × 1~~	~~150 MVar × 1~~
Compensation Rate	75.5 %	67.1 %	75.5 %	67.1 %

Fig. 2.16 shows the voltage profile in the severest condition. In the severest case, there will be about 5 kV voltage rise at the opened terminal. The result tells us that the Asnæsværket or Kyndbyværket 400 kV bus voltage has to be kept lower than 415 kV, when one (small) shunt reactor is out of service.
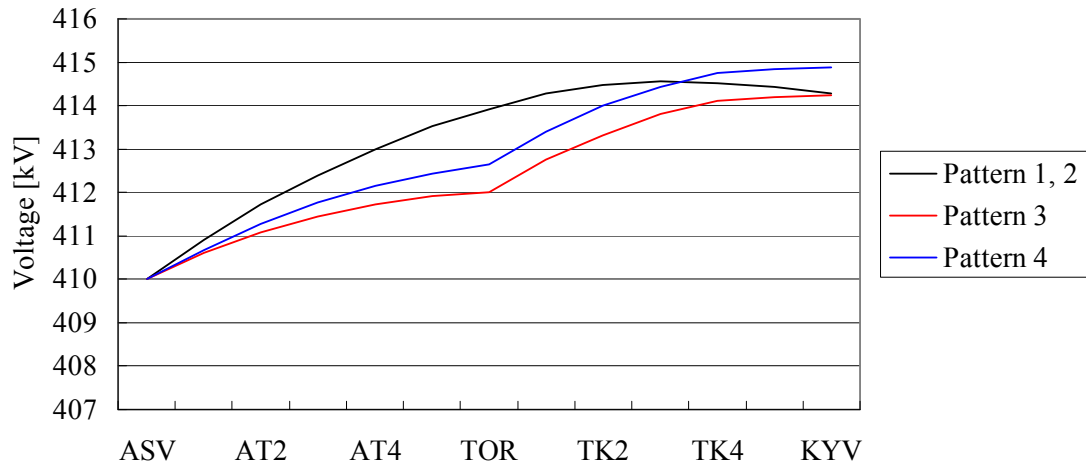
2-34

Fig. 2.16 Voltage variation in the Kyndbyværket – Asnæsværket line when one small shunt reactor is out of service and KYV side is opened.

2.10   Conclusion

The reactive power compensation analysis has been performed for the compensation patterns in Table 2-6 (reproduced below as Table 2-14). The analysis includes:

- Voltage profile in the cable line
- Active power loss
- Effect on the transmission capacity
- Leading current interruption capability

Table 2-14 Studied Compensation Patterns of the Kyndbyværket – Asnæsværket Line (Reproduced)

	Pattern 1	Pattern 2	Pattern 3	Pattern 4
Asnæsværket	300 MVar	250 MVar	150 MVar	150 MVar
Torslunde	–	–	300 MVar	250 MVar
Kyndbyværket	300 MVar	300 MVar	150 MVar	150 MVar
Compensation Rate	100.7 %	92.2 %	100.7 %	92.2 %

The analysis does not reveal a reason to choose one pattern over the others. Thus, it is recommended to choose Pattern 1 for the following reasons:

- It will be the cheapest solution because of the small number of shunt reactor units.
- As it uses only 300 MVar unit, it has an advantage in keeping spare reactors in stock.

Pattern 1 is assumed in this PhD project.

If the cable line has to be in-service even when the shunt reactor is out of service, it is recommended to adopt smaller unit size as in Table 2-12 (reproduced below as Table 2-15). Among these patterns, Patterns 1' and 3' are preferred as they use only 150 MVar unit. When one shunt reactor is out of service and the cable line is in-service, the Asnæsværket or Kyndbyværket 400 kV bus voltage has to be kept lower than 415 kV.

Table 2-15 Proposed Compensation Patterns with Smaller Unit Sizes

	Pattern 1'	Pattern 2'	Pattern 3'	Pattern 4'
Asnæsværket	150 MVar × 2	100 MVar × 1 150 MVar × 1	150 MVar × 1	150 MVar × 1
Torslunde	–	–	150 MVar × 2	100 MVar × 1 150 MVar × 1
Kyndbyværket	150 MVar × 2	150 MVar × 2	150 MVar × 1	150 MVar × 1
Compensation Rate	100.6 %	92.2 %	100.6 %	92.2 %

References

[1]   A. Ametani, *Distributed-Parameter Circuit Theory*, Corona Pub. Co., 1990 (in Japanese).

[2]   IEC/TR 60909-2 ed. 2.0, "Short-circuit currents in three-phase a.c. systems - Part 2: Data of electrical equipment for short-circuit current calculations," (2008)

[3]   Central Station Engineers, *Electrical Transmission and Distribution Reference Book*, 4th Edition, Westinghouse Electric Corporation, 1964.

[4]   J. Lewis Blackburn, *Symmetrical Components for Power Systems Engineering*, CRC Press, 1993.

[5]   Jesus Vargas, Armando Guzman, Jorge Robles, "Underground/submarine cable protection using a negative-sequence directional comparison scheme," 26th Annual Western Protective Relay Conference, Spokane, Washington, October 25-28, 1999

[6]   CIGRE WG B1.19, "General Guidelines for the Integration of a New Underground Cable System in the Network," *CIGRE Technical Brochure* 250, 2004.

[7]   N. Nagaoka and A. Ametani, "Transient Calculations on Crossbonded Cables," *IEEE Trans. on Power Apparatus and Systems*, vol. PAS-102, no. 4, 1983.

[8]   A. Ametani, Y. Miyamoto, and N. Nagaoka, "An Investigation of a Wave Propagation Characteristic on a Crossbonded Cable," *IEEJ Trans. PE*, vol. 123, no. 3, pp. 395-401, 2003 (in Japanese).

[9]   Bjørn Gustavsen "Panel Session on Data for Modeling System Transients. Insulated Cables", Proc. IEEE. Power Engineering Society Winter Meeting , 2001

[10]   A. Ametani, "A GENERAL FORMULATION OF IMPEDANCE AND ADMITTANCE OF CABLES," *IEEE Transactions on Power Apparatus and Systems*, vol. PAS-99, no. 3 May/June 1980.

[11]   A. Ametani, "On the Impedance and the Admittance in the EMTP Cable Constants / Parameters," European EMTP-ATP Users Group Meeting, Delft, the Netherlands, October 26-28, 2009.

[12]   W. Scott-Meyer, *ATP Rule Book*, Can / Am EMTP User Group, 1982.

[13]   Energinet.dk, "*Technical Regulation 2.1.1 – Grid Dimensioning Rules*", available in Danish at: http://energinet.dk/SiteCollectionDocuments/Danske%20dokumenter/El/TF%202.1.1%20Net dimensioneringsreglergældende.pdf.

Chapter 3 Model Setup

3.1 Power Flow Data

The power flow data in the year 2015 was provided from Energinet.dk. The impedance and admittance of the 400 kV Kyndbyværket – Asnæsværket line are modified according to the values found in the previous chapter.

The power flow data provided from Energinet.dk include the peak load condition (south transit) and the off-peak load condition (north transit). A comparison of the total load in Zealand is shown in Table 3-1. As the severe temporary overvoltage can often be caused in the off-peak load condition, the north transit power flow data is used as the base of the model setup.

Table 3-1 Comparison of Total Demand in Zealand

North Transit	South Transit	North / South
1719 MW	2773 MW	62 %

Fig. 3.1 shows the power flow diagram in the off-peak load condition after the addition of the Kyndbyværket – Asnæsværket line.
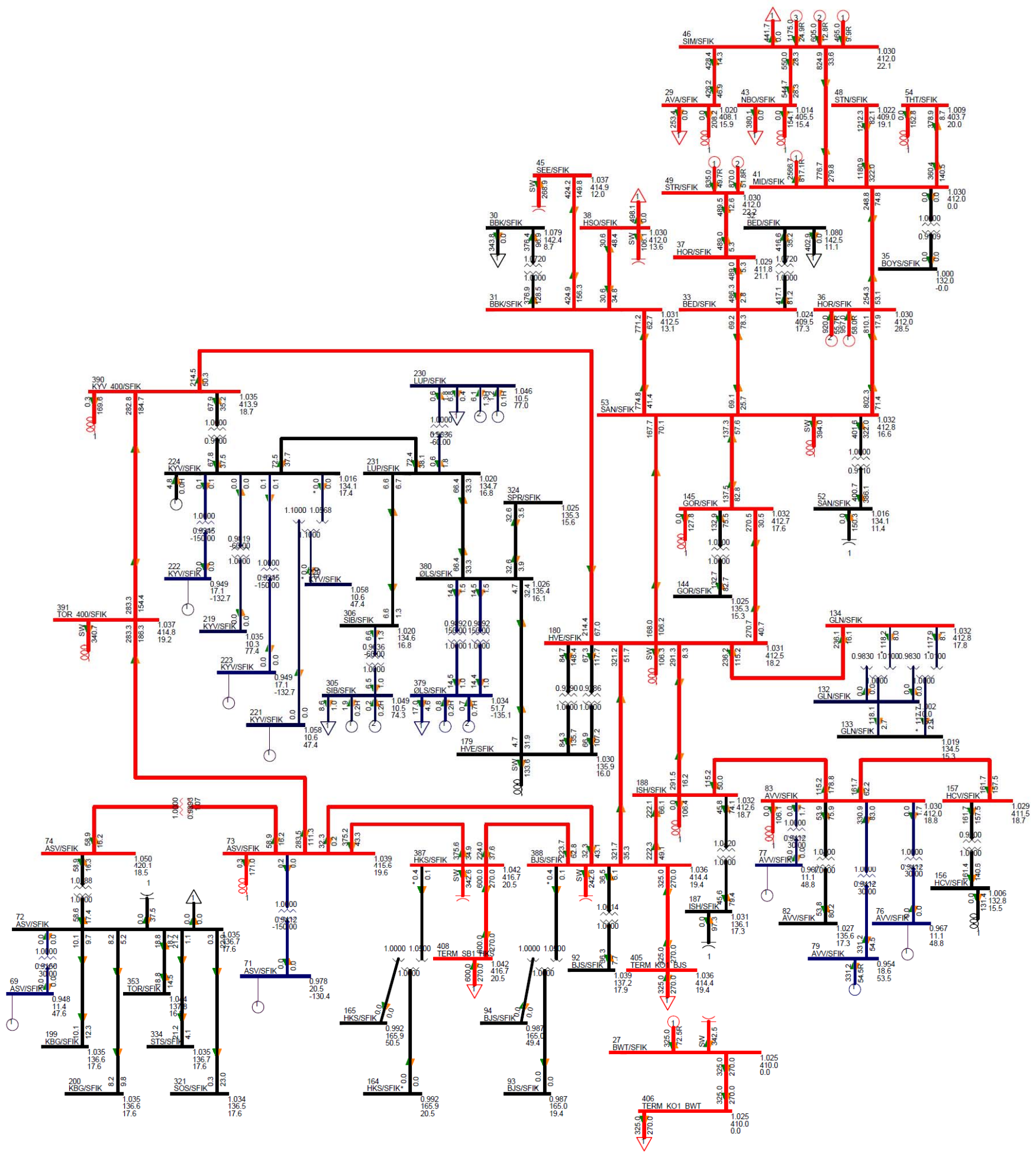
Fig. 3.1 Power flow diagram in the off-peak load condition after the installation of the Kyndbyværket – Asnæsværket line.

3-3

3.2 Modeled Area

The entire 400 kV network in Zealand is included in this model for the temporary overvoltage analysis and the slow-front overvoltage analysis. Fig. 3.2 shows the modeled area of the 400 kV network.
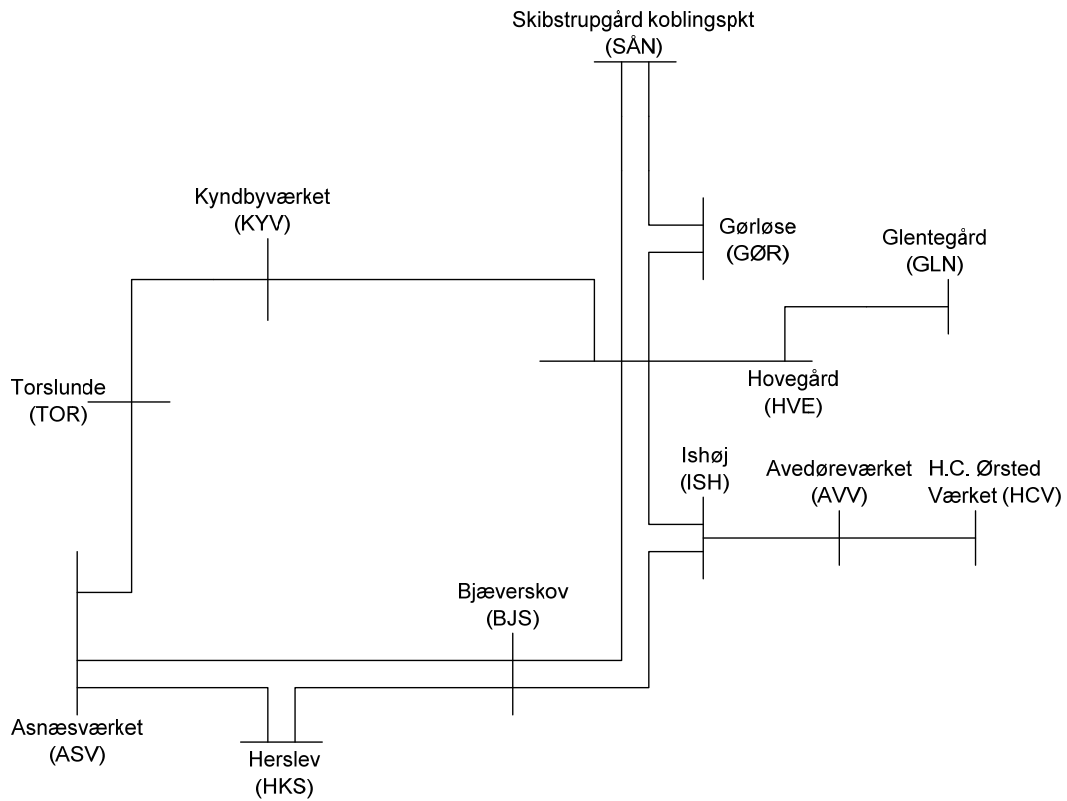
Fig. 3.2 Modeled area of the 400 kV network.

Fig. 3.3 shows an example of the simulation model created in ATP-Draw. Each component in the figure is explained in this section.

Fig. 3.3 Simulation model for the temporary overvoltage and slow-front overvoltage analysis in ATP-Draw.

The simulation model was set up also in PSCAD. Fig. 3.4 shows an example of the model created in PSCAD.

Hovegård – Kyndbyværket line
(upgraded to 400 kV operation)

Kyndbyværket – Asnæsværket line

Fig. 3.4 Simulation model for the temporary overvoltage and slow-front overvoltage analysis in PSCAD.

3.3 Underground Cables

3.3.1 Physical and Electrical Information

The simulation model includes the following four 400 kV cables:

- Al 1600 mm^2 XLPE cable (Al sheath)
- Al 400 mm^2 + Cu 1600 mm^2 XLPE cable (Pb sheath)
- Cu 1000 mm2 LPFF cable (Pb sheath + Al armour)
- Cu 1000 mm2 LPFF cable (Pb sheath)

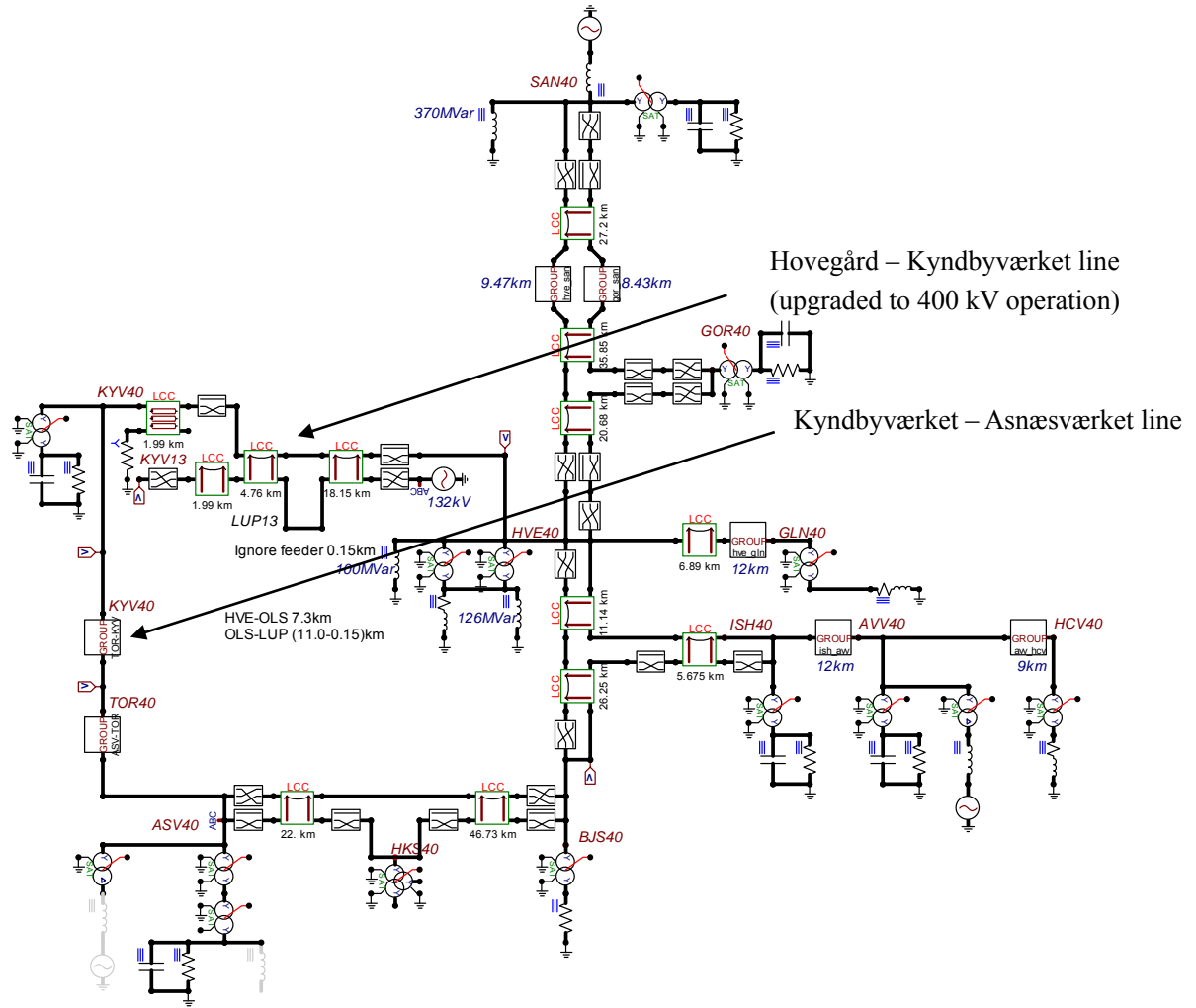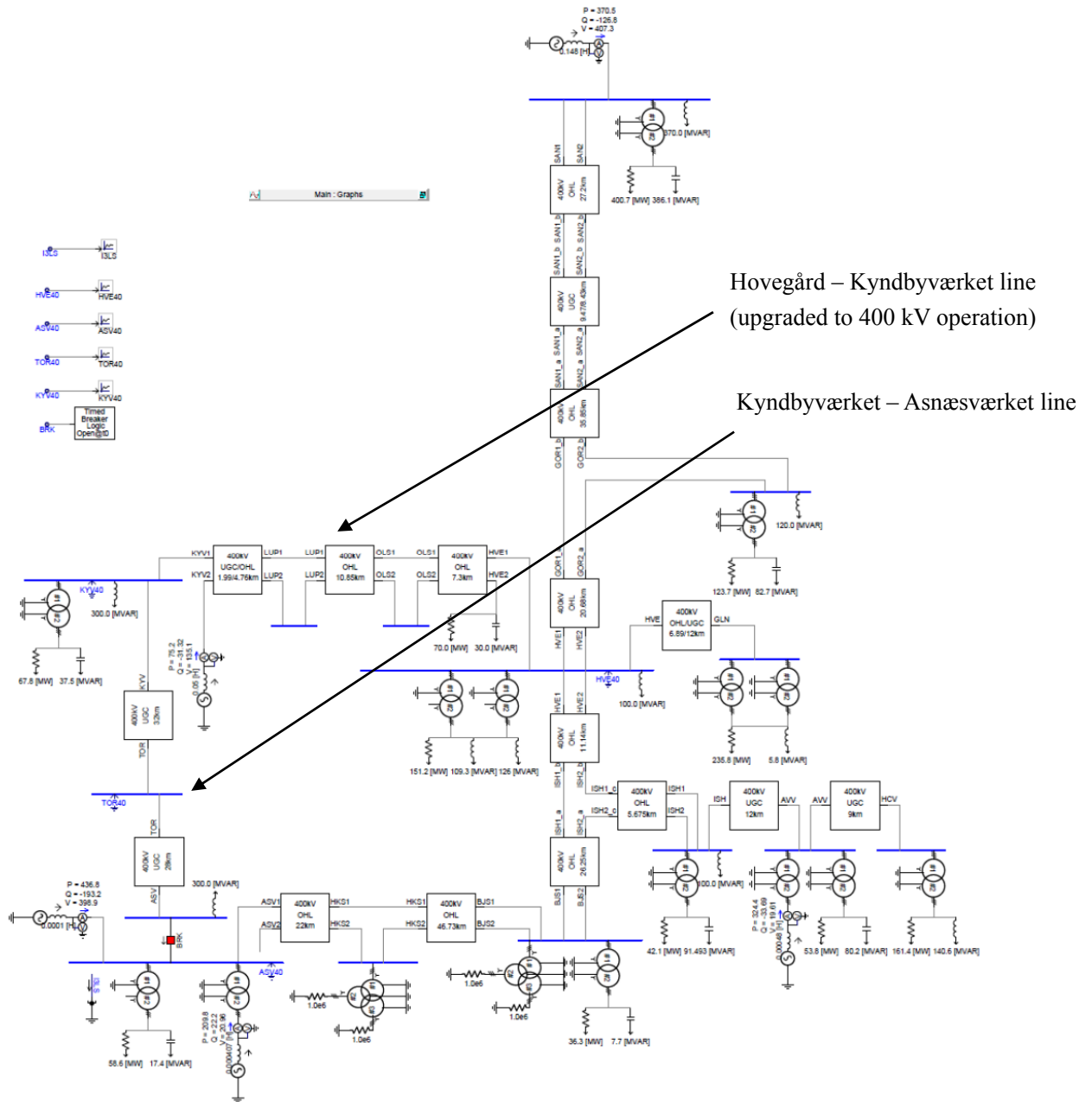Fig. 3.5 shows the locations of these 400 kV cables in the network. The first cable type is for the Kyndbyværket – Asnæsværket line. Additionally, this type was applied to the short section of the Hovegård – Kyndbyværket line near the Kyndbyværket substation, where the overhead line is designed as 132 kV. This short section (1.99 km) has to be replaced by 400 kV cables when the Hovegård – Kyndbyværket line is operated at 400 kV.

Since the other types of the cable are located far from the point of the interest of this PhD project, these cable models will not have a significant effect on the simulation results. These models have been developed mainly for the future use at Energinet.dk.

(1) Al 1600 mm² XLPE cable (Al sheath)
(2) Al 400 + Cu 1600 mm² XLPE cable (Pb sheath)
(3) Cu 1000 mm² LPFF cable (Pb sheath + Al armour)
(4) Cu 1000 mm² LPFF cable (Pb sheath)
(5) Al 2000 mm² XLPE cable (Cu sheath, no data, ignored)
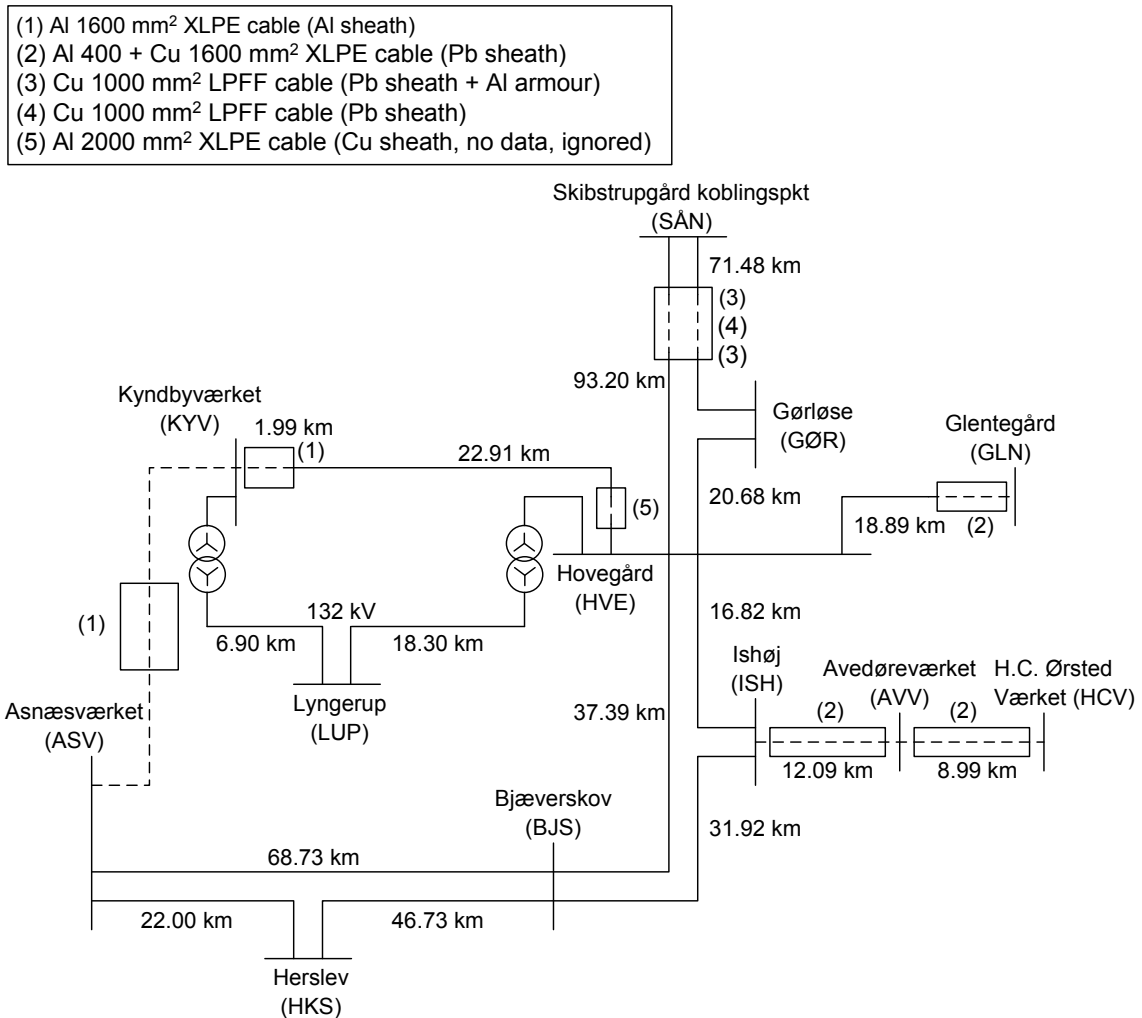
Fig. 3.5 Four types of cables in the simulation model.

(1) Al 1600 mm² XLPE cable (Al sheath): Kyndbyværket – Asnæsværket line

Physical and electrical information of this type of the 400 kV cable is shown in Table 3-2. As the Kyndbyværket – Asnæsværket line has not been constructed yet, it is not possible to obtain exact parameters. Instead, the standard data was assumed based on *ABB XLPE Underground Cable Systems – User's Guide (rev. 3)* [1].

Table 3-2 Physical and Electrical Information for the 400 kV Cable used at ASV – KYV (1)

Conductor	R1	Inner radius of the tubular core	mm	0
	R2	Outer radius of the tubular core	mm	26.0
	ρc	Resistivity	Ωm	2.84E-08
	μc	Relative permeability		1
Conductor Screen	Rsi	Outer radius of conductor screen	mm	28.0
Insulation	μI1	Relative permeability		1
	εI1	Relative permittivity		2.852
	Rso	Outer radius of the insulation	mm	55.0
Metallic Sheath	R3	Inner radius of metallic sheath	mm	58.0
	R4	Outer radius of metallic sheath	mm	59.2
	ρs1	Resistivity		2.84E-08
	μs1	Relative permeability		1
Outer Covering	μI2	Relative permeability		1
	εI2	Relative permittivity		2.4
Completed Cable	R5	Average outer radius of cover	mm	63.5

It is not possible to model semiconductive layers inside and outside the insulation in the subroutine CABLE CONSTANTS. Hence, semiconductive layers inside and outside the insulation were modeled as a part of the insulation since their resistivity is large enough in comparison to the conductor or metallic sheath.

Because of this modification, the insulation appears thicker in the ATP-Draw model than the actual thickness, and the charging capacity of the cable appears smaller than its actual value. In order to compensate for this error, relative permittivity of the insulation was converted using the following equation [2]:

$$\varepsilon I1 = \frac{\ln(R3/R2)}{\ln(Rso/Rsi)}\varepsilon I0 = \frac{\ln(58.0/26.0)}{\ln(55.0/28.0)} \cdot 2.4 = 2.852 \qquad \text{Eqn. 3.1}$$

Relative permittivity of the insulation was converted in the same manner for other 400 kV cables.

The Kyndbyværket – Asnæsværket line has both a land part and a submarine part. The submarine part has an armour conductor outside of the metallic sheath. However, the armour was not included in the model mainly because the armour causes only a minor effect on the transient overvoltage, which will be discussed in Section 3.3.8.

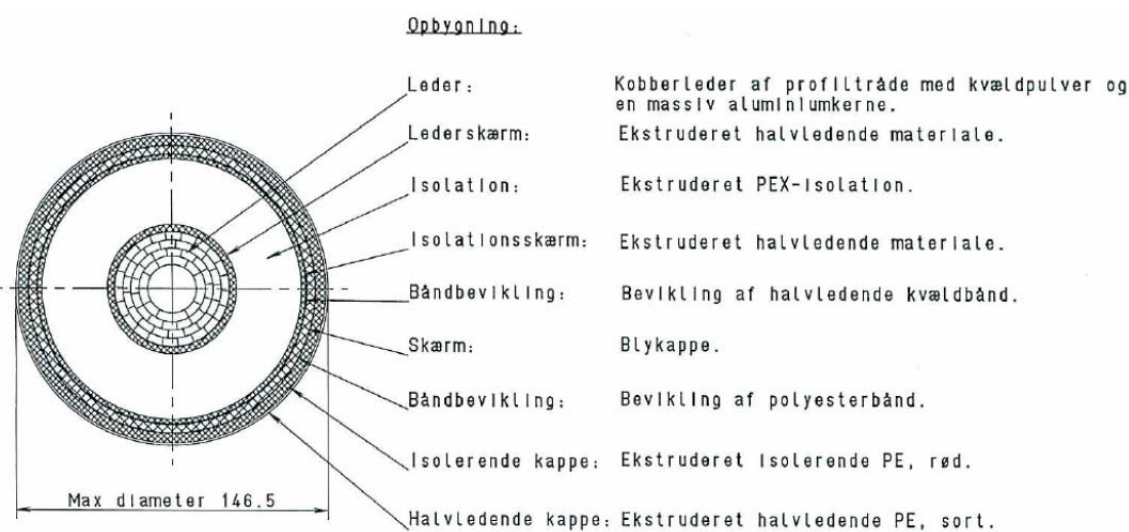(2) Al 400 mm^2 + Cu 1600 mm2 XLPE cable (Pb sheath)

Physical and electrical information of this type of the 400 kV cable is shown in Table 3-3.

Table 3-3 Physical and Electrical Information for the 400 kV Cable

used at ISH – AVV – HCV and HVE – GLN (2)

Conductor	R1	Inner radius of the tubular core	mm	0
	R2	Outer radius of the tubular core	mm	25.50
	ρc	Resistivity	Ωm	1.724E-08
	μc	Relative permeability		1
Conductor Screen	Rsi	Outer radius of conductor screen	mm	28.80
Insulation	μI1	Relative permeability		1
	εI1	Relative permittivity		2.96
	Rso	Outer radius of the insulation	mm	57.80
Metallic Sheath	R3	Inner radius of metallic sheath	mm	60.25
	R4	Outer radius of metallic sheath	mm	63.85
	ρs1	Resistivity		2.20E-08
	μs1	Relative permeability		1
Outer Covering	μI2	Relative permeability		1
	εI2	Relative permittivity		2.4
Completed Cable	R5	Average outer radius of cover	mm	69.60

The core of this cable has a copper in the center and the aluminum around it. Since CABLE CONSTANTS subroutine and PSCAD cannot deal with two different conductors without insulation between them, the core is assumed to be composed only of the copper. The copper has lower resistance than the aluminum, and thus this is a conservative assumption.

Physical and electrical information of the cable has been provided from NKT Cables through Energinet.dk. The provided data sheet is shown in Fig. 3.6.

Opbygning:

Leder:	Kobberleder af profiltråde med kvældpulver og en massiv aluminiumkerne.
Lederskærm:	Ekstruderet halvledende materiale.
Isolation:	Ekstruderet PEX-isolation.
Isolationsskærm:	Ekstruderet halvledende materiale.
Båndbevikling:	Bevikling af halvledende kvældbånd.
Skærm:	Blykappe.
Båndbevikling:	Bevikling af polyesterbånd.
Isolerende kappe:	Ekstruderet isolerende PE, rød.
Halvledende kappe:	Ekstruderet halvledende PE, sort.

Max diameter 146.5

Hovedstadsprojektet, 400 kV kabelsystem til GLN-MÄK & HVE

Mekaniske og elektriske data.

Ledertværsnit	mm²	1600
Lederdiameter	mm	51,0
Diameter over halvledende tape på leder	mm	51,6
Diameter over ekstruderet indre halvleder	mm	57,6
Tykkelse af PEX isolation, nominel	mm	29,0
Diameter over ekstruderet isolation, nominel	mm	115,6
Diameter over ekstruderet ydre halvleder	mm	119,6
Diameter over halvledende kvældbånd, nominel	mm	120,5
Tykkelse af blykappe, nominel	mm	3,6
Diameter over blykappe, nominel	mm	127,7
Diameter over polyesterbånd, nominel	mm	128,2
Tykkelse af PE-kappe med ekstruderet halvledende lag	mm	5,5
Udvendig diameter, nominel	mm	139,2
Udvendig diameter, max	mm	146,5
Kabelvægt (omtrentlig)	kg/m	42
Mindste tilladte bøjeradius	mm	2100
Største tilladte træk i kablet	kN	80 *
Jævnstrømsmodstand af Cu pr. fase ved 20 °C	Ω/km	0,0113
Kapacitet pr. fase	µF/km	0,20
Tilladelig lederstrøm i 1 sekund ved begyndelsestemperatur 90 °C med sluttemperatur 250 °C	kA	228
Tilladelig skærmstrøm i 1 sekund med sluttemperatur 200 °C	kA	40

Fig. 3.6 Provided data on Cable (2).

(3) Cu 1000 mm2 LPFF cable (Pb sheath + Al armour)

Physical and electrical information of this type of the 400 kV cable is shown in Table 3-4.

Table 3-4 Physical and Electrical Information for the 400 kV Cable
used at HVE – SÅN and GØR – SÅN (3)

Conductor	R1	Inner radius of the tubular core	mm	8.65
	R2	Outer radius of the tubular core	mm	20.65
	ρc	Resistivity	Ωm	1.724E-08
	μc	Relative permeability		1
Conductor Screen	Rsi	Outer radius of conductor screen	mm	21.25
Insulation	μI1	Relative permeability		1
	εI1	Relative permittivity		2.56
	Rso	Outer radius of the insulation	mm	45.25
Metallic Sheath	R3	Inner radius of metallic sheath	mm	46.20
	R4	Outer radius of metallic sheath	mm	49.40
	ρs1	Resistivity		2.20E-07
	μs1	Relative permeability		1
Insulation	μI2	Relative permeability		1
	εI2	Relative permittivity		2.4
Armour	R5	Inner radius of metallic sheath	mm	53.90
	R6	Outer radius of metallic sheath	mm	61.90
	ρs1	Resistivity		2.84E-08
	μs1	Relative permeability		1
Outer Covering	μI2	Relative permeability		1
	εI2	Relative permittivity		2.4
Completed Cable	R7	Average outer radius of cover	mm	66.30

Physical and electrical information of the cable has been provided from Energinet.dk. The provided data sheet is shown in Fig. 3.7.
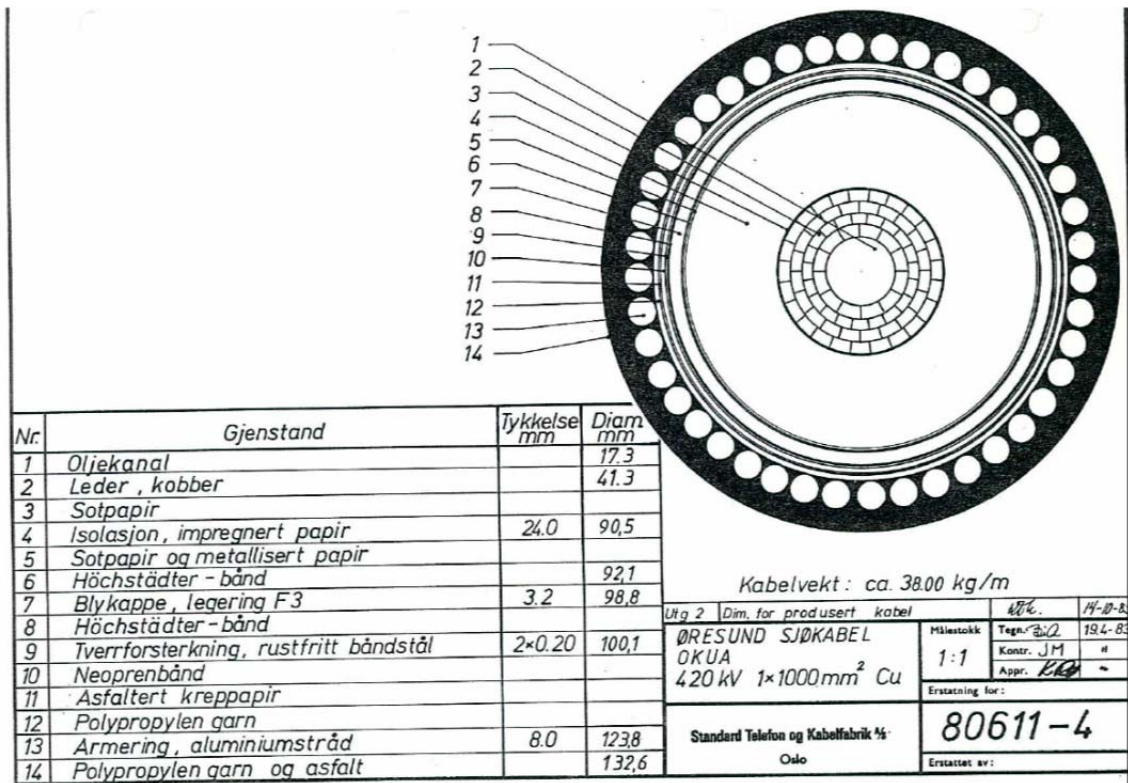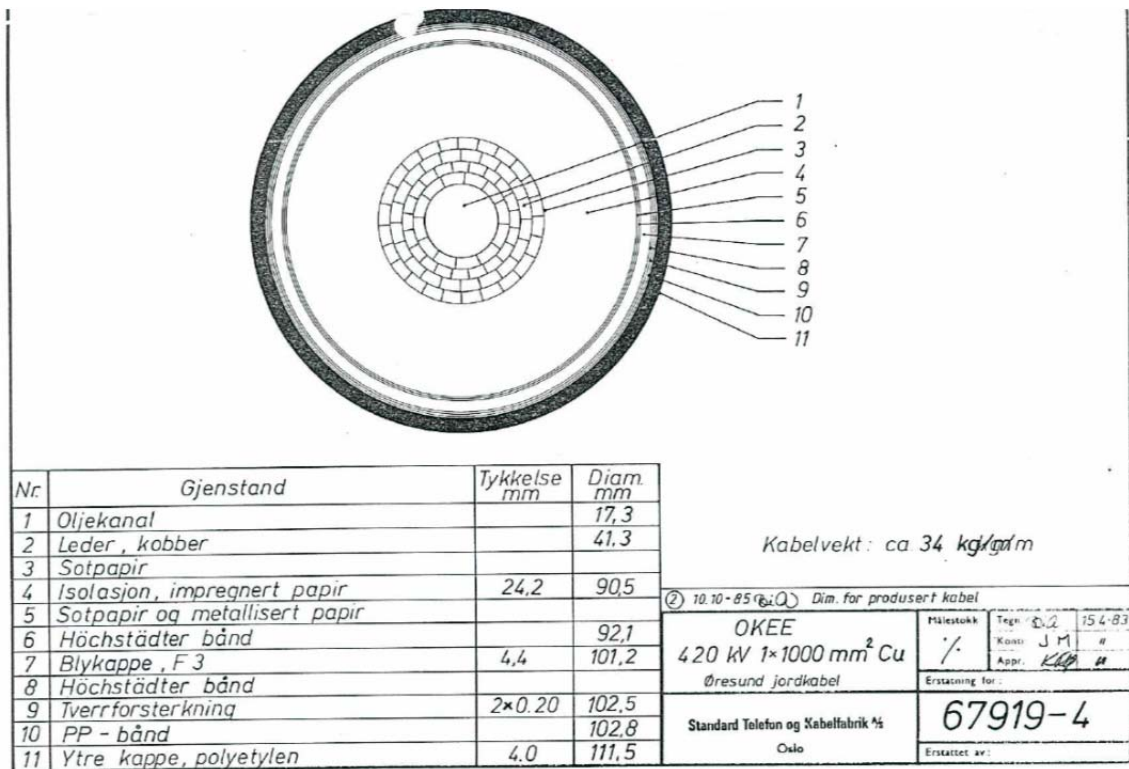
Nr.	Gjenstand	Tykkelse mm	Diam. mm
1	Oljekanal		17.3
2	Leder , kobber		41.3
3	Sotpapir		
4	Isolasjon, impregnert papir	24.0	90,5
5	Sotpapir og metallisert papir		
6	Höchstädter - bånd		92,1
7	Blykappe , legering F3	3.2	98,8
8	Höchstädter - bånd		
9	Tverrforsterkning, rustfritt båndstål	2×0.20	100,1
10	Neoprenbånd		
11	Asfaltert kreppapir		
12	Polypropylen garn		
13	Armering , aluminiumstråd	8.0	123,8
14	Polypropylen garn og asfalt		132,6

Kabelvekt : ca. 38.00 kg/m

Utg 2 | Dim. for produsert kabel

ØRESUND SJØKABEL OKUA
420 kV 1×1000 mm² Cu

Målestokk 1:1

Erstatning for :

Standard Telefon og Kabelfabrik ⅍
Oslo

80611 - 4

Erstattet av :

Fig. 3.7 Provided data on Cable (3).

(4) Cu 1000 mm2 LPFF cable (Pb sheath)

Physical and electrical information of this type of the 400 kV cable is shown in Table 3-5.

Table 3-5 Physical and Electrical Information for the 400 kV Cable
used at HVE – SÅN and GØR – SÅN (4)

Conductor	R1	Inner radius of the tubular core	mm	8.65
	R2	Outer radius of the tubular core	mm	20.65
	ρc	Resistivity	Ωm	1.724E-08
	μc	Relative permeability		1
Conductor Screen	Rsi	Outer radius of conductor screen	mm	21.05
Insulation	μI1	Relative permeability		1
	εI1	Relative permittivity		2.532
	Rso	Outer radius of the insulation	mm	45.25
Metallic Sheath	R3	Inner radius of metallic sheath	mm	46.20
	R4	Outer radius of metallic sheath	mm	50.60
	ρs1	Resistivity		2.20E-08
	μs1	Relative permeability		1
Outer Covering	μI2	Relative permeability		1
	εI2	Relative permittivity		2.4
Completed Cable	R5	Average outer radius of cover	mm	55.75

Physical and electrical information of the cable has been provided from Energinet.dk. The provided
data sheet is shown in Fig. 3.8.

Nr.	Gjenstand	Tykkelse mm	Diam. mm
1	Oljekanal		17,3
2	Leder , kobber		41,3
3	Sotpapir		
4	Isolasjon, impregnert papir	24,2	90,5
5	Sotpapir og metallisert papir		
6	Höchstädter bånd		92,1
7	Blykappe , F 3	4,4	101,2
8	Höchstädter bånd		
9	Tverrforsterkning	2×0.20	102,5
10	PP - bånd		102,8
11	Ytre kappe, polyetylen	4.0	111,5

Kabelvekt : ca. 34 kg/m

② 10.10-85 ⟨GiQ⟩   Dim. for produsert kabel

OKEE
420 kV 1×1000 mm² Cu
Øresund jordkabel

Standard Telefon og Kabelfabrik ⅍
Oslo

67919-4

Fig. 3.8 Provided data on Cable (4).

3.3.2 Cable Layout

All 400 kV cables were assumed to be buried in a flat formation as shown in Fig. 3.9. The buried depth of 1.3 m and the phase spacing 0.3 m are assumed to be common for all the four cable models.
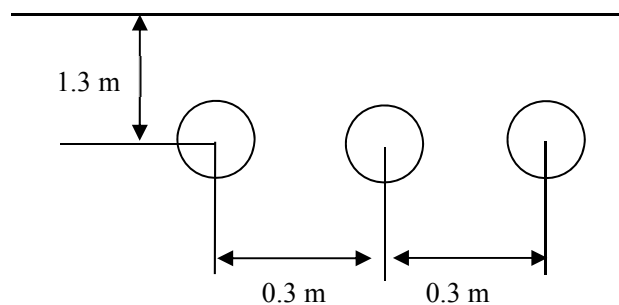
Fig. 3.9 Cable layout.

3.3.3 Cable Route

The assumed route of the Kyndbyværket – Asnæsværket line is illustrated in Fig. 3.10 by a red dotted line. The cable line is assumed to be composed of land and submarine sections. The length of each section is:

- Asnæsværket to Torslunde: 28 km (only land section)
- Torslunde to Kyndbyværket
    - Land section: 22 km
    - Submarine section: 10 km

Fig. 3.10 Cable route.

The cable model in the land section is cross-bonded, whereas the cable model in the submarine section is solidly-bonded. The length of the minor section and the number of major / minor sections are shown in Table 3-6.

Table 3-6 Cross-bonding of the Kyndbyværket – Asnæsværket line

	Asnæsværket – Torslunde	Torslunde – Kyndbyværket
Length of minor section	1867 m	1833 m
Number of minor sections	15	12
Number of major sections	5	4

Finally, sheath bonding is modeled as shown in Fig. 3.11 and Fig. 3.12. Each node between minor sections is named as AT1, AT2, …, AT15 for the Asnæsværket – Torslunde section and KT1, KT2, …, KT14 for the Torslunde – Kyndbyværket section. These node names are later used to specify fault locations or monitoring points for the overvoltage.
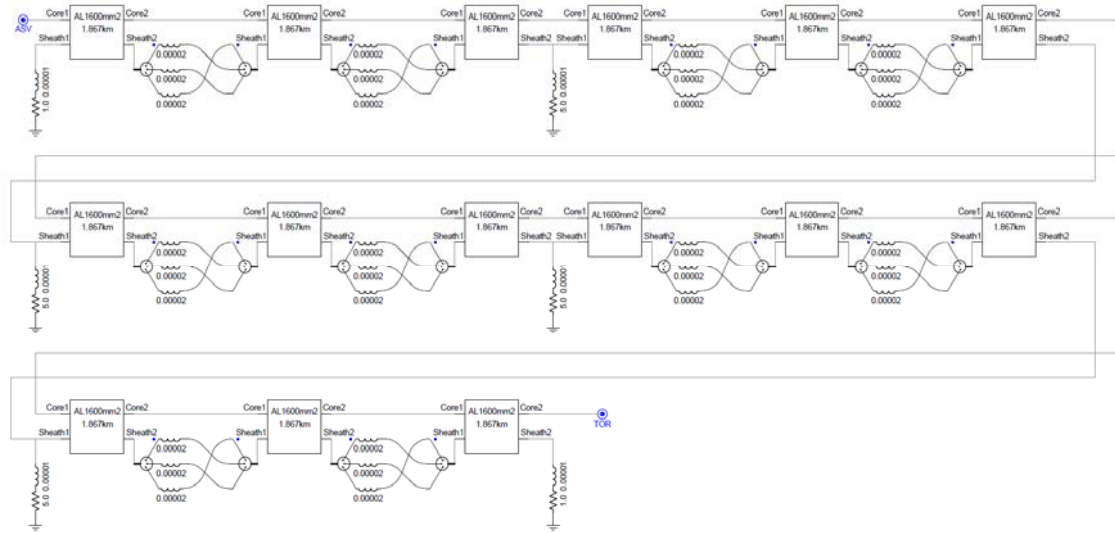
Fig. 3.11 Modeling of cross-bonding (Asnæsværket – Torslunde).
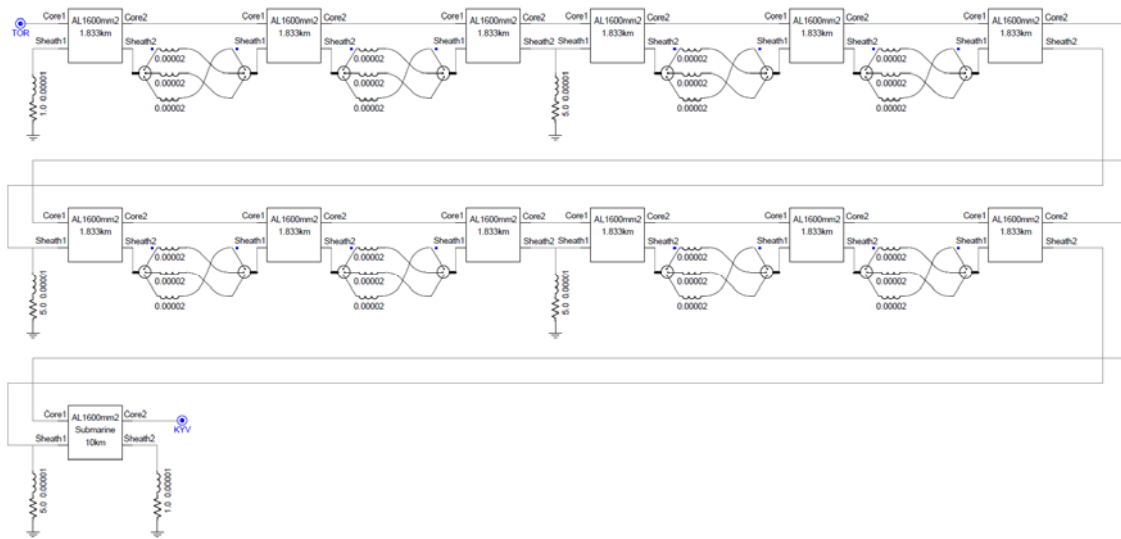
Fig. 3.12 Modeling of cross-bonding (Torslunde – Kyndbyværket).

3.3.4 Modeling of Auxiliary Components

The setup of cable models requires the modeling of cross-bonding wires, grounding wires, and other grounding conditions. The following settings are commonly applied for all 400 kV cables:

(a) Impedance of cross-bonding wires: <u>20 µH</u>

Typical length of the cross-bonding wire from joint to link box is about 10 m. The impedance was assumed to be 1µH/m.

(b) Impedance of grounding wires: <u>10 µH</u>

Typical length of the grounding wire is about 10 m. The impedance was assumed to be 1µH/m.

(c) Grounding resistance

Substation: <u>1 ohm</u>
Normal Joint: <u>5 ohm</u>

(d) Ground resistivity: <u>100 ohm-m</u>

3.3.5   Effects of Cable Models

The PhD project set up the simulation model both in ATP-EMTP and PSCAD. Different cable models are adopted in ATP-EMTP and PSCAD. The comparison of the cable models are given in Table 3-7.

Table 3-7 Comparison of cable models in ATP-EMTP and PSCAD

	ATP-EMTP	PSCAD
Model name	Bergeron	Frequency dependent (phase)
Frequency dependent	Non-frequency dependent	Frequency dependent
Model domain	Modal domain	Phase domain

The resonance overvoltage analysis in Chapter 4 used the Bergeron model in ATP-EMTP since the analysis was done before the release of PSCAD X4.4. When the PhD project was on the half-way, however, the Manitoba HVDC Research Centre released PSCAD X4.4, which had an option to calculate the earth-return impedance by the numerical integration of Pollaczek's equation. The numerical integration of Pollaczek's equation helped to resolve the numerical instability encountered in many cases. All transient analyses, except for the resonance overvoltage analysis, were conducted after the release of PSCAD X4.4, and the frequency dependent (phase) model in PSCAD was used for the analyses. Note that steady-state analyses used the steady-state (power-frequency) calculation function in ATP-EMTP.

It is important for the setup of the Bergeron model to appropriately select the target frequency, at which the cable impedance and admittance are calculated. It is a common practice, especially for the temporary overvoltage analysis, to set the target frequency at 50 Hz as a severe assumption. The lower target frequency leads to a smaller resistance, which normally causes a higher overvoltage. In the PhD project, the target frequency was first set at 50 Hz. After the dominant frequency in the overvoltage is known, however, the target frequency was changed to the dominant frequency in order to obtain more reasonable results.

Since different cable models are adopted, frequency responses of the cable impedances are obtained from both cable models in order to find the difference of these models. Fig. 3.13 and Fig. 3.14 show the comparison of frequency responses of positive and zero sequence impedances of the Kyndbyværket – Asnæsværket line. The target frequency of the Bergeron model is set to 50 Hz. Considering the main focus of the PhD project, frequency responses are obtained in the range 0 – 2000 Hz at 10 Hz step.

For both positive and zero sequence impedances, natural frequencies of the cable match between two different models. The results indicate that natural frequencies of the network with the cable, approximately 450 Hz and 1330 Hz, can be found by both cable models with an equal accuracy.
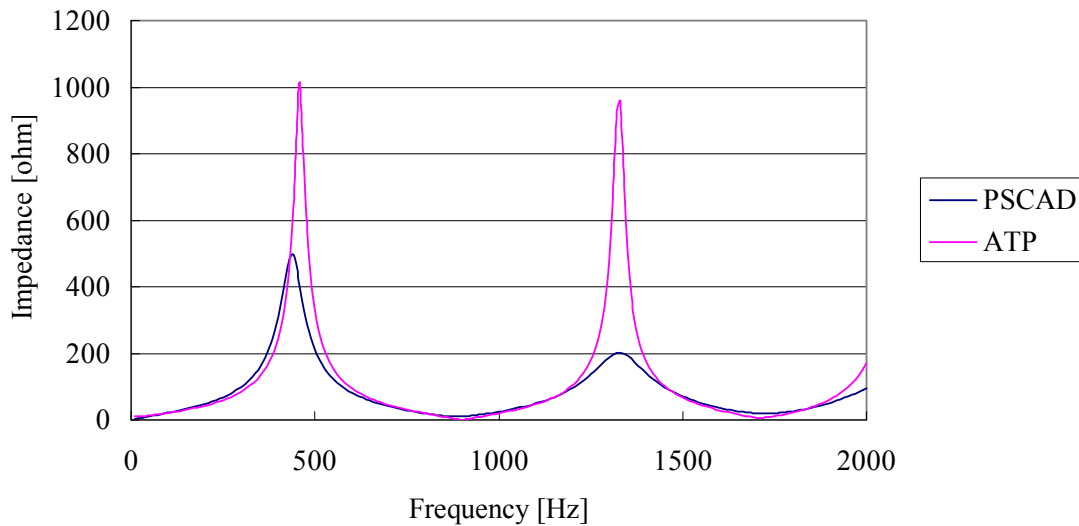

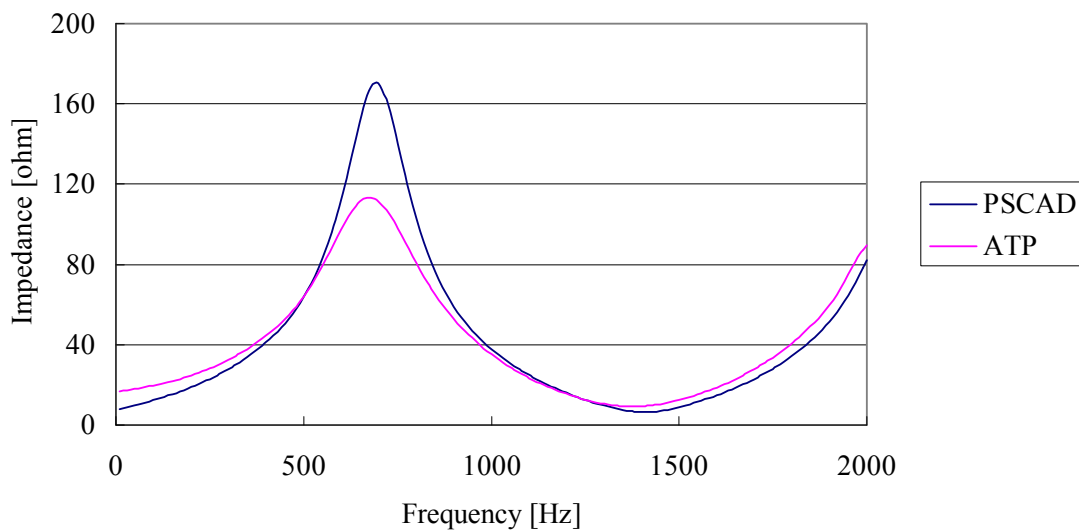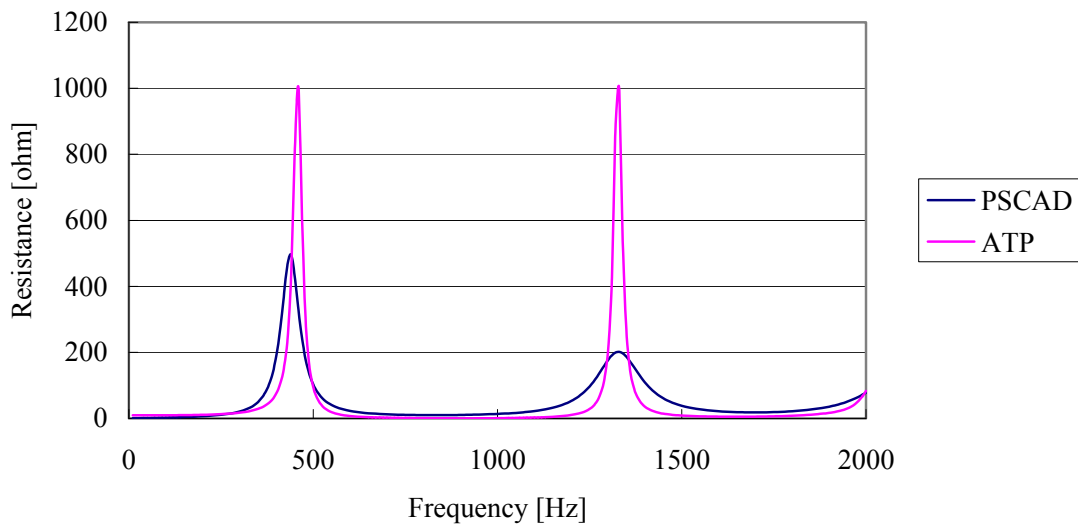**Fig. 3.13 Frequency response of positive sequence impedance of the KYV – ASV line.**

Fig. 3.14 Frequency response of zero sequence impedance of the KYV – ASV line.

The differences can be more clearly seen in Fig. 3.15 and Fig. 3.16 where positive sequence resistance and reactance are separately derived. Both resistance and reactance have peaks and zeros at the same frequencies, but the magnitudes of the resistance and reactance at their peaks are approximately two times higher than in the Bergeron model in ATP-EMTP.

Fig. 3.15 Frequency response of positive sequence resistance of the KYV – ASV line.
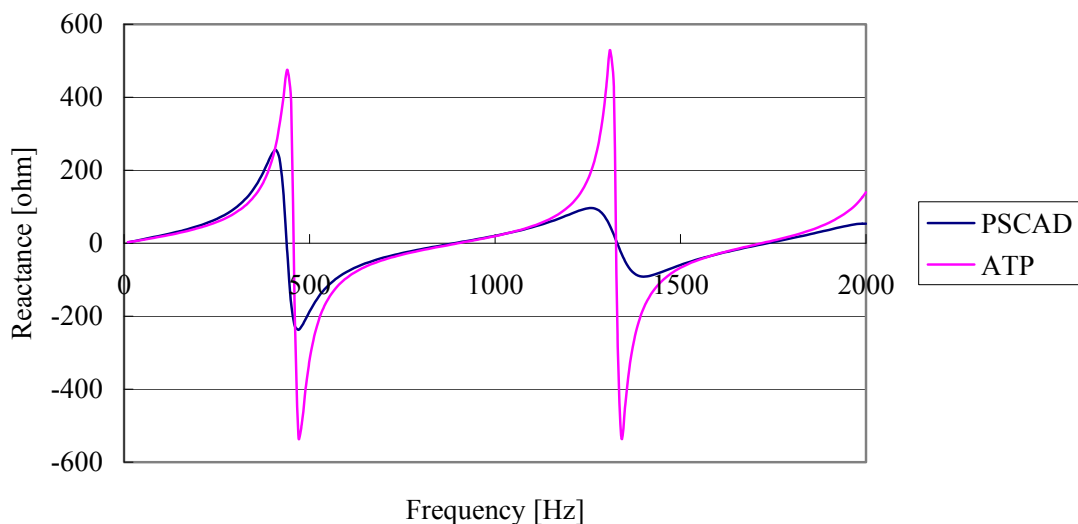
Fig. 3.16 Frequency response of positive sequence reactance of the KYV – ASV line.

As a comparison in the time domain simulation, the Kyndbyværket – Asnæsværket line is energized from the 400 kV voltage source behind the source impedance of 147 mH, which corresponds to the fault current 5 kA. It is expected that the line energization overvoltages with the two cable models become similar because the discrepancies of impedances between the two cable models are observed only around the natural frequencies in Fig. 3.13 to Fig. 3.16. Considering the length of the Kyndbyværket – Asnæsværket line, the dominant frequency in the overvoltages will be much lower than the natural frequencies 450 Hz and 1330 Hz.

Fig. 3.17 and Fig. 3.18 respectively show the comparison of the line energization overvoltages at the sending end and the receiving end. The waveforms of the overvoltages are similar in these cases, but the magnitudes of the overvoltages include 5.9 % deviation at the sending end and 7.9 % deviation at the receiving end. It is estimated that the deviation is caused by the small difference in resistance.
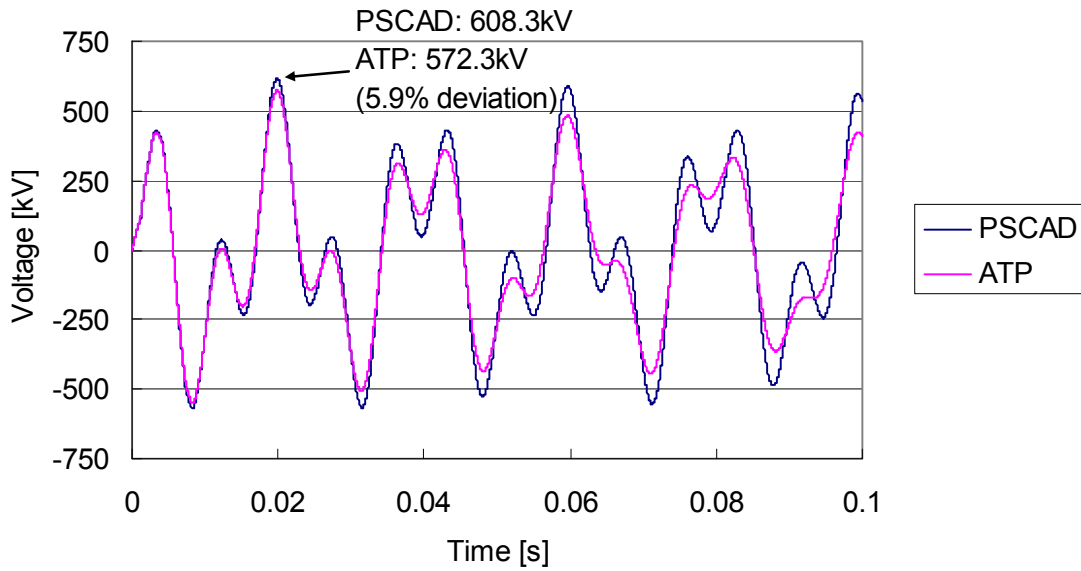
Fig. 3.17 Overvoltage caused by the energization of the KYV – ASV line (sending end).
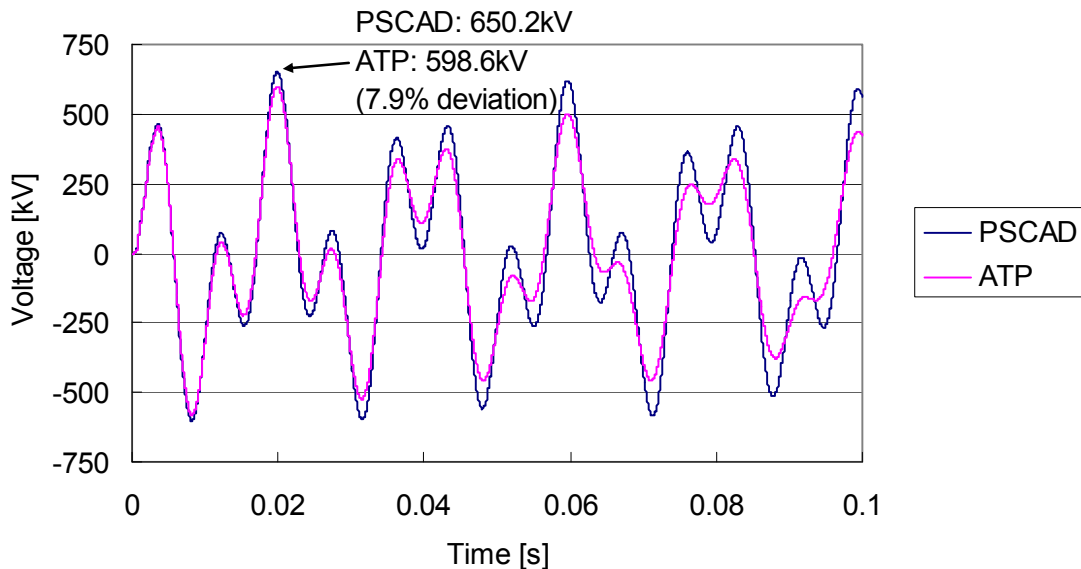
Fig. 3.18 Overvoltage caused by the energization of the KYV – ASV line (receiving end).

Fig. 3.19 shows frequency components contained in the line energization overvoltage. The frequency components are obtained by the Fourier transform of the line energization overvoltages

in the time window 0 – 0.06 s. The figure demonstrates that the results match well between PACAD and ATP-EMTP, and the dominant (transient) frequency is around 130 Hz for both cases.
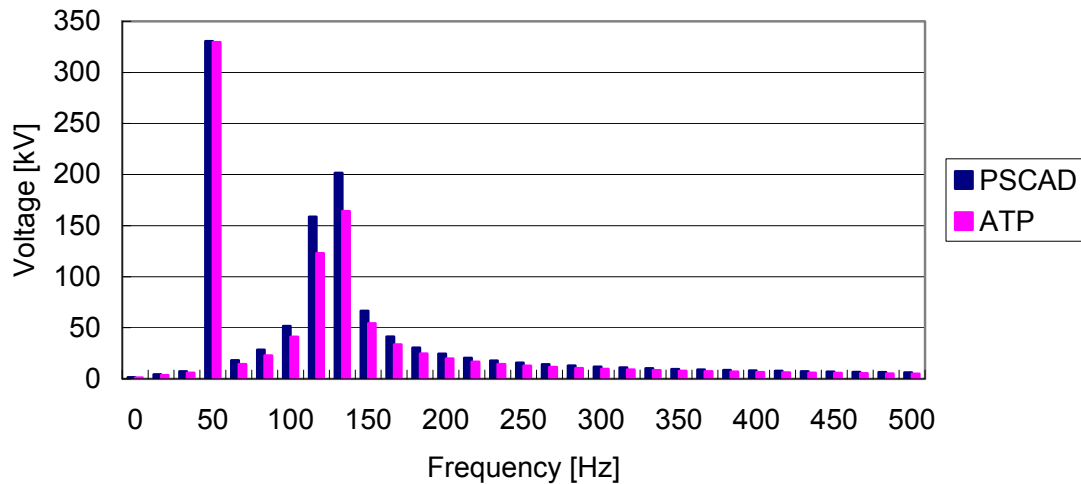
Fig. 3.19 Frequency components contained in the overvoltage caused by the energization of the KYV – ASV line (sending end).

Since the dominant frequency was found to be around 130 Hz, the target frequency of the Bergeron model was modified to 130 Hz. Fig. 3.20 and Fig. 3.21 show the comparison of the line energization overvoltages at the sending end and the receiving end, with the modified Bergeron model. With the lower target frequency, the magnitude of the overvoltages become higher, and the differences from the results in PSCAD become smaller.
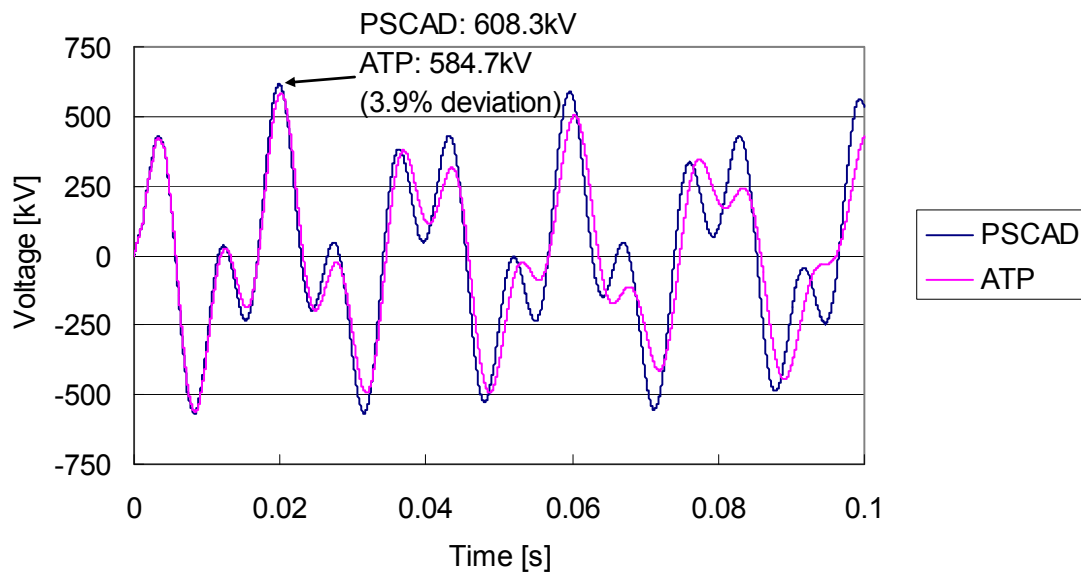
Fig. 3.20 Overvoltage caused by the energization of the KYV – ASV line
(sending end, target frequency: 130 Hz).
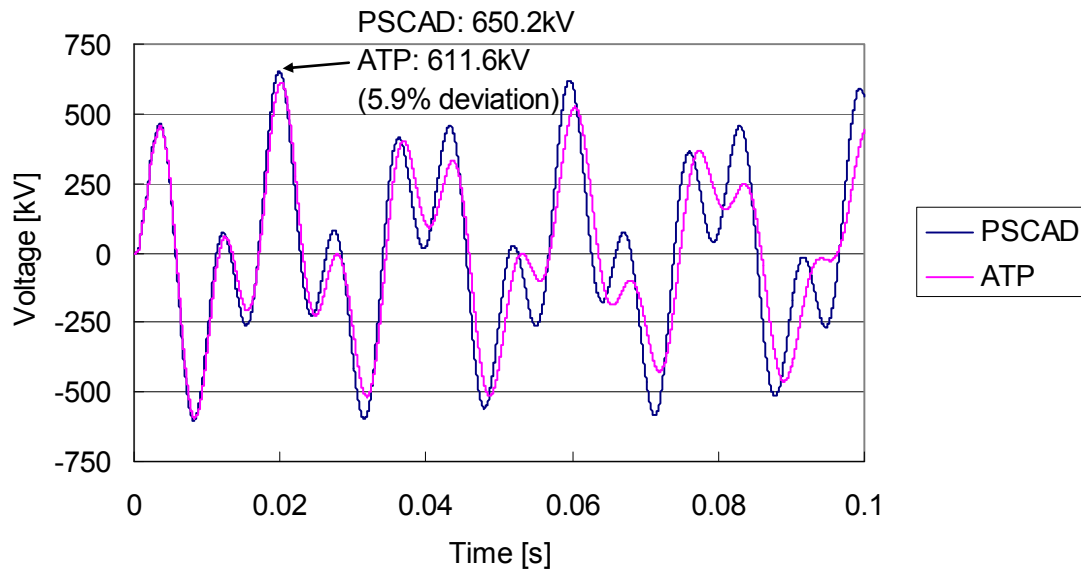
Fig. 3.21 Overvoltage caused by the energization of the KYV – ASV line
(receiving end, target frequency: 130 Hz).

From the results, the Bergeron model produces a similar overvoltage to the frequency dependent (phase) model during the first 20 ms after the energization. In finding the maximum overvoltage, the choice of cable models between the Bergeron model and the frequency dependent (phase) model does not have a noticeable impact. On the other hand, the overvoltages after the first 20 ms following energization have notable differences. It may require the use of frequency dependent (phase) model when matching simulation results to field measurements, although it is not included in the scope of the PhD project.

3.3.6   Effects of Cross-bonding

The sheath cross-bonding has to be modelled as it changes the cable impedances as discussed in Section 2.3.2. The analytical formulas and calculated results in the section show that the cable inductances become larger due to the cross-bonding.

Furthermore, Eqn. 4.14 in Section 4.1.3 shows how the cable impedances and admittances affect the propagation velocity of the overvoltages. Because of the larger cable inductance, the propagation velocity is slower for cross-bonded cables.

Fig. 3.22 shows the energization overvoltage when the Kyndbyværket – Asnæsværket line is energized from the Asnæsværket side. The black and red lines respectively show the overvoltage

when the cable line is cross-bonded and solidly-bonded. The figure demonstrates that the propagation velocity is slower in the cross-bonded cable case.
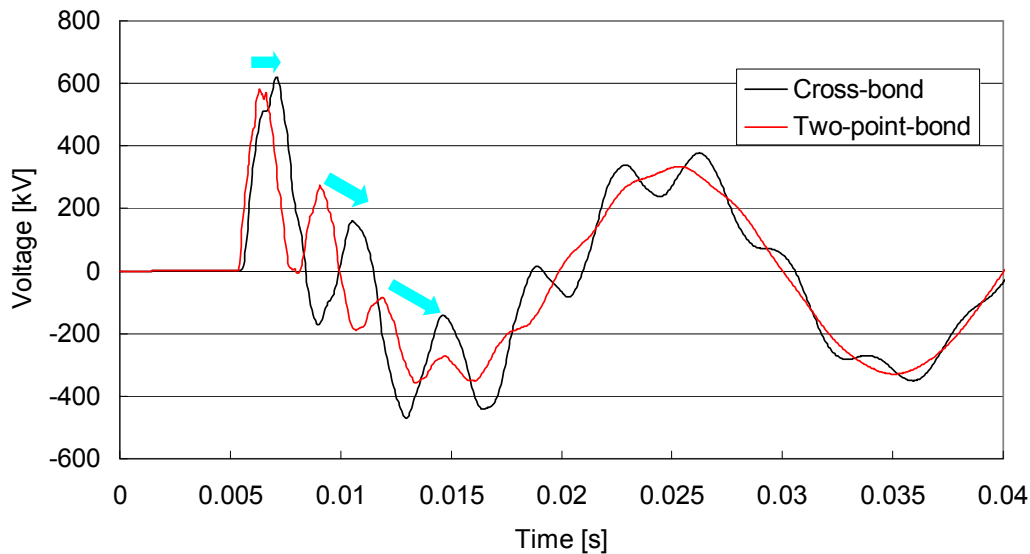

Fig. 3.22 Effect of cross-bonding.

3.3.7   Effects of Span Length

It is a common practice to reduce the number of cable joints as much as possible in order to reduce the cost and to shorten the construction duration. However, the cable span length (minor length) is normally limited by restrictions in the transportation or by the sheath voltage. The restrictions in the transportation mainly include:

- Number of turns cables can be wound around a drum
- Weight and height restrictions when a drum car has to go by road or cross bridges

The restriction in the sheath voltage differs from country to country and utility to utility. If the restriction comes from a utility's own safety codes, it may be possible to relax the restriction by applying more strict work codes, for example, to wear specific gloves.

Table 3-6 explains that the PhD project assumes the cable span length to be around 1800 – 1900 m, but this may be a difficult goal to achieve depending on the above mentioned restrictions. However, when numerous numbers of simulations are performed for statistical switching studies, it is convenient to have larger cable span lengths in order to reduce the computational burden.

This section studies the effects of assuming longer cable span length. The study was conducted with the Kyndbyværket – Asnæsværket line, but the submarine part was removed from the line. The sensitivity analysis considers the following parameters:

- Cable span length: 2, 4, 6, 8, and 16 km
- Total cable length: 24, 48, 72, 96 km

For Fig. 3.23 to Fig. 3.27, the highest overvoltages are compared for cable energization with different cable span lengths. When the cable span length is increased to 4, 6 and 8 km, the errors are below 5 %. When the cable span length is further increased to 16 km as in Fig. 3.27, the error goes up to 9 %.

From the results of this study, the statistical switching studies in Section 5.1 increases the cable span length to 6 km for 72 km cable line and to 8 km for 96 km cable line.
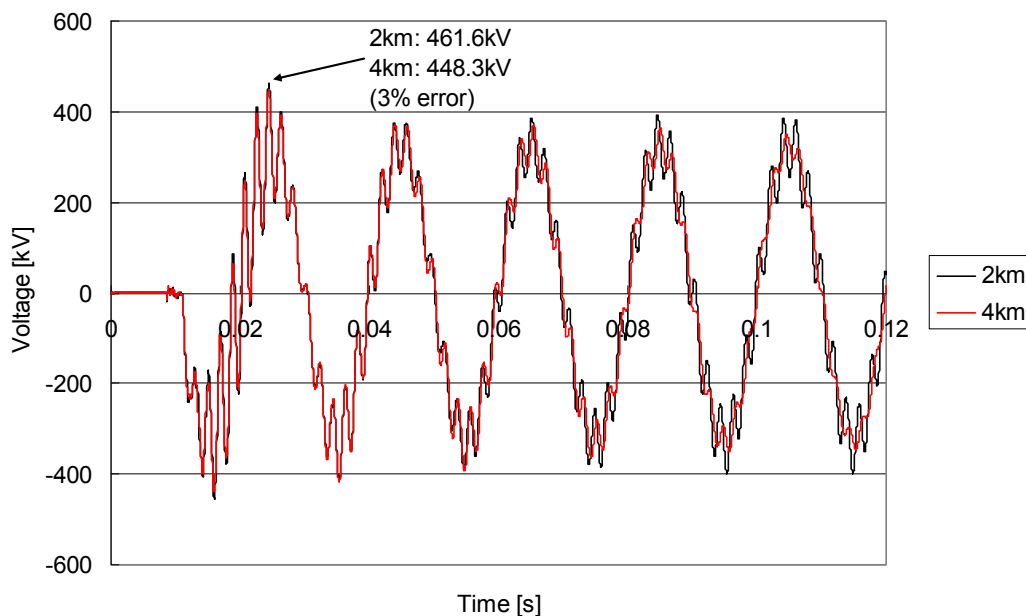
Fig. 3.23 Effect of cable span length for 24 km cable line (2 km → 4 km).
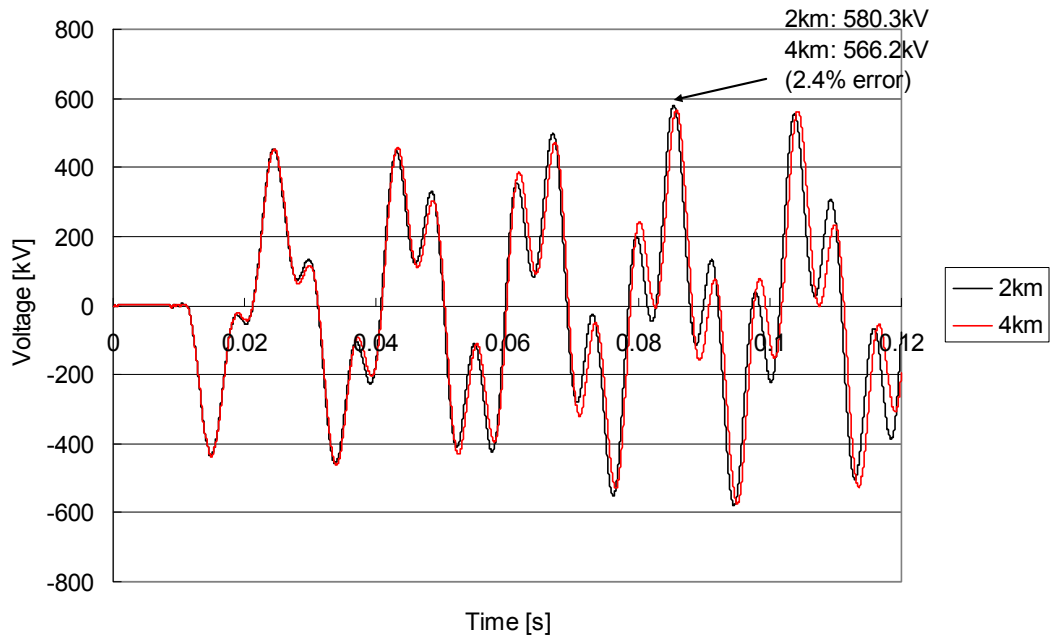
Fig. 3.24 Effect of cable span length for 48 km cable line (2 km → 4 km).
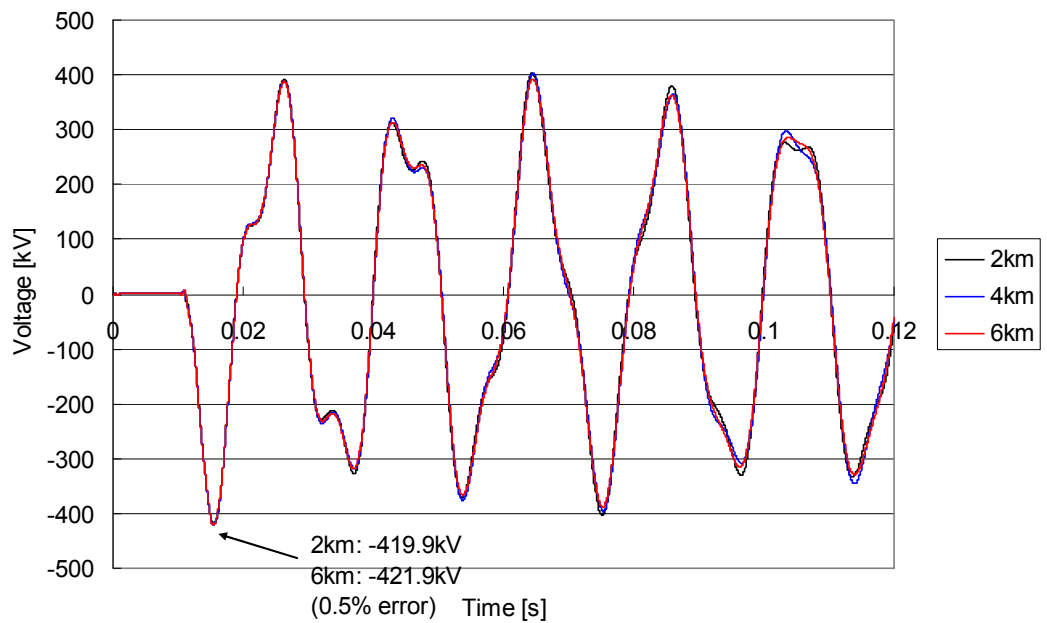
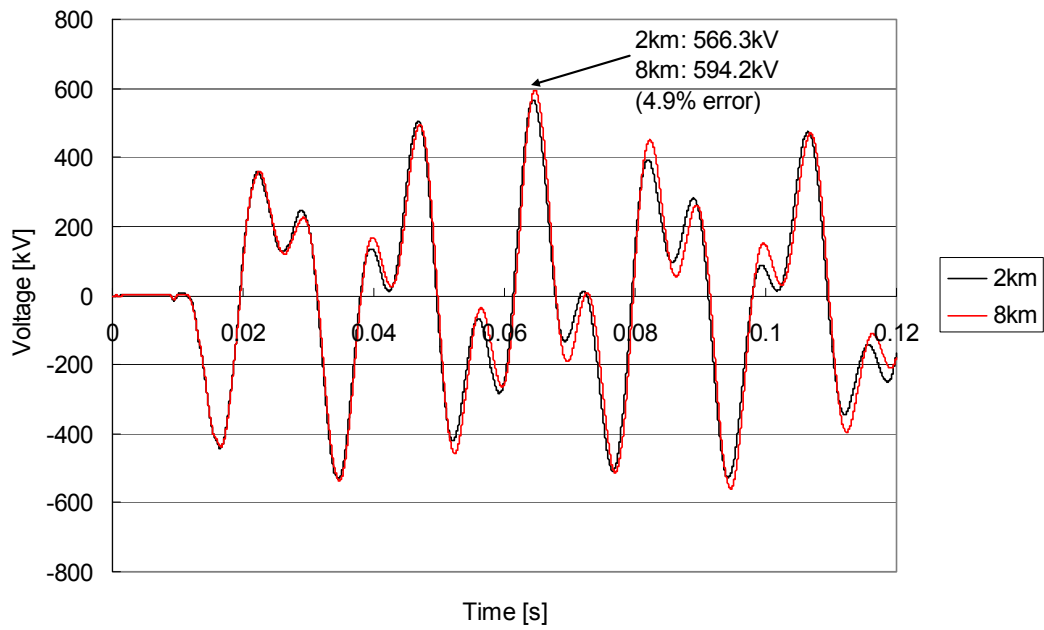**Fig. 3.25 Effect of cable span length for 72 km cable line (2 km → 6 km).**

Fig. 3.26 Effect of cable span length for 96 km cable line (2 km → 8 km).
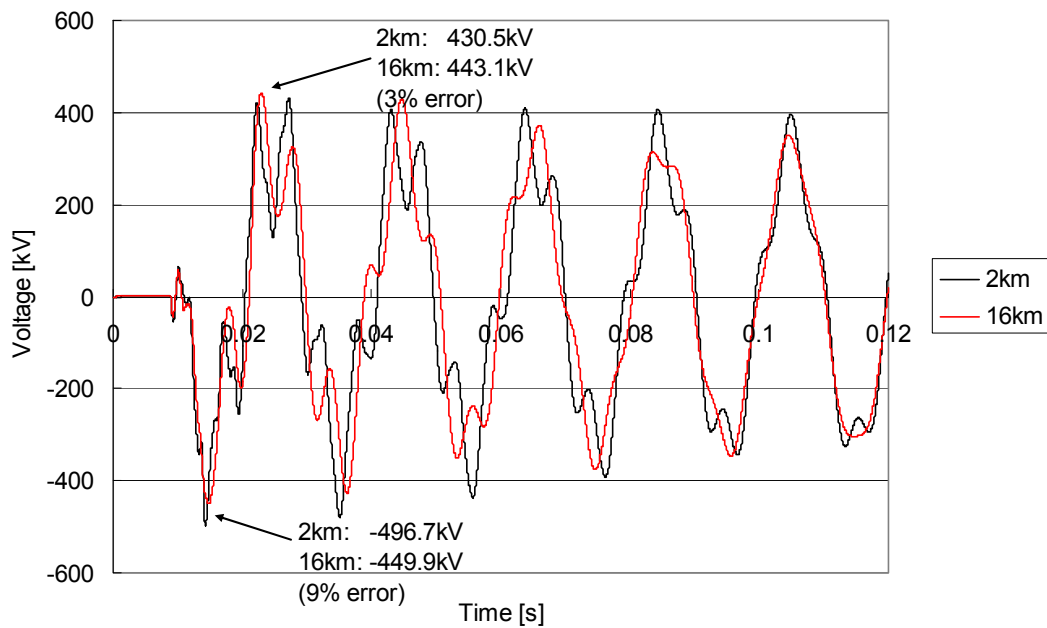

Fig. 3.27 Effect of cable span length for 24 km cable line (2 km → 16 km).

3.3.8 Effects of Armour

The Kyndbyværket – Asnæsværket line has both land part and submarine part. The submarine part has an armour conductor outside of the metallic sheath, but the armour was not included in the simulation models of the PhD project. This section studies the effects of armour when it is included in the simulation model.

As in the land part of the Kyndbyværket – Asnæsværket line, it was not possible to obtain the exact parameters. The standard data was derived from *ABB XLPE Submarine Cable Systems, Attachment to XLPE Land Cable Systems - User's Guide (rev. 5)* [3] as shown in Table 3-8. Since R5 and R6 were not available and were determined from a reasonable engineering estimation.

Table 3-8 Physical and Electrical Information of Cable (1), Submarine Part

Conductor	R1	Inner radius of the tubular core	mm	0
	R2	Outer radius of the tubular core	mm	23.7
	ρc	Resistivity	Ωm	2.84E-08
	μc	Relative permeability		1
Conductor Screen	Rsi	Outer radius of conductor screen	mm	25.7
Insulation	μI1	Relative permeability		1
	εI1	Relative permittivity		2.853
	Rso	Outer radius of the insulation	mm	52.9
Metallic Sheath	R3	Inner radius of metallic sheath	mm	55.9
	R4	Outer radius of metallic sheath	mm	59.0
	ρs1	Resistivity		2.20E-07
	μs1	Relative permeability		1
Insulation	μI2	Relative permeability		1
	εI2	Relative permittivity		2.4
Armour	R5	Inner radius of metallic sheath	mm	63.5
	R6	Outer radius of metallic sheath	mm	67.5
	ρs1	Resistivity		2.84E-08
	μs1	Relative permeability		1
Outer Covering	μI2	Relative permeability		1
	εI2	Relative permittivity		2.4
Completed Cable	R7	Average outer radius of cover	mm	70.5

In order to find the effects of armour on the energization overvoltages, the Kyndbyværket – Asnæsværket line was energized from the 400 kV voltage source behind the source impedance of 147 mH, which corresponds to the fault current 5 kA. Fig. 3.28 and Fig. 3.29 respectively show the comparison of the energization overvoltages at the sending end and the receiving end. The waveforms demonstrate that the armour does not have noticeable effects on the energization overvoltages.
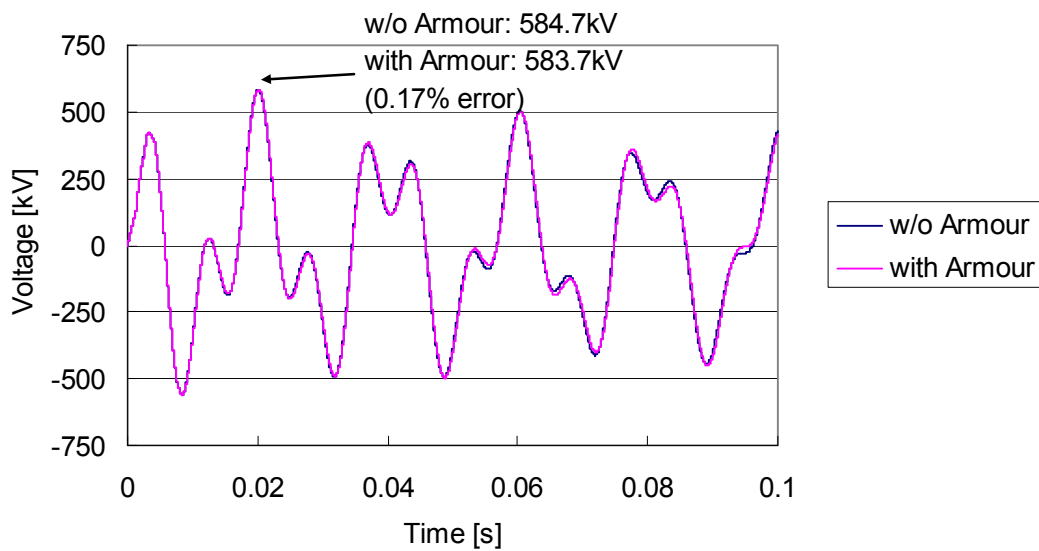

Fig. 3.28 Effects of armour on the energization overvoltage (sending end).
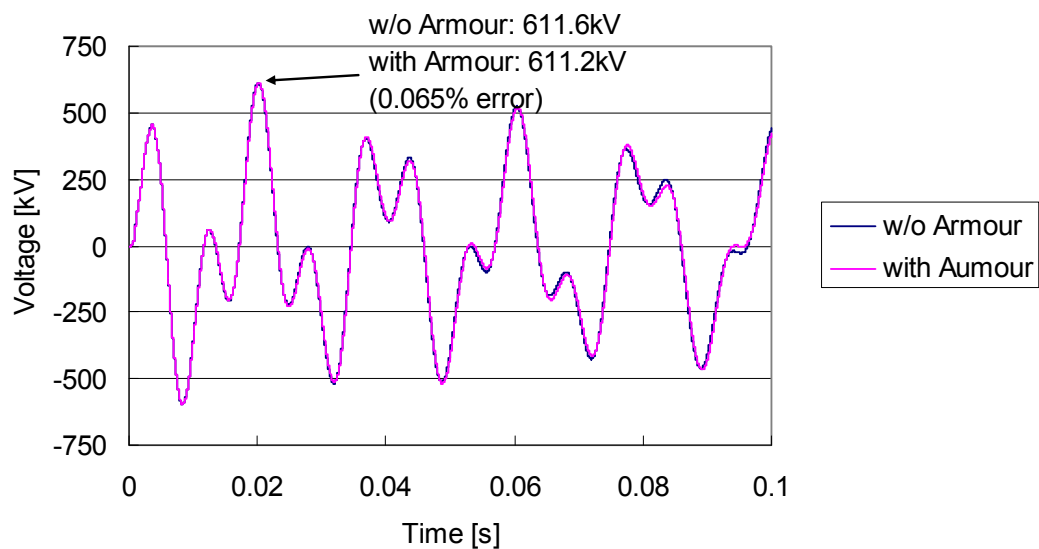
Fig. 3.29 Effects of armour on the energization overvoltage (receiving end).

3.4 Overhead Transmission Lines

3.4.1 Conductor and Tower Configuration

400 kV overhead lines were modelled using a frequency dependent model (J. Marti model). Input data for ATP-EMTP are shown in Table 3-9, and a cross-section diagram of transmission lines and ground wires are shown in Fig. 3.30.

Table 3-9 Overhead Line Data

Types	Inner Radius [mm]	Outer Radius [mm]	Resistance per conductor [ohm/km]	Number of conductors in a bundle	Separation between conductors [cm]
Transmission Line (Martin)	6.025	18.085	0.04259	2	40
Ground Wire	4.65	8.10	0.208	–	–
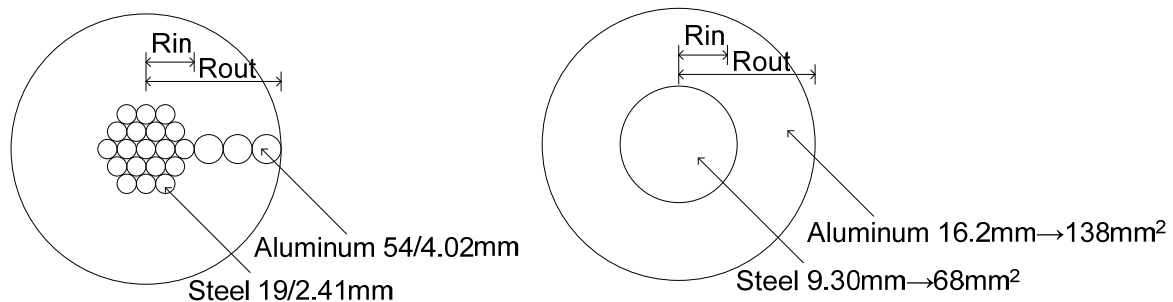
Fig. 3.30 Cross-section diagram of transmission line (left) and ground wire (right).

Fig. 3.31 shows the typical tower configuration for the 400 kV overhead lines. The layout of transmission lines and ground wires were derived from the typical tower configuration as shown in Table 3-10. This standard layout was applied to all 400 kV overhead lines.

Table 3-10 Layout of Standard 400 kV OHLs

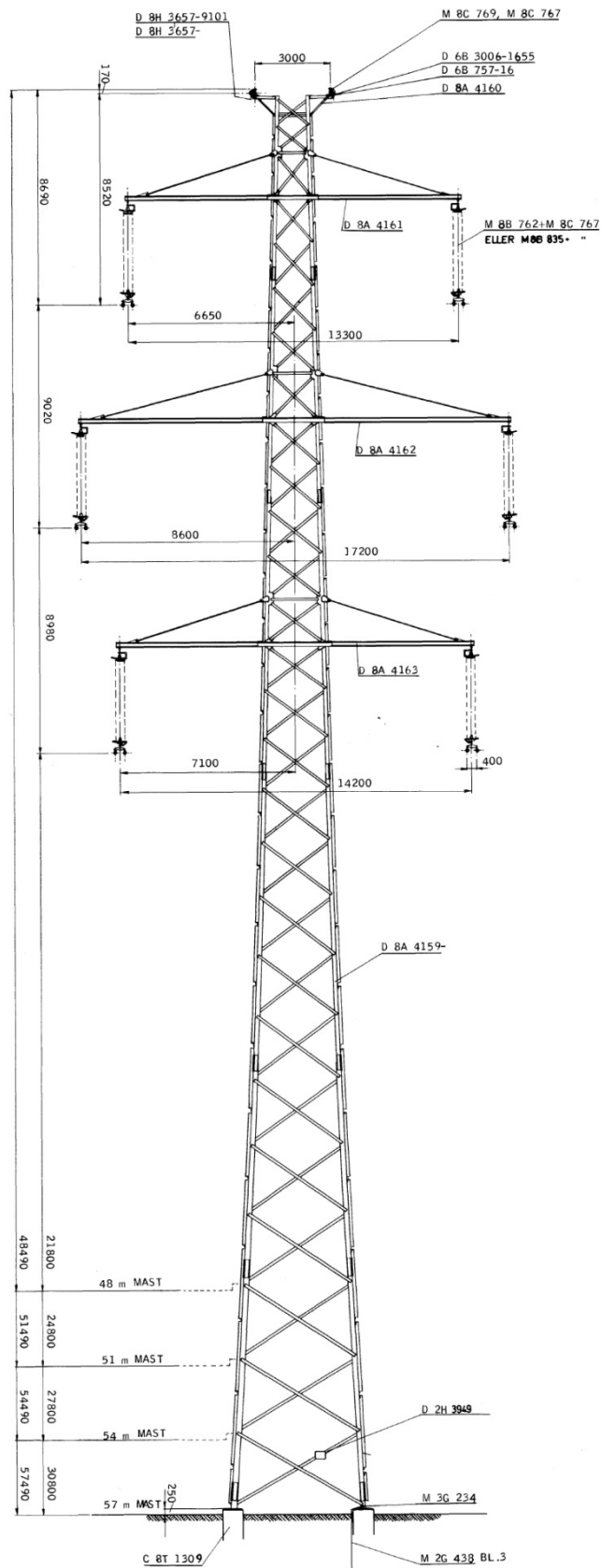| Types	Horizontal position [m]	Vertical position [m]
Transmission Lines	±6.65	34.0
	±8.60	26.0
	±7.10	20.0
Ground wires	±3.00	41.0

Fig. 3.31 Tower configuration of standard 400 kV OHLs.

3.4.2   Phase Configuration

The phase configuration of 400 kV overhead lines is also provided from Energinet.dk. Fig. 3.32 shows the phase configuration of the existing 400 kV overhead lines.
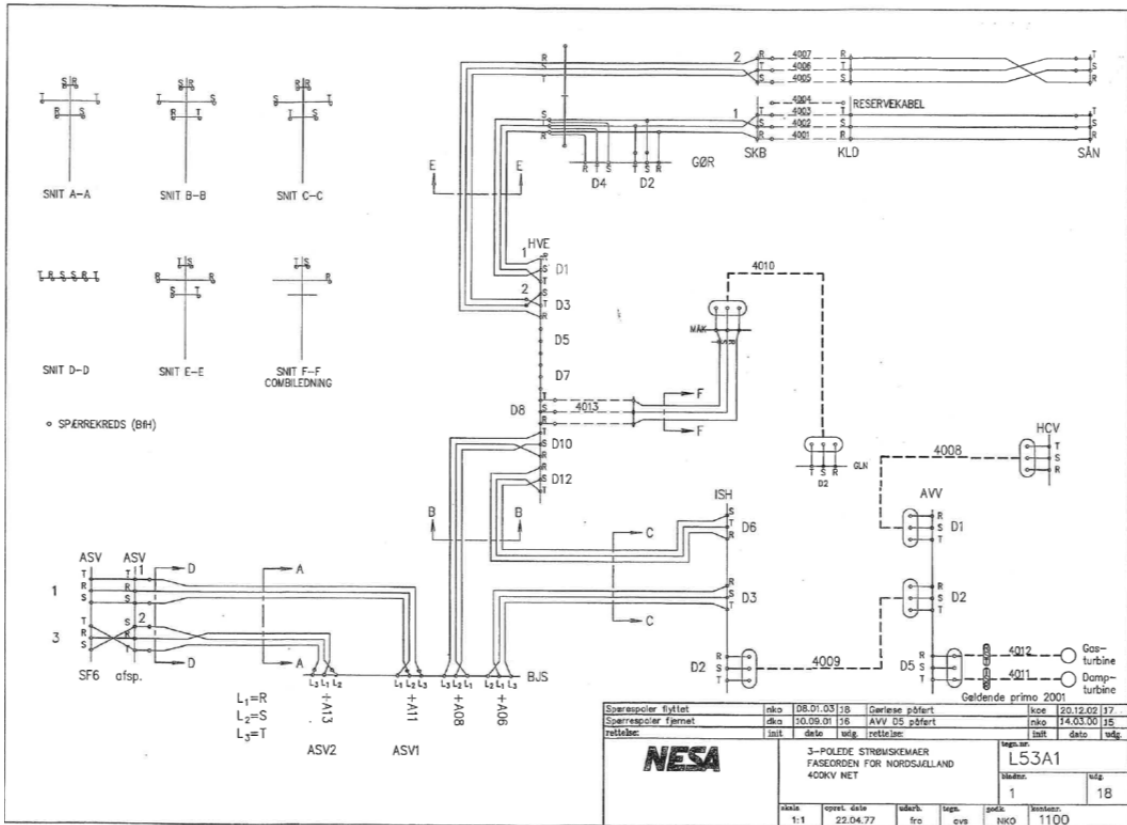

Fig. 3.32 Phase configuration of the existing 400 kV OHLs.

As for the Hovegård – Kyndbyværket line, it was assumed that the line has the same phase configuration after the line is upgraded to the 400 kV operation.

3.4.3   Comparison between PSCAD and ATP-EMTP

In PSCAD, it is not possible to model a hollow ground wire as shown in Table 3-9 since the inner radius is always considered to be zero. To keep a satisfactory accuracy of the PSCAD model for an overhead line, the sequence impedance of the double circuit tower line between Asnæsværket and Herslev is calculated in PSCAD and ATP-EMTP. It is assumed that the Asnæsværket – Bjæverskov line is cut at Herslev for the convenience in measurement.

Fig. 3.33 and Fig. 3.34 show a comparison of sequence impedances. A frequency dependent phase model is used in PSCAD. The comparison shows the error in the model by PSCAD is negligible as

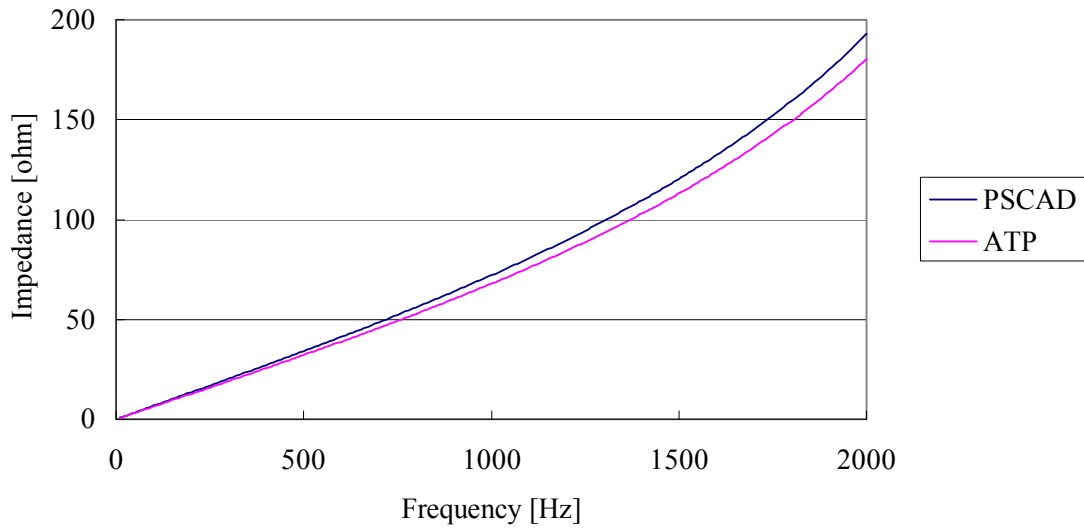the PhD project is focused on the frequency component less than 1 kHz.

Fig. 3.33 Comparison of the positive sequence impedance of 400 kV overhead line.
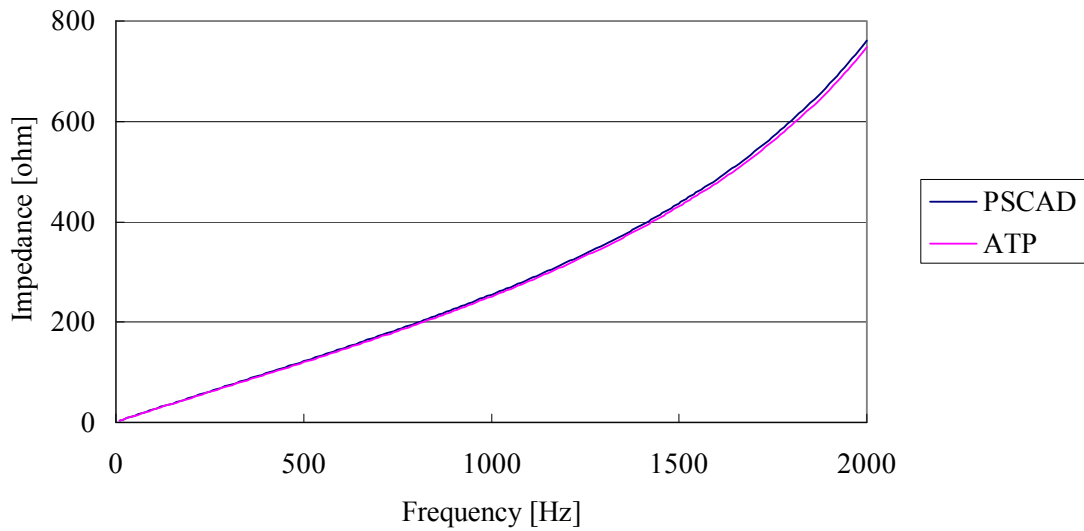

Fig. 3.34 Comparison of the zero sequence impedance of 400 kV overhead line.

3.5 Transformers

(1) 400/132 kV transformers

Model parameters of all 400/132 kV transformers were derived from the PSS/E data provided by Energinet.dk. Since all the 400/132 kV transformers except the one in GLN are modelled as two winding transformers in the PSS/E data, only the impedance between the primary and secondary windings is available. In the EMTP data, the impedance was split half and half in pu to the primary and to the secondary. The parameters are given in Table 3-11.

Table 3-11 Model Parameters of 400 kV Transformers

	R1 (ohm)	R2 (ohm)	X1 (mH)	X2 (mH)
BJS	0.968	0.1054	191.9	20.90
ISH	0.528	0.0575	138.1	15.04
AVV	0.560	0.0610	122.9	13.39
HCV	0.416	0.0453	94.7	10.32
HVE	0.904	0.0984	165.5	18.02
	0.512	0.0558	130.2	14.18
GLN	0.432	0.0470	98.4	10.72
	0.432	0.0470	98.4	10.72
GØR	0.312	0.0340	77.6	8.45
SÅN	0.296	0.0322	65.6	7.14

The saturation characteristic of 400/132 kV transformers was not available from Energinet.dk. Instead, a severe saturation characteristic within a reasonable extent, which is shown in Table 3-12 and Fig. 3.35, has been assumed for the analysis. Here, Phi is the flux linkage. The saturation characteristic was set only in transformer inrush simulations.

Table 3-12 Applied Saturation Characteristic of 400 kV Transformers

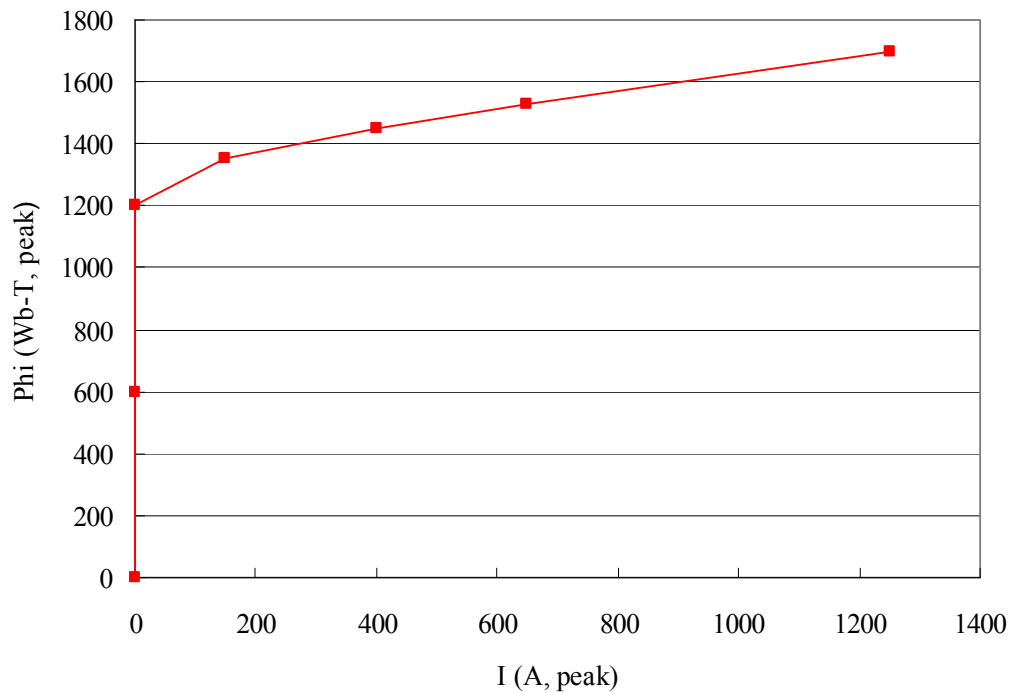| I (A, peak)	Phi (Wb-T, peak)
0	0
0.05	600.00
1.01	1200.00
150.00	1350.00
400.00	1450.00
650.00	1530.00
1250.00	1700.00

Fig. 3.35 Applied saturation characteristic of 400 kV transformers.

In the simulations of transformer energizations, it is necessary to include the hysteresis characteristic of a transformer. In ATP-EMTP, the hysteresis characteristic is obtained using the subroutine HYSDAT. Assuming the positive saturation point at 1.4 pu, the hysteresis characteristic in Table 3-13 is obtained. The positive saturation point is, in definition, the point in the first quadrant where the hysteresis loop changes from being multi-valued to being single-valued.

Table 3-13 Hysteresis Characteristic of 400 kV Transformers (Positive Saturation at 1.4 pu)

I (A, peak)	Phi (Wb-T, peak)
-100.000	-1407.353
-12.500	-1333.147
7.500	-1228.235
17.500	-955.294
33.750	827.353
52.500	1091.765
90.000	1253.824
166.250	1364.706
400.000	1450.000
550.000	1458.529

The positive saturation point at 1.4 pu could be too severe. In order to perform a sensitivity analysis, another hysteresis characteristic is derived assuming the positive saturation point at 1.3 pu as shown in Table 3-14. The inrush current will be reduced when this characteristic is adopted instead of the characteristic in Table 3-13.

Table 3-14 Hysteresis Characteristic of 400 kV Transformers (Positive Saturation at 1.3 pu)

I (A, peak)	Phi (Wb-T, peak)
-37.500	-1310.294
-4.688	-1241.206
2.813	-1143.529
6.563	-889.412
12.656	770.294
19.688	1016.471
33.750	1167.353
62.344	1270.588
150.000	1350.000
206.250	1357.941

(2) Generator step-up transformers

Model parameters of all the generator step-up transformers were also derived from the PSS/E data provided by Energinet.dk. Table 3-15 summarizes the model parameters of the generator step-up transformers.

Table 3-15 Model Parameters of Generator Step-up Transformers

	HV Side	LV Side	R1 (ohm)	R2 (ohm)	X1 (mH)	X2 (mH)
ASV	400 kV	21.0 kV	0.160	0.00044	47.2	0.130
AVV	400 kV	19.5 kV	0.172	0.00041	58.4	0.139
	400 kV	11.5 kV	1.511	0.00125	396.1	0.327
			1.511	0.00125	396.1	0.327

	HV Side	LV Side	R1 (ohm)	R2 (ohm)	X1 (mH)	X2 (mH)
ASV	132 kV	12.0 kV	0.091	0.0008	25.6	0.211
KYV	132 kV	10.0 kV	2.108	0.0121	134.2	0.770
	132 kV	18.0 kV	0.068	0.0013	13.1	0.244
			0.061	0.0011	12.3	0.229

(3) Phase shifting transformer

Model parameters of a phase shifting transformer in Asnæsværket were obtained from Energinet.dk's document *Modelling of tap changers of the ASNÆSVÆRKETS 400/132 kV TRANSFORMER using the DIgSILENT PowerFactory software* [4]. The document contains the following two tables for the phase shifter and the voltage amplitude tap changer.

Table 3-16 Data of Phase Shifter Given at Each Tap Position

Trin Nr.	UHv [kV]	Rt at 500 [%]	Xt at 500 [%]	Loading [%]	Vinkel [deg]
1	399,97	0,000	0,000	100	0,00
2	395,73	0,004	0,013	100	1,07
3	391,36	0,009	0,027	100	2,12
4	387,11	0,013	0,040	100	3,15
5	381,91	0,017	0,053	100	4,15
6	378,19	0,022	0,067	100	5,13
7	371,99	0,026	0,080	100	6,08
8	367,70	0,031	0,095	100	7,02
9	371,38	0,031	0,095	100	8,09
10	374,39	0,031	0,095	100	9,18
11	376,53	0,031	0,095	100	10,28
12	378,49	0,031	0,095	100	11,40
13	381,44	0,031	0,095	100	12,53
14	384,12	0,031	0,095	100	13,68
15	386,22	0,031	0,095	100	14,84
16	388,25	0,031	0,095	100	16,02
17	390,05	0,031	0,095	100	17,20
18	391,54	0,031	0,095	100	18,40
19	392,70	0,031	0,095	100	19,61
20	395,34	0,031	0,095	100	20,83
21	396,50	0,031	0,095	100	22,05

Table 3-17 Data of Voltage Amplitude Tap Changer Given at Each Tap Position

Trin Nr.	UHv [kV]	Rt at 500 [%]	Xt at 500 [%]	Loading [%]	Vinkel [deg]
1	447,23	0,197	15,399	100	0
2	443,62	0,197	15,329	100	0
3	440,01	0,196	15,259	100	0
4	436,40	0,196	15,189	100	0
5	432,79	0,196	15,119	100	0
6	429,18	0,195	15,049	100	0
7	425,57	0,195	14,979	100	0
8	421,96	0,194	14,919	100	0
9	418,35	0,194	14,849	100	0
10	414,74	0,194	14,779	100	0
11	411,13	0,193	14,709	100	0
12	407,52	0,193	14,639	100	0
13	403,91	0,193	14,569	100	0
14	399,97	0,192	14,499	100	0
15	396,69	0,193	14,449	100	0
16	393,08	0,194	14,389	100	0
17	389,47	0,195	14,339	100	0
18	385,86	0,196	14,279	100	0
19	382,25	0,197	14,229	100	0
20	378,64	0,198	14,179	100	0
21	375,03	0,199	14,119	100	0
22	371,42	0,200	14,069	100	0
23	367,81	0,201	14,019	100	0
24	364,20	0,202	13,959	100	0
25	360,59	0,203	13,909	100	0
26	356,98	0,204	13,849	100	0
27	353,37	0,205	13,798	100	0

The tap positions were selected according to the PSS/E power flow data. The tap positions were set at Tap No. 2 for the phase shifter and at Tap No. 15 for the voltage amplitude tap changer, respectively.

3.6 Shunt Reactors

Chapter 2 concluded that one unit of a 400 kV 300 MVar shunt reactor should be installed at Kyndbyværket and Asnæsværket, respectively. These shunt reactors should be directly connected to the Kyndbyværket – Asnæsværket line, but not to the buses.

In most analyses, the shunt reactors were modelled as a linear inductance as it yields higher overvoltages. When it is necessary, the shunt reactors are modelled with their saturation characteristics. These saturation characteristics were provided by Energinet.dk, but their capacities were 70 and 140 MVar. Assuming that the saturation characteristic of a 300 MVar shunt reactor was equal to that of a 140 MVar shunt reactor, the saturation characteristic was derived as shown in Table 3-18 and Fig. 3.36.

Mutual inductances between phases were not considered since 300 MVar shunt reactors would have to be a single phase shunt reactor.

Table 3-18 Saturation Characteristic of 400 kV 300 MVar Shunt Reactors

I (A, peak)	Phi (Wb-T, peak)
0	0
116.64	218.32
233.28	436.63
349.93	654.95
466.57	873.26
583.21	1091.58
699.85	1298.97
816.50	1506.37
933.14	1702.86
1049.78	1877.51
1166.42	2052.16
1283.07	2161.32
1399.71	2292.31
1516.35	2412.38
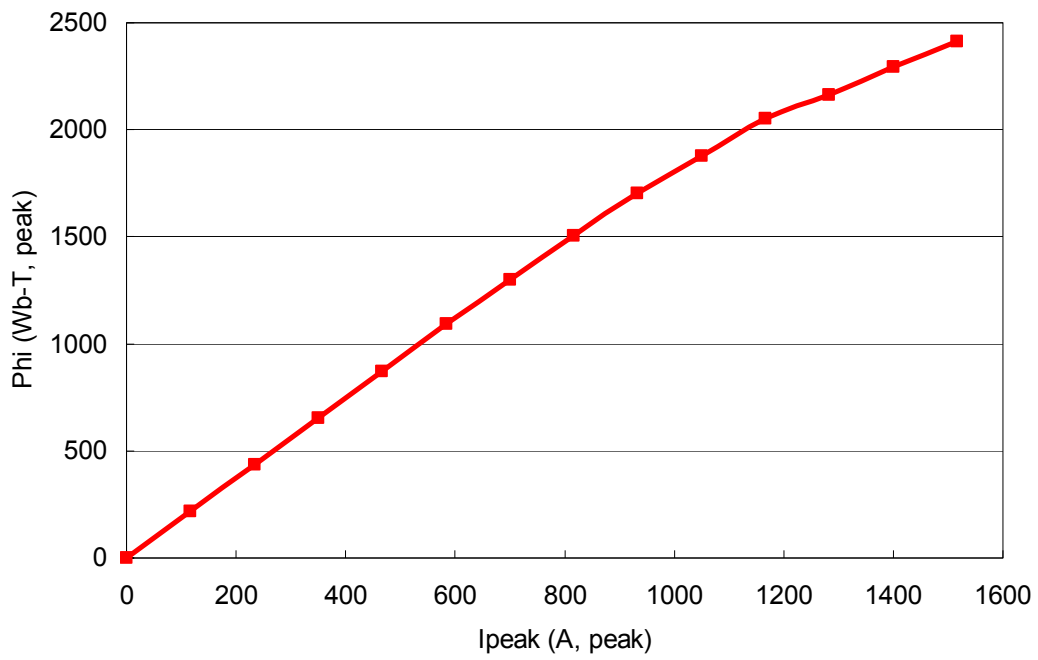
Fig. 3.36 Saturation characteristic of 400 kV 300 MVar shunt reactors.

3.7 Surge arresters

The V-I characteristic of existing 400 kV surge arresters was provided by Energinet.dk as shown in Table 3-19 and Fig. 3.37. The surge arrester model was built by a nonlinear branch (Type 92 in ATP-EMTP).

Table 3-19 V-I characteristic of Surge Arresters

I (A)	V (V)
1.0E-03	4.81E+05
1.0E-02	5.09E+05
1.0E-01	5.44E+05
1.0E+00	5.78E+05
1.0E+01	6.13E+05
1.0E+02	6.47E+05
5.0E+02	6.84E+05
1.0E+03	7.04E+05
2.0E+03	7.32E+05
5.0E+03	7.75E+05

Line discharge class 3 was assumed for the existing surge arresters. The energy absorption capability of these surge arresters are given as:

- 2.6 MJ (= 7.8 kJ/kV × 336 kV) for impulse
- 4.4 MJ (= 13 kJ/kV × 336 kV) for thermal stress

For the new surge arresters installed for the Kyndbyværket – Asnæsværket line, the line discharge class can be upgraded to Class 5 when necessary. Since the energy absorption capability of Class 5 surge arresters is not available for the thermal stress, it was derived by linear approximation.

- 5.7 MJ (= 17 kJ/kV × 336 kV) for impulse
- $9.5 \,\text{MJ} \left(= 17 \,\text{kJ/kV} \times \dfrac{13 \,\text{kJ/kV (Class3, for thermal stress)}}{7.8 \,\text{kJ/kV (Class3, for impulse)}} \times 336 \,\text{kV} \right)$ for thermal stress
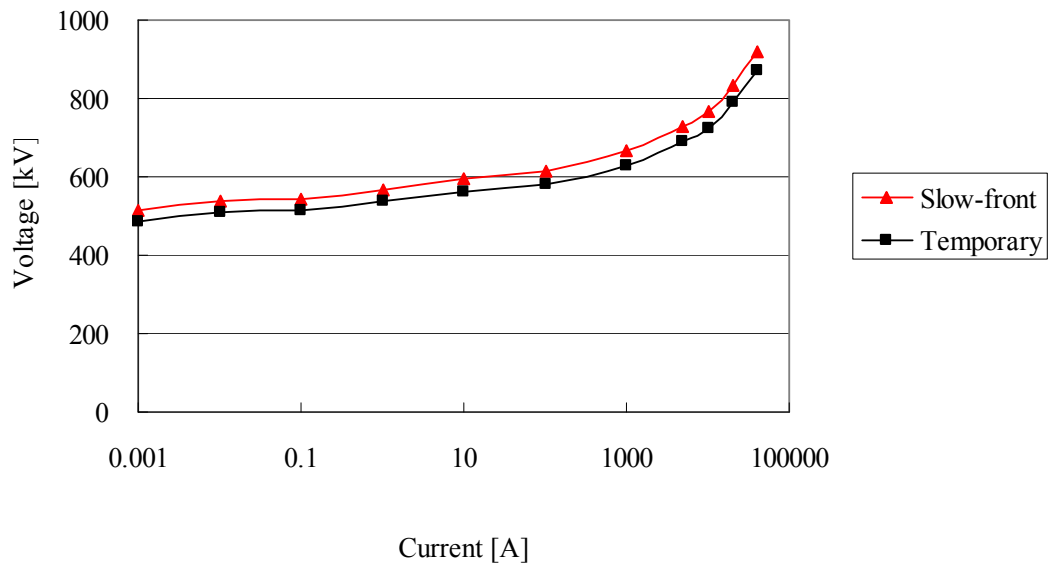
Fig. 3.37 V-I characteristic of surge arresters.

It is the normal practice in the insulation coordination to ensure that surge arresters are the weakest equipment against overvoltages. They protect other important equipment in a substation, but they themselves are considered sacrificable in unforeseeable events. Since a failure of a surge arrester can lead to the unavailability of equipment which has been protected by it, they should not fail in foreseeable events.

The withstand voltages of surge arresters can be an issue for the temporary overvoltage with low damping. Temporary overvoltages found in Chapter 4 were evaluated against surge arrester ratings, i.e. energy absorption capability and withstand voltages. Table 3-20 shows the withstand voltages (phase to ground, rms) of surge arresters assumed in the analysis.

Table 3-20 Withstand Voltages of Surge Arresters

Maximum continuous operating voltage		269 kV (1.16 pu)
Power frequency withstand voltage (1 min)		364 kV (1.58 pu)
Temporary overvoltage	10 sec	370 kV (1.60 pu)
	1 sec	390 kV (1.69 pu)

For efficient overvoltage analysis, most of the simulations were performed without the surge arrester model. When a high overvoltage occurs compared with the withstand voltages, the simulation was repeated with the surge arrester model in order to evaluate the effectiveness and energy absorption of the surge arrester.

3.8 Generators

In EMTP simulations, generators are often modeled as an ideal voltage sources without the generator impedance. The generator impedance jX''_d (subtransient direct-axis impedance) of a generator has to be considered outside of the voltage source.

In contrast, in power flow calculations, generators models normally include jX''_d inside themselves. Results of power flow calculations, as a result, do not give us the magnitude and the phase angle of the voltage source behind jX''_d.

In Fig. 3.38, the magnitude V_b and phase angle θ_b of the generator terminal voltage is know from the results of the power flow calculation. In order to set up the generator models in EMTP simulations, it is necessary to find the magnitude V_g and phase angle θ_g of the ideal voltage source from the generator terminal voltage and the output of the generator $P+jQ$.

Generator terminal   Ideal voltage source
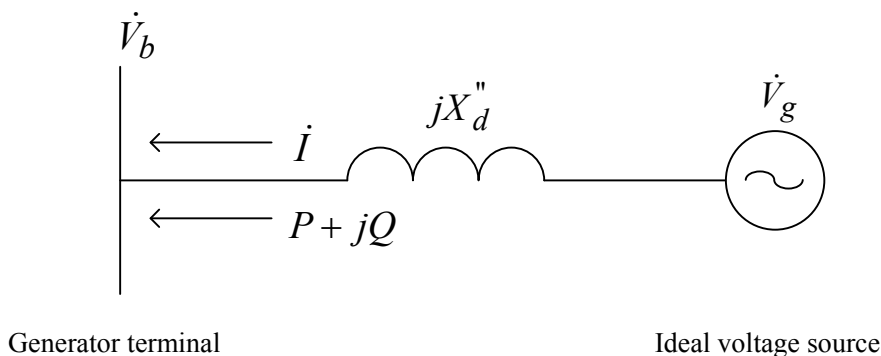
Fig. 3.38 Setup of generator models.

$\dot{V}_b = V_b \cdot e^{j\theta_b}$: generator terminal voltage (phase-to-phase)

$X = X_d''$: subtransient direct-axis reactance

$\dot{V}_g = V_g \cdot e^{j\theta_g}$: voltage source behind the subtransient reactance

$$P + jQ = \sqrt{3} \cdot \dot{V}_b \cdot \dot{I}^* = \frac{\dot{V}_b(\dot{V}_g^* - \dot{V}_b^*)}{-jX}$$

$$= j\frac{\dot{V}_b(\dot{V}_g^* - \dot{V}_b^*)}{X}$$

$$= j\frac{V_b V_g e^{j(\theta_b - \theta_g)} - V_b^2}{X}$$

$$P = \frac{V_b V_g \sin(\theta_g - \theta_b)}{X}$$

$$Q = \frac{V_b V_g \cos(\theta_g - \theta_b) - V_b^2}{X}$$

Modifying the above equations, V_g and θ_g are found by the following equations:

$$\theta_g = \tan^{-1}\frac{P}{Q + \dfrac{V_b^2}{X}} + \theta_b$$

$$V_g = \frac{XP}{V_b \sin(\theta_g - \theta_b)}$$

In the off-peak load condition, only two large generators are in-service at Asnæsværket (ASV) and Avedøreværket (AVV). Distributed generations operating in the HV network are not included in the simulation model. It is a common practice since their effects on the EHV network can be ignored and their operating conditions cannot be monitored in the real-time operation.

Table 3-21 shows the input data for generator models obtained from power flow calculation results. Since line parameters in power flow calculations are different from those in EMTP simulations, it is sometimes necessary to slightly adjust the values in in Table 3-21 in order to have an appropriate initial power flow conditions for the transient overvoltage analysis. Also, in some analyses, network conditions were modified in order to consider severer conditions. In such cases, it is necessary to adjust the generator model setting in order to produce appropriate initial conditions.

Table 3-21 Calculated Data for Generators

	Rated Voltage	P (MW)	Q (MVar)	X (mH)	V_g (kV)	θ_g (deg)
ASV	21.0 kV	384	-116.3	0.407	19.24	-109.8
AVV	19.5 kV	331.2	83.8	0.480	20.06	68.4

3.9 Loads

Load models were connected to 132 kV buses of 400 kV substations. First, the power flows in the 400/132 kV transformers were obtained from the power flow calculation results. These power flows were then converted to equivalent RL or RC circuits. The equivalent circuits were connected to 132 kV buses as constant impedance load models. When the reactive power was fed from the 400 kV buses, a RL equivalent circuit is adopted. Otherwise, when the reactive power was fed from the 132 kV buses, a RC equivalent circuit is adopted.

The conversion to the equivalent circuits is necessary only in ATP-EMTP. In PSCAD, active and reactive power loads obtained from the power flows in the 400/132 kV transformers can be connected to the 132 kV buses without the conversion. The conversion is then automatically performed inside PSCAD.

Table 3-22 shows the active and reactive loads and the constant impedance load models assumed in the off-peak load condition.

Table 3-22 Load Models in Off-peak Load Condition

	Bus #	P [MW]	Q [MVar]	R [ohm]	L [mH]	R [ohm]	C [uF]
ASV	Total	80.5	23.2	-	-	216.4	4.238
BJS	92	38.8	-5.0	-	-	449.1	0.913
ISH	187	42.1	69.7	-	-	413.9	12.733
AVV	82	50.5	-68.6	-	-	345.0	12.532
HCV	156	172.0	167.1	12497	38647	-	-
HVE	179	149.9	266.6	8540	48344	-	-
KYV	224	77.2	-35.9	-	-	225.7	6.558
GLN	133	265.4	17.0	17388	3545	-	-
GOR	144	125.3	-73.0	-	-	139.1	13.336
SAN	52	400.8	-319.0	-	-	43.5	58.276

References

[1] *XLPE Underground Cable Systems – User's Guide (rev. 3)*, ABB.

[2] Bjørn Gustavsen "Panel Session on Data for Modeling System Transients. Insulated Cables", *Proc. IEEE. Power Engineering Society Winter Meeting*, 2001.

[3] *XLPE Submarine Cable Systems, Attachment to XLPE Land Cable Systems - User's Guide (rev. 5)*, ABB.

[4] *Modelling of tap changers of the ASNÆSVÆRKETS 400/132 kV TRANSFORMER using the DIgSILENT PowerFactory software*, Energinet.dk (company internal document of Energinet.dk).

Chapter 4 Temporary Overvoltage Analysis

Temporary overvoltages are the greatest concerns when studying long EHV AC cables. Because of the large charging capacity and large shunt reactors for the compensation, the natural frequencies of a network with the long EHV AC cables tend to be much lower than those of a conventional network without the EHV cables. As such, in conventional networks, switching operations such as cable energization and fault clearance are considered as causes of slow-front overvoltages, but they need to be considered as causes of temporary overvoltages in a network with long EHV AC cables.

Even though several studies on temporary overvoltages of long EHV AC cables have been published, there is no widely accepted guideline on the temporary overvoltage analysis with the long EHV AC cables [1]-[4]. When we standardize the temporary overvoltage analysis on long EHV AC cables, there are the following technical difficulties:

- Simulation models need to include a wide area away from the point of interest.
- A severe overvoltage occurs only in particular operating conditions.

As for the first point, it is necessary to model a very wide area away from the point of interest in order to accurately reproduce low frequency components of a temporary overvoltage. However, it is not always possible to obtain precise information of all equipment. The availability largely depends on a utility's practice. A compromise to some extent is often necessary. In addition, large models can slow down a simulation depending on the adopted models and simulation software, which almost prohibits a daily analysis.

Model reduction is discussed to deal with this problem, but in order to obtain a reduced model, a full model has to be built first. It is not recommended to obtain a reduced model from power flow data, since it can match only the fundamental frequency response of the network. As such, the model reduction can contribute to speed up the simulation, but modeling of a very wide area is still necessary.

As for the second point, temporary overvoltages such as the resonance overvoltages and the overvoltages caused by load shedding are low probability phenomena. Only certain and particular network conditions can yield a severe overvoltage that can lead to an equipment failure. Major difficulties exist in finding these certain and particular network conditions. Evaluating a low-probability high-consequence risk is also difficult but must be done when and after the cables are installed. The risks may be avoided via carefully prepared operational countermeasures, but not all utilities can take operational countermeasures as it can be a major burden for system analysts.

4-2

Considering these difficulties, the PhD project takes the following steps:

- Start from the full model created in the previous chapter
- Confirm the full model runs within a reasonable duration which enables analyses of the model on a daily rush basis. Otherwise, consider the reduction of the model.
- Consider the most severe scenario to characterize problems
- Perform sensitivity analysis on source impedances, load levels, and 132 kV networks

4.1 Series Resonance Overvoltage

4.1.1   Overview

When inductance L and capacitance C are connected in series, the total impedance or series impedance becomes zero at the frequency $f_n = \dfrac{1}{2\pi\sqrt{LC}}$. When a voltage source of this frequency is connected to the series circuit as shown in Fig. 4.1, an infinitely large current flows into the series circuit in theory. Because of this large current, the voltages across the inductance V_L and the capacitance V_C become infinite if the resistance of the circuit is neglected. This is called series resonance, and V_L and V_C are the resonance overvoltage.
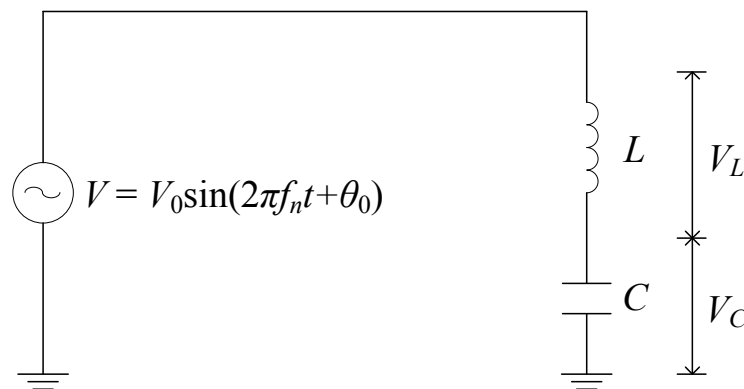
Fig. 4.1 Simple series resonance circuit.

The series resonance overvoltage can occur in an actual power system. Fig. 4.2 shows an example of series resonance circuits. When one transmission line is energized, a part of the energization overvoltage travels into the series resonance circuit which is composed of transformer inductance L and cable capacitance C, as shown by the red arrow in the figure. If the energization overvoltage contains the natural frequency f_n of the series resonance circuit, the series resonance overvoltage can be caused at the secondary side of the transformer. Therefore, when studying the series resonance overvoltage, we need to know both the dominant frequency contained in the energization overvoltage and the natural frequency of the series resonance circuit.
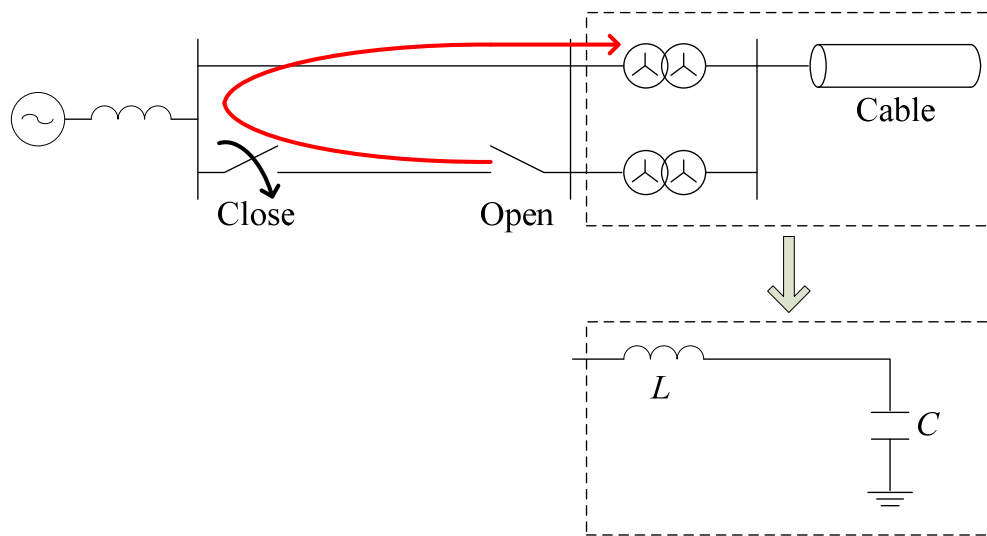
Fig. 4.2 Example of series resonance circuits in actual power systems.

In addition, when the transmission line energized in Fig. 4.2 is a long EHV cable line, the dominant frequency contained in the energization overvoltage could be very low, depending on the source impedance. The low-frequency overvoltage is weakly damped, which can lead to a severe resonance overvoltage at a far location.

In this PhD project, the series resonance overvoltage is studied in the following procedure:

- Find the most severe switching scenarios
- Simulate the most severe switching scenarios to find the dominant frequency contained in the energization overvoltage
- Find the natural frequency of the series resonance circuit composed of transformer inductance and cable capacitance
- Check the match of two frequencies – dominant frequency and natural frequency
- Simulate the most severe switching scenarios when the two frequencies are matched

4.1.2   Most Severe Scenarios

According to the study procedure, we start from identifying the most severe switching scenarios related to the Kyndbyværket – Asnæsværket line.

Fig. 4.3 shows the assumed most severe scenario for the Kyndbyværket 132 kV network. The series resonance overvoltage is caused by the energization of the Kyndbyværket – Asnæsværket line from the Kyndbyværket side. The energization overvoltage first travels to the Asnæsværket side (open

end) and reflected back to the Kyndbyværket side. A part of the reflected overvoltage travels into the Kyndbyværket – Hovegård line; the other part of the reflected overvoltage travels into the series resonance circuit composed of the 400/132 kV Kyndbyværket transformer and the charging capacity of the Kyndbyværket 132 kV network.

The source impedance and the charging capacity will be adjusted to match the dominant frequency and resonance frequency.

As the loads in the Kyndbyværket 132 kV network will damp the series resonance overvoltage on the secondary side of the 400/132 kV Kyndbyværket transformer, the series resonance overvoltage is more severe under the low load condition.
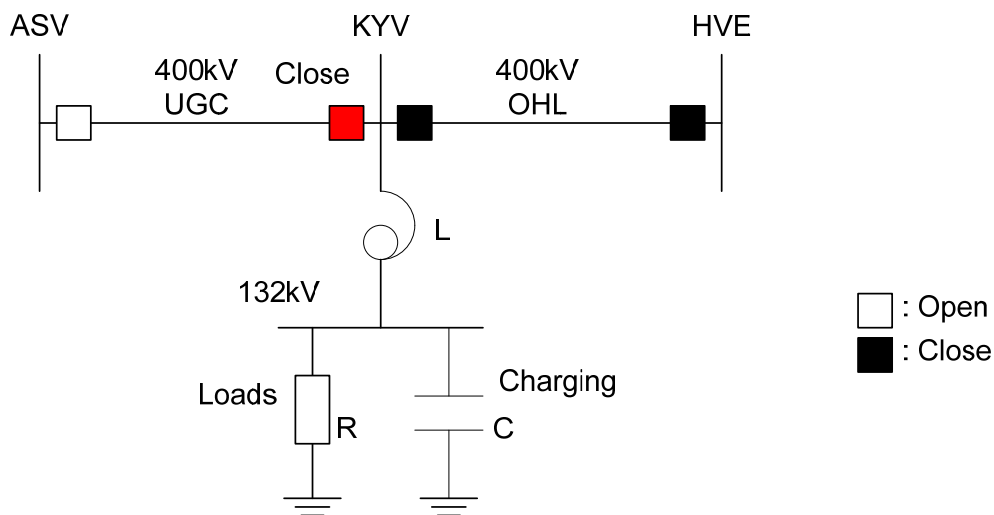
Fig. 4.3 Assumed most severe scenario for the KYV 132 kV network.

Fig. 4.4 shows the assumed most severe scenario for the Asnæsværket 132 kV network. The series resonance overvoltage is caused by the energization of the Kyndbyværket – Asnæsværket line from the Asnæsværket side. The energization overvoltage first travels to the Asnæsværket side (open end) and reflected back to the Asnæsværket side. A part of the reflected overvoltage travels into the Asnæsværket – Bjæverskov line; the other part of the reflected overvoltage travels into the series resonance circuit composed of the 400/132 kV Asnæsværket transformer and the charging capacity of the Asnæsværket 132 kV network.

The large generator at Asnæsværket is assumed to be out of service since the generator contributes to the damping of the energization overvoltage.
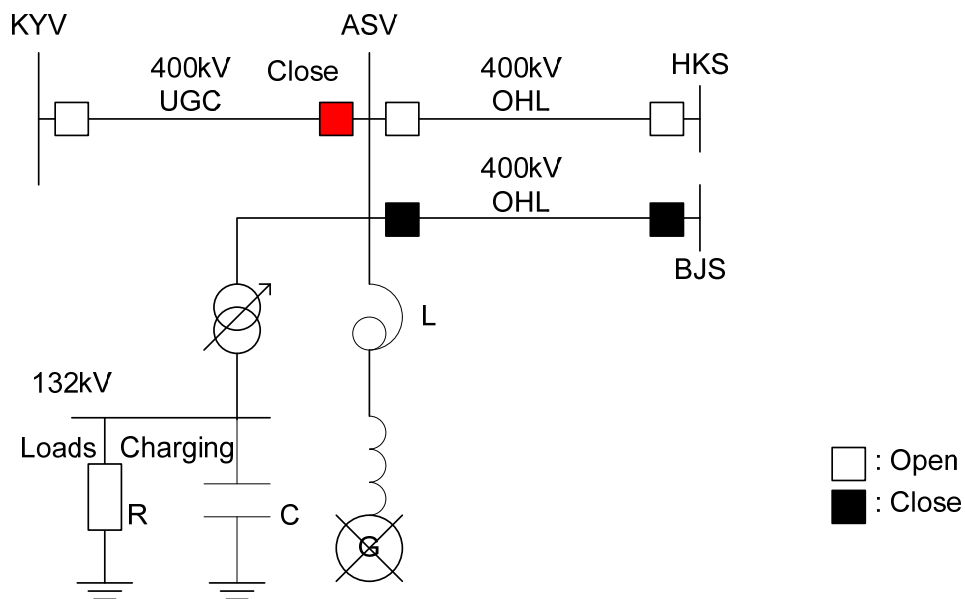
Fig. 4.4 Assumed most severe scenario for the ASV 132 kV network.

Here, the Kyndbyværket – Asnæsværket line is energized from Bjæverskov since the generator at Asnæsværket does not have a black start capability. If the generator has the black start capability, the energization from the generator at Asnæsværket can be the most severe scenario which needs to be studied.

4.1.3   Dominant Frequency in Energization Overvoltage

4.1.3.1   Derivations of Theoretical Formulas of Dominant Frequency

As discussed previously, severe temporary overvoltages, such as resonance overvoltages, only occur in particular network conditions, and considerable efforts are made in system studies to find these severe conditions. As the modeling of a broader area is necessary for the temporary overvoltage analysis, it is time consuming to set up cable line models and to perform time domain simulations and / or frequency scans in EMT-type programs.

As more long cables are installed, a simple estimation of the propagation velocity and the dominant frequency component without carrying out time domain simulations or frequency scans is desired for an efficient planning or operational planning of the network. For example, we can do without the resonance overvoltage analysis caused by the switching of a particular cable if we know the dominant frequency component caused by the switching of the cable does not match the natural

frequency of the network. With the knowledge on the estimated dominant frequency, therefore, the efforts to find severe conditions can be greatly reduced. Based on the impedance and admittance calculation in [5][6], this section addresses the estimation of the propagation velocity and the dominant frequency component contained in the switching overvoltage of long cables.

(a) Average Impedance and Admittance

The metallic sheaths of a long cable are generally cross-bonded in order to reduce both the sheath induced current and the sheath voltage. It has been found that the cross-bonding affect the impedance and the admittance of the cable and their derivation is given in [5][6].

Assuming each minor section of a cable has an equal length, the average impedance of the cross-bonded cable for one minor section is given in the following equation.

$$[Z] = ([z] + [R][z][R]^{-1} + [R]^{-1}[z][R])/3 \qquad \text{Eqn. 4.1}$$

Here, $[z]$ is the impedance of the cable per unit length for one minor section and $[R]$ is a rotation matrix.

$$[z] = \begin{bmatrix} [z_{CoCo}] & [z_{CoSh}] \\ [z_{CoSh}] & [z_{ShSh}] \end{bmatrix} \qquad \text{Eqn. 4.2}$$

$$[R] = \begin{bmatrix} 1 & 0 & 0 & 0 & 0 & 0 \\ 0 & 1 & 0 & 0 & 0 & 0 \\ 0 & 0 & 1 & 0 & 0 & 0 \\ 0 & 0 & 0 & 0 & 0 & 1 \\ 0 & 0 & 0 & 1 & 0 & 0 \\ 0 & 0 & 0 & 0 & 1 & 0 \end{bmatrix} \qquad \text{Eqn. 4.3}$$

where $[z_{CoCo}]$: impedance between conductors

$[z_{CoSh}]$: impedance between conductors and sheaths

$[z_{ShSh}]$: impedance between sheaths
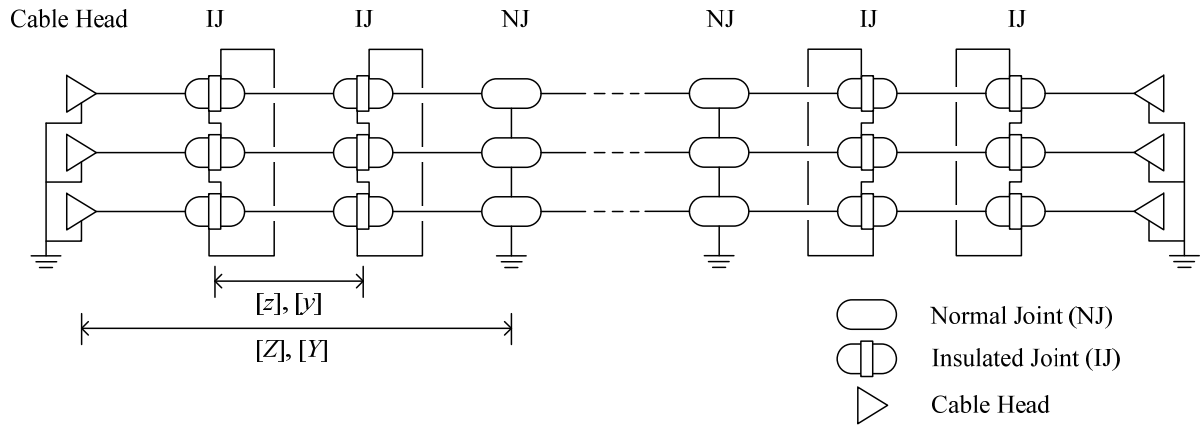
Fig. 4.5 Cross-bonding Diagram.

The calculation of the average impedance yields the following equations.

$$[Z] = \begin{bmatrix} [Z_{CoCo}] & [Z_{CoSh}] \\ [Z_{CoSh}]^T & [Z_{ShSh}] \end{bmatrix} \qquad \text{Eqn. 4.4}$$

$$[Z_{CoCo}] = [z_{CoCo}] \qquad \text{Eqn. 4.5}$$

$$[Z_{CoSh}] = \begin{bmatrix} Z_{AS} & Z_{AS} & Z_{AS} \\ Z_{BS} & Z_{BS} & Z_{BS} \\ Z_{CS} & Z_{CS} & Z_{CS} \end{bmatrix} \qquad \text{Eqn. 4.6}$$

$$[Z_{ShSh}] = \begin{bmatrix} Z_{SS} & Z_{SM} & Z_{SM} \\ Z_{SM} & Z_{SS} & Z_{SM} \\ Z_{SM} & Z_{SM} & Z_{SS} \end{bmatrix} \qquad \text{Eqn. 4.7}$$

Impedances in Eqn. 4.6 and Eqn. 4.7 are given by

$$\begin{cases} Z_{AS} = (z_{Aa} + z_{Ab} + z_{Ac})/3 \\ Z_{BS} = (z_{Ba} + z_{Bb} + z_{Bc})/3 \\ Z_{CS} = (z_{Ca} + z_{Cb} + z_{Cc})/3 \\ Z_{SS} = (z_{aa} + z_{bb} + z_{cc})/3 \\ Z_{SM} = (z_{ab} + z_{bc} + z_{ca})/3 \end{cases} \qquad \text{Eqn. 4.8}$$

In the subscripts of the impedances, capital letters show the phase of the conductor and lower letters show the phase of the metallic sheath.

Similarly, the average admittance of the cross-bonded cable for one minor section can be calculated as follows:

$$[Y] = ([y] + [R][y][R]^{-1} + [R]^{-1}[y][R]) / 3$$
$$= \begin{bmatrix} [Y_{CoCo}] & [Y_{CoSh}] \\ [Y_{CoSh}] & [Y_{ShSh}] \end{bmatrix}$$

Eqn. 4.9

$$[Y_{CoCo}] = y_{AA} \cdot I$$

Eqn. 4.10

$$[Y_{CoSh}] = -\frac{y_{AA}}{3}\begin{bmatrix} 1 & 1 & 1 \\ 1 & 1 & 1 \\ 1 & 1 & 1 \end{bmatrix}$$

Eqn. 4.11

$$[Y_{ShSh}] = y_{SS} \cdot I$$

Eqn. 4.12

In Eqn. 4.10 and Eqn. 4.12, *I* is an identity matrix.

Since the metallic sheath of the cross-bonded cable is earthed at the both ends of a major section, $[Z]$ and $[Y]$ can be reduced to 4 × 4 matrices. The reduction is, however, not performed as the dominant frequency can be found in a simpler form without the matrix reduction.

(b) Derivation of Theoretical Formulas

The main focus of the PhD project is to find the dominant frequency from $[Z]$ and $[Y]$ in simple theoretical formulas. For a given length of a line, one propagation velocity is linked to one dominant frequency by Eqn. 4.13.

$$f_i = \frac{1}{4\tau} = \frac{v_i}{4 \times (\text{line length})}$$

Eqn. 4.13

Thus, we need to find the propagation velocity of the dominant frequency component in simple theoretical formulas.

It is known that the propagation velocity of each mode is found by Eqn. 4.14 [7].

$$v_i = \frac{2\pi f_0}{\sqrt{z_i y_i}}$$

Eqn. 4.14

Here, z_i and y_i are i-th diagonal entries of modal impedance matrix $[Z_M]$ and admittance matrix $[Y_M]$, respectively. f_0 is the target frequency. ($i = 1, 2, \cdots, 6$)

Eqn. 4.14 can also be expressed in a compact form as

$$(v) = diag\left(\frac{2\pi f_0}{\sqrt{[Z_M][Y_M]}}\right) \qquad \text{Eqn. 4.15}$$

Modal impedance and admittance matrices can be found by diagonalizing $[Z]$ and $[Y]$, but the diagonalization process prohibits the derivation of theoretical formulas in a simple form. It is necessary to find $[Z_M][Y_M]$ from $[Z]$ and $[Y]$ without conducting diagonalization.

From the definition of modal impedance / admittance matrices,

$$[Z_M] = [T_v]^{-1}[Z][T_i], [Y_M] = [T_i]^{-1}[Y][T_v]$$

Here, $[T_v]$ and $[T_i]$ are voltage and current transformation matrices.

The product $[Z_M][Y_M]$ can be calculated as

$$\begin{aligned}[Z_M][Y_M] &= ([T_v]^{-1}[Z][T_i])([T_i]^{-1}[Y][T_v]) \\ &= [T_v]^{-1}[Z][Y][T_v] \\ &= [D]\end{aligned} \qquad \text{Eqn. 4.16}$$

where $[D]$ is the eigenvalue matrix of $[Z][Y]$.

Eqn. 4.16 shows that the entries of $[Z_M][Y_M]$ can be found from the eigenvalues of $[Z][Y]$. Using Eqn. 4.4 to Eqn. 4.12, the matrix $[Z][Y]$ is given as

$$[Z][Y] = \begin{bmatrix} F_{11}y_{AA} & F_{12}y_{AA} & F_{13}y_{AA} & F_{AX} & F_{AX} & F_{AX} \\ F_{21}y_{AA} & F_{22}y_{AA} & F_{23}y_{AA} & F_{BX} & F_{BX} & F_{BX} \\ F_{31}y_{AA} & F_{32}y_{AA} & F_{33}y_{AA} & F_{CX} & F_{CX} & F_{CX} \\ F_{AY} & F_{BY} & F_{CY} & F_{SS} & F_{SM} & F_{SM} \\ F_{AY} & F_{BY} & F_{CY} & F_{SM} & F_{SS} & F_{SM} \\ F_{AY} & F_{BY} & F_{CY} & F_{SM} & F_{SM} & F_{SS} \end{bmatrix} \qquad \text{Eqn. 4.17}$$

$$\begin{cases} F_{11} = z_{AA} - Z_{AS}, & F_{12} = z_{AB} - Z_{AS}, & F_{13} = z_{CA} - Z_{AS} \\ F_{21} = z_{AB} - Z_{BS}, & F_{22} = z_{AA} - Z_{BS}, & F_{23} = z_{BC} - Z_{BS} \\ F_{31} = z_{CA} - Z_{CS}, & F_{32} = z_{BC} - Z_{CS}, & F_{33} = z_{AA} - Z_{CS} \end{cases} \qquad \text{Eqn. 4.18}$$

$$F_{AX} = -(z_{AA} + z_{AB} + z_{CA})y_{AA}/3 + Z_{AS}y_{SS}$$

<div align="right">Eqn. 4.19</div>

F_{BX} and F_{CX} can be found similarly.

$$F_{AY} = Z_{AS}y_{AA} - (Z_{SS} + 2Z_{SM})y_{AA}/3$$

<div align="right">Eqn. 4.20</div>

F_{BY} and F_{CY} can be found similarly.

$$F_{SS} = -(Z_{AS} + Z_{BS} + Z_{CS})y_{AA}/3 + Z_{SS}y_{SS}$$

<div align="right">Eqn. 4.21</div>

$$F_{SM} = -(Z_{AS} + Z_{BS} + Z_{CS})y_{AA}/3 + Z_{SM}y_{SS}$$

<div align="right">Eqn. 4.22</div>

Instead of diagonalizing $[Z][Y]$, we propose to assume that the overvoltage caused by the energization of a cross-bonded cable is dominated by inter-phase modes and the eigenvectors of inter-phase modes are found in an ideal form in order to find the theoretical formulas in a simple form. This assumption is reasonable since the overvoltage caused by the cable energization is dominated by the coaxial mode when the dominant frequency found by Eqn. 4.13 is higher than approximately 1000 – 1500 Hz, depending on the physical and electrical construction of a cable. For a long cable, the dominant frequency is much lower than this and the overvoltage is dominated by inter-phase modes.

Since the ideal eigenvector of the first inter-phase mode is known as $T_{V1} = (-1/3 \ \ 2/3 \ \ -1/3 \ \ 0 \ \ 0 \ \ 0)^T$, the eigenvalue corresponds to this inter-phase mode can be estimated as

$$D_1 = -(2z_{AB} - z_{AA} - z_{AC})y_{AA} \quad \text{or}$$
$$= (2z_{AA} - z_{AB} - z_{BC})y_{AA}/2$$

<div align="right">Eqn. 4.23</div>

The eigenvalue corresponds to the second inter-phase mode $T_{V2} = (1/2 \ \ 0 \ \ -1/2 \ \ 0 \ \ 0 \ \ 0)^T$ is estimated as

$$D_2 = (z_{AA} - z_{AC})y_{AA}$$

<div align="right">Eqn. 4.24</div>

Once the eigenvalues are found by Eqn. 4.23 and Eqn. 4.24, the propagation velocities are found by

$$v_i = 2\pi f_0 / \sqrt{D_i}$$

<div align="right">Eqn. 4.25</div>

(f_0: target frequency, i = 1, 2)

Eqn. 4.23 to Eqn. 4.25 indicate that simple and readily available data give the estimation of dominant frequency.

(c) Effect of Source Impedance

Theoretical formulas are, so far, derived assuming there is no source impedance. It can be justified in the slow-front overvoltage analysis as the source impedance changes depending on the network condition and no source impedance is supposedly the most severe assumption.

We consider below the effect of the source impedance since it affects the dominant frequency. The amplitude of the overvoltage caused by the cable line energization will be mitigated by the introduction of the source impedance, but also the lowered dominant frequency may excite resonance and lead to higher resonance overvoltages.

First, when source impedance is given as lumped parameter impedance Z_0, it has to be converted to distributed parameter source impedance z_0 by Eqn. 4.26. Fig. 4.6 illustrates the reason why the conversion is necessary. By the conversion, the lumped parameter source impedance can be considered as a part of distributed parameter cable line. The dominant frequency for the distributed parameter model can be derived from Eqn. 4.13 and Eqn. 4.14.

$$z_0 = Z_0 \times \left(\frac{2\pi}{4} \right)^2 \qquad\qquad \text{Eqn. 4.26}$$

$$f = \frac{1}{2\pi\sqrt{LC}} \qquad\qquad\qquad f = \frac{1}{4\sqrt{LC}}$$
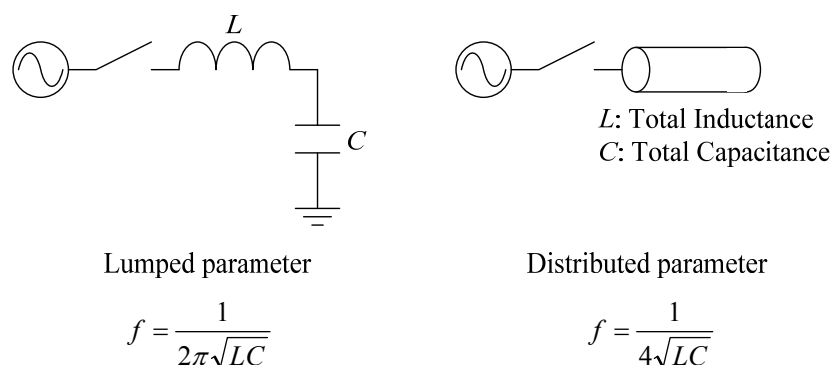
Fig. 4.6 Comparison of dominant frequency.

Assuming the source impedance is a part of the cable line, the eigenvalues correspond to the two inter-phase modes are estimated as:

$$D_1 = \{z_0 - (2z_{AB} - z_{AA} - z_{AC})\}y_{AA} \quad \text{or}$$
$$\quad = (z_0 + 2z_{AA} - z_{AB} - z_{BC})y_{AA}/2$$

Eqn. 4.27

$$D_2 = (z_0 + z_{AA} - z_{AC})y_{AA}$$

Eqn. 4.28

When the eigenvalues are found, the propagation velocity is calculated by Eqn. 4.25.

(d) Example

In order to verify the derived theoretical formulas, the dominant frequency calculated by the theoretical formulas is compared with that found by EMTP simulations.

The dominant frequency contained in the overvoltage caused by the energization of the Kyndbyværket – Asnæsværket line is very low because of the following two reasons:

- The Kyndbyværket – Asnæsværket line is very long (60 km)
- The fault current level around the Kyndbyværket – Asnæsværket line is very low

As only very low frequency components are contained, the Kyndbyværket – Asnæsværket line does not suit for the verification. In addition, the Kyndbyværket – Asnæsværket line has the submarine section near Kyndbyværket. Since the submarine cable is solidly-bonded, the dominant frequency is determined by the coaxial mode, whose frequency is much simpler to find. As the dominant frequency is not determined by the inter-phase mode, the derived theoretical formulas cannot be applied.

Considering these problems, the verification was performed by the following conditions:

- Assuming a switching station exists at Torslunde, the Asnæsværket – Torslunde line is energized from Asnæsværket
- The fault current level is adjusted by adding a dummy generator at Asnæsværket.

The source impedance of the dummy generator is changed from almost zero to infinite in order to cover a broad range of the fault current level. The theoretical dominant frequency is found for each source impedance as shown in Table 4-1. Since there are two inter-phase modes, an average of two modes is adopted as the theoretical propagation velocity and the dominant frequency, assuming equal contribution from the two modes.

Table 4-1 Source Impedance and Theoretical Dominant Frequency

Source Impedance (Dummy Generator)	0.1 mH	50 mH	100 mH	200 mH	Infinite

Network Source Impedance	0.1 mH	24.5 mH	37.5 mH	51.0 mH	71.4 mH
Propagation Velocity (mode 1)	97.6 m/μs	44.5 m/μs	37.0 m/μs	32.2 m/μs	27.5 m/μs
Propagation Velocity (mode 2)	86.9 m/μs	42.3 m/μs	35.7 m/μs	31.3 m/μs	27.0 m/μs
Propagation Velocity (average)	92.3 m/μs	43.4 m/μs	36.3 m/μs	31.7 m/μs	27.2 m/μs
Dominant Frequency	823.7 Hz	387.5 Hz	324.4 Hz	283.3 Hz	243.1 Hz

The EMTP simulations are performed with PSCAD in order to find dominant frequencies. Fig. 4.7 shows the simulation model set up for the analysis.
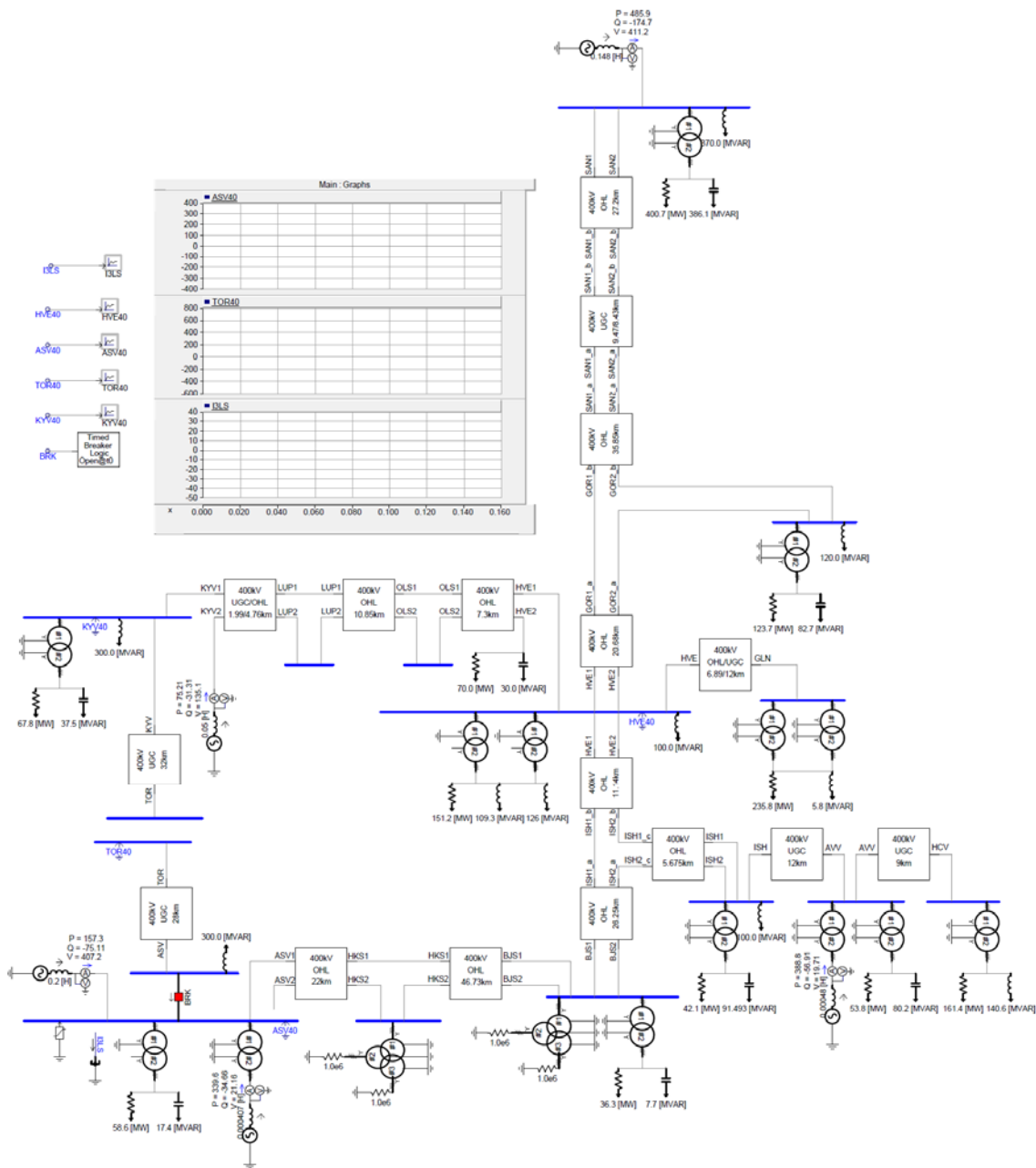
Fig. 4.7 PSCAD simulation model for finding the dominant frequency.

Fig. 4.8 to Fig. 4.12 show energization overvoltages at the open terminal Torslunde for different fault current levels. The dominant frequency in each case is found by performing Fourier transform to the voltage waveform.


(file Source0mH0.1s.adf; x-var Time) TOR40A   TOR40B   TOR40C

Fig. 4.8 Energization overvoltage at open terminal (dummy source 0.1 mH).

(file Source25mH0.1s.adf; x-var Time) TOR40A   TOR40B   TOR40C
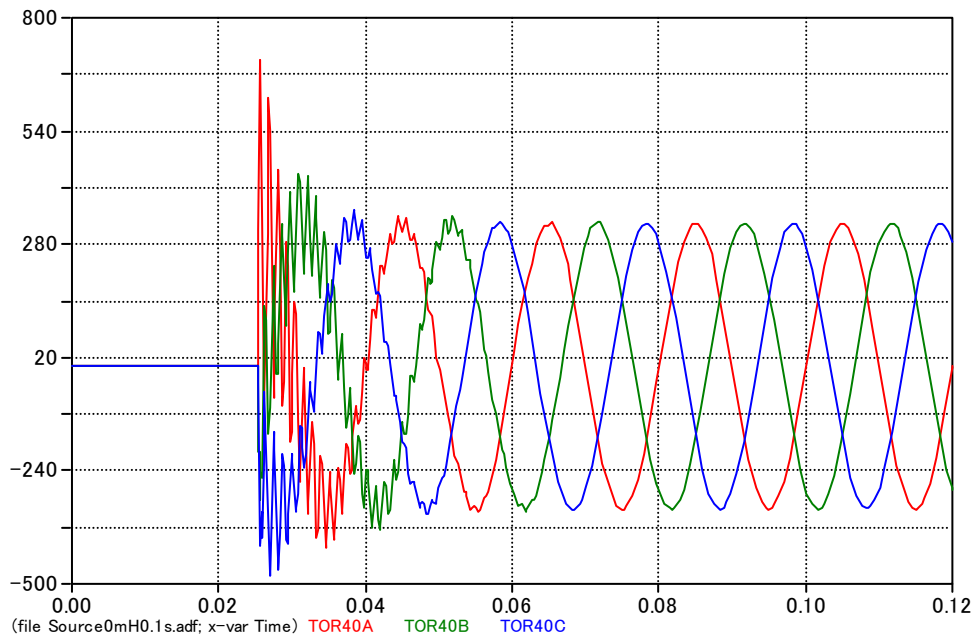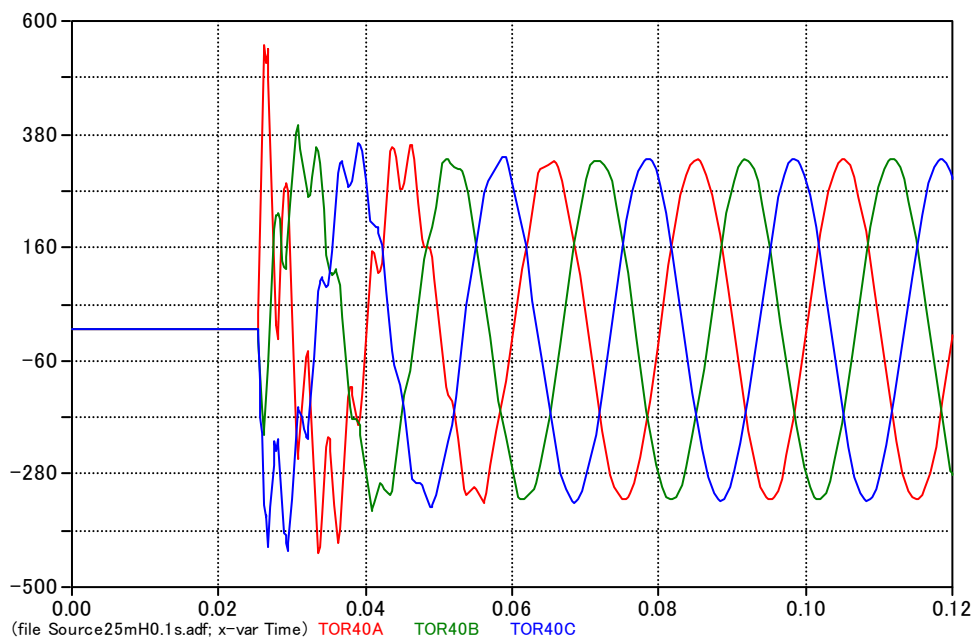
Fig. 4.9 Energization overvoltage at open terminal (dummy source 50 mH).
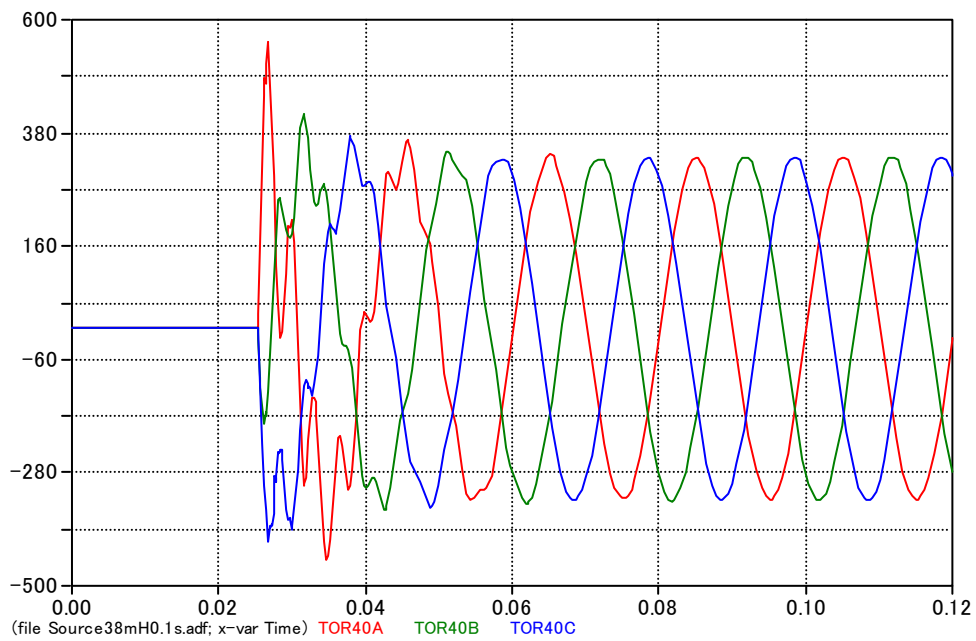
Fig. 4.10 Energization overvoltage at open terminal (dummy source 100 mH).
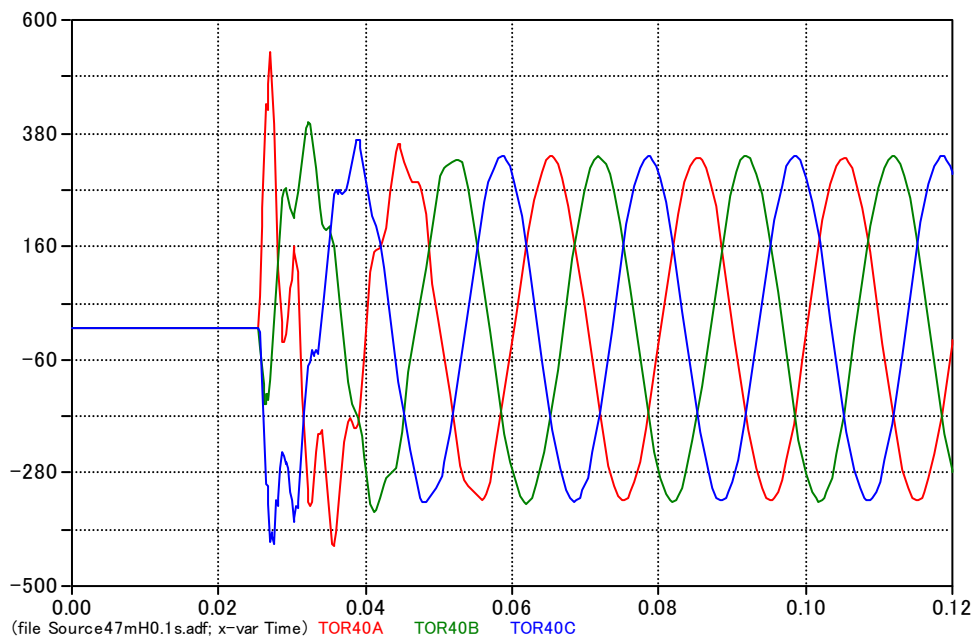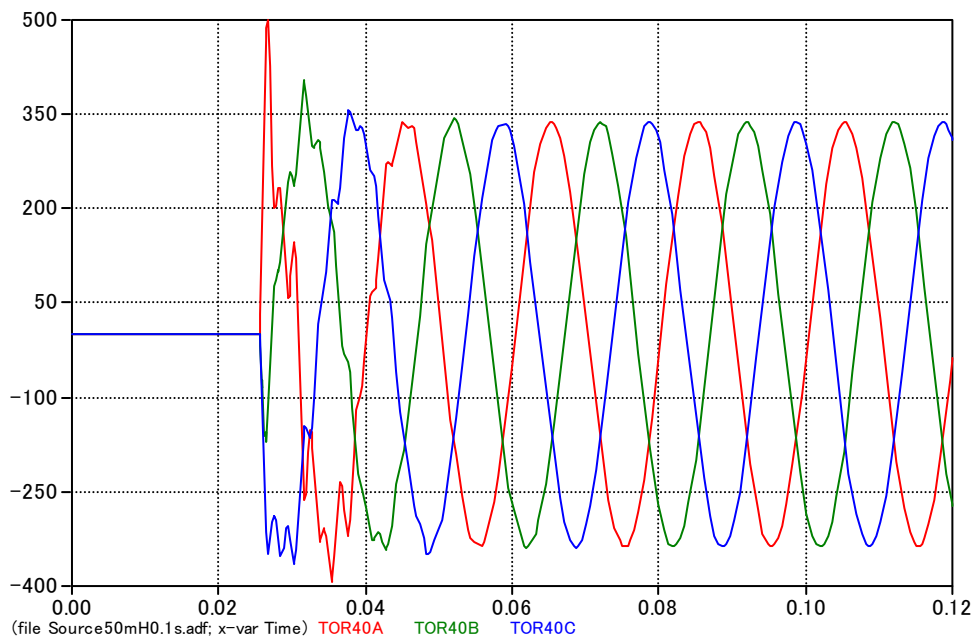

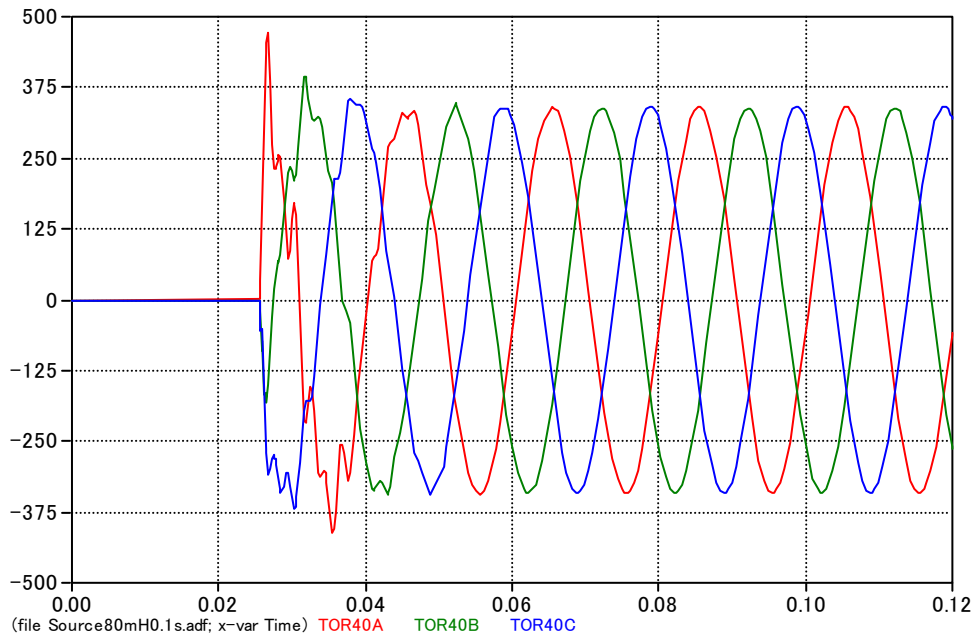**Fig. 4.11 Energization overvoltage at open terminal (dummy source 200 mH).**
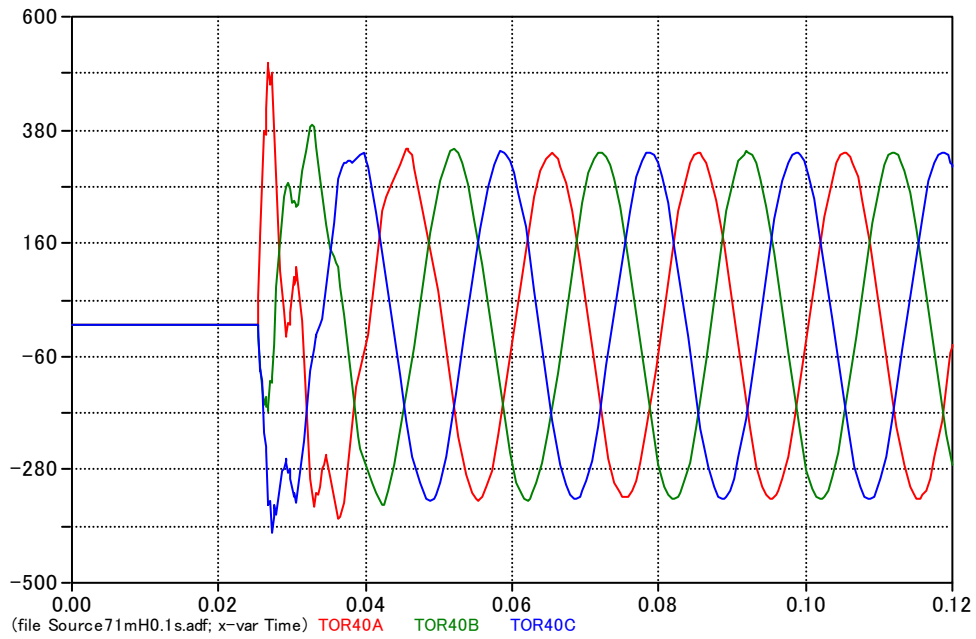
Fig. 4.12 Energization overvoltage at open terminal (no dummy source).

Fig. 4.13 illustrates the comparison of dominant frequencies derived by theoretical formulas and those found by EMTP simulations. The comparison shows that the derived theoretical formulas have very high accuracy.
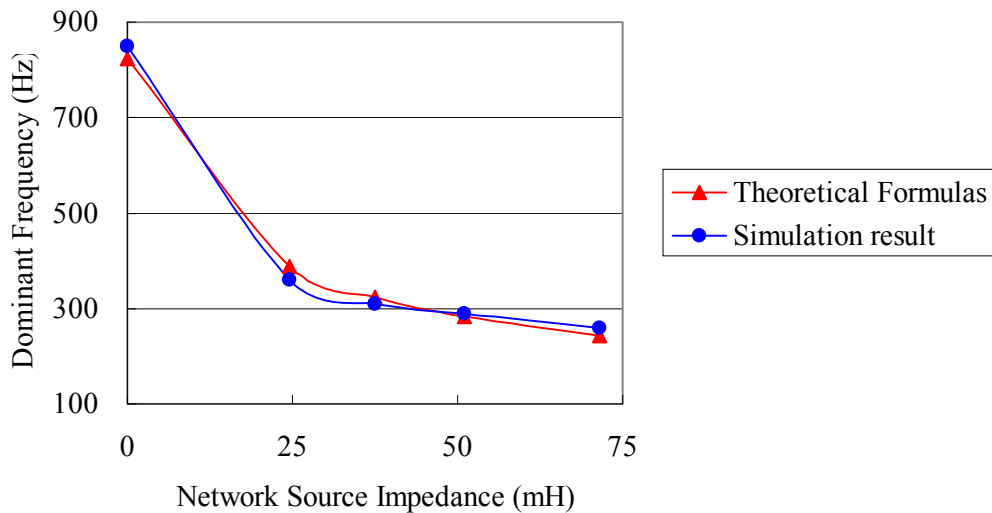
Fig. 4.13 Comparison of dominant frequencies found by theoretical formulas and EMTP simulations.

In addition to the Asnæsværket – Torslunde line, the energization of the Kyndbyværket – Torslunde line is studied for the verification. In the same way as in the Asnæsværket – Torslunde line, the fault current level is adjusted by adding a dummy generator at Kyndbyværket.

The Kyndbyværket – Torslunde line has a 10 km submarine section on the Kyndbyværket side. As the submarine cable is solidly-bonded, the propagation velocity in this section is faster compared with that in the cross-bonded section. Only for the verification, the 10 km submarine cable is replaced by the underground cable (cross-bonded) so that the theoretical formula can be applied.

The source impedance of the dummy generator is changed from almost zero to infinite in order to cover broad range of the fault current level. The theoretical dominant frequency is found for each source impedance as shown in Table 4-2. Since there are two inter-phase modes, an average of two modes is adopted as the theoretical propagation velocity and dominant frequency, assuming equal contribution from the two modes.

Table 4-2 Source Impedance and Theoretical Dominant Frequency

Source Impedance (Dummy Generator)	0.1 mH	50 mH	100 mH	200 mH	Infinite
Network Source Impedance	0.1 mH	24.5 mH	37.5 mH	51.0 mH	71.4 mH
Propagation Velocity (mode 1)	97.6 m/μs	58.7 m/μs	50.9 m/μs	45.5 m/μs	37.5 m/μs
Propagation Velocity (mode 2)	86.9 m/μs	44.6 m/μs	38.0 m/μs	33.5 m/μs	27.3 m/μs
Propagation Velocity (average)	92.3 m/μs	51.6 m/μs	44.5 m/μs	39.5 m/μs	32.4 m/μs
Dominant Frequency	720.7 Hz	403.5 Hz	347.3 Hz	308.5 Hz	252.9 Hz

The EMTP simulations are performed with PSCAD in order to find dominant frequencies. Fig. 4.20 to Fig. 4.24 show energization overvoltages at the open terminal Torslunde for different fault current levels. The dominant frequency in each case is found by performing Fourier transform to the voltage waveform.
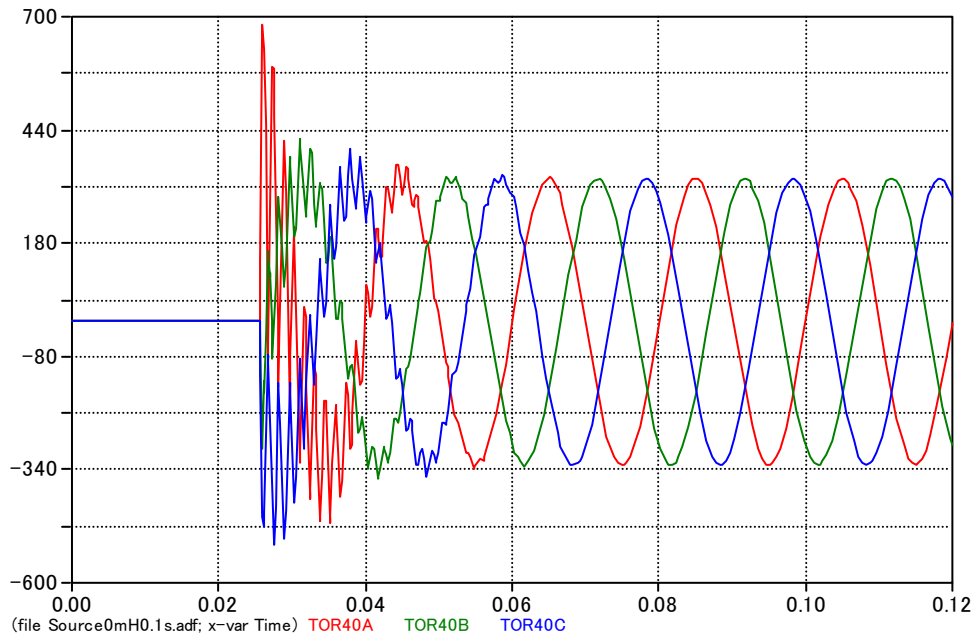
Fig. 4.14 Energization overvoltage at open terminal (dummy source 0.1 mH).
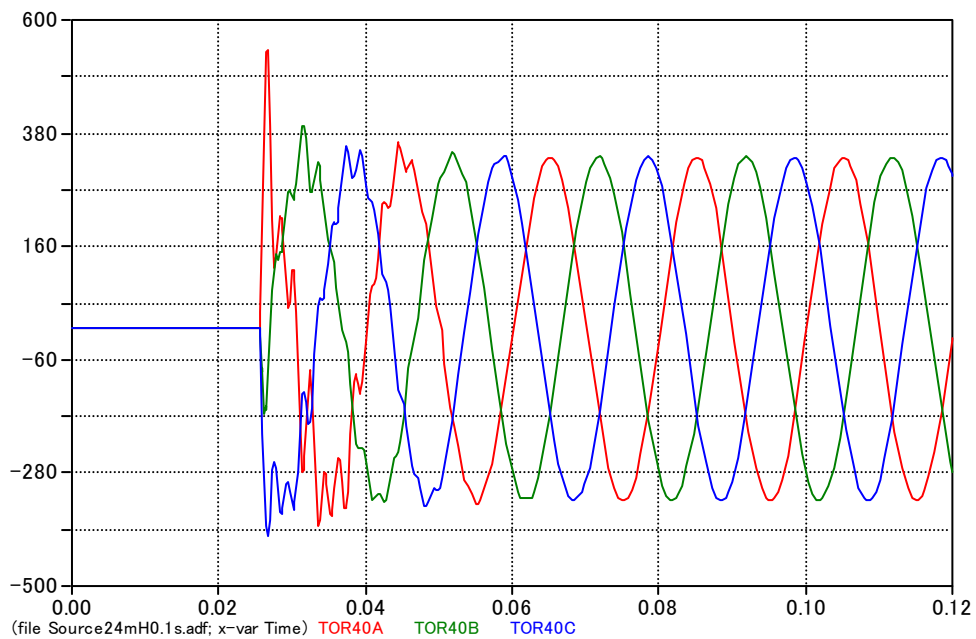
Fig. 4.15 Energization overvoltage at open terminal (dummy source 50 mH).
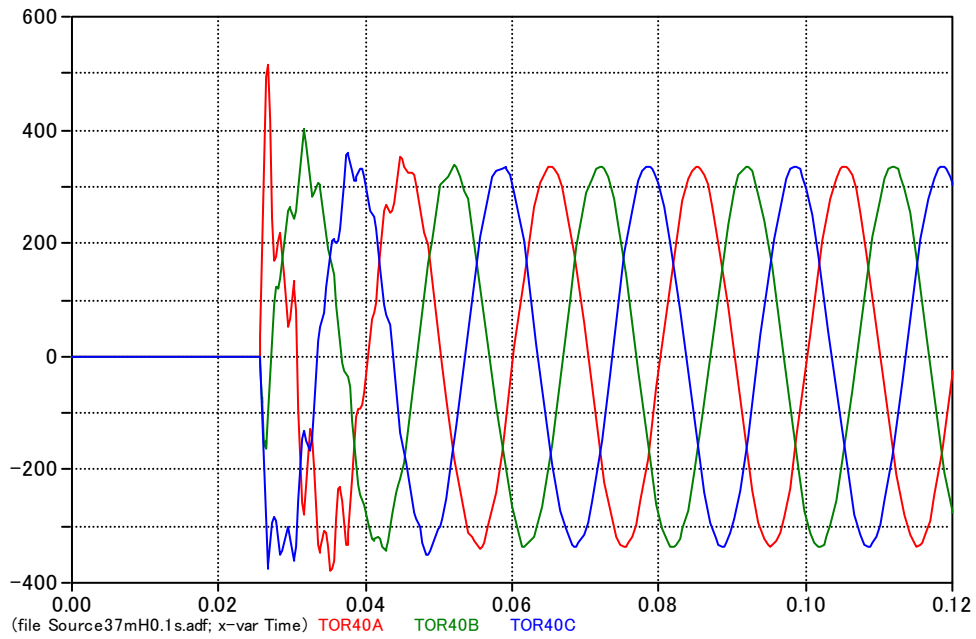
Fig. 4.16 Energization overvoltage at open terminal (dummy source 100 mH).

Fig. 4.17 Energization overvoltage at open terminal (dummy source 200 mH).

Fig. 4.18 Energization overvoltage at open terminal (no dummy source).

Fig. 4.19 illustrates the comparison of dominant frequencies evaluated by theoretical formulas and those found by EMTP simulations. The comparison shows that the derived theoretical formulas agree satisfactory with the simulation results with the largest error of 50 Hz.
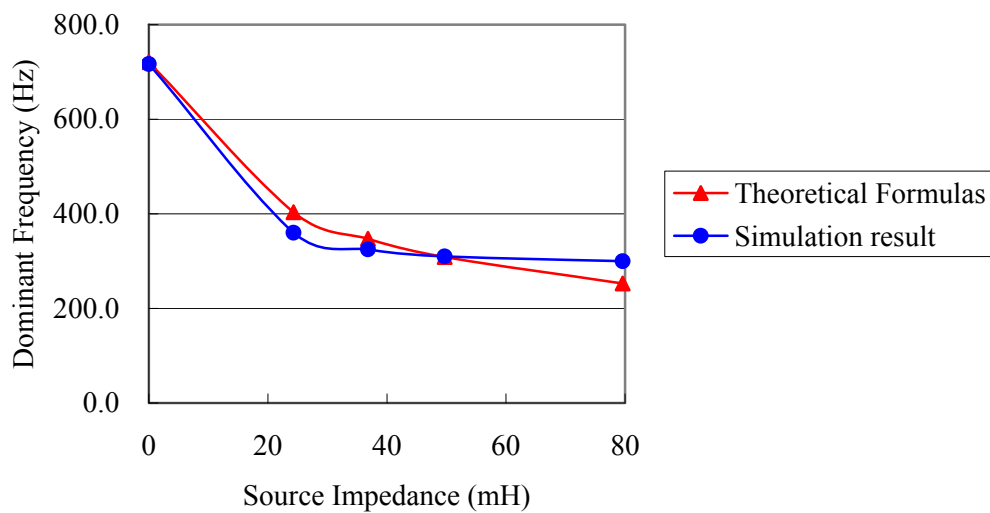
Fig. 4.19 Comparison of dominant frequencies found by theoretical formulas and EMTP simulations.

The following observations / evaluations can be made to the error of theoretical formulas:

- The error 50 Hz does not affect the practical usefulness of the theoretical formulas since the natural frequency of a series resonance circuit as described in Sections 4.1.1 and 4.1.2 can range much broader than 50 Hz due to different load conditions.

- From the comparison for source impedance 0.1 mH, the inter-phase modes are estimated accurately. The error was introduced by the effect of the source impedance

- The effect of the source impedance or a surrounding network is actually a difficult problem, and a clear solution to this problem has not been found yet. In the energization of the Asnæsværket – Torslunde line, the surrounding network is closer to the ideal condition since the Asnæsværket – Herslev line (22 km) and the Herslev – Bjæverskov line (47 km) is long and the distance to the neighboring voltage source is longer than 100 km. In contrast, in the energization of the Kyndbyværket – Torslunde line, the Kyndbyværket – Lyngerup line (7 km) and the Lyngerup – Hovegård line (18 km) is short for typical 400 kV lines and the distance to the neighboring voltage source is shorter. The energization overvoltage of the Kyndbyværket – Torslunde line is, therefore, more affected by the reflection at nearby substations (Lyngerup and Hovegård), which is not considered in the theoretical formulas.

4.1.3.2   Off-peak Load Condition

First, the dominant frequency in an energization overvoltage is studied in the off-peak load condition. When a transmission line, either an overhead line or a cable, is energized from a weaker source, which has a larger source impedance (off-peak load condition), the magnitude of the energization overvoltage becomes lower and the dominant frequency becomes lower. In general, the off-peak load condition is a more severe assumption because of the following reasons:

- Damping from the loads (more important)
  The loads in the Asnæsværket or Kyndbyværket 132 kV network will damp the series resonance overvoltage on the secondary side of the 400/132 kV transformer. The load level has to be low in order to have a severe resonance.

- Damping from the network (transformers, lines, and etc.)
  The lower dominant frequency means an extended duration of the overvoltage. The high frequency components, which raise the magnitude of the overvoltage in a stiff source case, typically dies out quickly due to the large damping (losses).

However, this general notion may not be true in the energization of the Kyndbyværket – Asnæsværket line. In Section 3.3, the Kyndbyværket – Asnæsværket line was energized from the

400 kV voltage source behind source impedance 147 mH, which corresponds to the fault current 5 kA. In that case, the dominant frequency was already low (100 – 150 Hz) in the energization, due to the large charging capacity of the cable. If we make the source impedance larger, the dominant frequency goes down towards 50 Hz, and it is hard to observe the energization overvoltage as the magnitude becomes lower. The dominant frequency in the peak load condition is, therefore, studied in the next section.

Here, in the off-peak load condition, the Kyndbyværket – Asnæsværket line is energized from the Kyndbyværket side according to Fig. 4.3. Only one large generator in AVV and the equivalent generator in SAN are assumed to be in-service in the simulation. The cable line is energized at the phase b voltage peak.

The energization overvoltage is shown in Fig. 4.20 and Fig. 4.21. Fig. 4.20 is the voltage waveform at the sending end (Kyndbyværket side), and Fig. 4.21 is the voltage waveform at the receiving end (Asnæsværket side cable open terminal). As can be seen from the figure, the waveforms look not like typical energization overvoltages due to the length of the cable and the large charging capacity. High frequency components are contained in the waveforms with very small proportions.
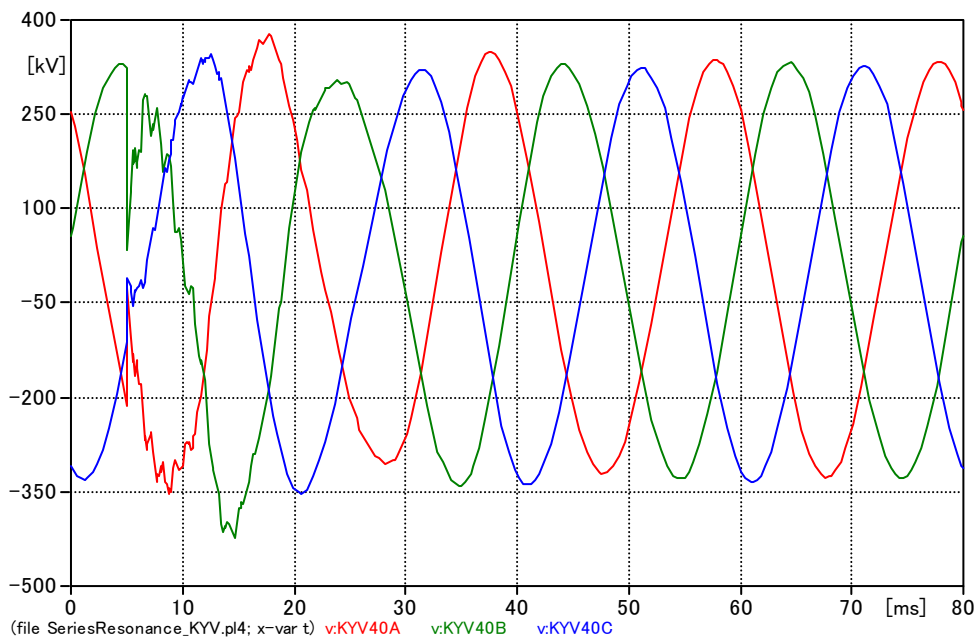
Fig. 4.20 Energization overvoltage of the KYV – ASV line from the KYV side (sending end).
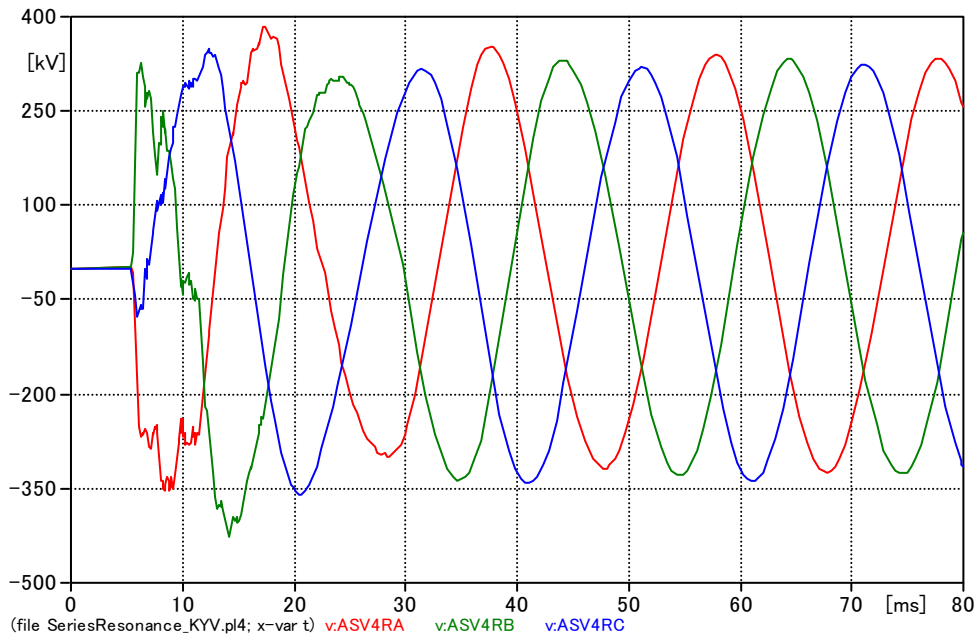
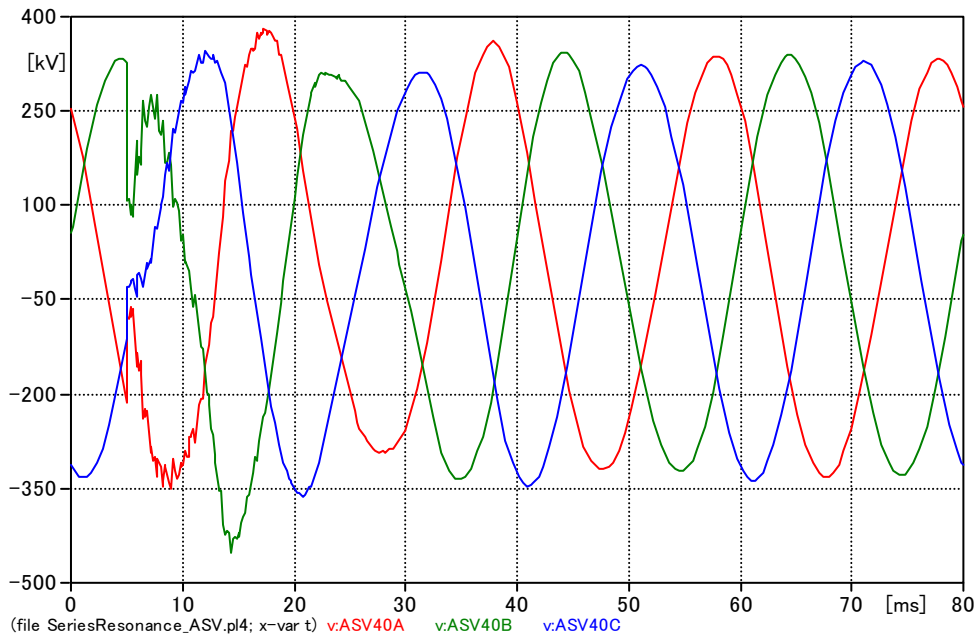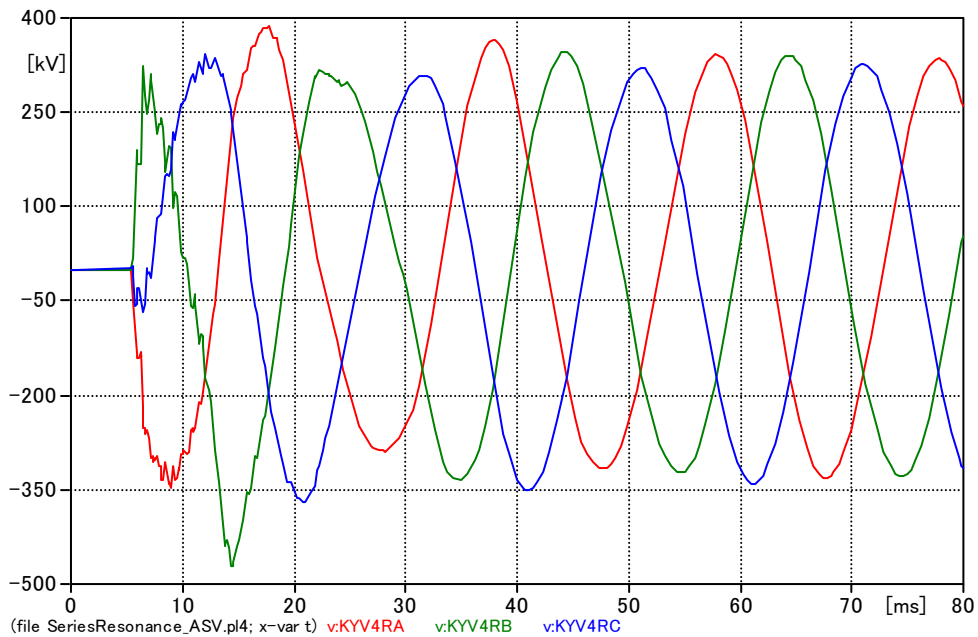**Fig. 4.21 Energization overvoltage of the KYV – ASV line from the KYV side (receiving end).**

Fig. 4.22 shows frequency components contained in the overvoltage caused by the energization of the Kyndbyværket – Asnæsværket line. The Fourier transform is applied to the waveform at the sending end since the series resonance overvoltage is expected at the Kyndbyværket 132 kV bus.
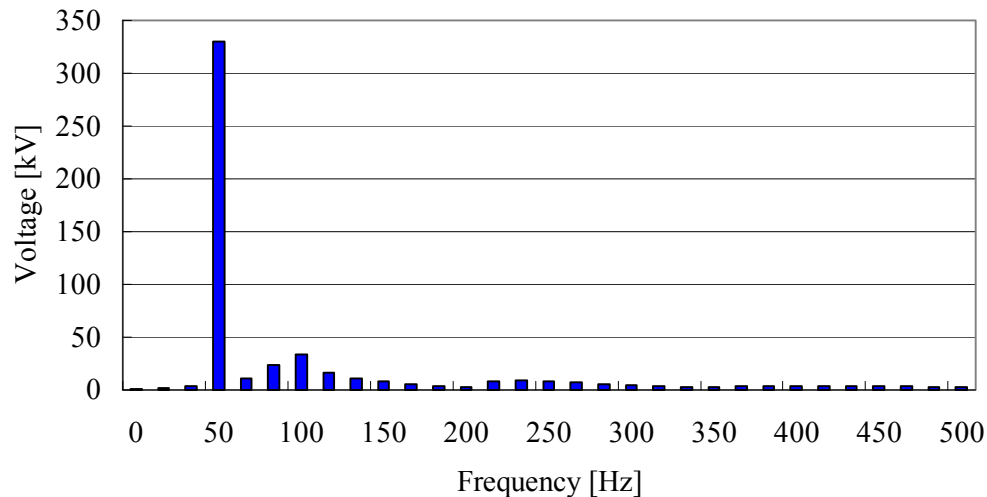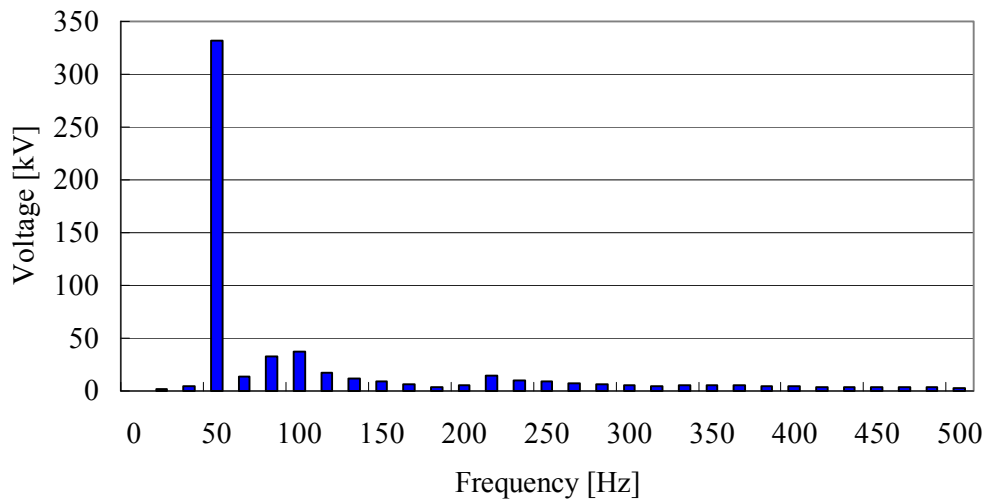

Fig. 4.22 Frequency components contained in the overvoltage caused by the energization of the KYV – ASV line from the KYV side.

Fig. 4.22 demonstrates that frequency components other than the fundamental frequency are not large enough to cause series resonance frequency. The analysis is however continued in order to show that there is no problem related to the series resonance overvoltage.

Fig. 4.23 shows the frequency components in 1 Hz step. In order to obtain it, it is necessary, due to the limitation of ATP-EMTP tools, to run the simulation for 1 second and apply Fourier transform to the waveform of 1 second. Because of it, the frequency components except for the fundamental frequency is reduced compared to Fig. 4.22.

According to Fig. 4.23, in order to cause a severe series resonance overvoltage, it is necessary to set the natural frequency of the Kyndbyværket 132 kV network to 90 – 100 Hz. The amplification from the 400 kV side to the 132 kV side needs to be very high.
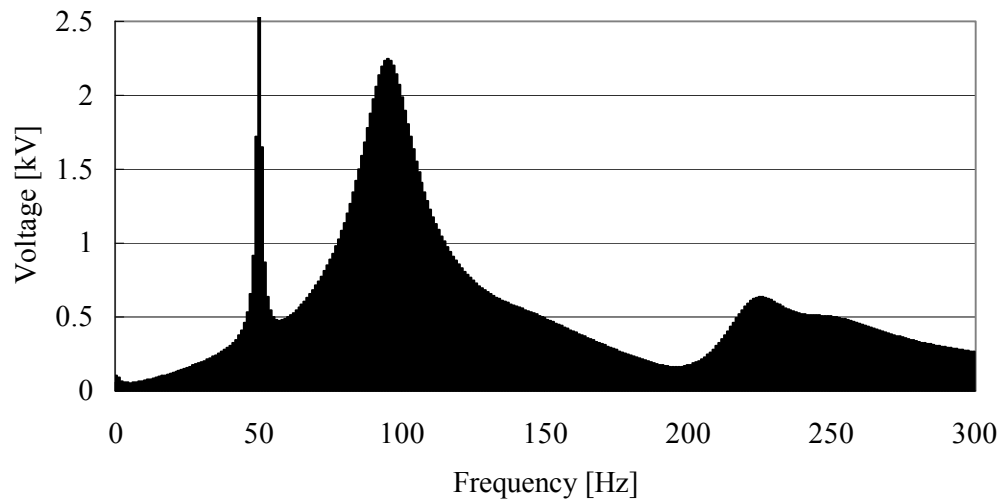
Fig. 4.23 Frequency components contained in the overvoltage caused by the energization of the KYV − ASV line from the KYV side (1Hz step).

Second, the Kyndbyværket – Asnæsværket line is energized from the Asnæsværket side according to Fig. 4.4. The cable line is energized at the phase b voltage peak.

The energization overvoltage is shown in Fig. 4.24 and Fig. 4.25. Fig. 4.24 is the voltage waveform at the sending end (Asnæsværket side), and Fig. 4.25 is the voltage waveform at the receiving end (Kyndbyværket side cable open terminal). As in the energization overvoltage from the Kyndbyværket side, high frequency components are contained in the waveforms with very small proportions.

Fig. 4.24 Energization overvoltage of the KYV – ASV line from the ASV side (sending end).

Fig. 4.25 Energization overvoltage of the KYV – ASV line from the ASV side (receiving end).

Fig. 4.26 and Fig. 4.27 show frequency components contained in the overvoltage caused by the energization of the Kyndbyværket – Asnæsværket line from the Asnæsværket side. The Fourier transform is applied to the waveform at the sending end since the series resonance overvoltage is expected at the Asnæsværket 132 kV bus.

Fig. 4.26 Frequency components contained in the overvoltage caused by the energization of the KYV – ASV line from the ASV side.
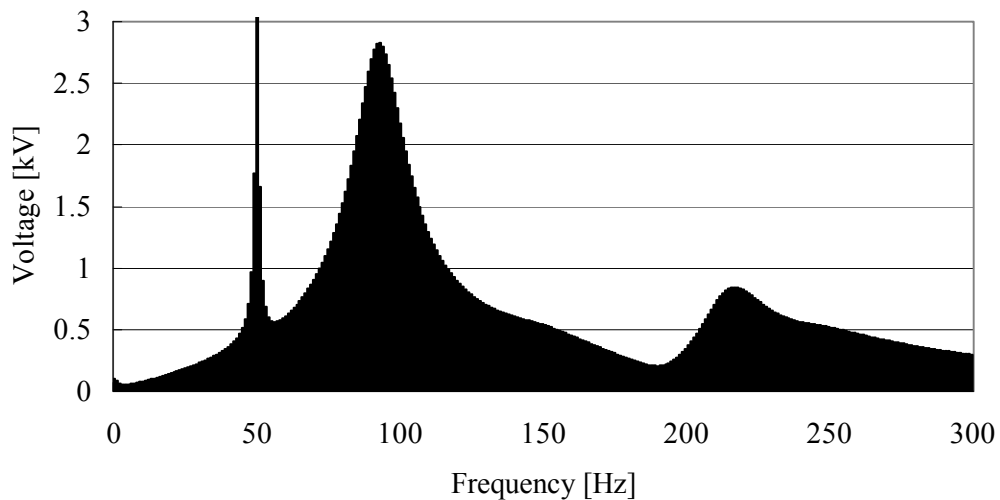
Fig. 4.27 Frequency components contained in the overvoltage caused by the energization of the KYV – ASV line from the ASV side (1Hz step).

As in the energization from the Kyndbyværket side, the natural frequency of the Asnæsværket 132 kV has to be set to 85 − 100 Hz in order to cause a severe series resonance overvoltage. The amplification from the 400 kV side to the 132 kV side needs to be very high.

4.1.3.3 Peak Load Condition

In order to have a larger magnitude of the energization overvoltage, energizations from the stiffer voltage source, namely in the peak load condition, is additionally studied. To make the voltage source stiffer, the large generator at Asnæsværket is assumed to be in-service. In addition, equivalent generators are modeled near the line, that is, at the HVE and BJS 132 kV buses. Adding equivalent generators at the ASV and KYV 132 kV buses would be more efficient to make the voltage source stiffer, but it is not considered since these voltage sources will suppress the series resonance overvoltage at the ASV and KYV 132 kV buses.

The source impedances for these equivalent generators are derived from the results of the short circuit current calculation in the peak load condition as shown in Table 4-3. Only the short circuit current from the 132 kV network is considered

Table 4-3 Source Impedances of 132 kV Equivalent Generators

132 kV Buses	Short Circuit Current	Source Impedance
Hovegård	19.6 kA	12.4 mH
Bjæverskov	13.3 kA	18.2 mH

Fig. 4.28 shows these additions of generators in the simulation model in the peak load condition.
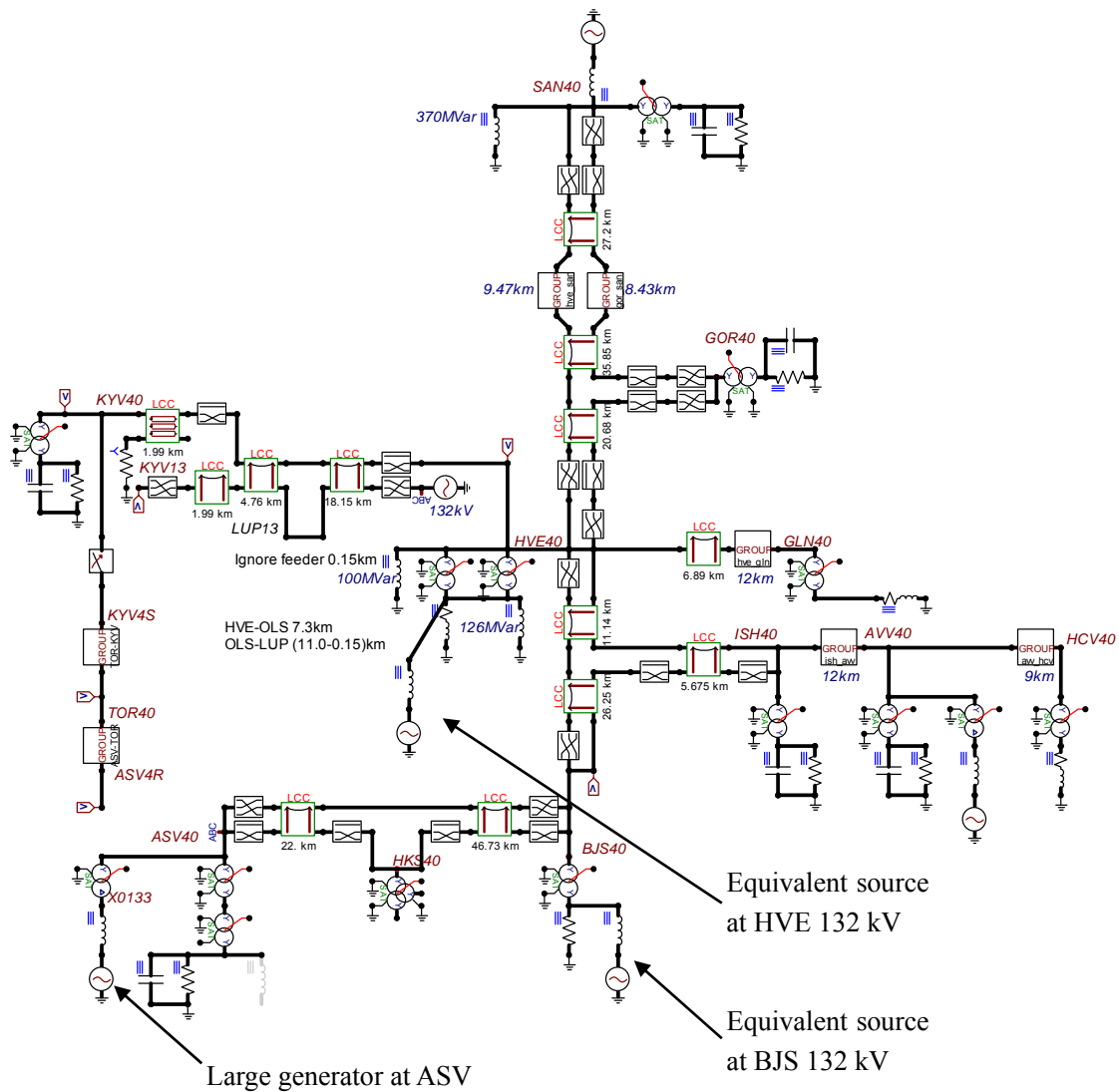
Fig. 4.28 Addition of generators to set up the peak load condition.

Fig. 4.29 and Fig. 4.30 show energization overvoltages of the Kyndbyværket – Asnæsværket line when the line is energized from the Kyndbyværket side. In overall, the waveforms of the overvoltages are similar to the ones observed in the off-peak load condition. The change of the loading condition does not have a significant difference on the energization overvoltage. It is mainly because the fault current level at the Kyndbyværket 400 kV bus is very small, only 11.4 kA, even in the peak load condition.

Only one notable difference is that the energization overvoltages in the peak load condition have more damping. In the off-peak load condition, non-fundamental components can be observed in the

waveform even at 80 ms. In contrast, in the peak load condition, we can observe only a fundamental frequency component after 40 ms.
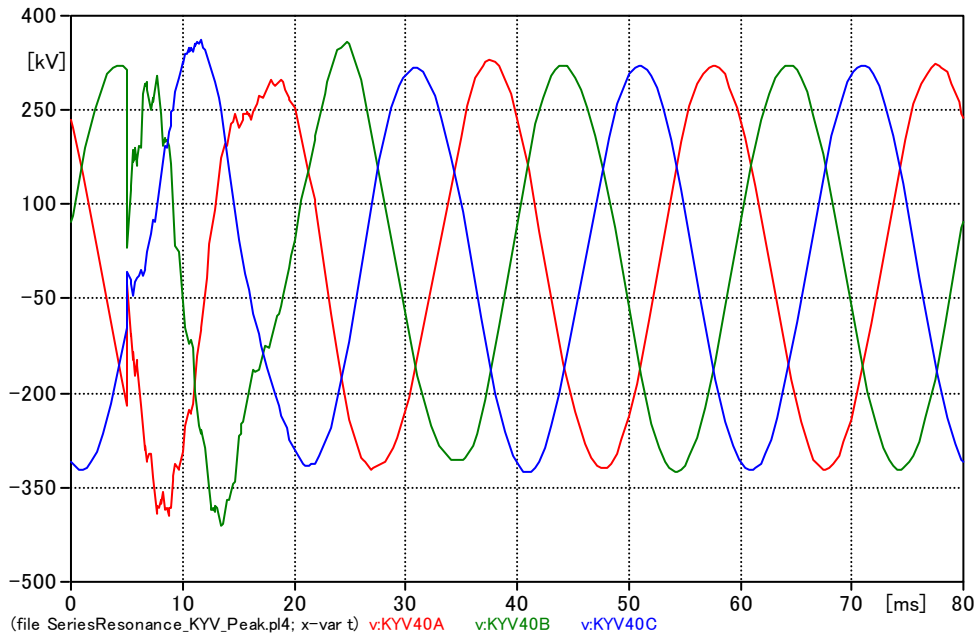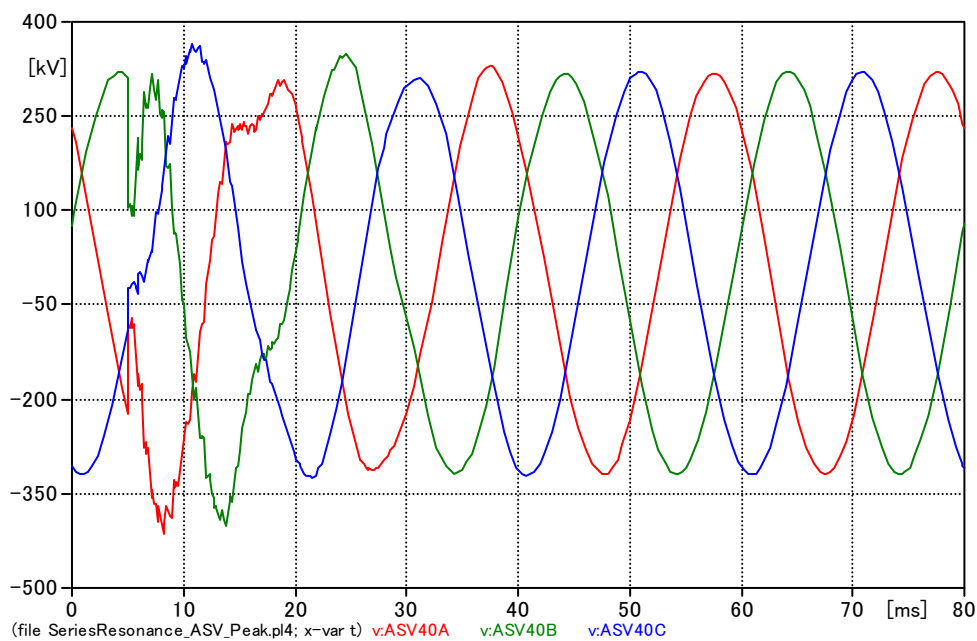

Fig. 4.29 Energization overvoltage of the KYV – ASV line from the KYV side (peak load, sending end).
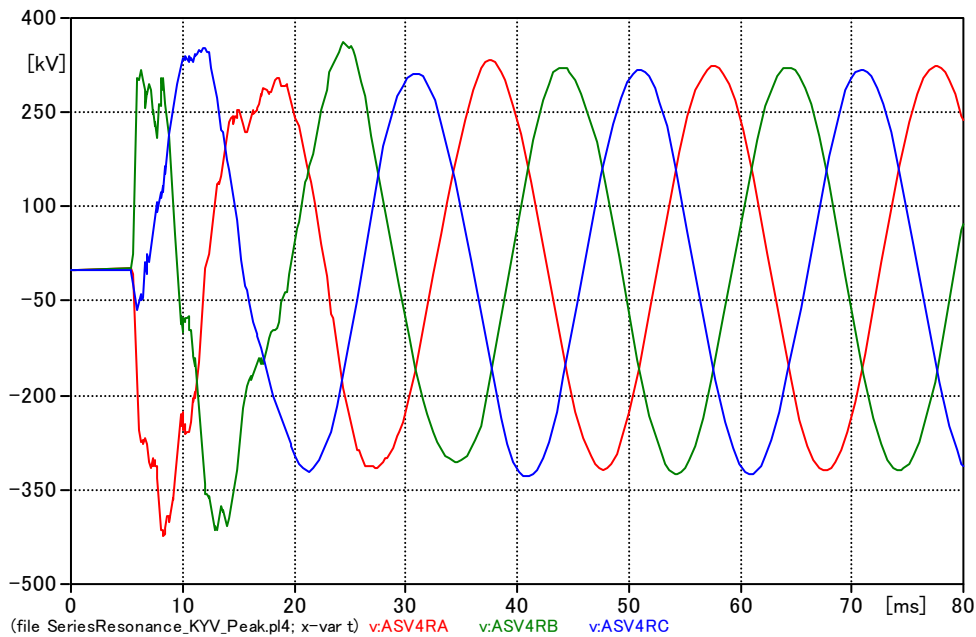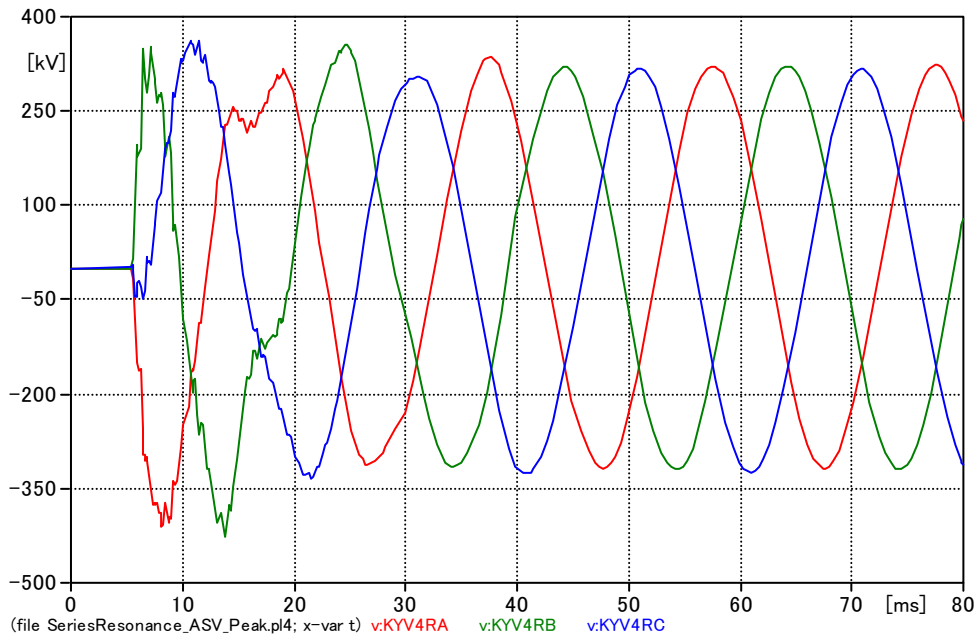

Fig. 4.30 Energization overvoltage of the KYV – ASV line from the KYV side (peak load, receiving end).

Fig. 4.31 and Fig. 4.32 show frequency components contained in the overvoltage caused by the energization of the Kyndbyværket – Asnæsværket line. The dominant frequency goes up to 120 – 125 Hz, which explains the more damping observed in the voltage waveforms. Compared to the off-peak load condition, the distribution of frequency components becomes flatter. It is clear that the off-peak load condition is more severe in terms of the overvoltage which propagates into the Kyndbyværket 132 kV bus.
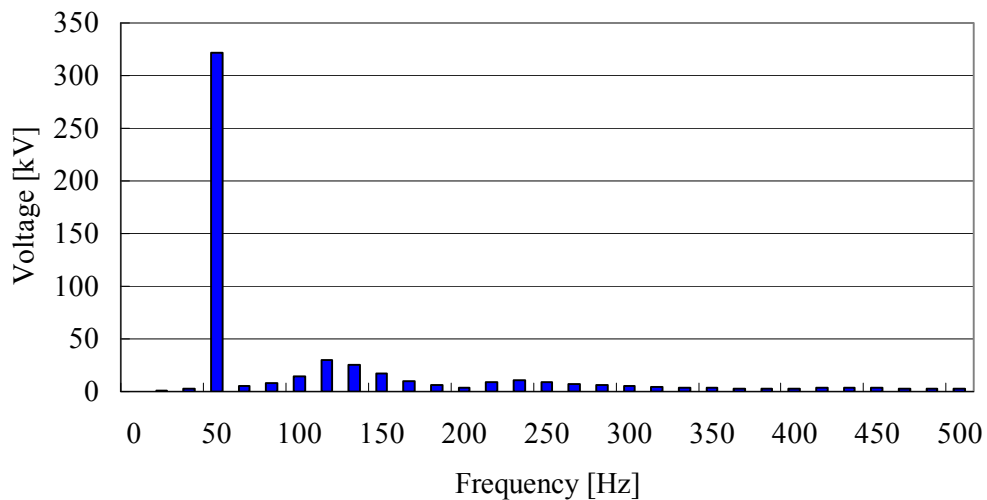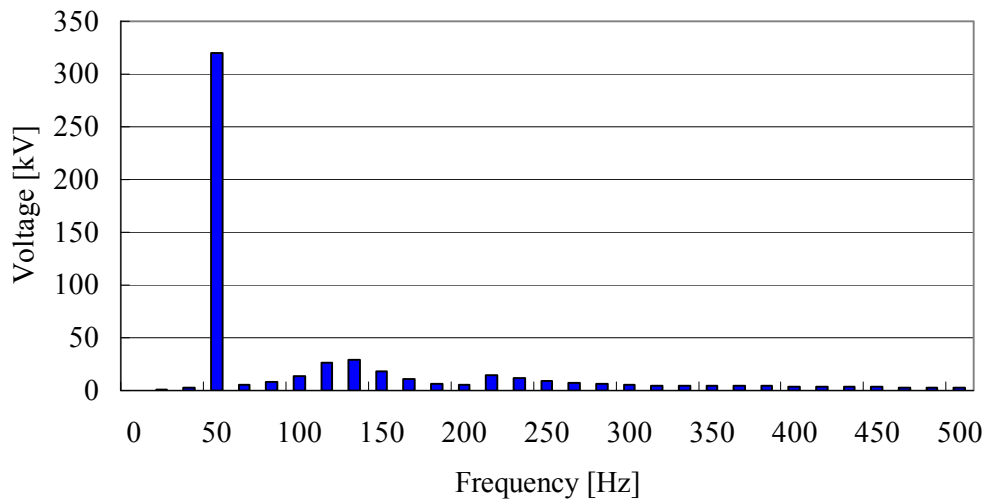

Fig. 4.31 Frequency components contained in the overvoltage caused by the energization of the KYV – ASV line from the KYV side (peak load).
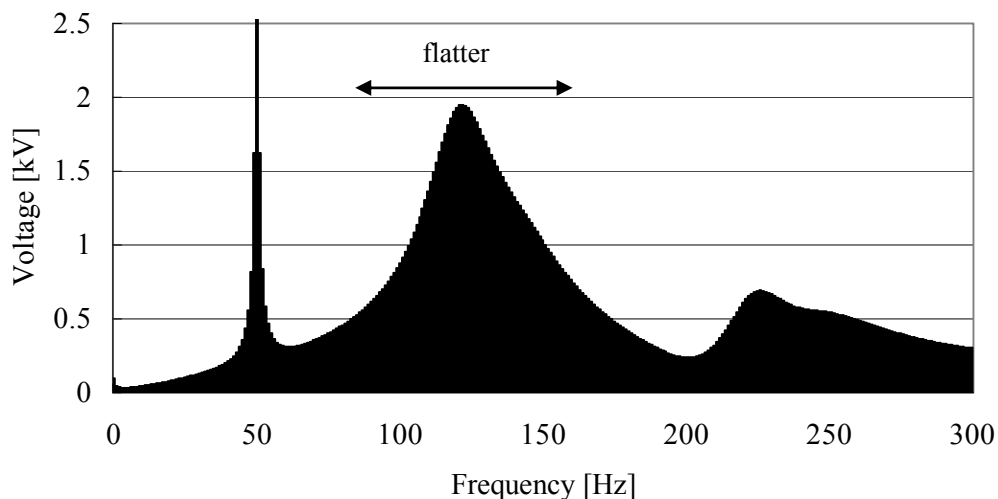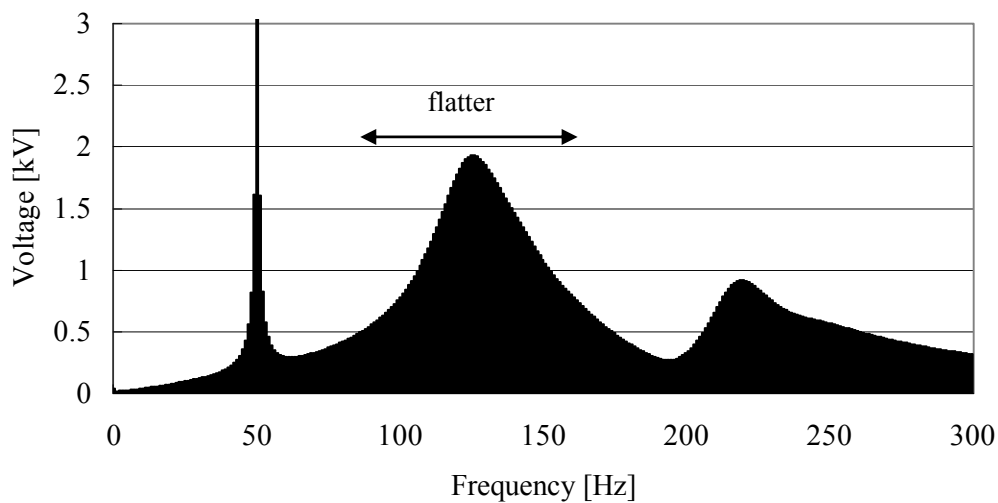

Fig. 4.32 Frequency components contained in the overvoltage caused by the energization of the KYV – ASV line from the KYV side (peak load, 1Hz step).

Second, the Kyndbyværket – Asnæsværket line is energized from the Asnæsværket side according to Fig. 4.4. The cable line is energized at the phase b voltage peak as in the off-peak case.

The energization overvoltage is shown in Fig. 4.33 and Fig. 4.34. Again, the waveforms of the energization overvoltages are similar to the ones in the off-peak load condition, but with a higher damping. It is mainly because the fault current level at the Asnæsværket 400 kV bus is very small, only 11.4 kA, even in the peak load condition.

(file SeriesResonance_ASV_Peak.pl4; x-var t)   v:ASV40A   v:ASV40B   v:ASV40C

Fig. 4.33 Energization overvoltage of the KYV – ASV line from the ASV side (peak load, sending end).

Fig. 4.34 Energization overvoltage of the KYV – ASV line from the ASV side (peak load, receiving end).

Fig. 4.35 and Fig. 4.36 show frequency components contained in the overvoltage caused by the energization of the Kyndbyværket – Asnæsværket line from the Asnæsværket side in the peak load condition. As in the energization from the Kyndbyværket side, the dominant frequency goes up to 120 – 125 Hz, which explains the better damping observed in the voltage waveforms. Compared to the off-peak load condition, the distribution of frequency components becomes flatter. It is clear that the off-peak load condition is more severe in terms of the overvoltage which propagates into the Kyndbyværket 132 kV bus.

Fig. 4.35 Frequency components contained in the overvoltage caused by the energization of the KYV – ASV line from the ASV side (peak load).

Fig. 4.36 Frequency components contained in the overvoltage caused by the energization of the KYV – ASV line from the ASV side (peak load, 1Hz step).

4.1.4   Natural Frequency of Series Resonance Circuit

In the previous section, it has been found that the dominant frequency contained in the overvoltage caused by the energization of the Kyndbyværket – Asnæsværket line from the Kyndbyværket side ranges from 85 Hz to 100 Hz. In order to cause the series resonance overvoltage, the natural frequency of the Kyndbyværket 132 kV network has to be between 85 Hz and 100 Hz.

As discussed in Section 4.1.1, the natural frequency of the Kyndbyværket 132 kV network can be found as $f_n = \dfrac{1}{2\pi\sqrt{LC}}$ using 400/132 kV transformer inductance L and 132 kV cable capacitance C. In order to set the natural frequency to 90 Hz, Eqn. 4.29 has to be satisfied.

$$\frac{1}{2\pi\sqrt{0.02088 \times C}} = 90 \qquad\qquad \text{Eqn. 4.29}$$

$C = 149.8$ [μF]

Cable capacitance 149.8 μF corresponds to 819.8 MVar in the 132 kV network. This amount of cable capacitance is too large to assume in the 132 kV network. In terms of the cable length, assuming the typical cable capacitance per length 0.2 μF/km, cable capacitance 149.8 μF corresponds to 132 kV cable of about 750 km in circuit length. From the above, it is reasonable to conclude that the series resonance overvoltage will not occur in the Kyndbyværket 132 kV network due to the installation of the Kyndbyværket – Asnæsværket line.

The series resonance overvoltage is, however, studied from an academic interest. When 132 kV cable capacitance 149.8 μF is connected to the Kyndbyværket 132 kV bus, it results in the natural frequency of the Kyndbyværket 132 kV network to 90 Hz and, at the same time, will raise the steady-state system voltage around the Kyndbyværket substation. A shunt reactor has to be assumed at the Kyndbyværket 132 kV bus, so as to prevent the steady-state overvoltage.

In order to 100 % compensate for the large reactive power produced from the cable capacitance 149.8 μF, the shunt reactor $L = 67.65$ mH has to be connected to the Kyndbyværket 132 kV bus. However, this shunt reactor shifts the natural frequency of the Kyndbyværket 132 kV network to 100 Hz, which is not ideal to cause a severe series resonance. In order to shift the natural frequency lower, the cable capacitance is increased to 170.0 μF. It is confirmed that this increase does not cause the steady-state overvoltage.

In the above mentioned condition, the frequency scan is performed to find the natural frequency of the Kyndbyværket 132 kV network. Fig. 4.37 shows the result of the frequency scan. As can be seen from the figure, the natural frequency of the Kyndbyværket 132 kV network is successfully set to 95 Hz.
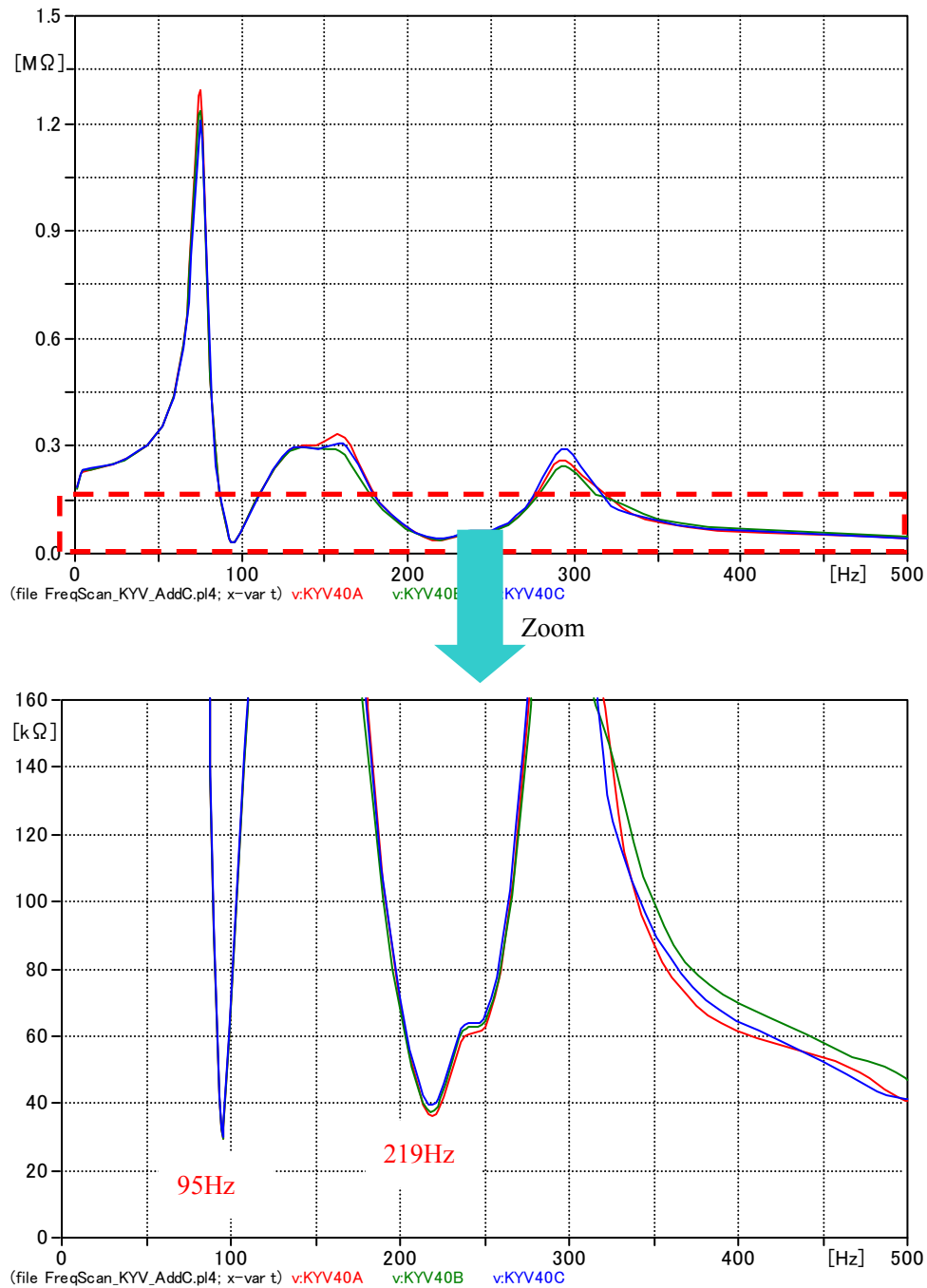
Fig. 4.37 Series resonance frequency of the KYV network.

In order to have severe series resonance, it is necessary to have a high voltage amplification ratio from the Kyndbyværket 400 kV bus to the 132 kV bus. The amplification ratio is shown in Fig. 4.38. It is observed in the figure that the amplification ratio is approximately 6 at 88 Hz, which is not very high.
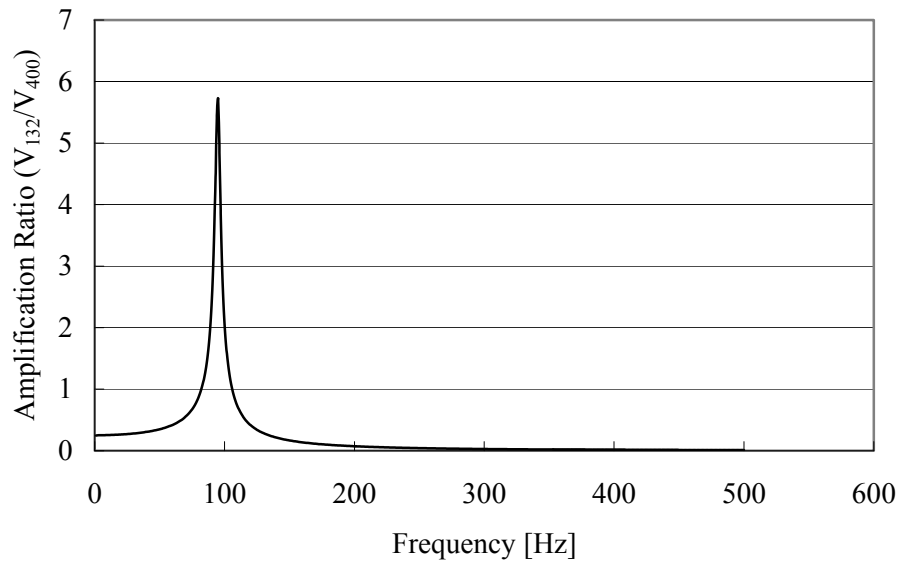
Fig. 4.38 Voltage amplification ratio from the KYV 400 kV bus to the 132 kV bus.

The amplification ratio is highly affected by the loading condition. In terms of the amplification ratio, the assumed condition is already severe since it is derived in the off-peak load condition. If it is necessary to assume the no load condition in the Kyndbyværket 132 kV network, it significantly increases the amplification ratio. Fig. 4.39 shows that the amplification ratio increases to around 25 in the no load condition.
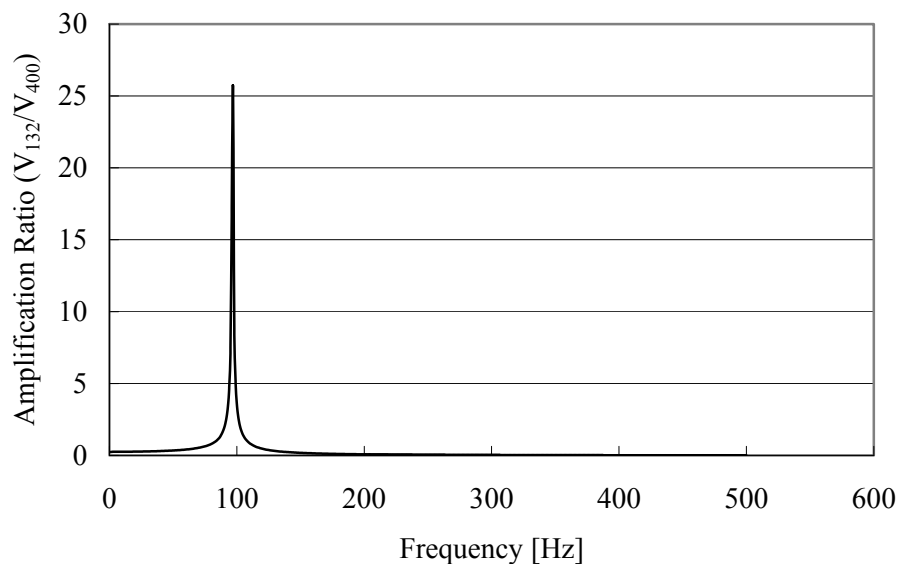
Fig. 4.39 Voltage amplification ratio from the KYV 400 kV bus to the 132 kV bus in the no load condition.

The same analysis is performed for the Asnæsværket 132 kV network. According to Eqn. 4.30, 132 kV cable capacitance 77.7 µF is assumed in the Asnæsværket 132 kV network. Again, this cable capacitance corresponds to 425.4 MVar or 388.6 km in circuit length in the Asnæsværket 132 kV network. It is thus concluded that the series resonance overvoltage will not occur in the Asnæsværket 132 kV network due to the installation of the Kyndbyværket – Asnæsværket line.

$$\frac{1}{2\pi\sqrt{(0.0000362 + 0.0402) \times C}} = 90 \qquad \text{Eqn. 4.30}$$

$C = 77.7$ [µF]

Fig. 4.40 shows the result of the frequency scan. As can be seen from the figure, the natural frequency of the Asnæsværket 132 kV network is successfully set to 100 Hz. The natural frequency is shifted from 90 Hz to 100 Hz by the inductance $L = 130.4$ mH, which represents the shunt reactor to compensate for the large reactive power from the 132 kV cable. It is not possible in this case to lower the natural frequency by increasing 132 kV cable capacitance as it causes steady-state overvoltage.

In order to have severe series resonance, it is necessary to have a high voltage amplification ratio from the Asnæsværket 400 kV bus to the 132 kV bus. The amplification ratio is shown in Fig. 4.41. It is clear in the figure that the amplification ratio is approximately 3.5 at 100 Hz, which is not very high.
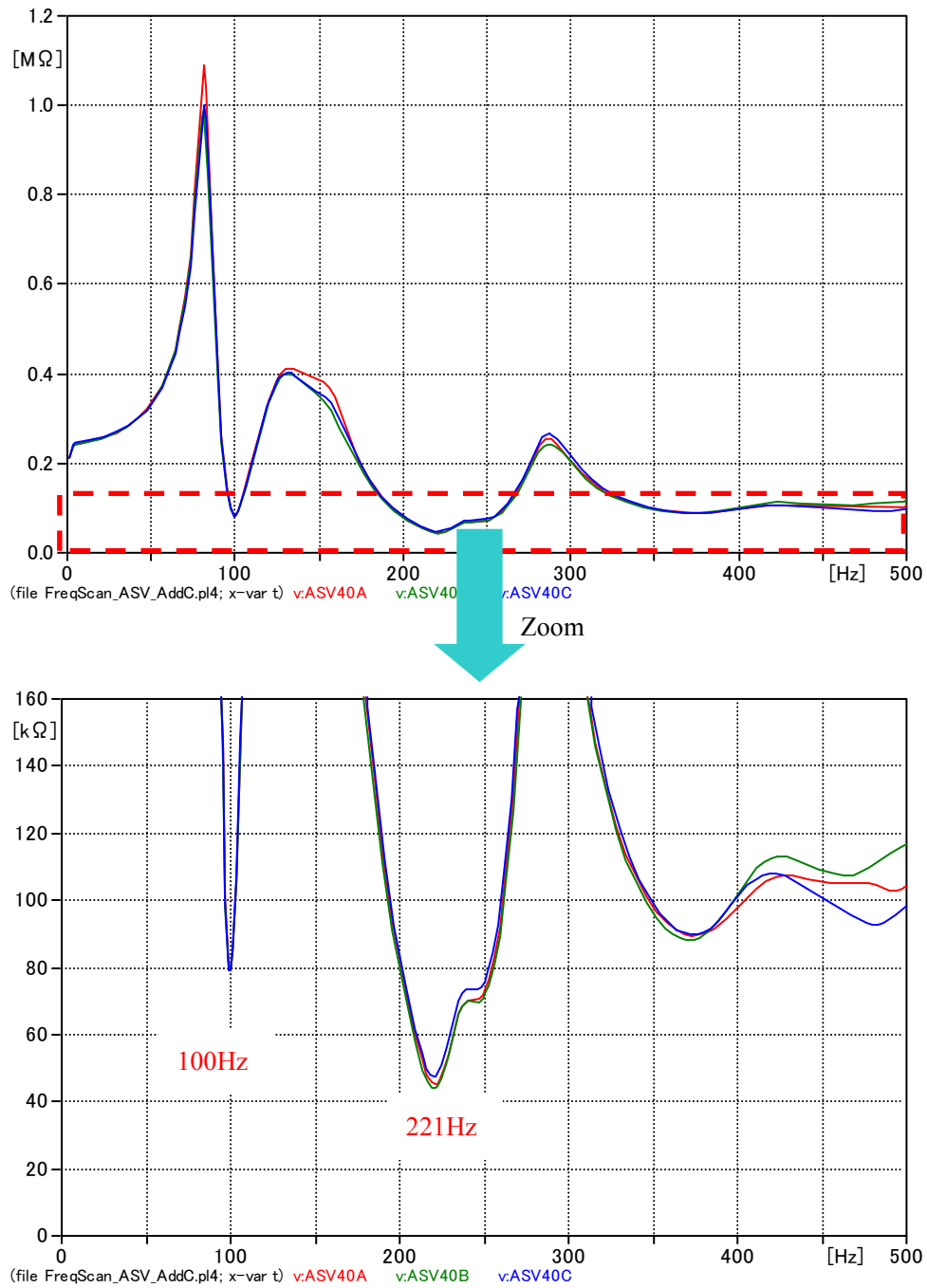
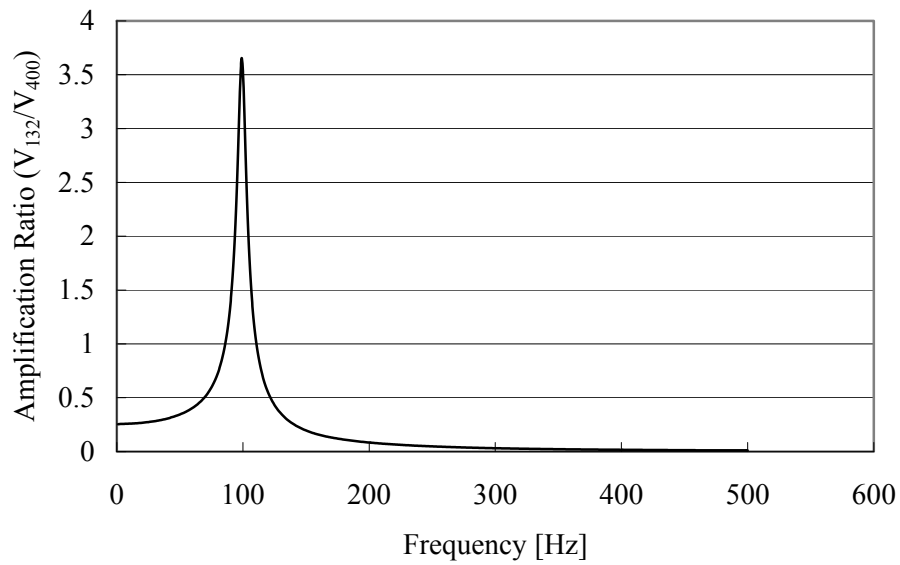**Fig. 4.40 Series resonance frequency of the ASV network.**

Fig. 4.41 Voltage amplification ratio from the ASV 400 kV bus to the 132 kV bus.

In the no load condition, the amplification ratio is increased to around 43 as shown in Fig. 4.42.
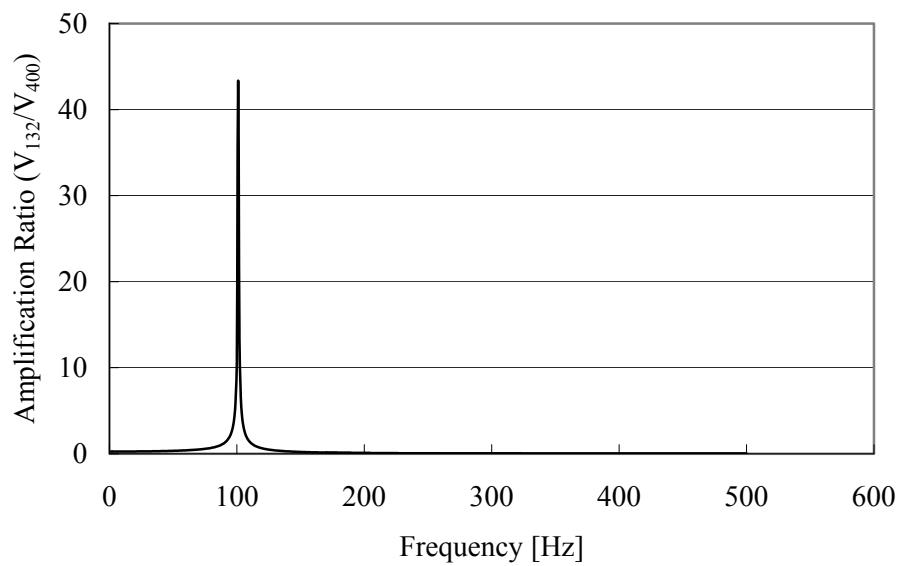

Fig. 4.42 Voltage amplification ratio from the ASV 400 kV bus to the 132 kV bus in the no load condition.

4.1.5   Simulation Results of Series Resonance Overvoltage

The time domain simulations are performed to find the series resonance overvoltage in the assumed most severe condition. First, the Kyndbyværket – Asnæsværket line is energized from the Kyndbyværket side and the overvoltage in the Kyndbyværket 132 kV bus is monitored as shown in Fig. 4.43.
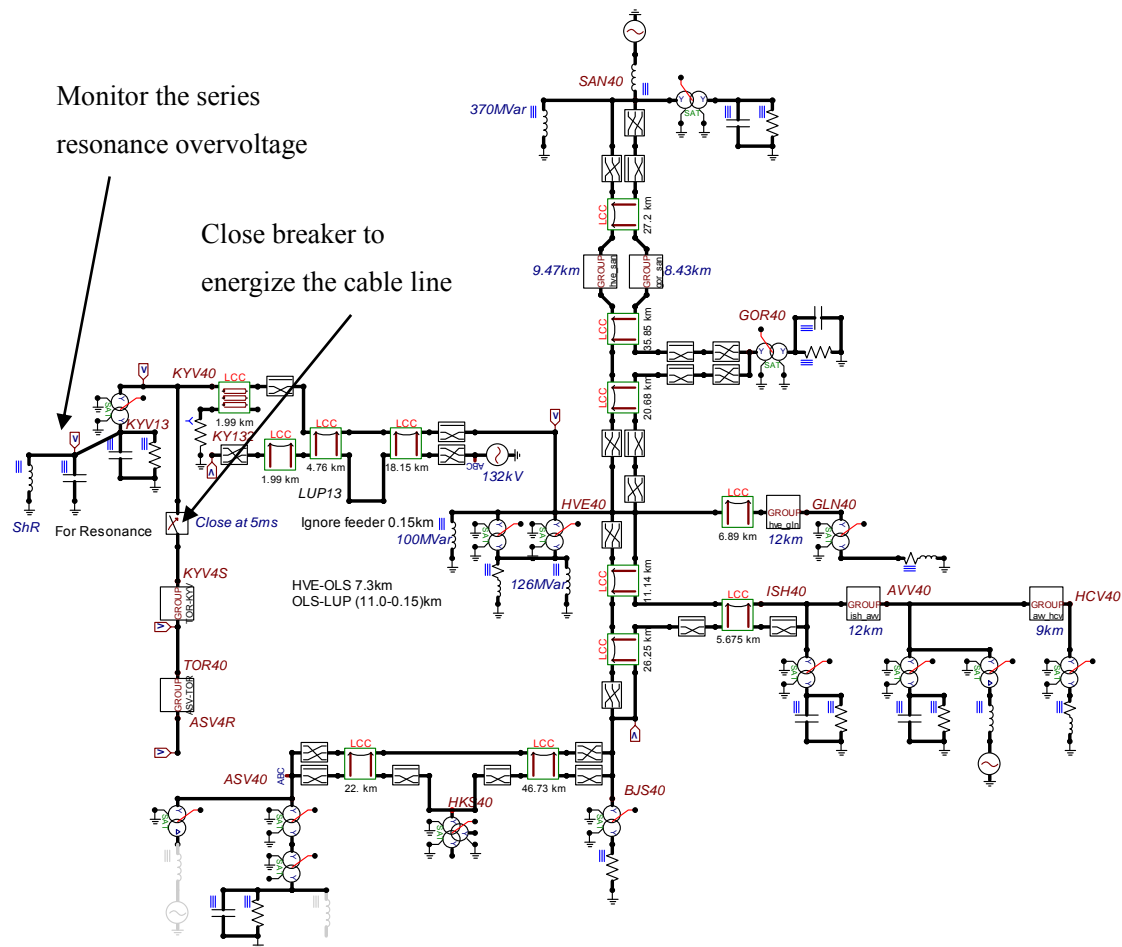
Fig. 4.43 Simulation model to find the series resonance overvoltage in the Kyndbyværket 132 kV bus.

Results of the time domain simulations are shown in Fig. 4.44. In the figure, the upper graph shows the phase to ground overvoltage, and the lower graph shows the phase to phase overvoltage. According to IEC 60071, the standard short-duration power-frequency withstand voltage for the 132 kV equipment is (185), 230 or 275 kV (rms). The same withstand voltages are applied to both the phase to ground overvoltage and the phase to phase overvoltage. Here, the application to the

phase to phase overvoltage depends on the physical construction of the equipment. Fig. 4.44 shows that the series resonance overvoltage in the assumed most severe condition does not exceed the withstand voltage. The phase to phase overvoltage decays below 230 kV (peak) after one cycle.
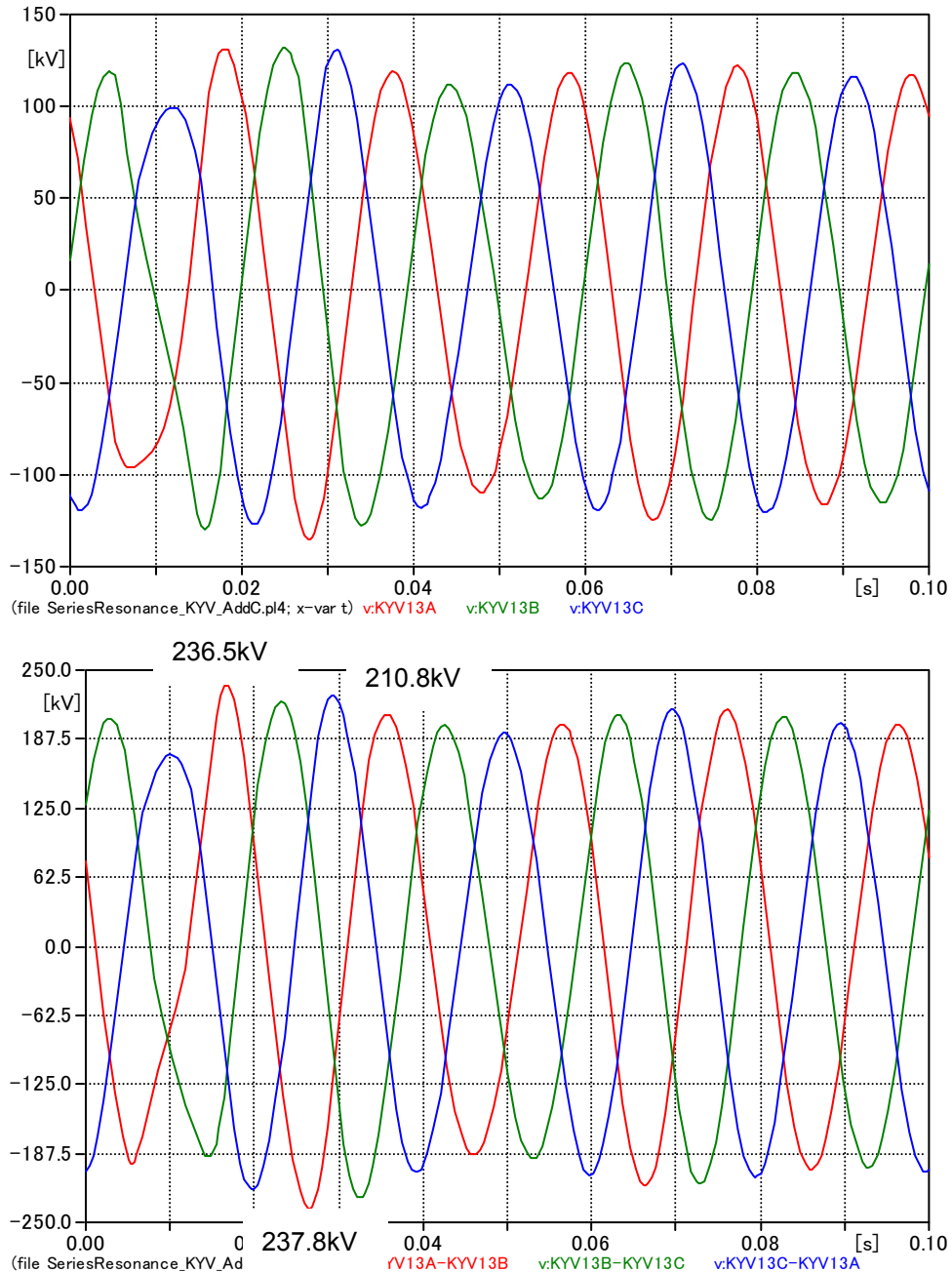

Fig. 4.44 Series resonance overvoltage in the KYV 132 kV bus in the off-peak load condition
(upper: phase to ground, lower: phase to phase).

The same simulations are repeated with the no load condition. Fig. 4.45 shows the results of the simulations. Only minor difference is observed compared with the results in the off-peak load condition.
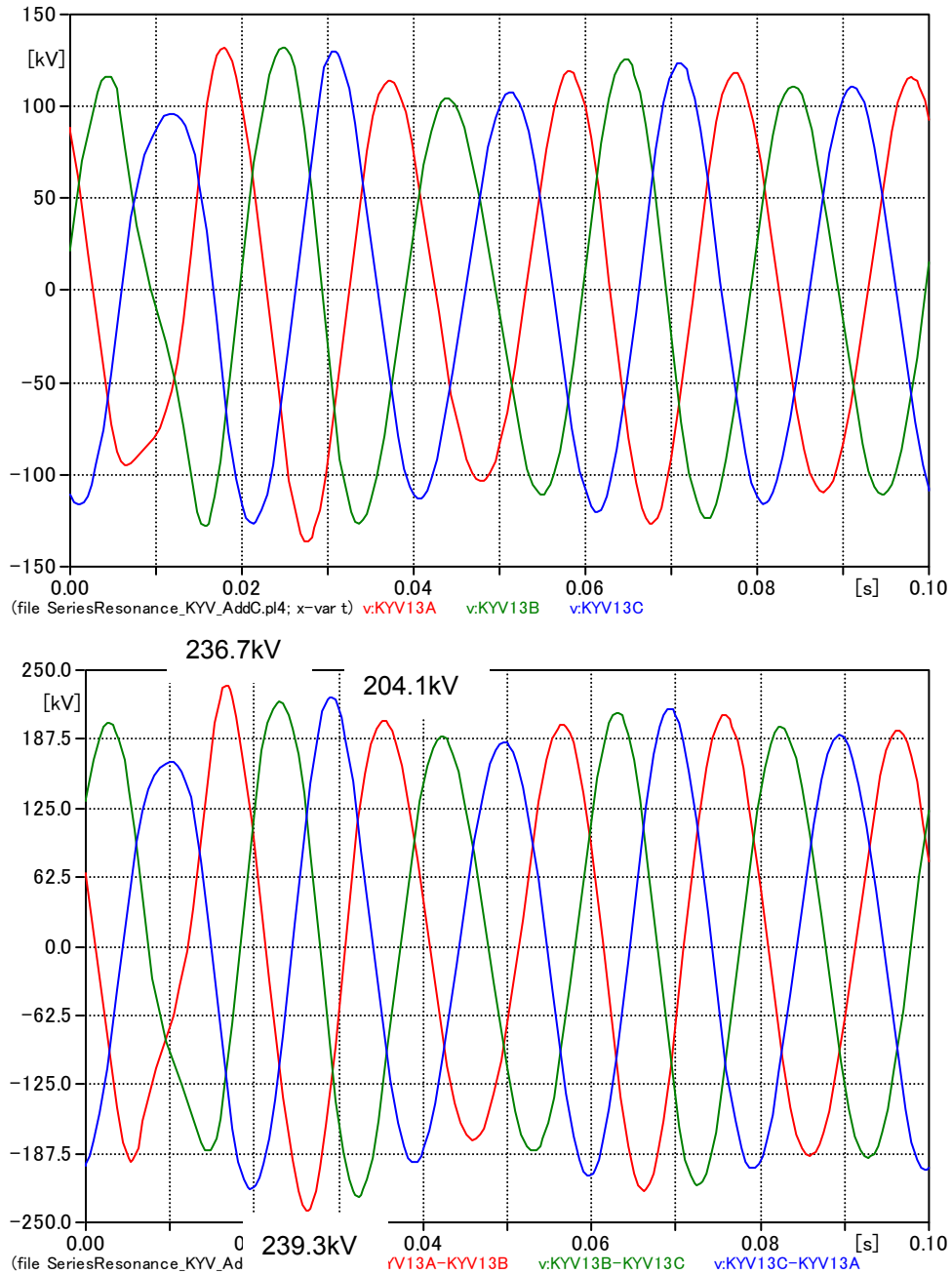

Fig. 4.45 Series resonance overvoltage in the KYV 132 kV bus in the no load condition

(upper: phase to ground, lower: phase to phase).

Second, the Kyndbyværket – Asnæsværket line is energized from the Asnæsværket side and the overvoltage in the Asnæsværket 132 kV bus is monitored. Fig. 4.46 and Fig. 4.47 show the series resonance overvoltage found with the off-peak load condition and the no load condition, respectively.

The overvoltage level is higher compared with the overvoltage in the Kyndbyværket 132 kV bus, but it is still much lower than the withstand voltage as long as the withstand voltage 230 or 275 kV is selected. The phase to phase overvoltage decays below 230 kV after one cycle. As in the overvoltage in the Kyndbyværket 132 kV bus, the load level has only minor impact on the overvoltage level. It is because the load level is already low in the off-peak load condition.
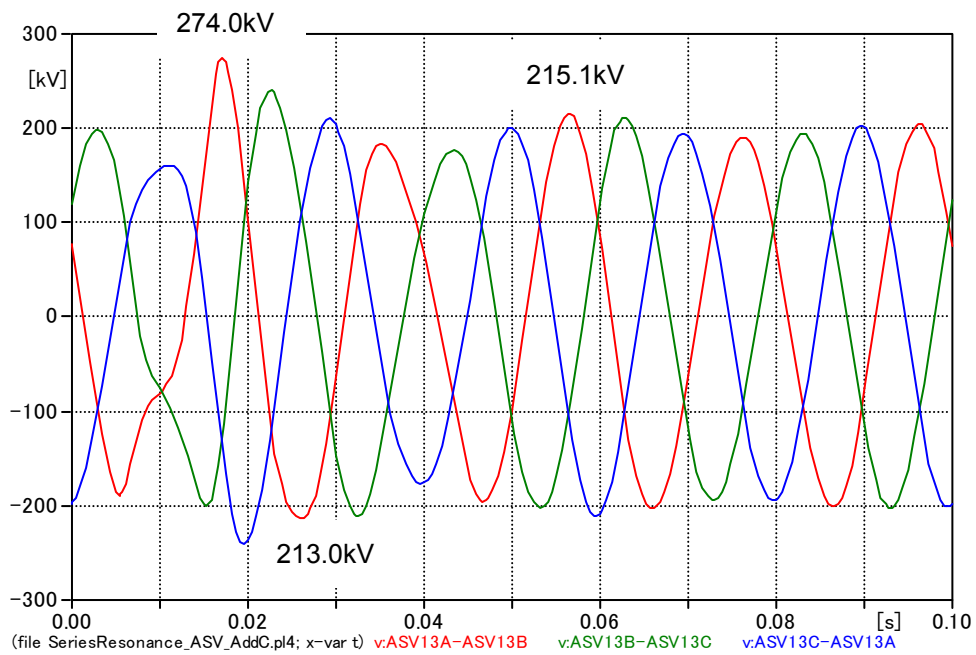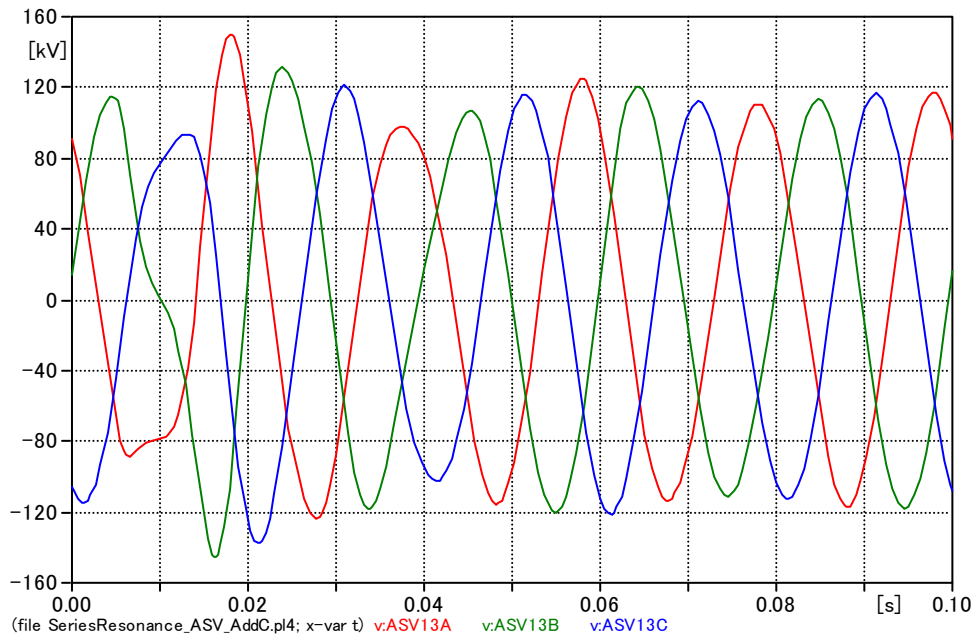
Fig. 4.46 Series resonance overvoltage in the ASV 132 kV bus in the off-peak load condition (upper: phase to ground, lower: phase to phase).
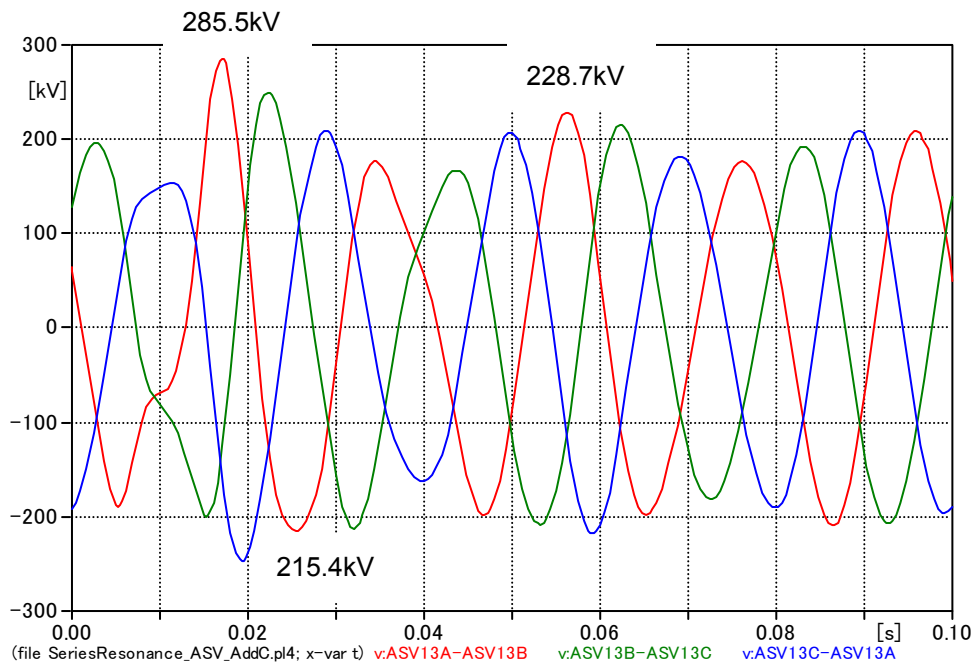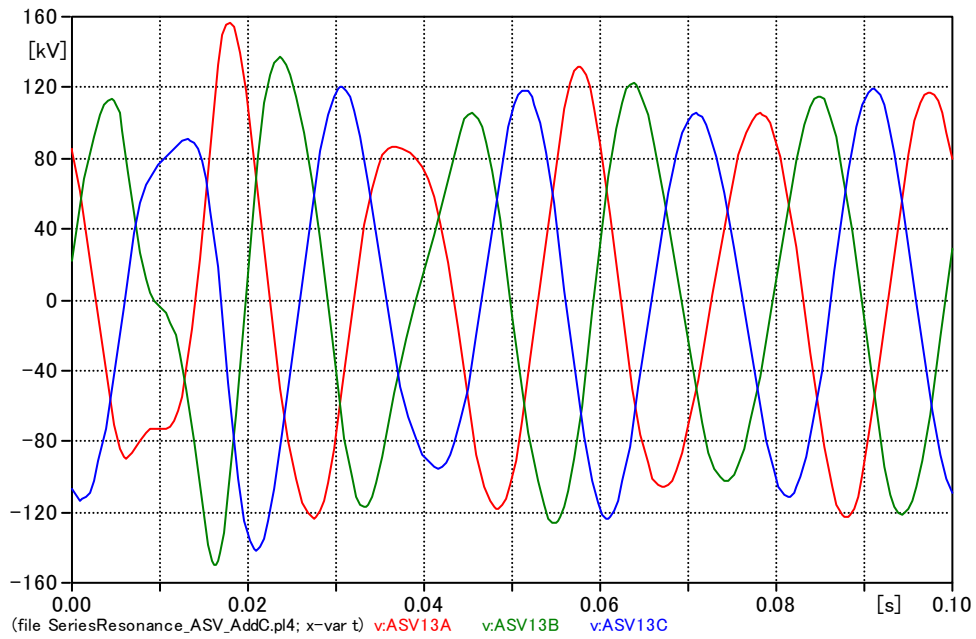
Fig. 4.47 Series resonance overvoltage in the ASV 132 kV bus in the no load condition
(upper: phase to ground, lower: phase to phase).

4.2 Parallel Resonance Overvoltage

4.2.1   Overview

When inductance L and capacitance C are connected in parallel, the total impedance or series impedance becomes infinitely large at the frequency $f_n = \dfrac{1}{2\pi\sqrt{LC}}$. When a current source of this frequency is connected to the parallel circuit as in Fig. 4.48, infinitely large voltage might appear, in theory, on the source side of the inductance and the capacitance. Such a voltage is called parallel resonance overvoltage.
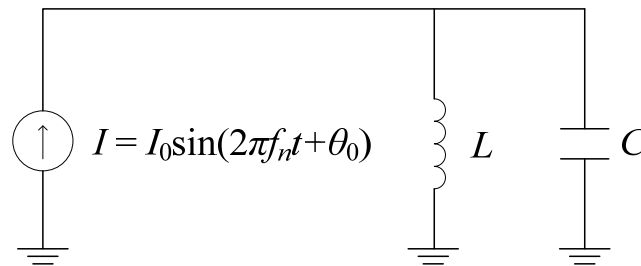

Fig. 4.48 Simple parallel resonance circuit.

The parallel resonance overvoltage can occur in an actual power system. For example, transformer energization, cable energization, and HVDC can be a source of a harmonic current that excites a parallel resonance circuit. Among the potential harmonic current sources, an inrush current caused by the transformer energization is considered to be the most onerous one because of its high harmonic contents, low frequency, low damping, and long duration.

Fig. 4.49 shows a simplified circuit that can lead to a severe parallel resonance overvoltage caused by the transformer energization. When the 400 kV transformer is energized, harmonic current contained in the inrush current flows through parallel resonance circuit composed of charging capacity C, shunt reactor for reactive power compensation L, and equivalent source impedance L_0.

The harmonic equivalent circuit is also shown in Fig. 4.49. The inrush current is expressed as harmonic current source. The voltage source behind the equivalent source impedance is ignored since the voltage source only generates fundamental frequency voltage.
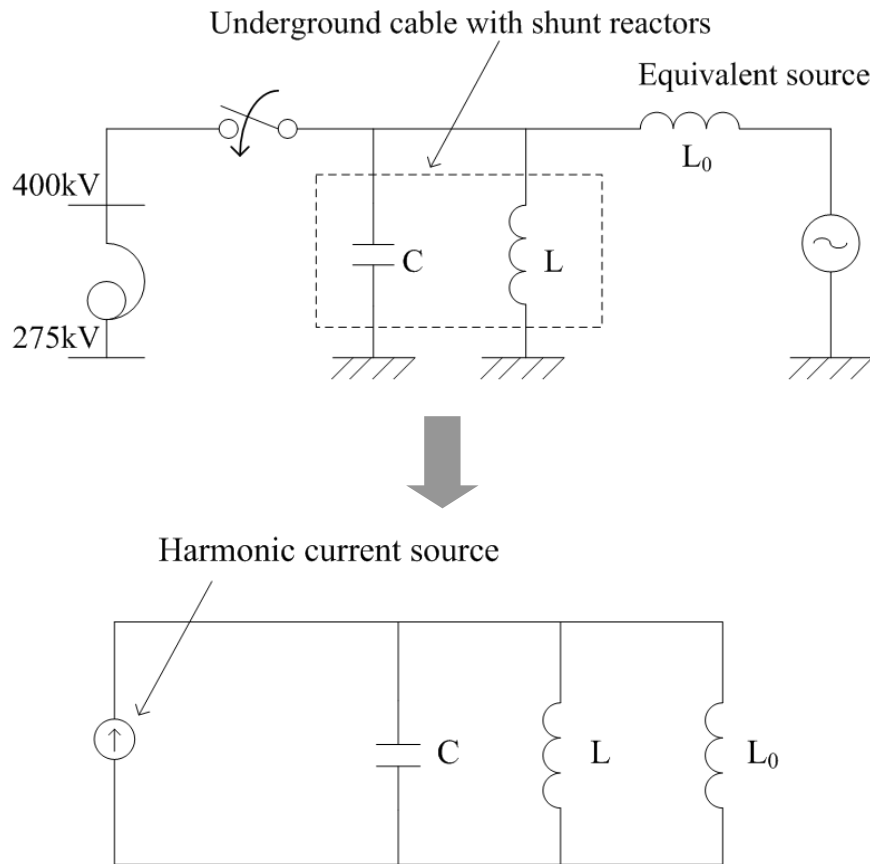
Fig. 4.49 Equivalent circuit of parallel resonance caused by transformer inrush.

The condition for the parallel resonance is:

$$\omega_n C = \frac{1}{\omega_n L} + \frac{1}{\omega_n L_0}$$

$$f_n = \frac{1}{2\pi}\sqrt{\frac{1}{CL} + \frac{1}{CL_0}} \qquad \text{Eqn. 4.31}$$

Here, f_n is the natural frequency of the parallel resonance circuit.

Since the second harmonic current is contained in the inrush current with a higher proportion compared to the other harmonic components, a parallel resonance overvoltage is most severe when the natural frequency of the parallel circuit is 100 Hz, that is:

$$f_n = \frac{1}{2\pi}\sqrt{\frac{1}{CL} + \frac{1}{CL_0}} = 100 \qquad \text{Eqn. 4.32}$$

When the compensation rate of the cable is 100 %, the natural frequency ignoring the source impedance is 50 Hz, that is:

$$f_n = \frac{1}{2\pi}\sqrt{\frac{1}{CL}} = 50$$

Eqn. 4.33

The source impedance will raise the natural frequency, and it becomes 100 Hz when $L_0 = L / 3$ as shown in Eqn. 4.34.

$$
\begin{aligned}
f_n &= \frac{1}{2\pi}\sqrt{\frac{1}{CL} + \frac{1}{CL_0}} \\
&= \frac{1}{2\pi}\sqrt{\frac{1}{CL} + \frac{3}{CL}} \\
&= \frac{1}{2\pi}\sqrt{\frac{1}{CL} \times 2} \\
&= 100
\end{aligned}
$$

Eqn. 4.34

However, the source impedance is usually much smaller than $L / 3$ in most networks in typical operating conditions. The natural frequency, therefore, becomes 100 Hz in weak networks such as in the black start operations. The load level is generally low in weak networks, and it highly contributes to a severe parallel resonance overvoltage.

In this PhD project, the parallel resonance overvoltage is studied in the following procedure:
- Find the natural frequency of the parallel resonance circuit
- Set the natural frequency to 100 Hz by adjusting source impedance
- Simulate the most severe switching scenarios (transformer energization) with the natural frequency 100 Hz

4.2.2   Most Severe Scenarios

As discussed in the previous section, the transformer energization will be studied in the PhD project as the most severe switching scenarios. In order to cause parallel resonance, a transformer needs to be energized through a cable whose charging current is compensated by shunt reactors.

Fig. 4.50 shows the assumed most severe scenario for the energization of the 400 / 132 kV Kyndbyværket transformer. The transformer is energized through the Kyndbyværket – Asnæsværket line. The voltage source for the energization is assumed on the Bjæverskov side, and

the source impedance is adjusted so that the natural frequency of the parallel resonance circuit becomes 100 Hz. The Kyndbyværket – Hovegård line is assumed to be opened in order to have a large source impedance (weak network) and to limit the propagation path of the inrush current.

If the generator at Asnæsværket has black start capability, the Kyndbyværket – Hovegård line can be opened assuming the black start operation from Asnæsværket. It, in theory, causes more severe overvoltages because of limited propagation paths of the inrush current and lower load level.
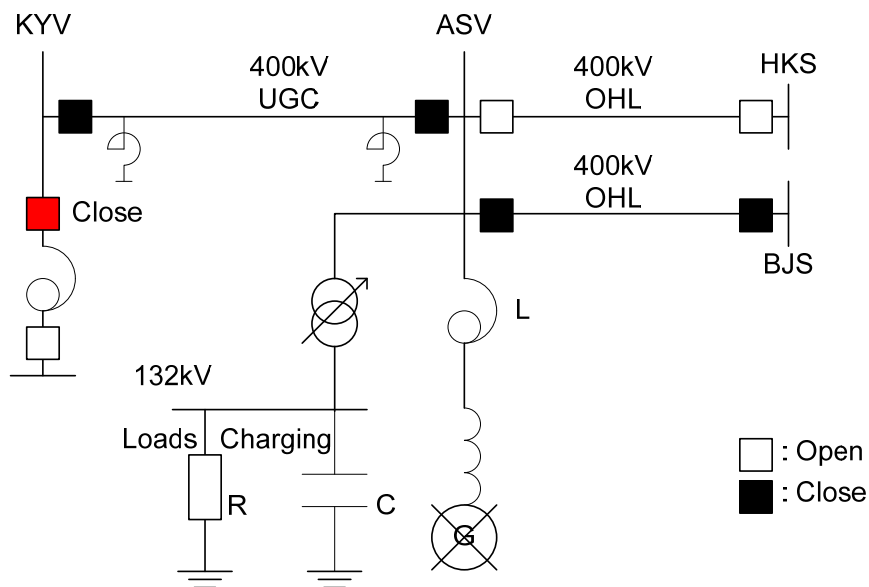

Fig. 4.50 Assumed most severe scenario for the energization of KYV transformer.

Fig. 4.51 shows the assumed most severe scenario for the energization of the 400 / 132 kV Asnæsværket transformer and phase shifting transformer. The transformers are energized through the Kyndbyværket – Asnæsværket line.

As the generator at Kyndbyværket has the black start capability, the most severe scenario assumes the black start operation from Kyndbyværket. As such, the following three lines are assumed not to be in service.

- Asnæsværket – Herslev line
- Asnæsværket – Bjæverskov line
- Kyndbyværket – Hovegård line

It may not be possible to adjust the natural frequency of the parallel resonance frequency exactly at

100 Hz because of the limited number of available generators at Kyndbyværket. Even with that condition, severe overvoltages are often caused due to limited propagation paths of the inrush current and lower load level.
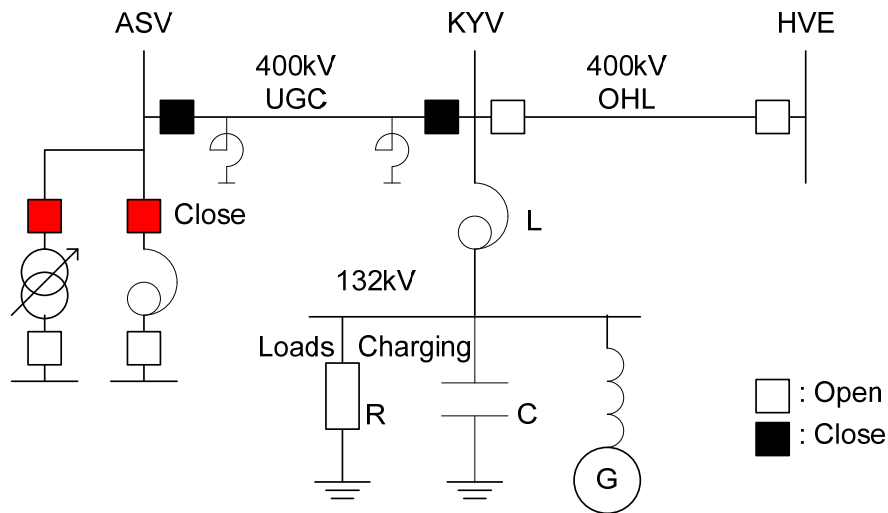

Fig. 4.51 Assumed most severe scenario for the energization of ASV transformers.

4.2.3   Natural Frequency of Parallel Resonance Circuit

First, the energization of the 400 / 132 kV Kyndbyværket transformer is studied. The natural frequencies of the network are found by frequency scan using the simulation model illustrated in Fig. 4.52. The operating condition of the network is modified according to the most severe scenario in Fig. 4.50.

Since it is expected to have the natural frequency at 100 Hz, the target frequency of all the Bergeron models is set to 100 Hz.
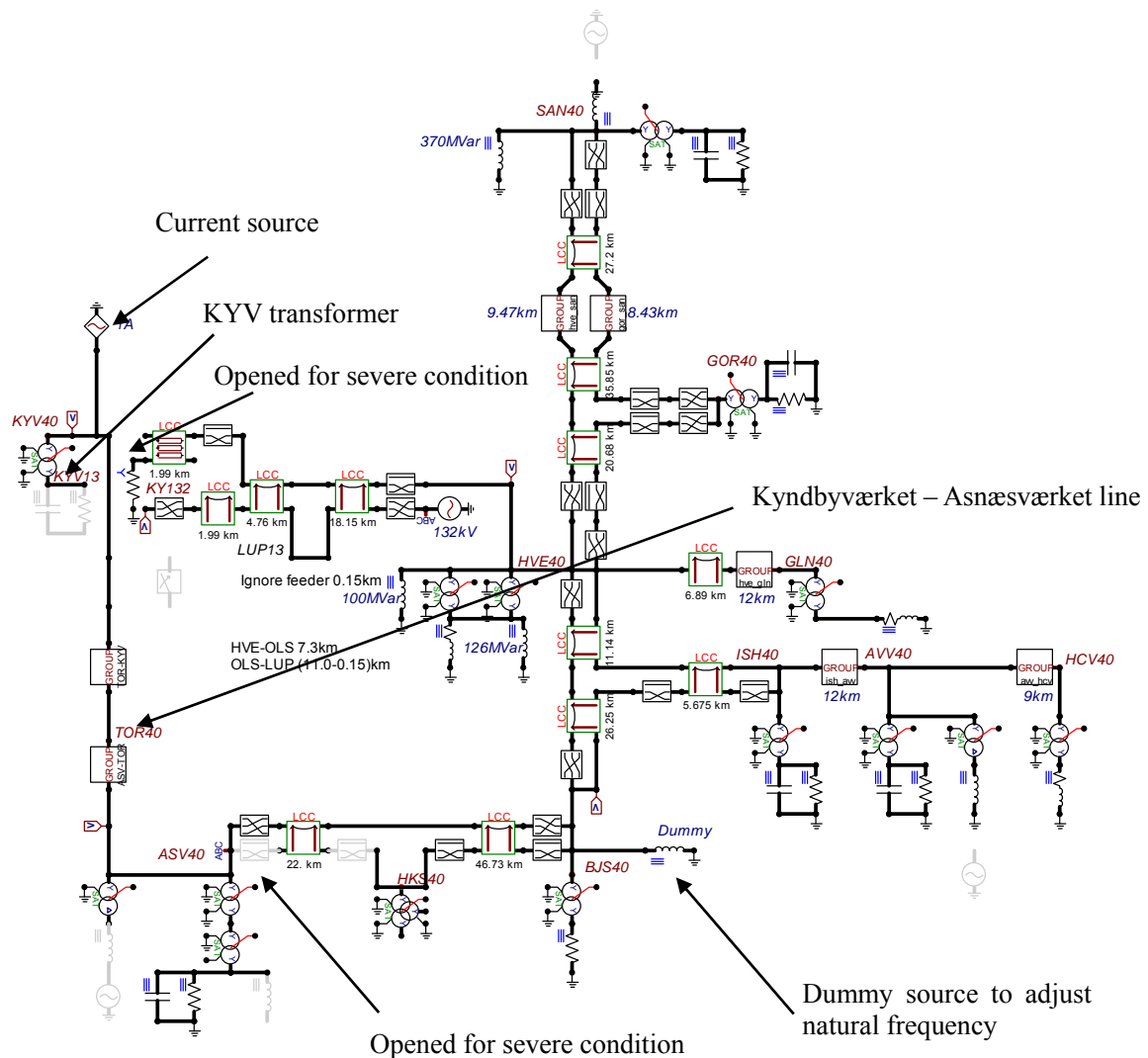
Fig. 4.52 Simulation model for frequency scan for the energization of KYV transformer.

Results of the frequency scan are shown in Fig. 4.53. Natural frequencies are found at 92 Hz and 324 Hz in the figure. The magnitude of the impedance is 1306 ohm at 92 Hz and goes down to 878 ohm at 100 Hz.

To have a natural frequency at 92 Hz means that the network is already too weak in the off-peak condition. In order to have a peak at 100 Hz, it is necessary to have a smaller source impedance according to Eqn. 4.31. In order for it, the dummy source impedance 450 mH is added to the Bjæverskov 400 kV bus as illustrated in Fig. 4.52.

Results of the frequency scan after the adjustment is shown in Fig. 4.54. The figure shows that the

natural frequency is successfully shifted from 92 Hz to 100 Hz. The magnitude of the impedance at 100 Hz is increased to 1376 ohm.
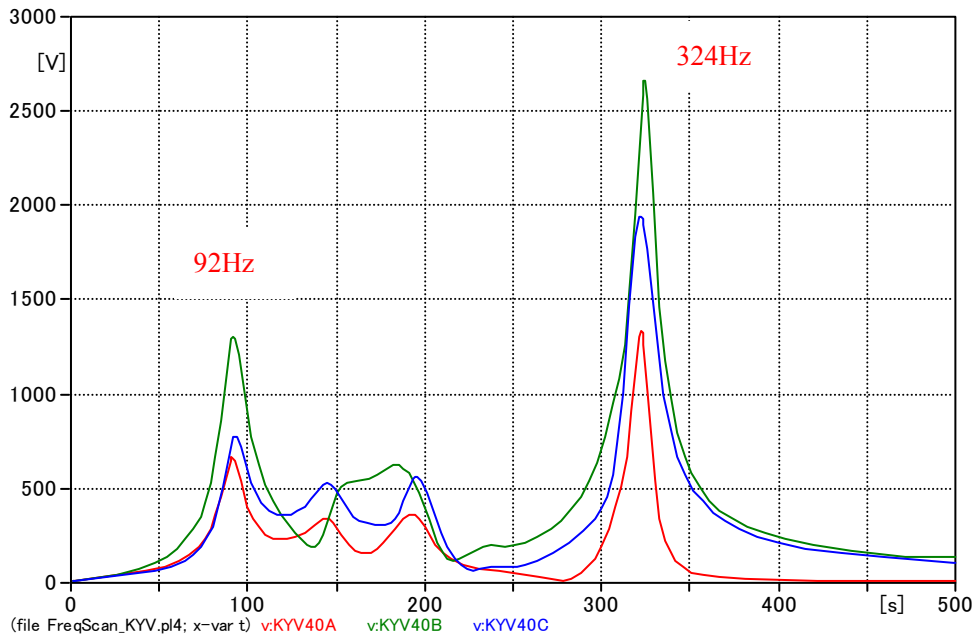

Fig. 4.53 Natural frequencies of the network in the energization of KYV transformer in the off-peak load condition.
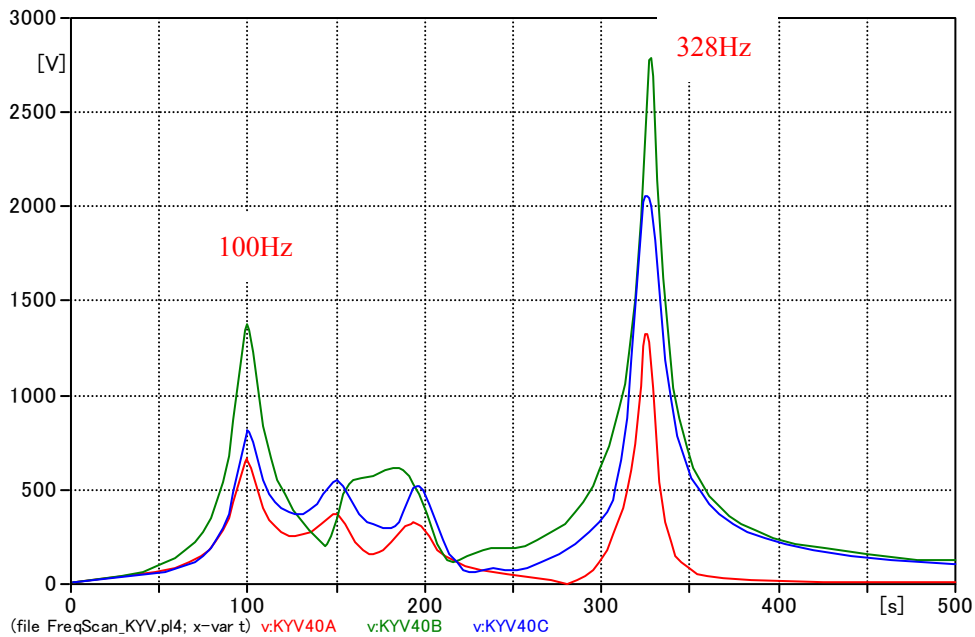

Fig. 4.54 Natural frequencies of the network in the energization of KYV transformer after the source impedance adjustment.

Second, the energization of the 400 / 132 kV Asnæsværket transformer and phase shifting transformer is studied. Assuming the black start restoration from the KYV generator, the operating condition of the network is modified according to the most severe scenario in Fig. 4.51.

In the black start restoration scenario, the following steps are assumed:

(1)   Black start Kyndbyværket 132 kV generator

(2)   Restore the Kyndbyværket 132 kV load 20 MW

(3)   Energize the Kyndbyværket 400 / 132 kV transformer from the secondary side

(4)   Energize the Kyndbyværket – Asnæsværket line from the Kyndbyværket side

(5)   Energize the 400 / 132 kV Asnæsværket transformer or phase shifting transformer

The parallel resonance overvoltage is studied in Step (5).

Fig. 4.55 shows the results of the frequency scan. Initially, only one Kyndbyværket 132 kV generator, Machine 224 in the provided PSS/E data, is assumed to be in-service. The source impedance 578.5 mH which corresponds to this generator is connected to the Kyndbyværket 132 kV bus. The figure shows that the network has a very sharp peak at 52 Hz. The magnitude of the impedance is 6773 ohm, but it goes down to 168 ohm at 100 Hz.
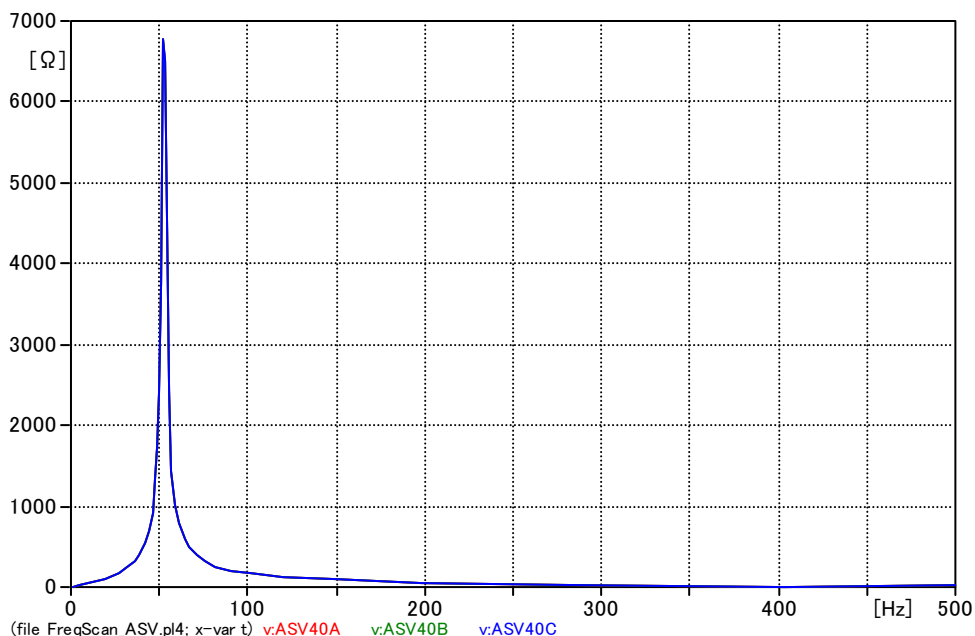

Fig. 4.55 Natural frequencies of the network in the energization of ASV transformer in the black start restoration.

As discussed in the previous section, the natural frequency of the network is located at 50 Hz without a source impedance and loads. The results show that the source impedance and the loads increase the natural frequency only by 2 Hz because of the following reasons:

- The source impedance is very large since the capacity of the assumed black start generator is small (28.57 MVA).
- The source impedance is large since there is only one 400 / 132 kV Kyndbyværket transformer.
- The load level is very low (20 MW) due to the assumed black start restoration scenario.

In order to shift the natural frequency to 100 Hz, it is necessary to assume a smaller source impedance. Assuming many other generators in the Kyndbyværket 132 kV network are in-service, the source impedance is decreased from 578.5 mH to 8 mH. The source impedance 8 mH corresponds to the fault current level 30.3 kA at the Kyndbyværket 132 kV bus. As shown in Fig. 4.56, the natural frequency is successfully shifted to 100 Hz. The magnitude of the impedance is 9439 ohm at 100 Hz.

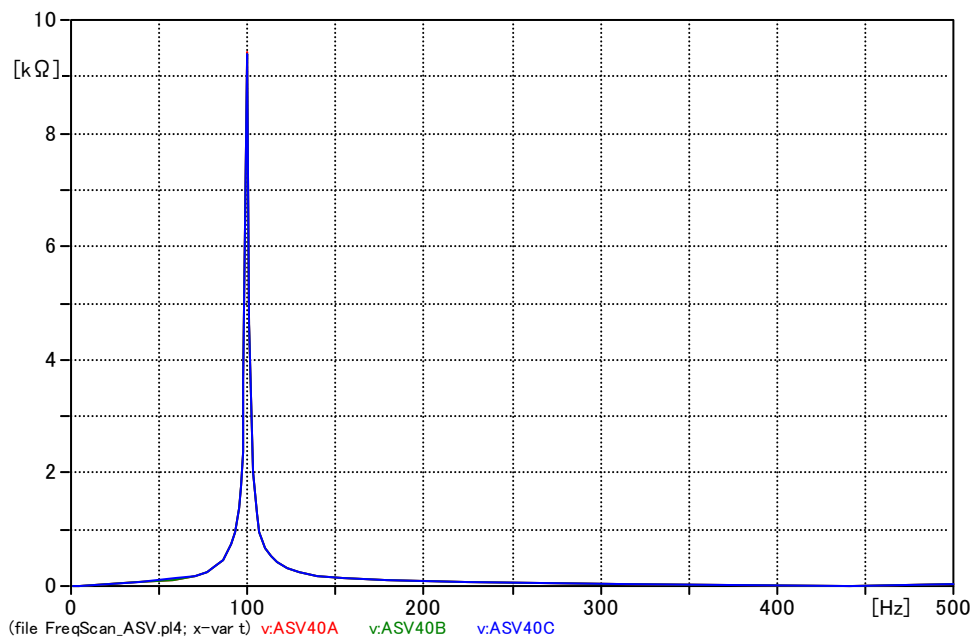(file FreqScan_ASV.pl4; x-var t)   v:ASV40A   v:ASV40B   v:ASV40C

Fig. 4.56 Natural frequencies of the network in the energization of ASV transformer after the source impedance adjustment.

As it is assumed that many other generators are in-service, it is not realistic to assume that only 20

MW load is restored at the Kyndbyværket 132 kV. In Fig. 4.57, the Kyndbyværket 132 kV load is increased from 20 MW to the off-peak load 67.8 MW. The load increase does not shift the natural frequency, but lowered the magnitude of the impedance to 7364 ohm.
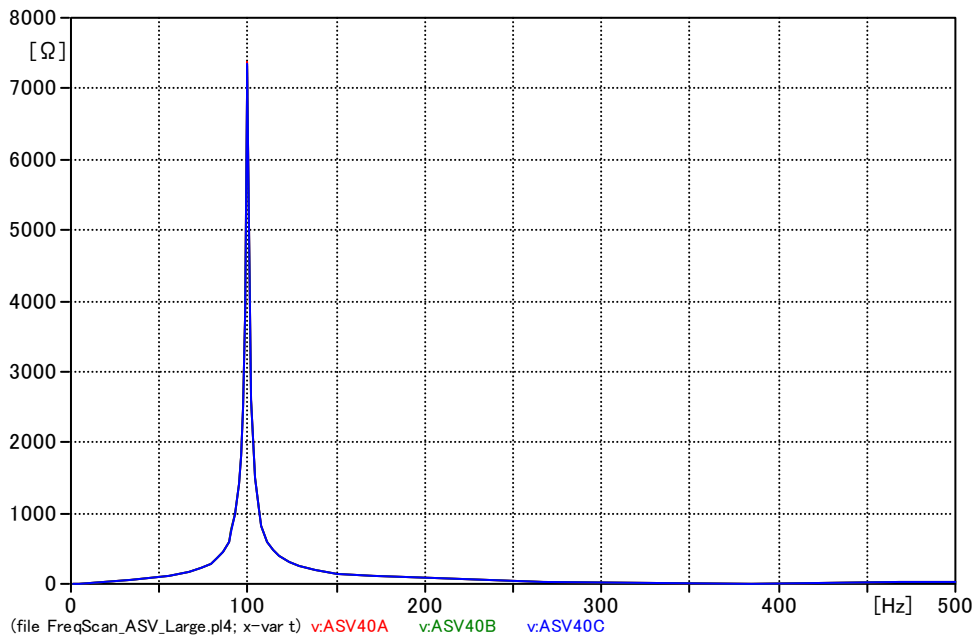

(file FreqScan_ASV_Large.pl4; x-var t) v:ASV40A   v:ASV40B   v:ASV40C

Fig. 4.57 Natural frequencies of the network in the energization of ASV transformer after the source impedance adjustment with increased load.

Even though, the natural frequency is successfully shifted to 100 Hz, it may not be realistic to assume the fault current level 30.3 kA at Kyndbyværket 132 kV bus. In order to make it more realistic the following modified restoration scenario is considered:

(1)   Black start Kyndbyværket 132 kV generators

(2)   Restore the Kyndbyværket 132 kV load 67.8 MW (off-peak)

(3)   Energize the Kyndbyværket 400 / 132 kV transformer from the secondary side

(4)   Energize the Kyndbyværket – Hovegård line from the Kyndbyværket side

(5)   Energize the two Hovegård 400 / 132 kV transformers

(6)   Start up generators connected to the Hovegård 132 kV network

(7)   Restore the Hovegård 132 kV load 151.2 MW (off-peak)

(8)   Energize the Kyndbyværket – Asnæsværket line from the Kyndbyværket side

(9)   Energize the 400 / 132 kV Asnæsværket transformer or phase shifting transformer

The parallel resonance overvoltage is studied in Step (9).

In the modified scenario, Hovegård is restored before Kyndbyværket in Steps (4) – (7). Since Hovegård has two 400 / 132 kV transformers, it is easier to have a small source impedance. The simulation model for the modified restoration scenario is illustrated in Fig. 4.58
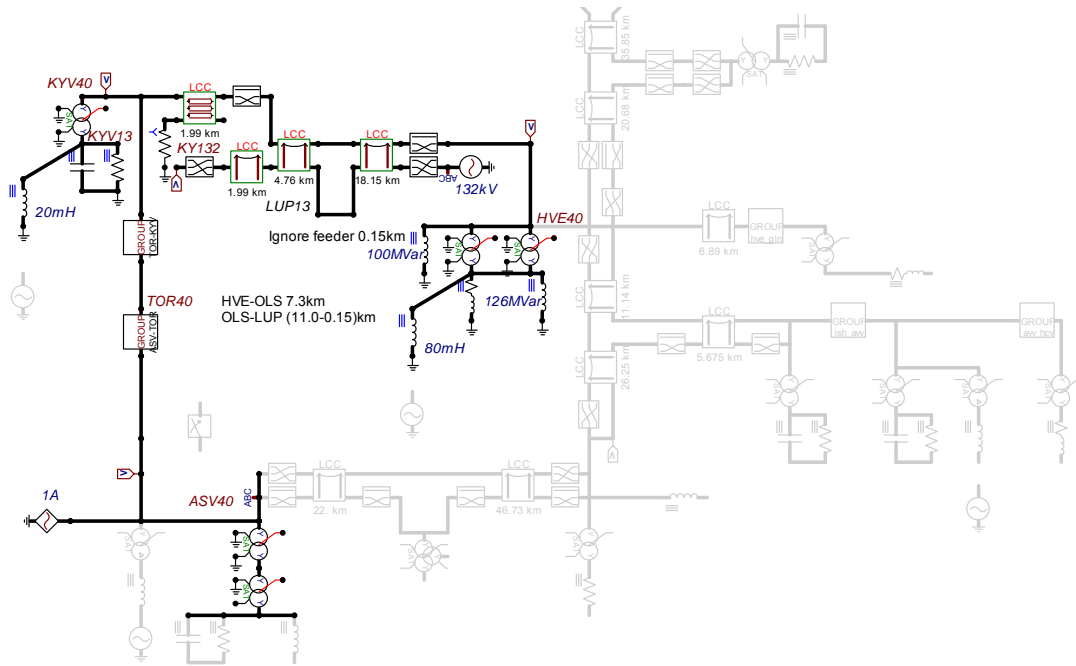

Fig. 4.58 Simulation model for frequency scan for the energization of ASV transformer after HVE is restored.

In the modified restoration scenario, it is possible to have a source impedance at the Hovegård 132 kV bus as well as the Kyndbyværket 132 kV bus. First, the source impedance at the Kyndbyværket 132 kV bus is increased from 8 mH to 20 mH. The source impedance 20 mH corresponds to the fault current level 12.1 kA. This is more realistic assumption compared with the original scenario. The source impedance at the Hovegård 132 kV bus is set to 80 mH in order to have the natural frequency at 100 Hz. The source impedance 80 mH corresponds to the fault current level 3.0 kA.

Fig. 4.59 shows the results of the frequency scan. It is observed in the figure that the natural frequency is successfully set at 100 Hz. The magnitude of the impedance at 100 Hz is 18846 ohm, which is extremely high.
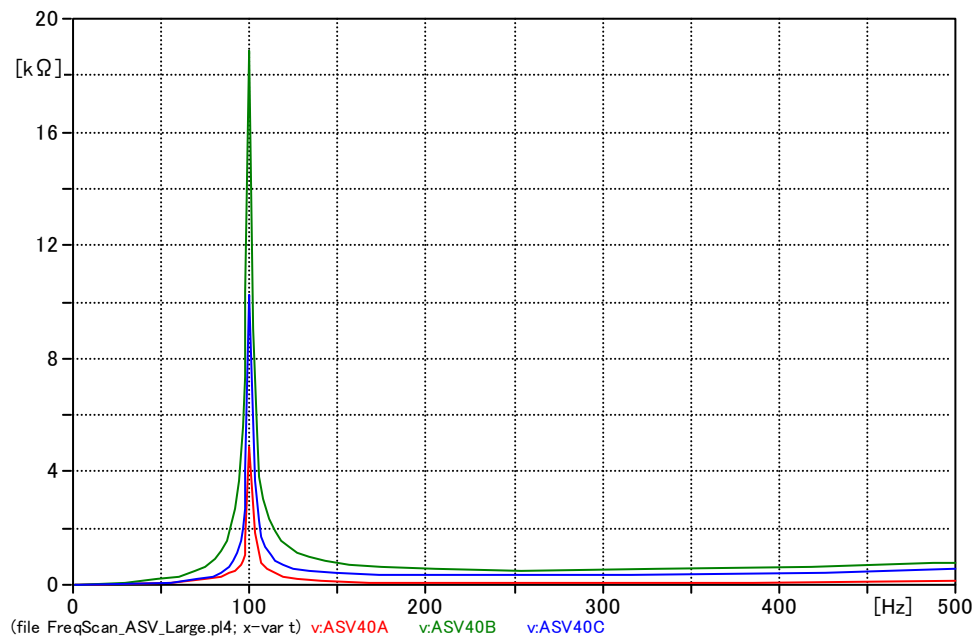
Fig. 4.59 Natural frequencies of the network in the energization of ASV transformer after HVE is restored and the source impedance is adjusted.

4.2.4   Simulation Results of Parallel Resonance Overvoltage

First, the energization of the Kyndbyværket 400 / 132 kV transformer is studied. The natural frequency of the network is set to 100 Hz as adjusted in Fig. 4.54. The hysteresis characteristic of the transformer is set as Table 3-13, assuming the positive saturation point at 1.4 pu. The remanent flux is assumed in phase a (85 %) and phase b (-85 %).

Results of the time domain simulation are shown in Table 4-4. Since the inrush current highly depends on the switch timing, the switch timing is changed from 0 ms to 19 ms by 1 ms step. The highest overvoltage 469.5 kV is observed when the switch timing is 11 ms. The waveforms of the parallel resonance overvoltage and inrush current with the switch timing 11 ms are shown in Fig. 4.60 and Fig. 4.61.

The parallel resonance overvoltage in Fig. 4.60 is not very high. Even if the highest overvoltage level is continued for 10 seconds, the overvoltage is within withstand voltages of related equipment (1.60 pu for the assumed arrester). The magnitude of the inrush current in Fig. 4.61 is reasonable as the highest inrush current 4008 A is eight times larger than the rated current of the transformer (350 MVA, 505 A).

Table 4-4 Parallel Resonance Overvoltage Caused by the KYV Transformer Energization

| Switch Time	Overvoltage [kV]		
	Phase a	Phase b	Phase c
0 ms	360.4	411.7	395.0
1 ms	377.9	405.5	398.1
2 ms	394.6	391.1	397.1
3 ms	409.6	393.2	374.2
4 ms	443.8	387.0	385.2
5 ms	435.8	422.5	392.8
6 ms	420.8	427.7	400.4
7 ms	402.7	406.7	410.2
8 ms	436.8	408.4	430.1
9 ms	448.6	409.6	434.7
10 ms	438.8	423.4	459.0
11 ms	433.8	430.5	469.5
12 ms	433.1	422.0	465.8
13 ms	411.5	407.8	435.3
14 ms	401.1	424.5	421.6
15 ms	413.6	428.0	420.2
16 ms	430.9	433.7	398.8
17 ms	424.5	392.9	378.0
18 ms	418.5	400.3	373.6
19 ms	400.6	397.3	381.4
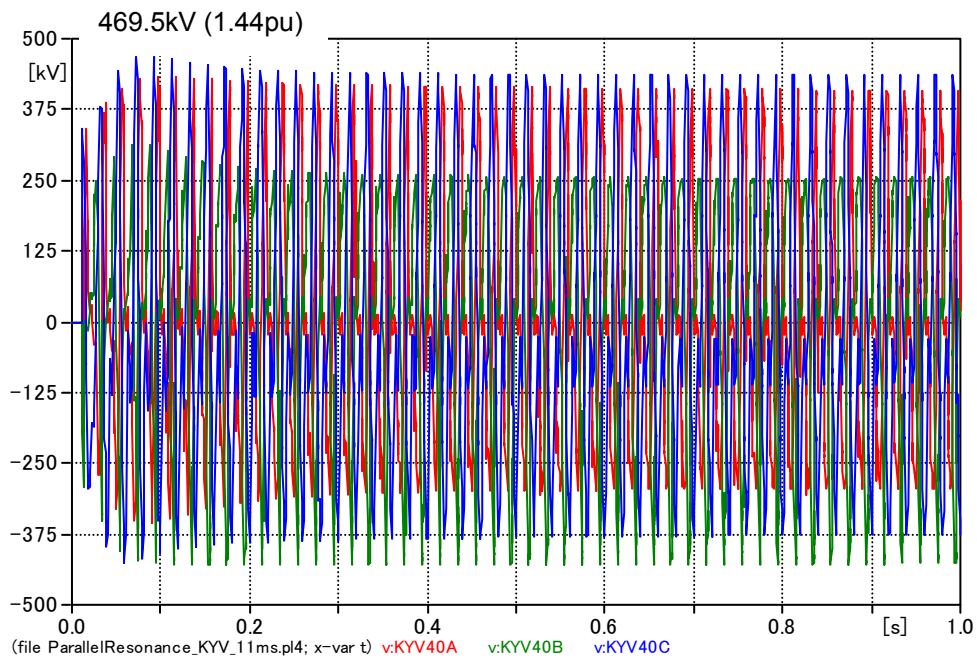
Fig. 4.60 Parallel resonance overvoltage caused by the KYV transformer energization.
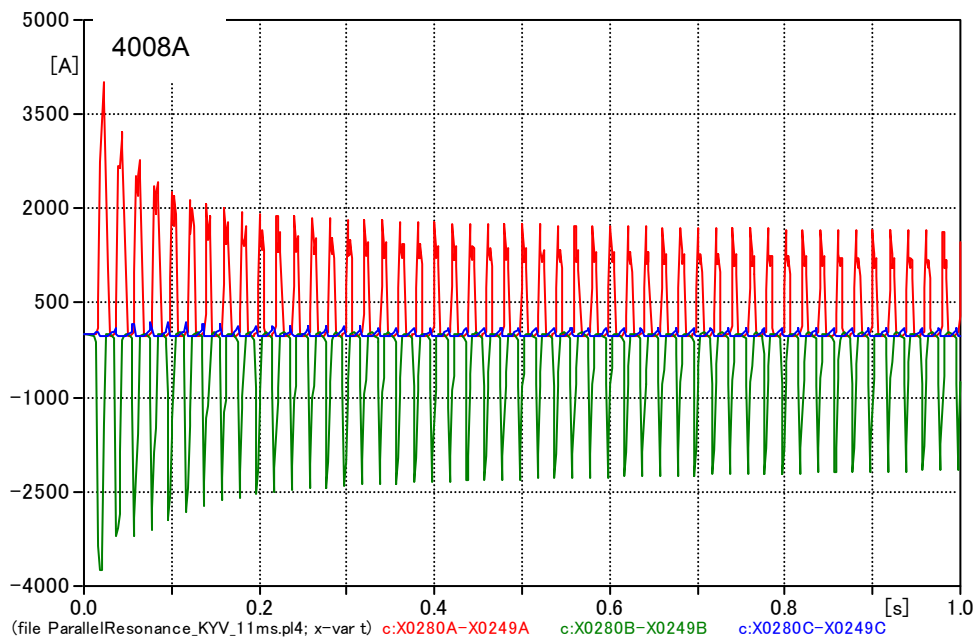
Fig. 4.61 Inrush current in the KYV transformer energization.

Second, the energization of the Asnæsværket 400 / 132 kV transformer is studied. The natural frequency of the network is set to 100 Hz as adjusted in Fig. 4.58 and Fig. 4.59. The hysteresis characteristic of the transformer is set as Table 3-13, assuming the positive saturation point at 1.4 pu. The remanent flux is assumed in phase a (85 %) and phase b (-85 %).

Results of the time domain simulation are shown in Table 4-5. Since the inrush current highly depends on the switch timing, the switch timing is changed from 0 ms to 19 ms by 1 ms step. The highest overvoltage 702.6 kV is observed when the switch timing is 14 ms. The waveforms of the parallel resonance overvoltage and inrush current with the switch timing 14 ms are shown in Fig. 4.62 and Fig. 4.63.

Table 4-5 Parallel Resonance Overvoltage Caused by the ASV Transformer Energization

| Switch Time	Overvoltage [kV]		
	Phase a	Phase b	Phase c
0 ms	567.0	386.6	559.5
1 ms	540.7	357.8	569.2
2 ms	356.8	329.2	387.5
3 ms	326.4	327.8	329.7
4 ms	332.6	330.4	350.3
5 ms	360.5	363.8	492.0
6 ms	399.5	569.2	576.5
7 ms	384.4	457.5	491.5
8 ms	347.0	498.9	435.5
9 ms	553.3	647.6	433.1
10 ms	503.2	647.6	530.4
11 ms	425.6	684.0	617.3
12 ms	632.5	653.1	473.4
13 ms	623.9	676.3	386.9
14 ms	702.6	575.5	344.4
15 ms	664.4	544.8	550.0
16 ms	699.2	419.3	597.1
17 ms	583.7	570.6	436.3
18 ms	594.4	508.1	435.9
19 ms	432.3	409.2	440.1
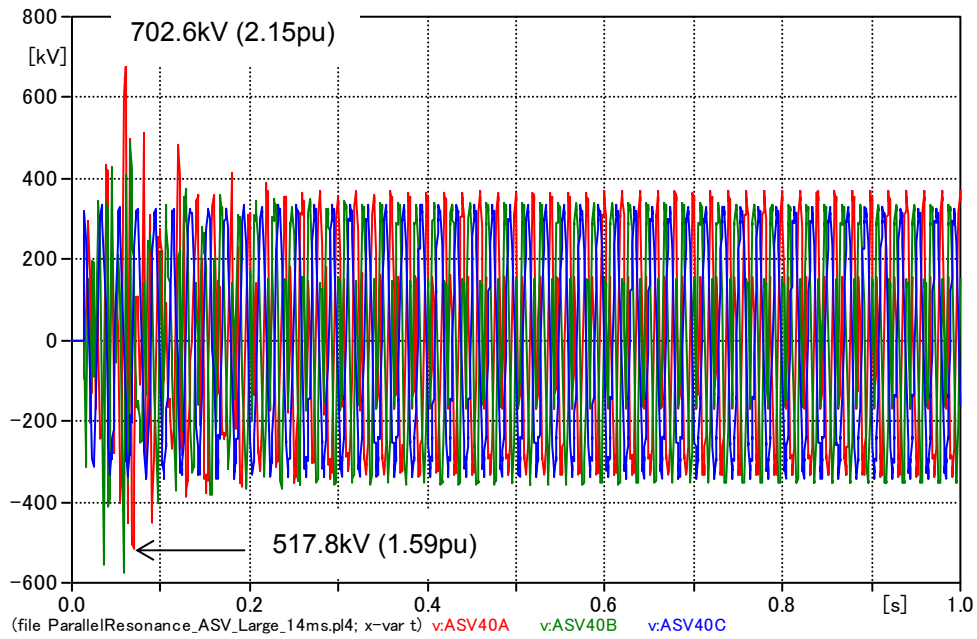
Fig. 4.62 Parallel resonance overvoltage caused by the ASV transformer energization.
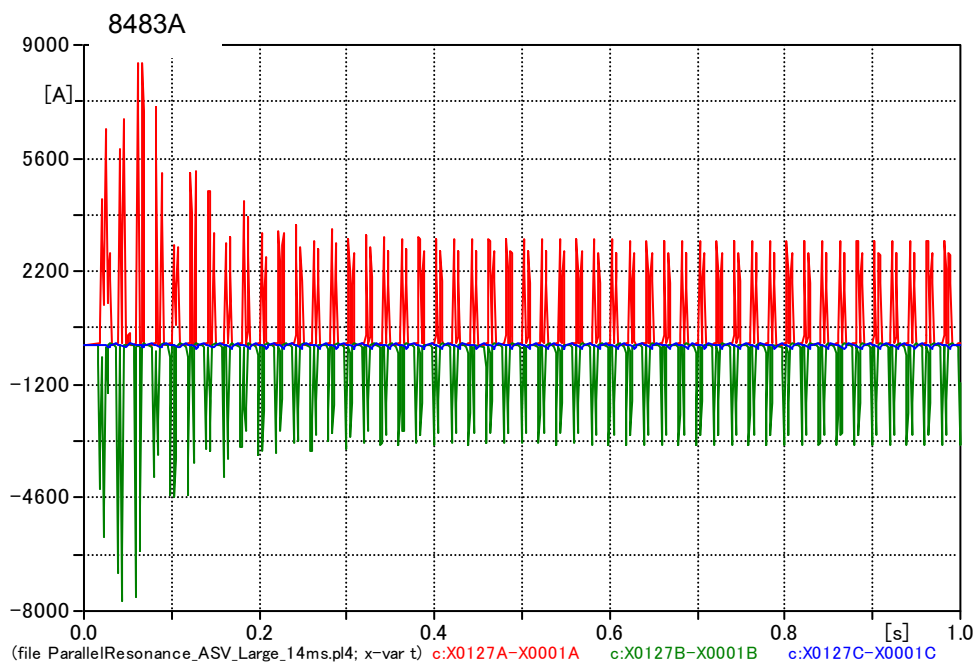
Fig. 4.63 Inrush current in the ASV transformer energization.

Even though the observed highest overvoltage 702.6 kV is very high as a temporary overvoltage, it is clear from the waveform that the overvoltage exceeding 700 kV lasts only for one impulse. It is thus reasonable to evaluate the overvoltage against the switching impulse withstand overvoltage 1050 kV and conclude the observed overvoltage is within the equipment standards. The highest overvoltage after half cycle is 518.7 kV, which is also within withstand voltages of related equipment (1.60 pu – 10 sec for the assumed arrester).

The highest inrush current 8483 A in Fig. 4.63 is too large, compared with the typical inrush current, as it is 12 times larger than the rated current of the transformer (500 MVA, 722 A).

As discussed in Section 3.5, the positive saturation point 1.4 pu is a severe assumption, which caused the large inrush current 8483 A. When the positive saturation point 1.3 pu is assumed, the highest overvoltage is lowered to 506.9 kV. The waveforms of the parallel resonance overvoltage and inrush current under this moderate assumption are shown in Fig. 4.64 and Fig. 4.65. The observed overvoltages are within withstand voltages of related equipment. The highest inrush current 5163 A is reasonable as it is seven times larger than the rated current of the transformer.
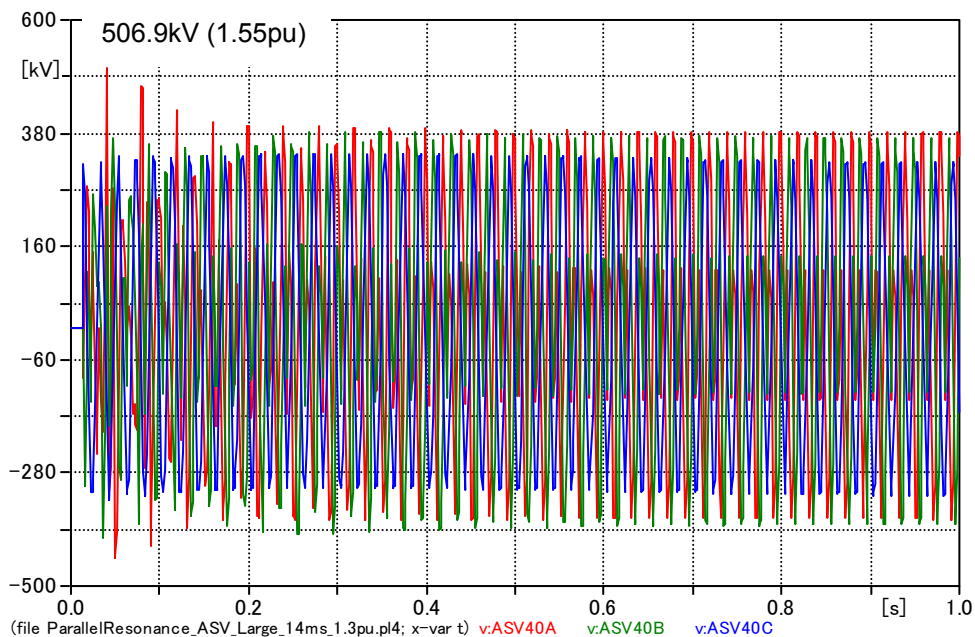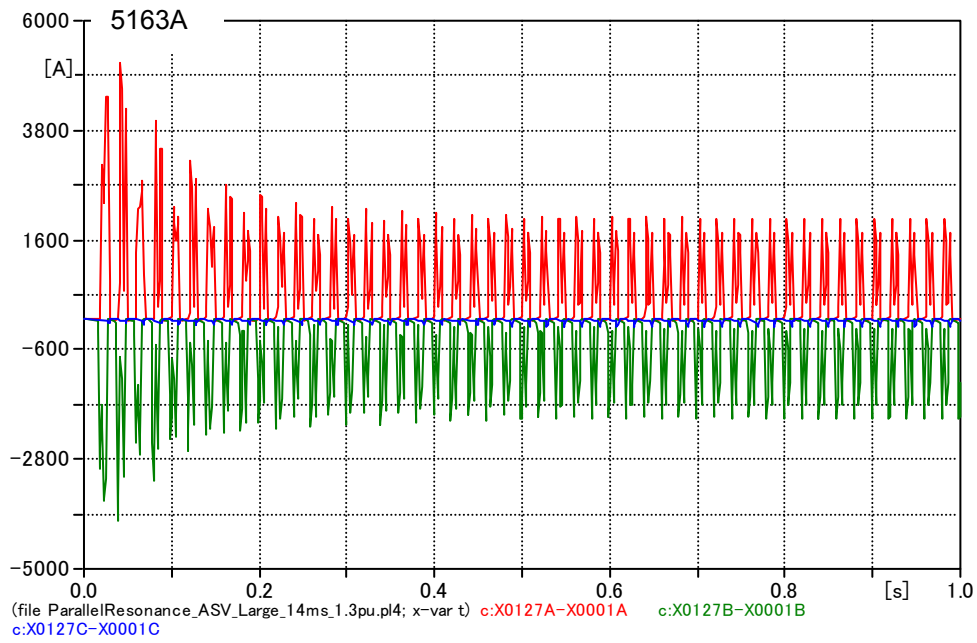

Fig. 4.64 Parallel resonance overvoltage caused by the ASV transformer energization (positive saturation point 1.3 pu).

Fig. 4.65 Inrush current in the ASV transformer energization

(positive saturation point 1.3 pu).

4.3 Overvoltage Caused by the System Islanding

4.3.1 Overview

When one end of a long cable is opened, a part of a network can be separated from the main grid together with the long cable. The equivalent circuit expressing the situation is illustrated in Fig. 4.66. Here, the assumed fault is a bus fault since a cable line fault will result in the removal of the cable line from the equivalent circuit.
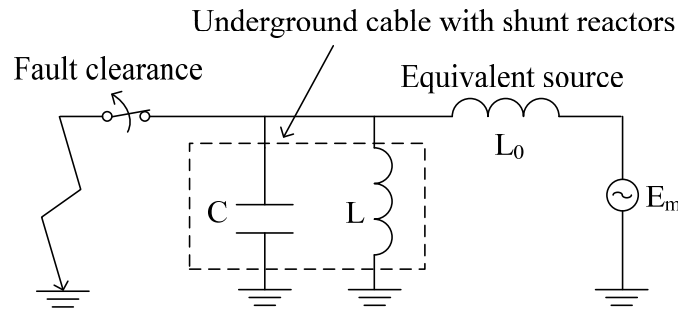

Fig. 4.66 Equivalent circuit of the system islanding.

From the above equivalent circuit, the overvoltage caused by the system islanding can be expressed by the following equations [8]:

$$v(t) = V_m \sin \omega t - \frac{\omega}{\omega_0} V_m \sin \omega_0 t \qquad \text{Eqn. 4.35}$$

$$V_m = \frac{E_m L}{L_0(1 - \omega^2 CL) + L}, \quad \omega_0 = \sqrt{\frac{1}{CL_0} + \frac{1}{CL}} \qquad \text{Eqn. 4.36}$$

where L_0 is source impedance of the weaker islanded system and E_m is the source voltage behind L_0. Charging capacity of the long cable and inductance of the shunt reactors directly connected to the cable are expressed by C and L, respectively.

Eqn. 4.35 shows that the overvoltage contains two frequency components, the nominal frequency ω and the resonance frequency ω_0. Since the overvoltage is caused by the superposition of two frequency components, the resulting overvoltage is oscillatory, and its level is often difficult to estimate before the simulation. The result of a simulation performed for the 500 kV Shin-Toyosu line is shown in Fig. 4.67 [1].
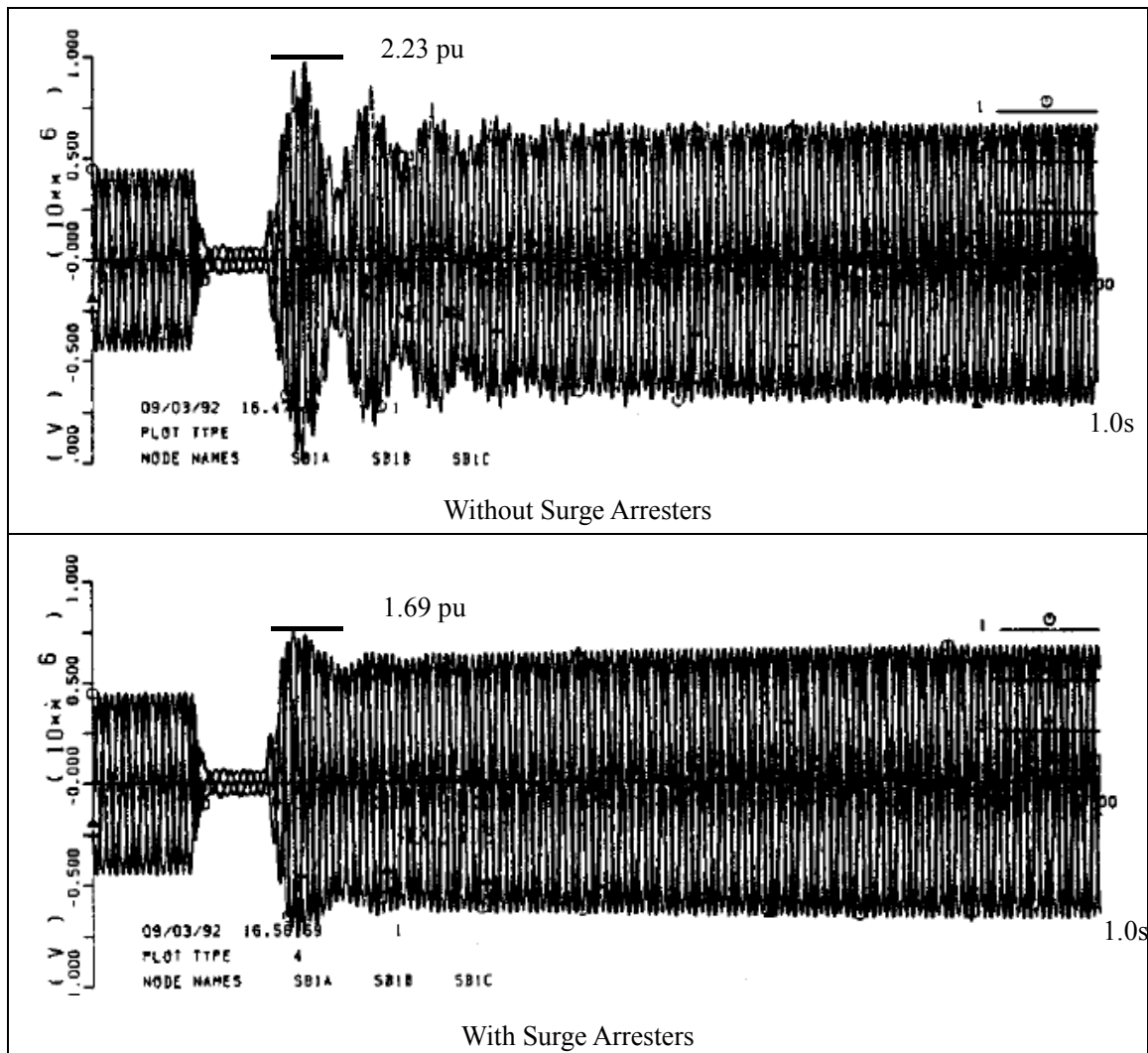
Fig. 4.67 Example of the overvoltage caused by the system islanding.

The overvoltage level is sensitive to L_0, which expresses the short circuit level in the islanded system. In order to find the most severe overvoltage, it is necessary to study different fault current levels or network conditions.

4.3.2   Study Conditions

This system islanding can easily occur when the long cable is installed in a radial network. As the Kyndbyværket – Asnæsværket line is installed as a part of the loop network, the system islanding can only occur in specific conditions. Among these specific conditions, an outage of the Hovegård – Kyndbyværket line (under 400 kV operation) is the most likely precondition in which an Asnæsværket 400 kV bus fault can lead to the system islanding. Fig. 4.68 illustrates the network

condition that leads to the system islanding. The islanded system is actually connected to the main grid through the 132 kV system, but the connection to the main grid is weak enough to cause the oscillatory overvoltage. The system islanding actually occurs in simulations as the simulation model in PSCAD does not include the connection in the 132 kV system. In this point, the study condition is more severe than the actual system.
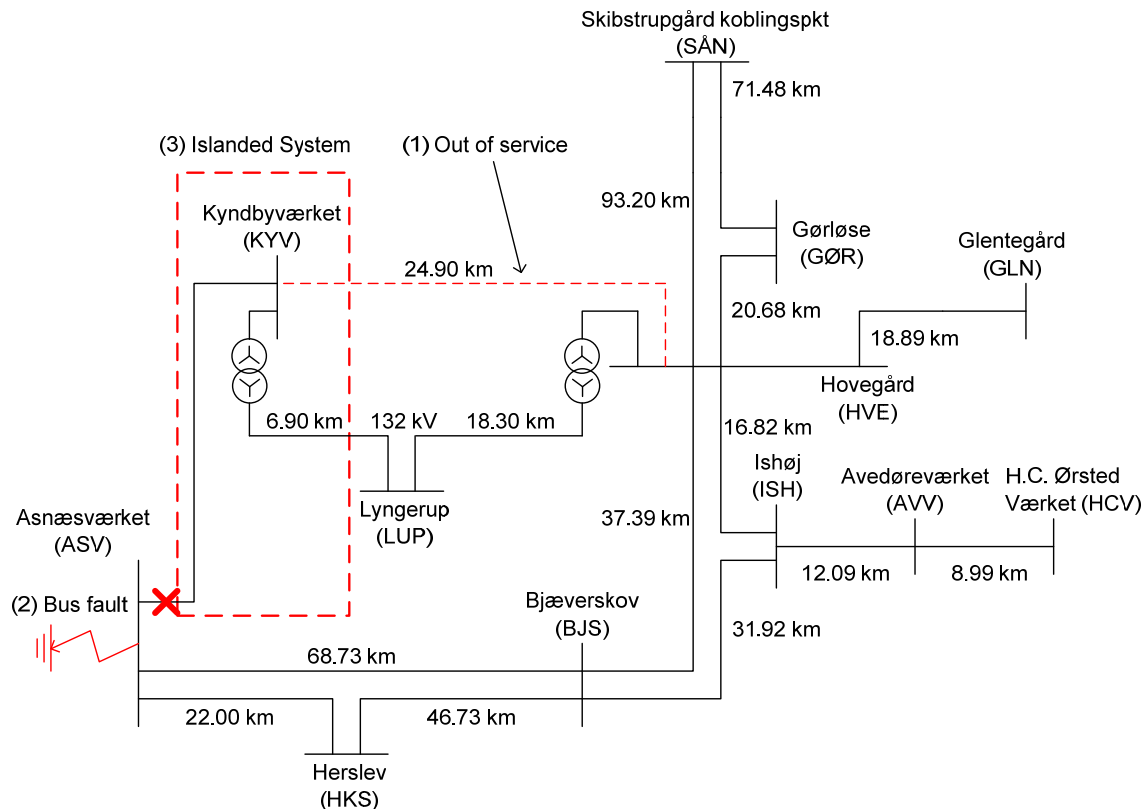

Fig. 4.68 ASV 400 kV bus fault and the system islanding.

Generators in the Kyndbyværket 132 kV network need to be modeled in order for the islanded system to experience the oscillatory overvoltage. A dummy generator was connected to the Kyndbyværket 132 kV bus through the source impedance whose value L_0 was considered as a parameter in order to study different fault current levels. Table 4-6 shows the fault current levels and their associated values of the source impedance considered in the analysis. Since there are no other generators in the islanded system, the calculation of the source impedance is straightforward. The maximum fault current level was set to 40 kA since the typical breaking capability of the 132 kV breakers in the Danish network was 40 kA.

Table 4-6 Source Impedances of the KYV 132 kV Dummy Generator

Fault current level at the KYV 132 kV bus [kA]	5	10	20	30	40
Source impedance of the dummy generator [mH]	48.5	24.3	12.1	8.09	6.06

Now, we consider study conditions where the Kyndbyværket 400 kV bus fault results in the system islanding. As the 400 kV transmission lines from Asnæsværket to Hovegård via Bjæverskov are all double circuit lines, the Kyndbyværket 400 kV bus fault will not lead to the system islanding in normal or N-1 preconditions. When we consider an outage of the Asnæsværket – Herslev line, however, the Kyndbyværket – Asnæsværket line is only weakly connected to the main grid via Bjæverskov in case of the Kyndbyværket 400 kV bus fault. As the Asnæsværket 400 kV bus is approximately 69 km away from Bjæverskov, the oscillatory overvoltage may occur depending on the fault current level at Asnæsværket. Fig. 4.69 shows the network condition which may lead to the oscillatory overvoltage.
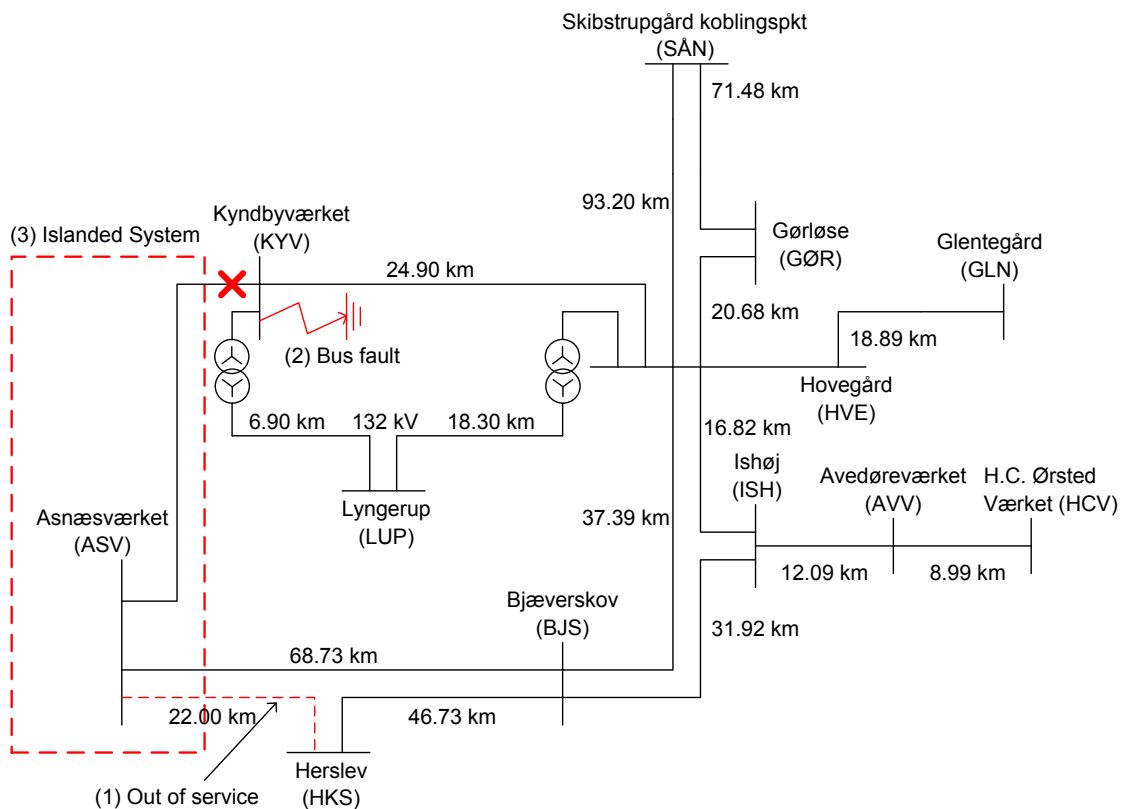

Fig. 4.69 KYV 400 kV bus fault and the system islanding.

Different fault current levels were considered also for the Kyndbyværket 400 kV bus fault. Based on the off-peak load condition, the fault current level at the Asnæsværket 132 kV bus was adjusted to 10, 20, 30, and 40 kA by adding a dummy generator to the Asnæsværket 132 kV bus. As the fault current level at the Asnæsværket 132 kV bus is 8.70 kA in the off-peak load condition, the remaining fault current has to be fed from the dummy generator.

Table 4-7 Source Impedances of the ASV 132 kV Dummy Generator

Fault current level at the ASV 132 kV bus [kA]	10	20	30	40
Fault current fed from the dummy generator [kA]	1.30	11.3	21.3	31.3
Source impedance of the dummy generator [mH]	186	21.5	11.4	7.75

Table 4-8 summarizes the study conditions for the overvoltage caused by the system islanding. The fault in the Torslunde 400 kV bus was additionally studied assuming there is a switching station at Torslunde. As for the fault type, only the three phase fault was considered as it was the most severe fault with respect to the overvoltage caused by the system islanding.

We can see which conditions can theoretically affect the overvoltage from Eqn. 4.35. While the charging capacity of the Kyndbyværket – Asnæsværket line cannot be changed, two other conditions, the source impedance L_0 and the shunt reactors L can be changed as the study condition. According to the conclusion of Chapter 2, one unit of 300 MVar shunt reactor needs to be connected to both sides of the Kyndbyværket – Asnæsværket line in Pattern 1. In this case, L takes a fixed value. When two units of 150 MVar shunt reactors are connected to both sides as in Pattern 1', one of the four shunt reactors can be taken out of service, which lowers the compensation rate to 75.5 %. This condition was studied as a more severe assumption.

Table 4-8 Study Conditions for the Overvoltage Caused by the System Islanding

Fault location	ASV, KYV, TOR 400 kV buses
Fault type	Three phase fault (no fault resistance)
Fault current level	(5,) 10, 20, 30, 40 kA at the ASV or KYV 132 kV bus
Shunt compensation	All shunt reactors in service (100.7 %) One 150 MVar shunt reactor out of service (75.5 %)

4.3.3   ASV 400 kV Bus Fault

4.3.3.1   All Shunt Reactors in Service

First, the simulations were performed with all reactors in service. Fig. 4.70 shows the overvoltage caused by the system islanding with the fault current level of 5 kA at the Kyndbyværket 132 kV bus. The highest overvoltage 744.6 kV was observed at the open-end of the cable in phase c.
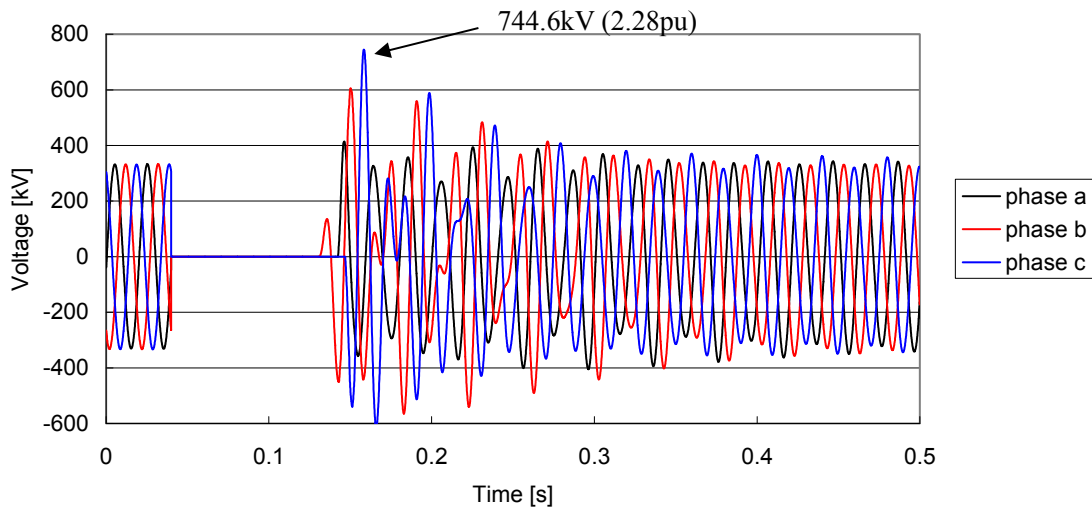

Fig. 4.70 Overvoltage caused by the ASV bus fault leading to the system islanding (all shunt reactors in service, fault current level: 5kA).

From the waveform of the overvoltage, it is clear that the resonant frequency is superimposed on the nominal frequency. The resonant frequency can be found by the Fourier transform of the waveform. Fig. 4.71 shows frequency components contained in the overvoltage. The resonant frequency of 75 Hz was found from the Fourier transform of the waveform of the overvoltage.
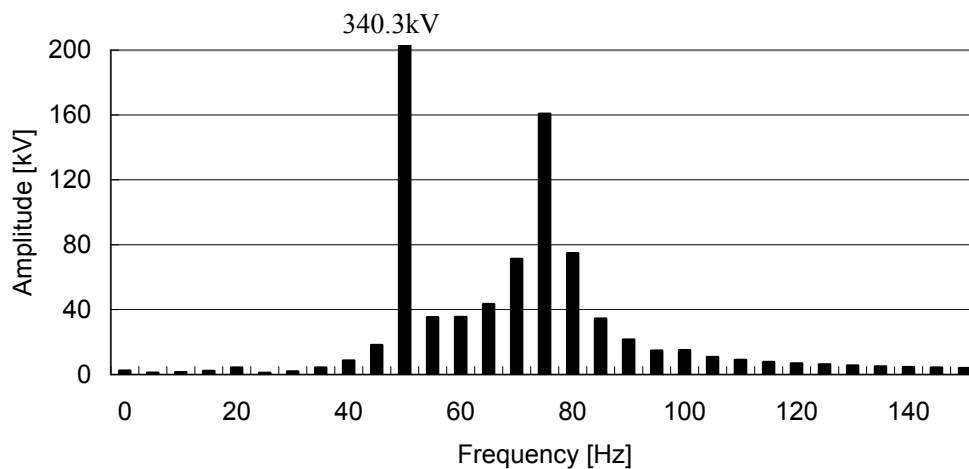

Fig. 4.71 Frequency components contained in the overvoltage caused by the ASV bus fault leading to the system islanding (all shunt reactors in service, fault current level: 5kA).

Here the resonant frequency can also be derived theoretically from Eqn. 4.35. The theoretical derivation gives the resonant frequency 76.6 Hz, which is close enough to the one derived from simulation results.

The overvoltage when the fault current level is increased to 10, 20, 30, and 40 kA is shown in Fig. 4.72 to Fig. 4.75.

Fig. 4.72 Overvoltage caused by the ASV bus fault leading to the system islanding (all shunt reactors in service, fault current level: 10kA).

Fig. 4.73 Overvoltage caused by the ASV bus fault leading to the system islanding (all shunt reactors in service, fault current level: 20kA).
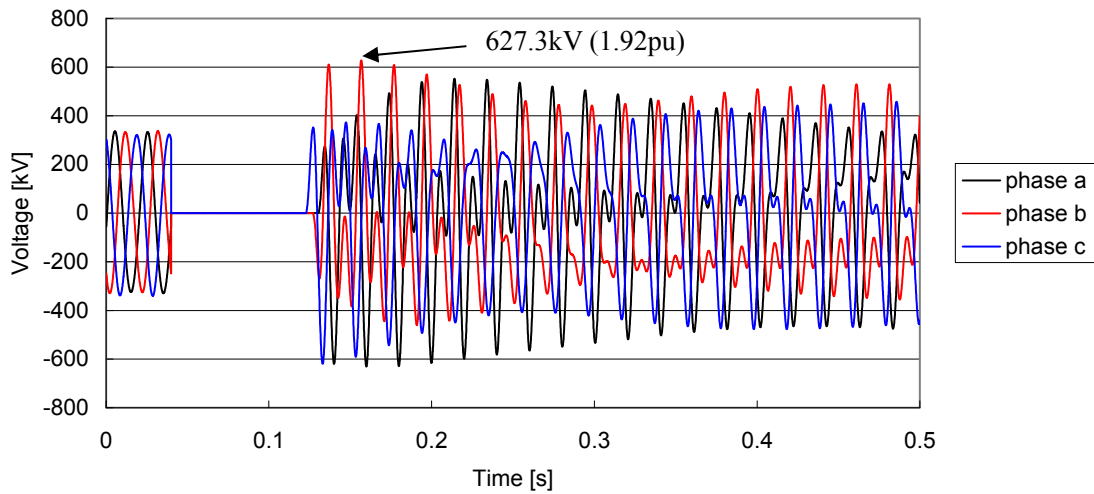
Fig. 4.74 Overvoltage caused by the ASV bus fault leading to the system islanding (all shunt reactors in service, fault current level: 30kA).
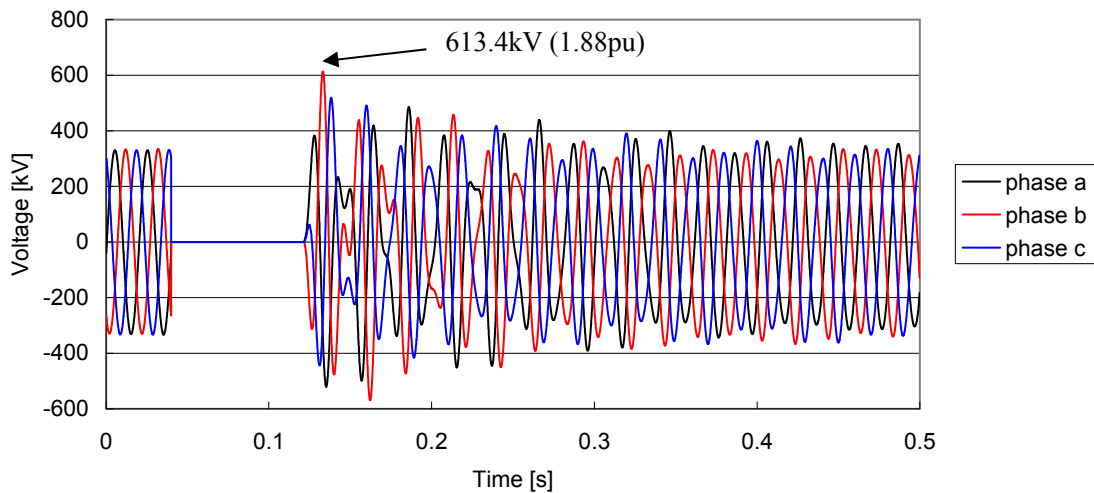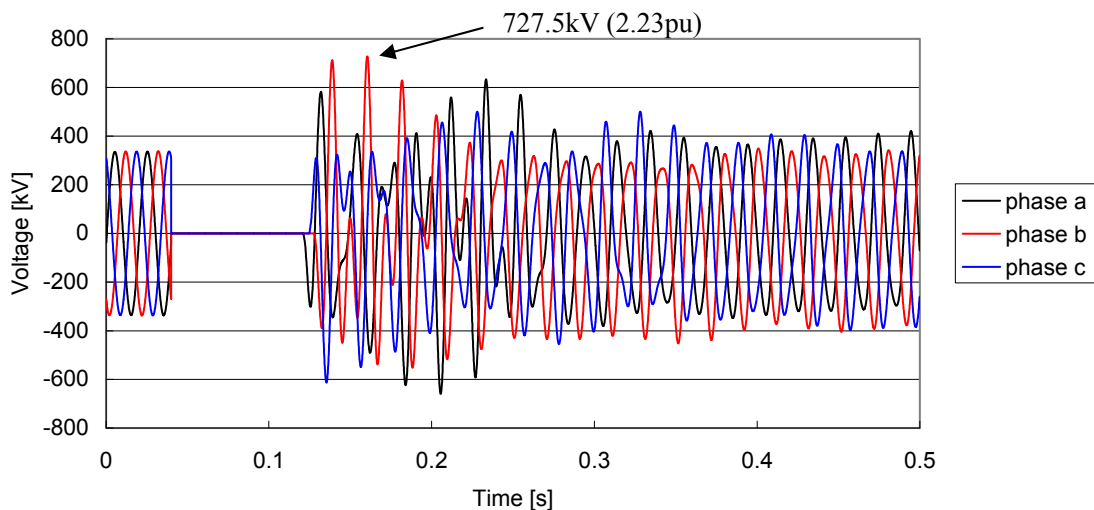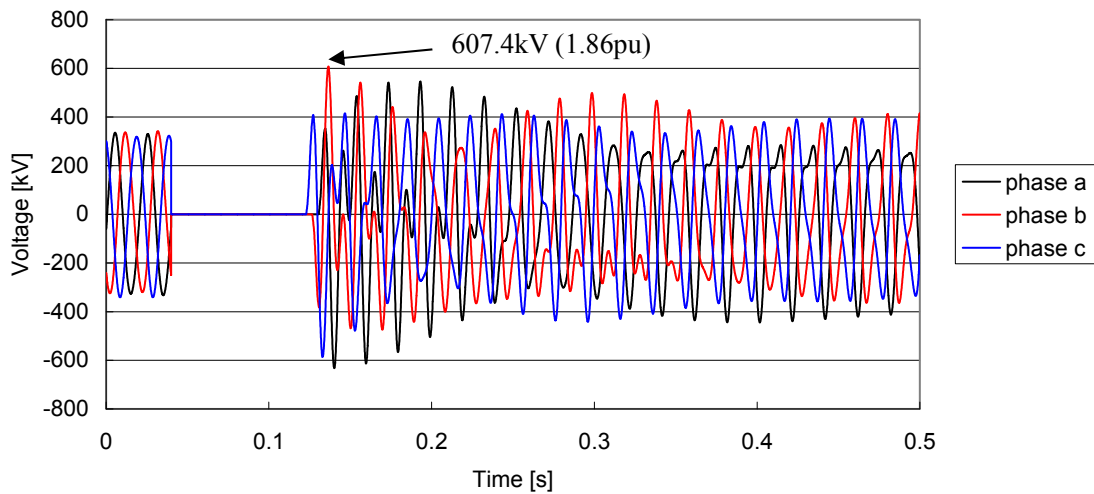

Fig. 4.75 Overvoltage caused by the ASV bus fault leading to the system islanding (all shunt reactors in service, fault current level: 40kA).

Fig. 4.76 shows the comparison of resonant frequencies derived from the theoretical formula and simulation results. The resonant frequencies derived from simulation results match closely to those derived from the theoretical formula. The deviation of 2.5 Hz can be considered as a round-off error as the Fourier transform identifies the resonant frequency with a 2.5 Hz step. This demonstrates that overvoltages as expected from Eqn. 4.35 are produced in the simulations.
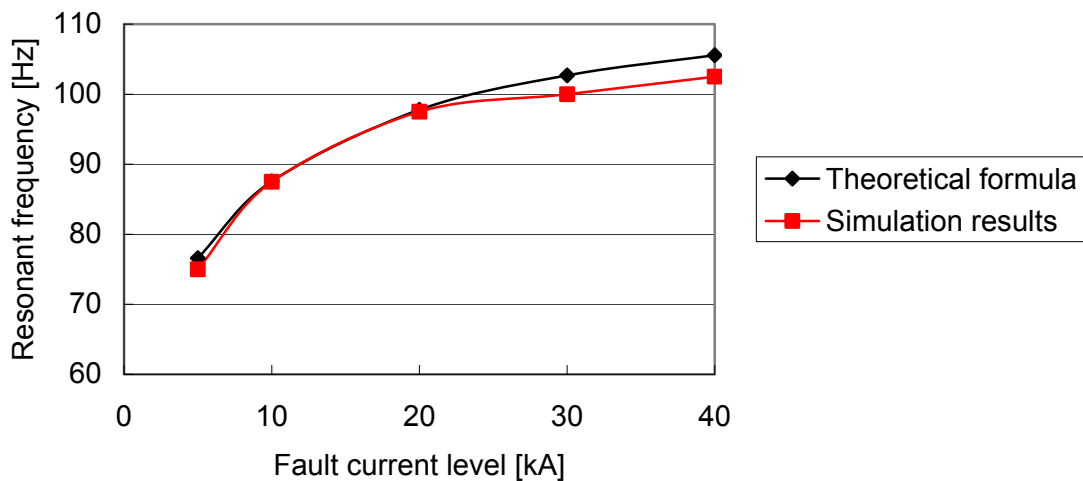
Fig. 4.76 Resonant frequencies derived from theoretical formula and simulation results.

Comparing the waveforms of the overvoltages, the most severe overvoltage was caused when the fault current level was set to 5 kA or 20 kA. The initial overvoltage level is slightly higher with the fault current level of 5 kA, but the sustained overvoltage with the frequency around 1 Hz can be observed with the fault current level of 20 kA.

The simulations were, so far, performed without surge arrester. Here, the overvoltage with the fault current level of 20 kA was evaluated against the ratings of the modeled surge arrester.

Fig. 4.77 shows the overvoltage with one surge arrester connected to the open-end of the cable when the fault current level was set to 20 kA. The highest overvoltage was lowered by the surge arrester. The low frequency oscillation (1 Hz) is not damped within 1 s, but the overvoltage level is lowered to 400 kV (1.22 pu) within 0.4 s. Considering the power frequency withstand voltage (1 min) 1.58 pu of the modelled surge arrester, it can endure the overvoltage shown in Fig. 4.77.

Fig. 4.77 Overvoltage caused by the ASV bus fault leading to the system islanding with an arrester (all shunt reactors in service, fault current level: 20kA).

Fig. 4.78 shows the energy absorbed by the surge arrester in the overvoltage. The energy absorbed by the surge arrester is within the energy absorption capability 9.5 MJ of the modeled surge arrester.
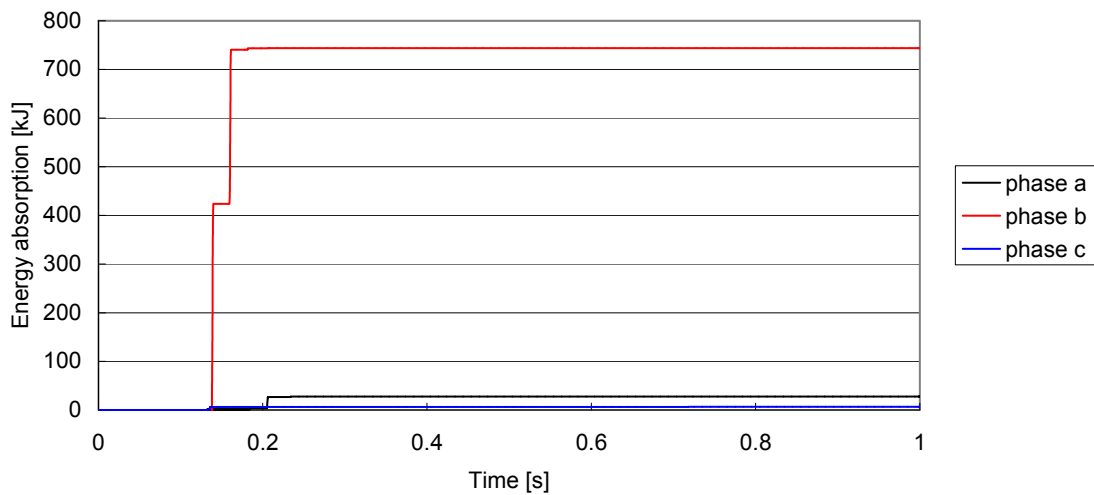
Fig. 4.78 Energy absorption by an arrester in the islanding overvoltage (all shunt reactors in service, fault current level: 20kA).

4.3.3.2 Effects of One Shunt Reactor out of Service

This section discusses the overvoltage with one 150 MVar shunt reactor out of service. As the overvoltage is highest at the open-end of the cable, it is most severe to take one shunt reactor at Asnæsværket out of service.

Fig. 4.79 to Fig. 4.83 show the overvoltages caused by the system islanding with the fault current levels of 5 to 40 kA. The overvoltage level becomes higher due to the lower compensation rate. The sustained overvoltage is observed due to the surplus reactive power supply in the islanded system.
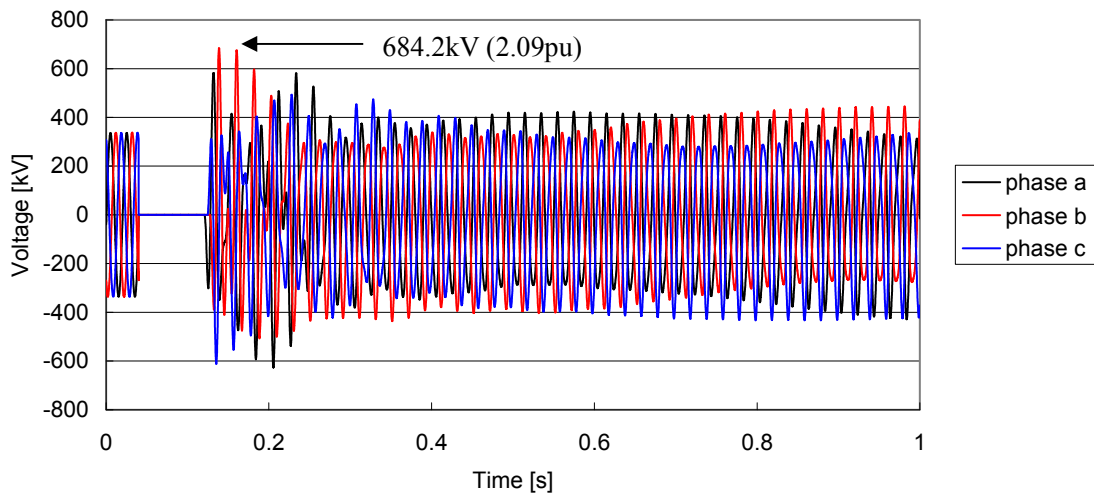

Fig. 4.79 Overvoltage caused by the ASV bus fault leading to the system islanding (one shunt reactors out of service, fault current level: 5kA).
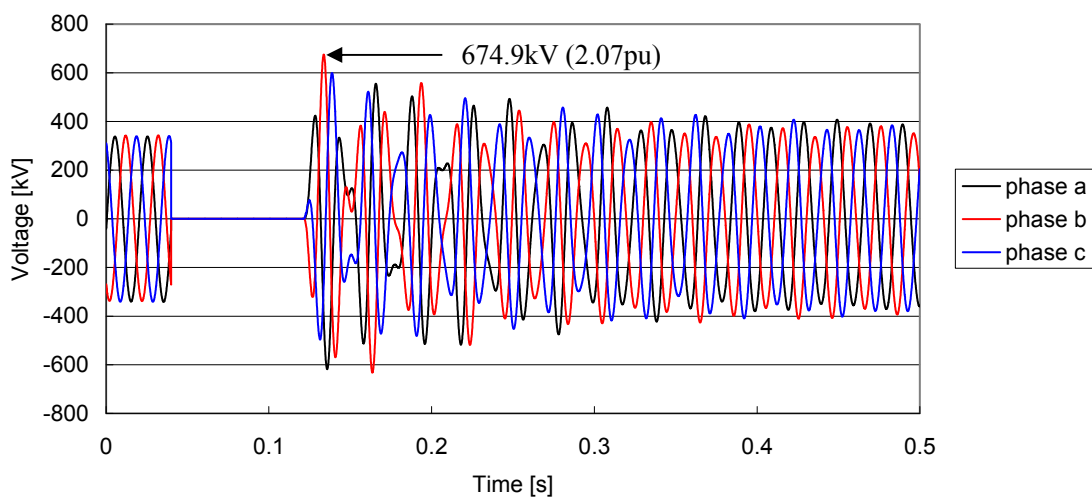
Fig. 4.80 Overvoltage caused by the ASV bus fault leading to the system islanding (one shunt reactors out of service, fault current level: 10kA).
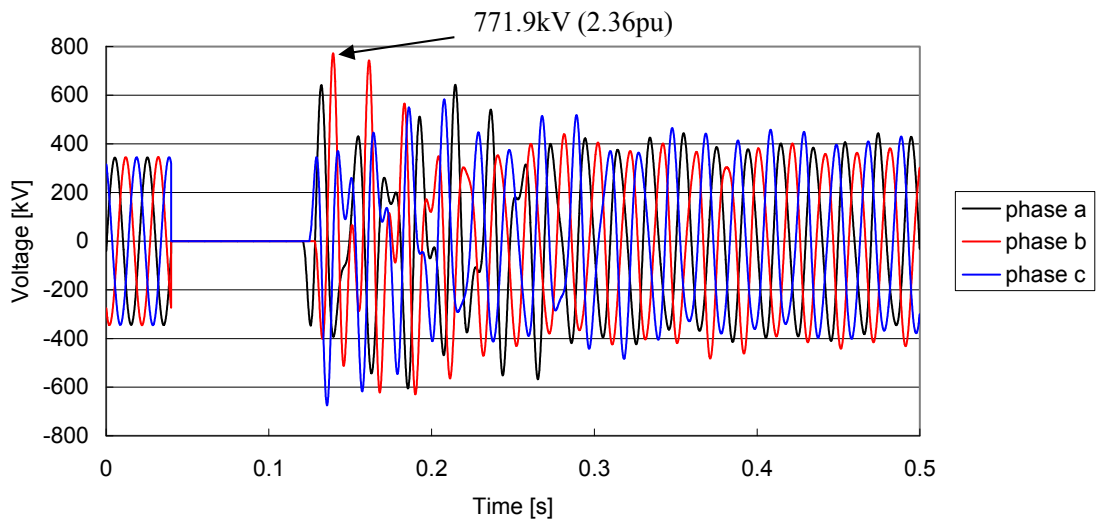
Fig. 4.81 Overvoltage caused by the ASV bus fault leading to the system islanding (one shunt reactors out of service, fault current level: 20kA).
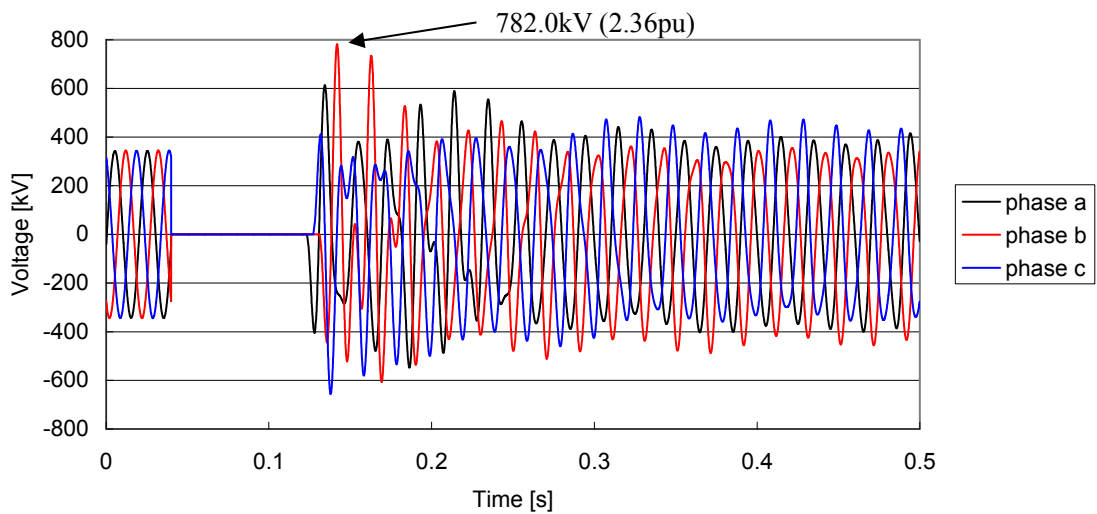
Fig. 4.82 Overvoltage caused by the ASV bus fault leading to the system islanding (one shunt reactors out of service, fault current level: 30kA).
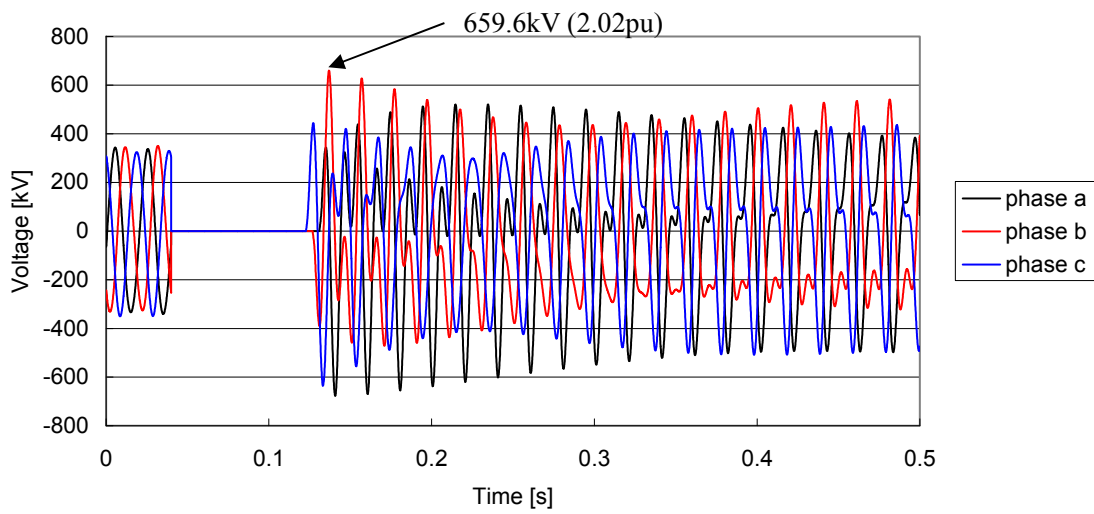
Fig. 4.83 Overvoltage caused by the ASV bus fault leading to the system islanding (one shunt reactors out of service, fault current level: 40kA).

Fig. 4.84 shows the comparison of resonant frequencies derived from the theoretical formula and simulation results. The resonant frequencies derived from simulation results match closely to those derived from the theoretical formula, as in the cases with all shunt reactors in service.
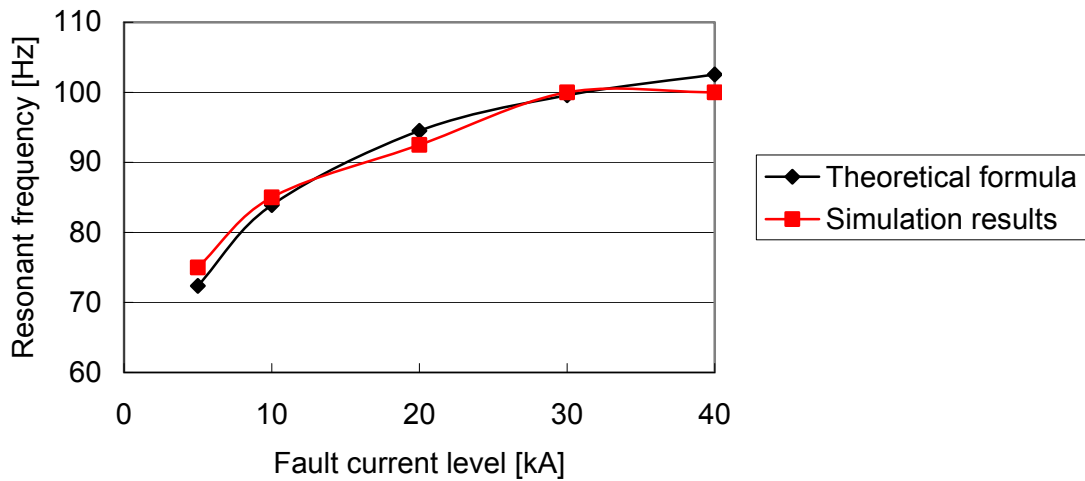
Fig. 4.84 Resonant frequencies derived from theoretical formula and simulation results (one shunt reactor out of service).

Comparing the waveforms of the overvoltages, the most severe overvoltage was caused when the fault current level was set to 5 kA or 40 kA. The initial overvoltage level is significantly higher with the fault current level of 5 kA, but the sustained overvoltage with the frequency around 1 Hz can be observed with the fault current level of 40 kA.

Here, the overvoltage with the fault current level of 5 kA was evaluated against the ratings of a surge arrester. Fig. 4.85 shows the overvoltage with one surge arrester connected to the open-end of the cable. The overvoltage level is lowered to 400 kV (1.22 pu) within 0.4 s. Considering the power frequency withstand voltage (1 min) 1.58 pu of the modelled surge arrester, it can endure the overvoltage shown in Fig. 4.85.
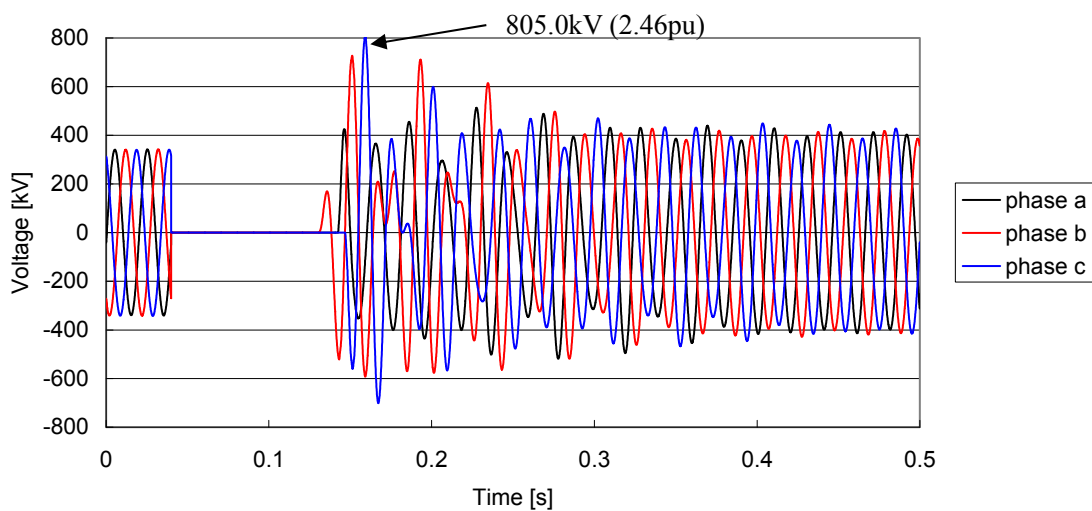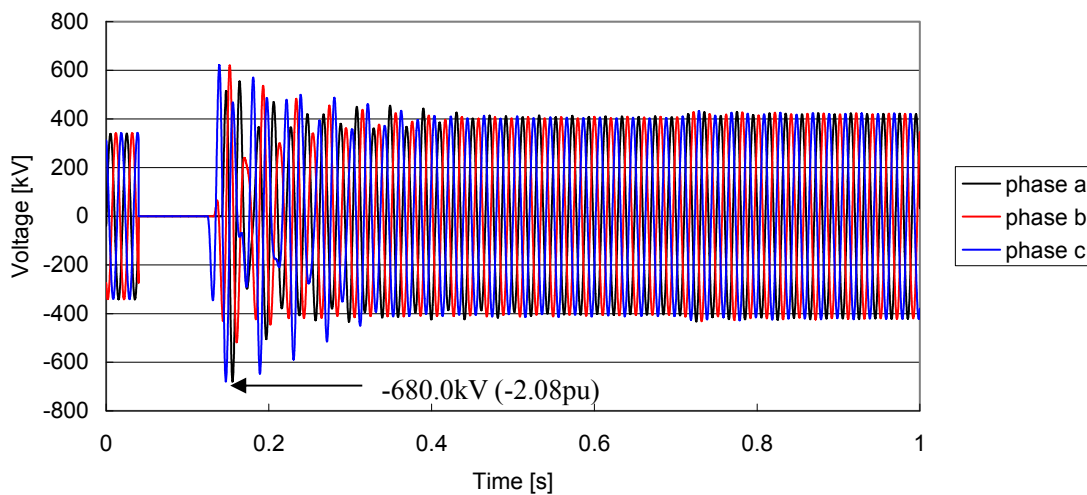

Fig. 4.85 Overvoltage caused by the ASV bus fault leading to the system islanding with an arrester (one shunt reactor out of service, fault current level: 5kA).

Fig. 4.86 shows the energy absorbed by the surge arrester in the overvoltage. The energy absorbed by the surge arrester is within the energy absorption capability 9.5 MJ of the modeled surge arrester.
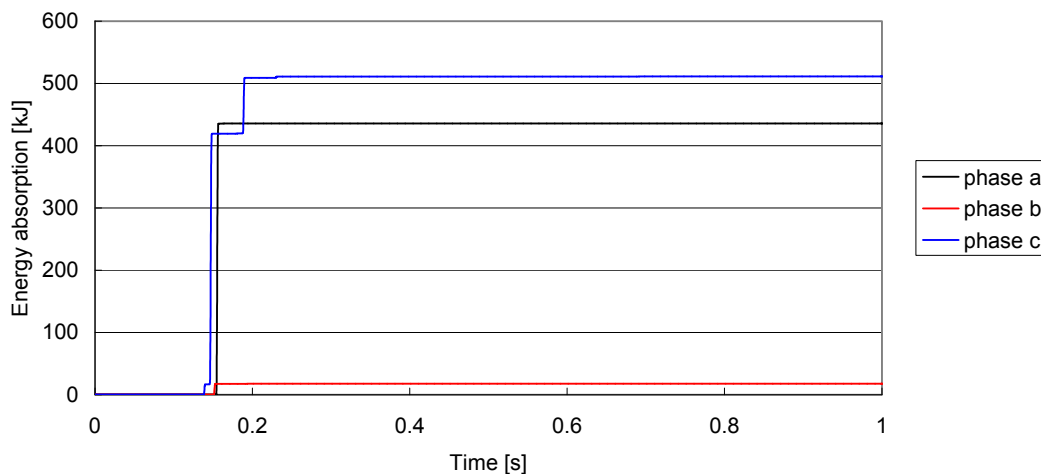
Fig. 4.86 Energy absorption by an arrester in the islanding overvoltage (one shunt reactor out of service, fault current level: 5kA).

Finally, the highest overvoltages caused by the system islanding due to the Asnæsværket 400 kV bus fault is summarized in Table 4-9. Values in red ink show the results with one surge arrester modeled at the open-end of the cable.

Table 4-9 Highest Overvoltages Caused by the System Islanding due to the ASV 400 kV Bus Fault

Fault current level	All shunt reactors in service	One shunt reactor out of service
5kA	744.6 kV (2.28 pu)	805.0 kV (2.46 pu) 680.0 kV (2.08 pu)
10kA	613.4 kV (1.88 pu)	674.9 kV (2.07 pu)
20kA	727.5 kV (2.23 pu) 684.2 kV (2.09 pu)	771.9 kV (2.36 pu)
30kA	627.3 kV (1.92 pu)	782.0 kV (2.36 pu)
40kA	607.4 kV (1.86 pu)	659.6 kV (2.02 pu)

4.3.3.3   Effects of Timing for Fault Clearing

This section studies the effects of the timing for the fault clearing. The fault clearing always occurs at current zero, but by changing the timing, it is possible to change the order of three phases.

In this analysis, it was assumed that all shunt reactors were in service. The fault current level at the Kyndbyværket 132 kV bus was set to 20 kA since the most severe overvoltage was observed with

this condition.

When the fault current level was 20 kA, the fault clearing occurs in the order of phase a, c, and b in Section 4.3.3.1. By delaying the fault clearing timing, the order can be changed to phase c, b, and a. Further delay can result in the order of phase b, a, and c. The magnitude of the highest overvoltages is highly affected by the phase angle of the voltage source when the fault is cleared. It is expected that the highest overvoltages are observed in different phases by changing the fault clearing timing.

Table 4-10 summarizes the highest overvoltages and the phases in which the highest overvoltages are observed. As expected, they are affected by the fault clearing timing. The highest overvoltages are observed in the last phase in the order of the fault clearing. The magnitude of the highest overvoltages becomes low for the last order of the fault clearing.

Table 4-10 Highest Overvoltages Caused by the System Islanding with Different Fault Clearing Timings

Order of the fault clearing	Highest overvoltages	Phase in which highest overvoltages are observed
Phase a→c→b	727.5 kV (2.23 pu)	Phase b
Phase c→b→a	726.3 kV (2.22 pu)	Phase a
Phase b→a→c	670.7 kV (2.05 pu)	Phase c

Fig. 4.87 shows the waveforms of the overvoltages with different fault clearing timings. The similarity of the waveforms suggests that the frequency components contained in the overvoltages do not change with the fault clearing timing. In addition, it is clear that the fault clearing timing does not have a noticeable effect on the damping characteristic of the overvoltages. These characteristics of the overvoltages are mainly determined by the fault current level, charging capacity, and the compensation rate of the cable line, and are not affected by the fault clearing timing.
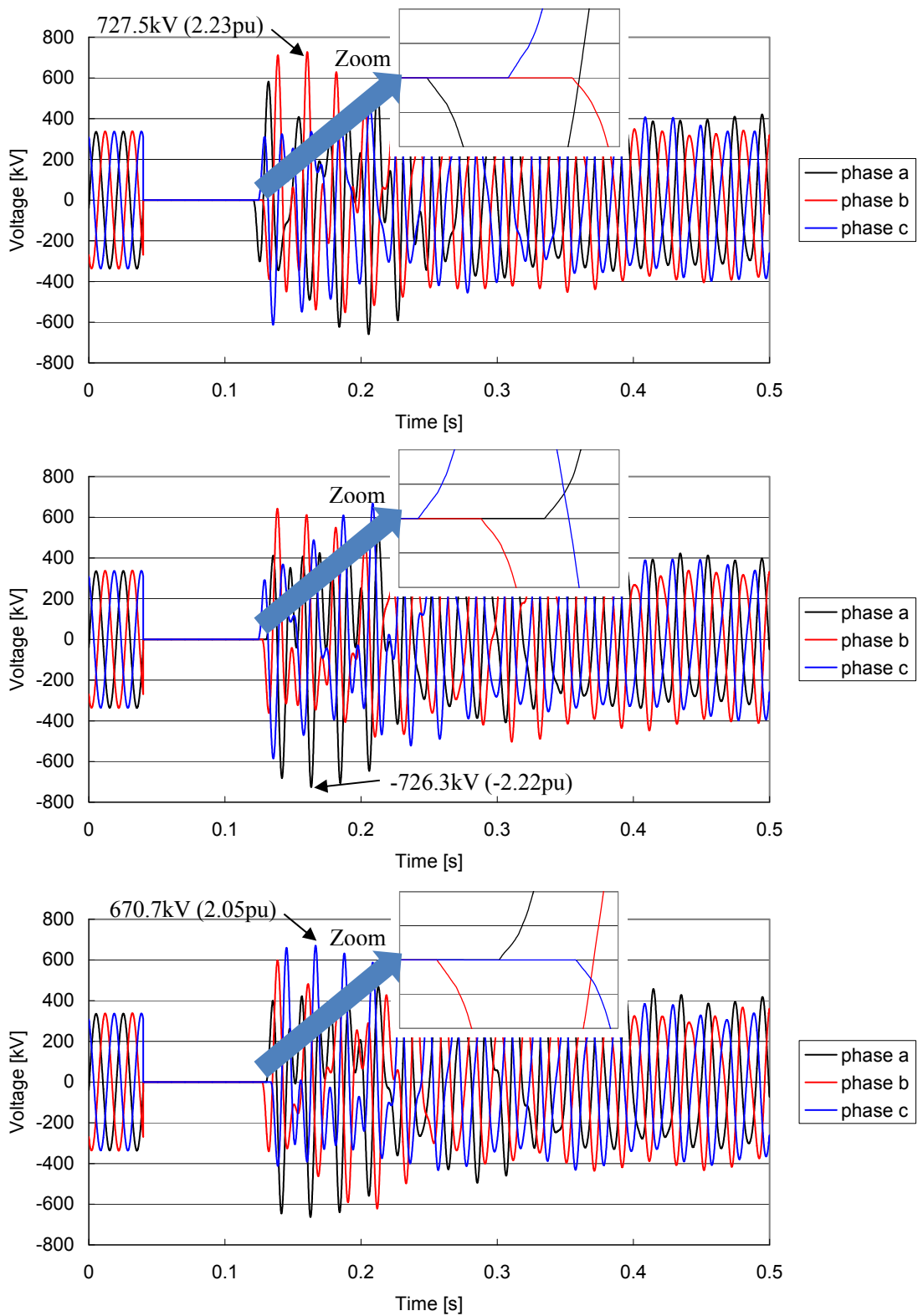
Fig. 4.87 Overvoltage caused by the system islanding with different fault clearing timings (top: phase c→b→a, middle: phase b→a→c, bottom: phase a→c→b).

4.3.4   KYV 400 kV Bus Fault

As mentioned in Section 4.3.2, an outage of the Asnæsværket – Herslev line is considered as the precondition. When the Kyndbyværket 400 kV bus fault occurs, the Asnæsværket 400 kV bus is weakly connected to the main grid via Bjæverskov, which may lead to the oscillatory overvoltage.

Fig. 4.88 shows the overvoltages caused by the system islanding with the fault current level of 10 kA. It has been confirmed that the oscillatory overvoltage does not occur with the fault current levels of 10, 20, 30, 40 kA. The Asnæsværket 400 kV bus is weakly connected to the main grid, but it is enough to damp the oscillatory overvoltage to a harmless level.
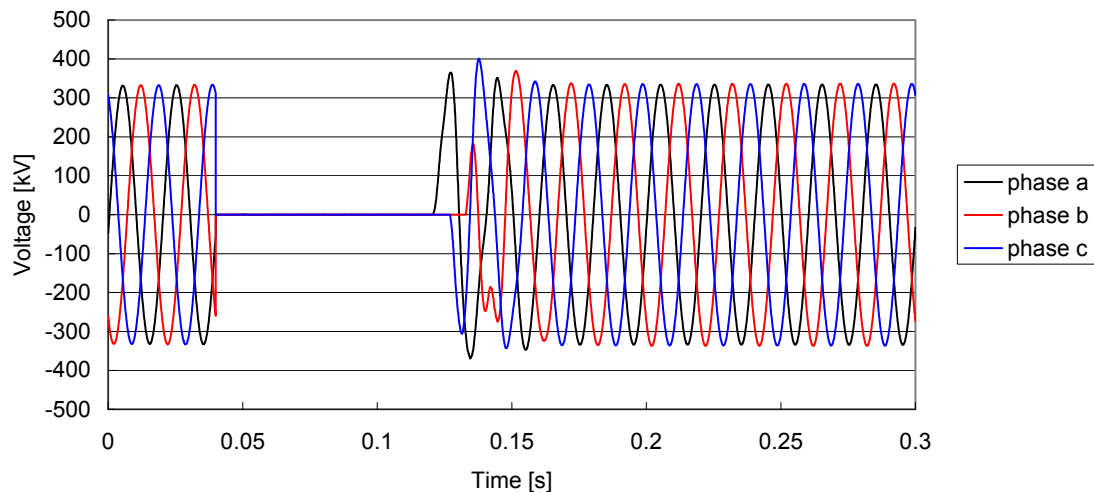
Fig. 4.88 Overvoltage caused by the KYV bus fault leading to the system islanding (all shunt reactors in service, fault current level: 10kA).

4.3.5   TOR 400 kV Bus Fault

The fault in the Torslunde 400 kV bus was additionally studied assuming there is a switching station at Torslunde. Compared with the Asnæsværket 400 kV bus fault without the switching station, the shunt reactors *L* in Eqn. 4.35 becomes twice larger and the charging capacity *C* becomes half, which affects the overvoltage.
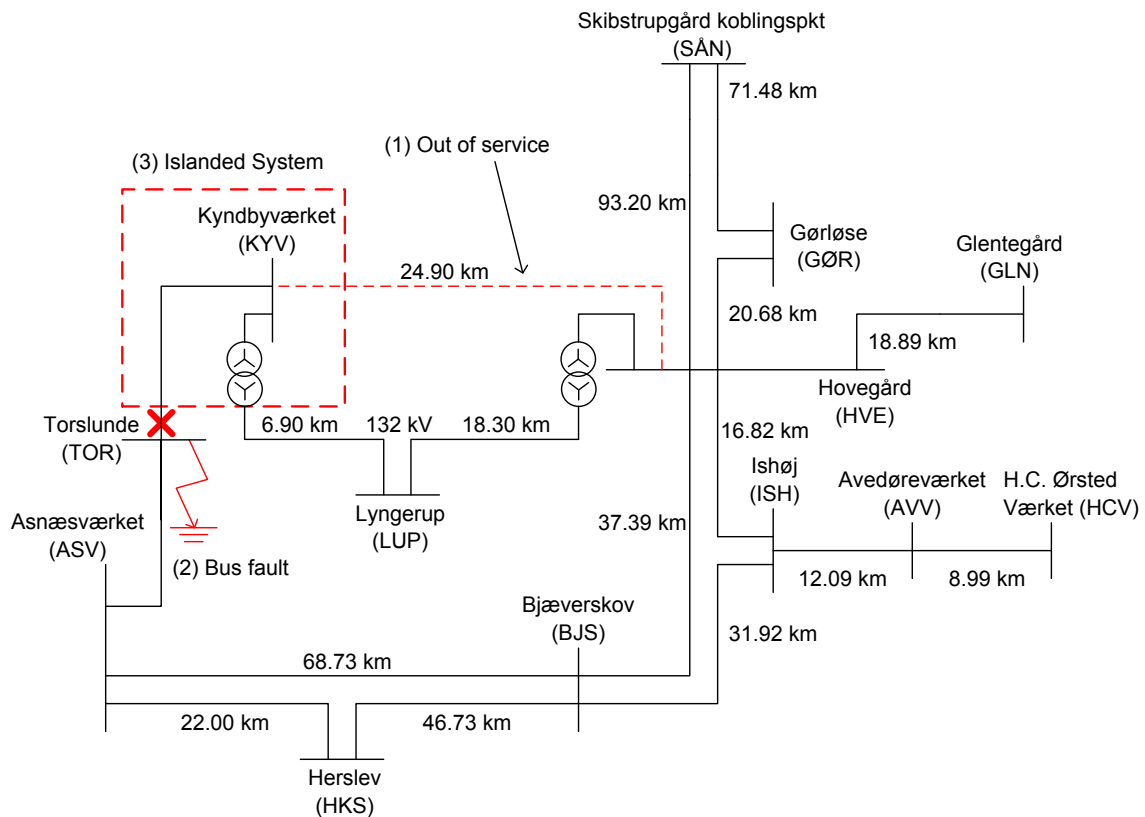
Fig. 4.89 TOR 400 kV bus fault and the system islanding.

Fig. 4.90 to Fig. 4.94 show the overvoltages caused by the system islanding with the fault current levels of 5 to 40 kA. The overvoltage becomes lower compared with the Asnæsværket 400 kV bus fault without the Torslunde switching station.
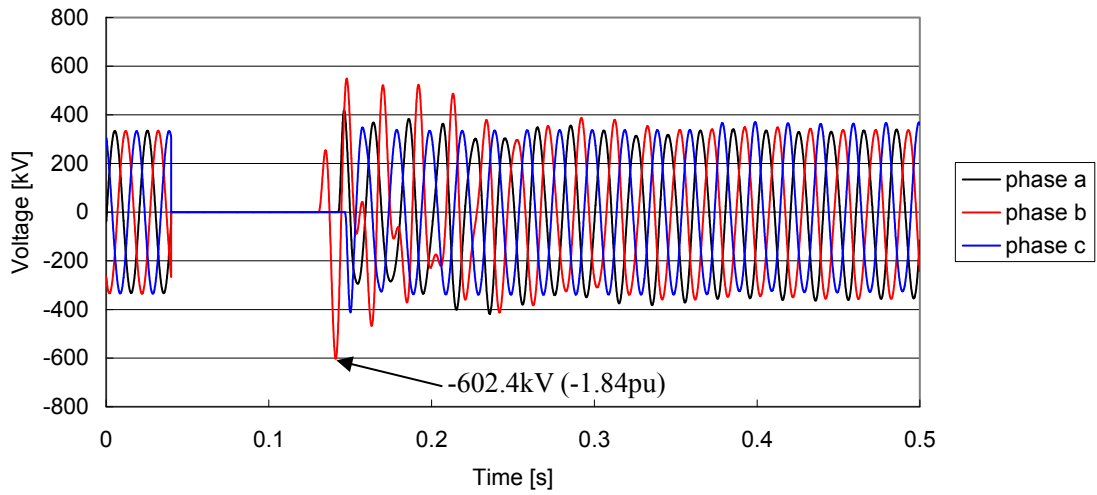
Fig. 4.90 Overvoltage caused by the TOR bus fault leading to the system islanding (fault current level: 5kA).
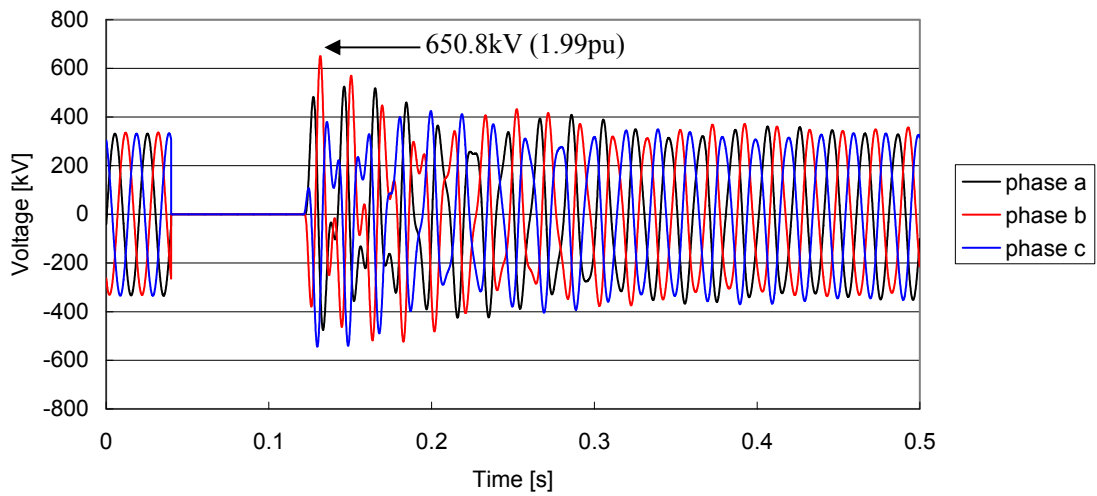
Fig. 4.91 Overvoltage caused by the TOR bus fault leading to the system islanding (fault current level: 10kA).
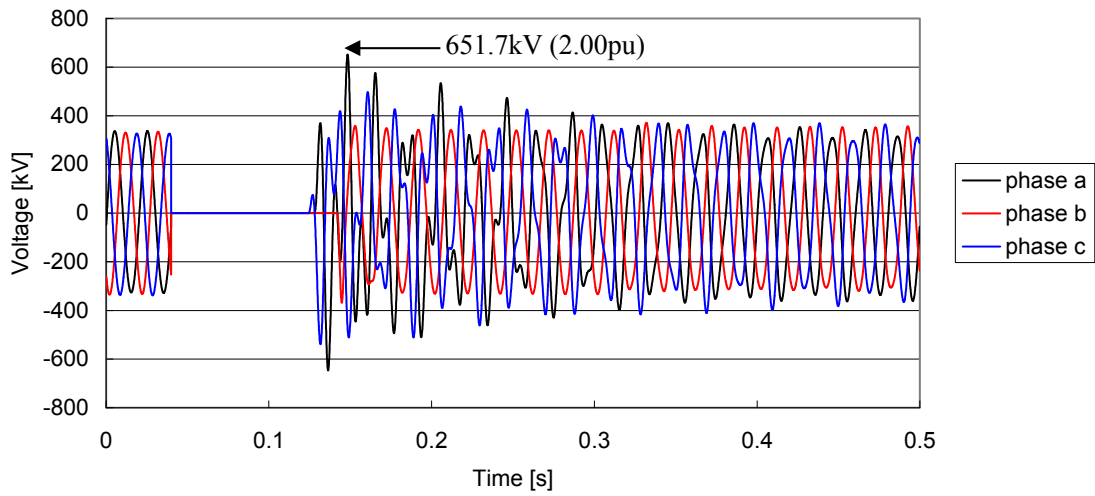
Fig. 4.92 Overvoltage caused by the TOR bus fault leading to the system islanding (fault current level: 20kA).
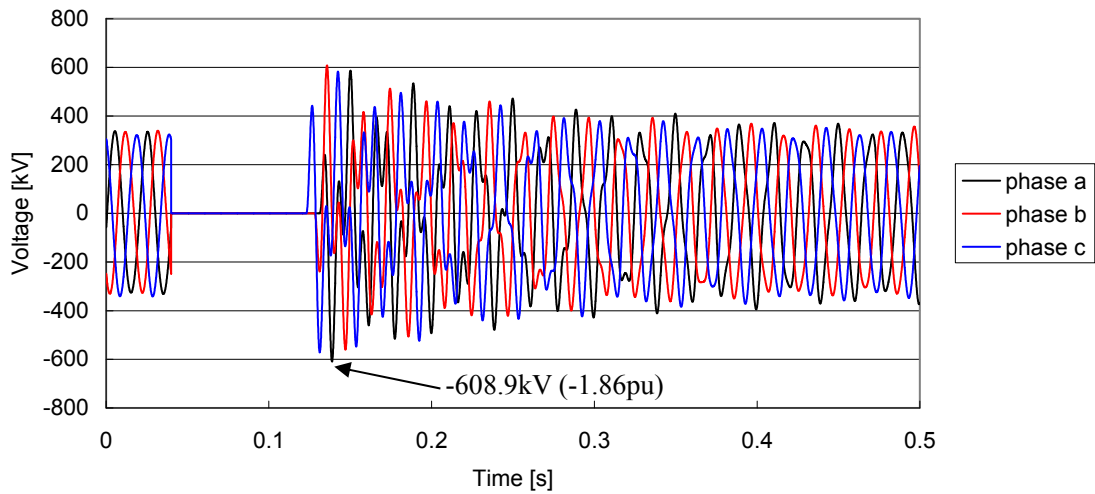
Fig. 4.93 Overvoltage caused by the TOR bus fault leading to the system islanding (fault current level: 30kA).
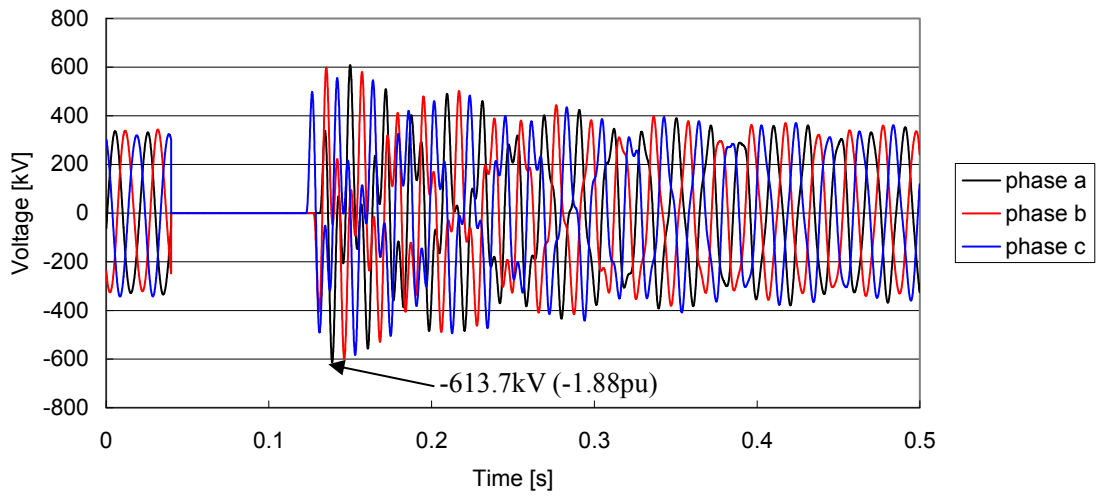
Fig. 4.94 Overvoltage caused by the TOR bus fault leading to the system islanding (fault current level: 40kA).

4.4 Conclusion

This chapter studied temporary overvoltages on the Kyndbyværket – Asnæsværket line. In Section 4.1, the series resonance overvoltage caused by the cable energization was studied. The most severe switching scenarios were first identified. The simulations were performed with the most severe assumptions of the Kyndbyværket 132 kV network and the Asnæsværket 132 kV network. The simulations found that the series resonance overvoltages in the assumed most severe conditions were much lower than the withstand voltages as long as the withstand voltage 230 or 275 kV was selected. The phase to phase overvoltage decayed below 230 kV (peak) after one cycle.

A simple estimation of the dominant frequency component without carrying out time domain simulations or frequency scans is useful for an efficient planning or operational planning of the network. Section 4.1.3.1 derived theoretical formulas of the dominant frequency. The comparison of dominant frequencies derived by theoretical formulas and those found by EMTP simulations shows that the derived theoretical formulas have the satisfactory accuracy.

Section 4.2 studied the parallel resonance caused by transformer inrush currents as the most severe scenarios. Among the potential harmonic current sources, an inrush current caused by the transformer energization is considered to be the most onerous one because of its high harmonic contents, low frequency, low damping, and long duration. Severe overvoltages were observed with the most severe scenarios, but they were within withstand voltages of related equipment.

Section 4.3 studied the overvoltage caused by the system islanding. A fault on the Kyndbyværket, Asnæsværket, and Torslunde 400 kV buses were studied with different fault current levels, different shunt compensation degrees, and different timings for the fault clearing. The study showed that the overvoltages were most severe when a fault occurs on the Asnæsværket 400 kV bus, but they were within withstand voltages of related equipment.

References

[1] N. Momose, H. Suzuki, S. Tsuchiya, T. Watanabe, "Planning and Development of 500 kV Underground Transmission System in Tokyo Metropolitan Area," *CIGRE Session 1998*, 37-202.

[2] *Assessment of the Technical Issues relating to Significant Amounts of EHV Underground Cable in the All-island Electricity Transmission System*, (available on the web) Tokyo Electric Power Company, November 2009, http://www.eirgrid.com/media/Tepco%20Report.pdf.

[3] M. Rebolini, L. Colla, F. Iliceto, "400 kV AC new submarine cable links between Sicily and the Italian mainland. Outline of project and special electrical studies," *CIGRE Session 2008*, C4-116.

[4] L. Colla, S. Lauria, F. M. Gatta, "Temporary Overvoltages due to Harmonic Resonance in Long EHV Cables," *IPST 2007*,
http://www.ipst.org/techpapers/2007/ipst_2007/papers_IPST2007/Session16/233.pdf

[5] N. Nagaoka, A. Ametani, "Transient Calculations on Crossbonded Cables," *IEEE Trans. on Power Apparatus and Systems*, vol. PAS-102, no. 4, April 1983.

[6] A. Ametani, Y. Miyamoto, N. Nagaoka, "An Investigation on a Wave Propagation Characteristic on a Crossbonded Cable," *IEEJ Trans. PE* , vol. 123-B, no.3, pp. 395-401, March 2003

[7] Stephen H. Hall, Howard L. Heck, *Advanced Signal Integrity for High-Speed Digital Designs*, Wiley-IEEE Press, March 2009

[8] T. Karasaki, T. Goto, A. Ametani, "An Abnormal Overvoltage due to Load Rejection on EHV Underground Transmission Lines", *International Conference on Power System Transients (IPST)*, September 1995.

Chapter 5 Slow-front Overvoltage Analysis

It has never been reported that the slow-front overvoltage exceeds insulation strengths of equipment in cable systems. Until now, SIWV (switching impulse withstand voltage) determined with power systems predominantly composed of overhead lines showed no problem with the power systems that contain the cable systems.

Presently, the slow-front overvoltage analysis is not conducted any more in the implementation study of overhead lines in most cases. It is known from past studies that the slow-front overvoltage does not exceed SIWV as long as the typical one (generally, 1050 kV for 420 kV equipment) is selected. In contrast, it is a typical practice to study the slow-front overvoltages for the installation of EHV cables, mainly due to the lack of past studies or experiences.

In the PhD project, slow-front overvoltages caused by line energization, ground fault, and fault clearing were studied in order to compare those in cables and overhead lines. The main interest of the study is to find the statistical distributions of the slow-front overvoltages.

5.1 Overvoltage Caused by Line Energization from Lumped Source

5.1.1 Overview

Statistical distributions of slow-front overvoltages have played an important role in determining insulation levels and considering insulation coordination of EHV systems. Especially, key values in the statistical distributions, such as 2 %, maximum, and mean values, have been considered as indicators when assessing the insulation performance of the EHV systems [1].

CIGRE Working Groups 13.02 and 13.05 studied the statistical distributions of line energization and reclosing overvoltages, gathering the simulation results by TNAs and digital computers from all over the world [2] – [5]. The results of the study have formed the basis of today's insulation coordination.

When the study by CIGRE WGs 13.02 and 13.05 was conducted in 1970s, the WGs focused on the overvoltages in EHV overhead lines. EHV cable lines were not included in the study since their installed amount was limited, though some EHV cables were already in service [6] – [10]. Therefore, statistical distribution of switching overvoltages of EHV cables is not available to date. Most of the insulation levels determined with overhead lines have been applied to cable systems.

Since the study by CIGRE WGs 13.02 and 13.05, the installed amount of EHV cables has grown to a level at which statistical evaluations are possible. CIGRE WG B1.07 reported that 5,555 circuit km and 1,586 circuit km of underground cables were installed respectively at 220 – 314 kV and 315 – 500 kV in 2007 [11][12]. Thanks to this increase of cable installations, it is now possible to obtain various data which contain physical and electrical parameters of installed cables as well as cable layouts.

Based on the obtained cable data, the PhD project derives the statistical distribution of energization overvoltages of EHV cables. Characteristics of the statistical distribution are found through a comparison between the statistical distributions of EHV cables and overhead lines.

5.1.2   Past Studies by CIGRE WGs

In the survey by CIGRE WG 13.02, energization overvoltages were decomposed into the power frequency (pf) component and the transient component. It discusses the effects of the following parameters:

- Line length
- Feeding network
- Shunt compensation
- Closing resistors
- Trapped charge

Additionally, the effects of the following parameters are briefly discussed, but with no simulation results or examples:

- Closing angle, pole span
- Line parameters
- Corona
- Saturation

Among these parameters, line length, feeding network, and shunt compensation are parameters relevant to the cable energization. Closing resistors are not used with cable lines since slow-front overvoltages associated with cable lines are known to be lower than those associated with overhead lines. Also, trapped charge is not relevant since autoreclose is not applied to cable lines.

For example for line length, CIGRE WG 13.02 found the effect of line length on energization overvoltages as illustrated in Fig. 5.1. The figure shows that the transient component becomes

lower for longer lines, but the pf component becomes higher for longer lines. As a result, the line length does not influence the overall overvoltage level as long as the line charging capacity is compensated at 70 %.
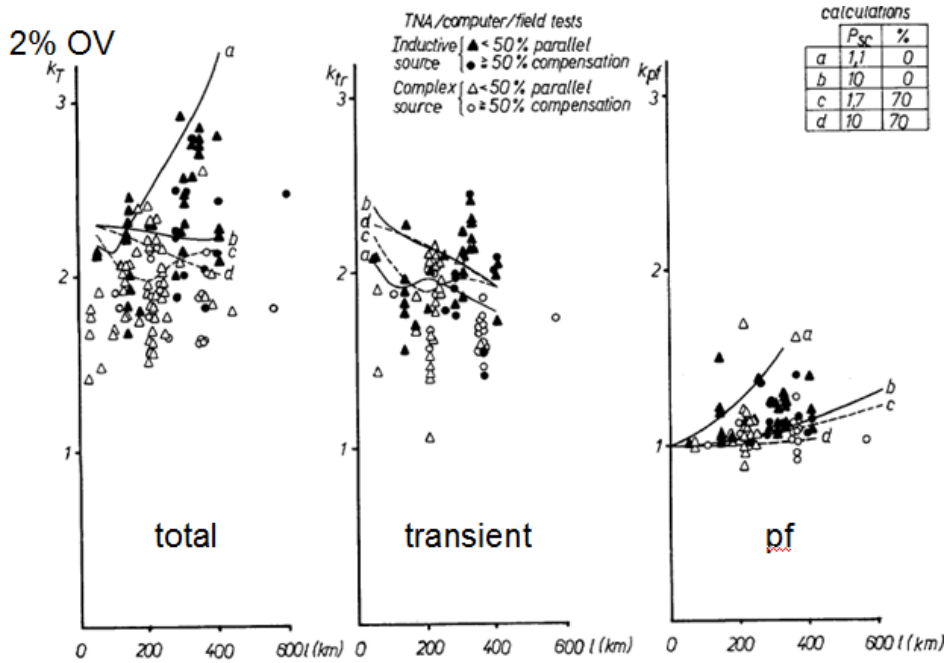
Fig. 5.1 Effects of line length on energization overvoltages (from [2]).
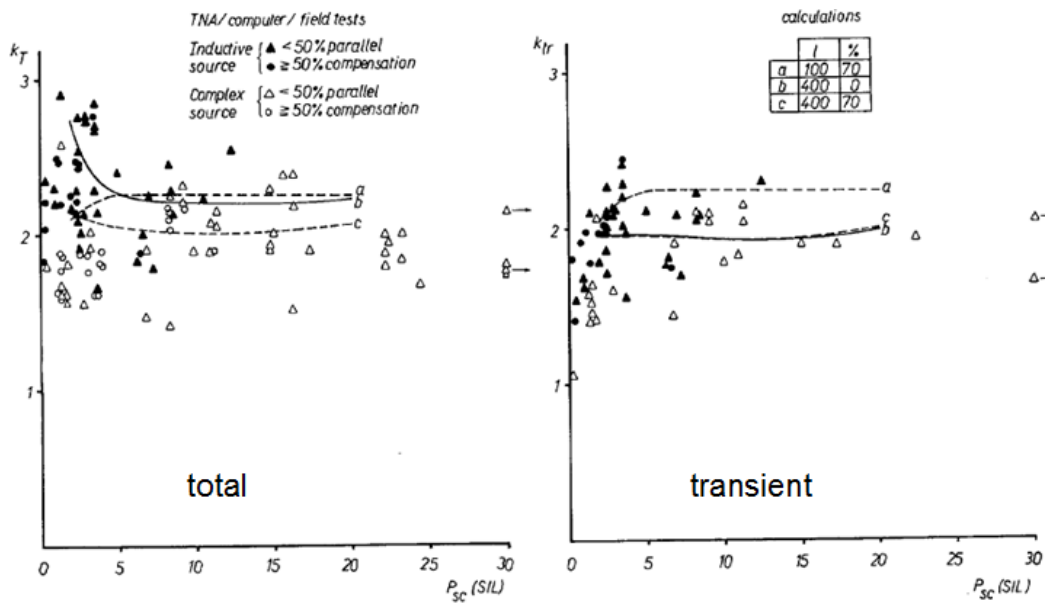
Fig. 5.2 Effects of feeding network on energization overvoltages (from [2]).

The effects of the feeding network are illustrated in Fig. 5.2. As the overvoltage curves are flat over the typical source impedance level, the feeding network (source impedance) causes a minor effect on the overvoltage level.

One of the purposes in this section is to find the characteristic of a cable energization overvoltage in comparison with an overhead line energization overvoltage as shown in Fig. 5.3. In the figure, effects of line length on overhead line energization overvoltages are found by CIGRE WG 13.02 and are expressed by black lines and dots. The red line shows effects of line length on cable energization overvoltages, which will later be found in this chapter. The red line is just an arbitrary line and is not based on simulation results at this moment.
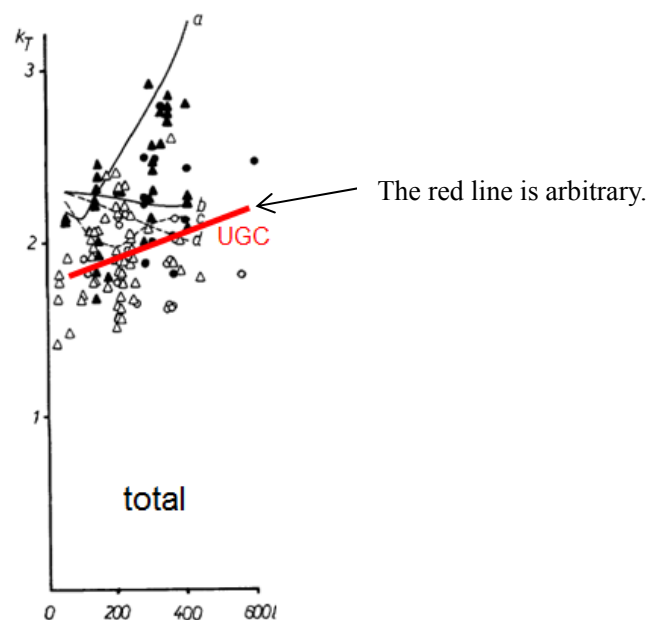
Fig. 5.3 Effect of line length on cable energization overvoltages (from [2]).

CIGRE WG 13.05 published the following three papers on the calculation of switching surges in Electra.

    I.   Comparison of transient network analyser results [3]

    II.   Network representation for energization and re-energization studies on lines fed by an inductive source [4]

    III.   Transmission line representation for energization and re-energization studies with complex feeding sources [5]

CIGRE WG 13.05 conducted more systematic studies with model networks with different TNAs, while the report by CIGRE WG 13.02 is a compilation of energization studies which different utilities carried out for their networks with TNAs and digital computers.

Reference [4] discusses the model setup for the energization studies. The studies were performed 40 years ago, but the modeling practice is basically the same as the today's practice.

- Generators

  Variation of subtransient inductance with time and AVR & governors are disregarded.

- Transformers

  Ignored: Frequency dependence of leakage inductance, magnetizing impedance

  Considered: Frequency dependence of resistance

- Lines

  Continuously transposed

  Corona effects are ignored.

- Breakers

  Prestrike is introduced in the statistical model.

  Pre-insertion resistor is considered.

Cumulative distributions of energization overvoltages are shown in [4] as in Fig. 5.4. The length of the line and the (inductive) feeding network were fixed in the analysis.
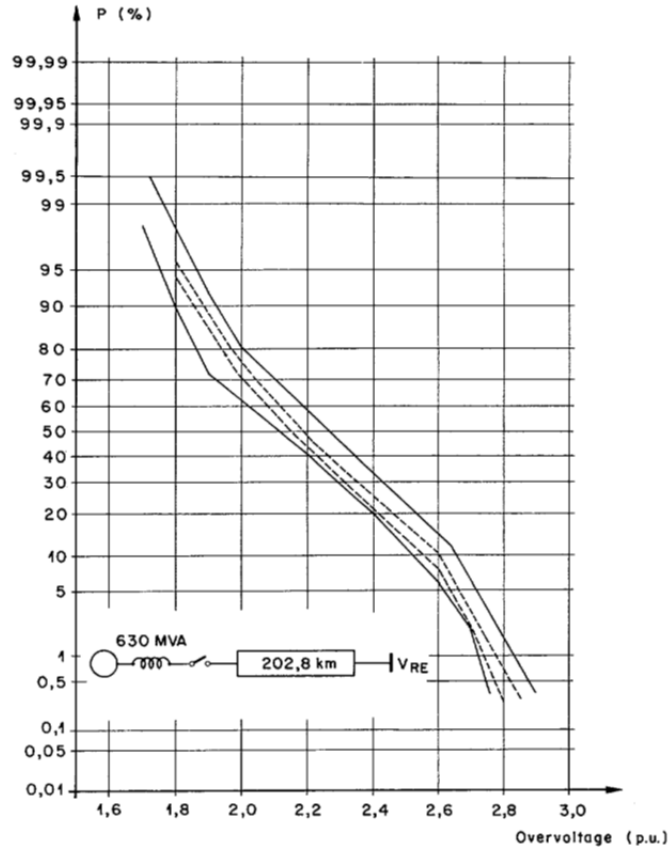
Fig. 5.4 Comparison of cumulative distribution of receiving end peaks obtained by digital and TNA methods with no pre-insertion breakers – 202.8 km line, 630 MVA source (from [4]).

Reference [5] studies energization from complex sources in order to find the effect of rapid initial rise of overvoltages. Fig. 5.5 shows the model network for the energization from the complex feeding sources. The line length was set to 265 km, which was close to the length 202.8 km in Fig. 5.4. The 450 km double-circuit transmission line realizes the rapid initial rise of overvoltages.
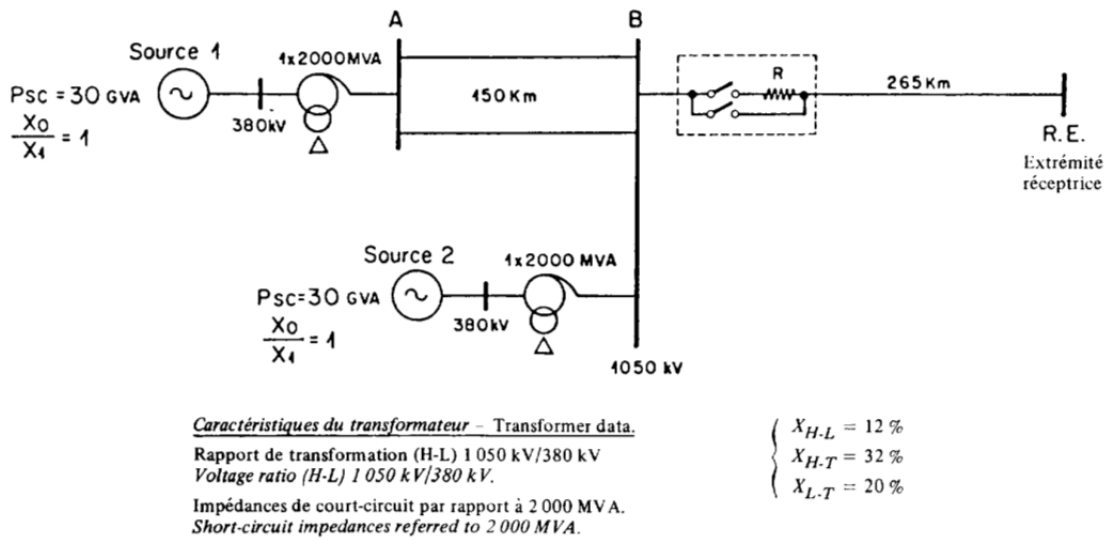
Fig. 5.5 Model network for the energization from complex sources (from [5]).

Fig. 5.6 shows the cumulative distribution of the energization overvoltages. Compared with Fig. 5.4, the overvoltage becomes significantly lower in case of the energization from complex feeding sources. With complex feeding sources, the overvoltages are not contained in the energized line, which leads to the lower overvoltage levels. The overvoltages can propagate into the complex feeding sources (from Bus B to Bus A in Fig. 5.5) and are damped in the complex feeding sources. With the inductive feeding sources, in contrast, the overvoltages are contained in the energized line since the surge impedance of the feeding source is much larger than that of the energized line. If the feeding source is inductive (lumped source), the total reflection occurs at Bus B in Fig. 5.5, and the reflected overvoltage goes back to the open end.
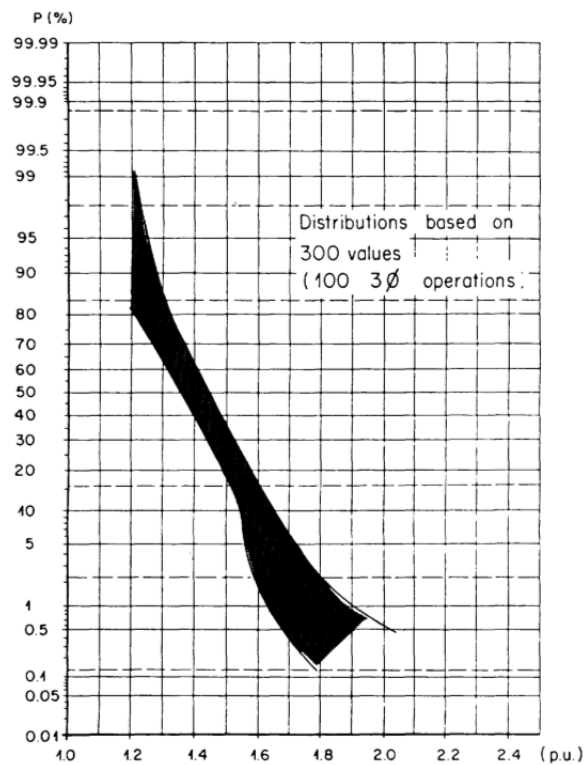
Fig. 5.6 Cumulative distribution of the overvoltage peak values: envelope of all available TNA results (from [5]).

5.1.3 Study Conditions and Parameters

The PhD project derives the statistical distributions of energization overvoltages of both EHV cables and overhead lines for comparison. The distribution of overhead lines had been already studied by CIGRE WGs 13.02 and 13.05 [2] – [5]. However, it was studied again in order to find the distributions with the same conditions and parameters as much as possible for cables and overhead lines, which would make it easier to compare the distributions.

5.1.3.1 Common Conditions and Parameters

First, we discuss the common conditions and parameters for cables and overhead lines. In this thesis, the statistical distributions of energization overvoltages were derived from the results of 200 line energization cases with the statistical (random) switching. CIGRE Working Group 13.05 conducted 100 line energizations to obtain the distribution. The number of energizations can be increased due to the higher computer capability for higher accuracy in finding key values in the statistical distributions. With the 200 line energization cases, 2 % value is the fourth highest value in the repeated simulations.

In the statistical switching, two kinds of randomness were considered. The first randomness is the phase angle (point-of-wave) when the line circuit breakers receive the command to close themselves. A uniform distribution from 0 to 360 degrees was assumed for this randomness. The second randomness is the difference of close timings between three phases. A normal distribution with standard deviation of 1 ms was assumed for the randomness.

CIGRE WG 13.02 considered parameters such as line length, feeding network, shunt compensation, existence of closing resistors, trapped charge, and so on [2]. Among them, this thesis focuses on two parameters: line length and feeding network.

Table 5-1 shows the variation of the two parameters. The line length is increased up to 96 km, considering the fact that the cable line as long as this level was studied [13]. The variation of the feeding network covers a weak source to a strong source within a reasonable range. Only the lumped parameter inductive source is considered as in the study by CIGRE WG 13.05. However, the source impedance 1 mH is also included in order to realize a steep initial voltage rise, which is expected in the line energization from a distributed parameter source [5].

Table 5-1 Study Conditions and Parameters for the Cable Energization Overvoltage

Line length	24, 48, 72, and 96 km
Feeding network	1, 15, 30, and 100 mH (corresponds to fault current of 735, 49, 25, and 7 kA at 400 kV)

In all the energization cases, the charging capacity of EHV cables is compensated by shunt reactors directly connected to the cables. The compensation rate is set to 100 % so that only a transient component of the overvoltage can be observed. The steady-state component of the overvoltage is not the focus here and can be calculated theoretically.

The shunt reactors are directly connected to the line at both line ends when the line length is 24, 48, or 72 km. When the line length is 96 km, the shunt reactors are additionally connected to the center of the line. Necessary capacity of shunt reactors for 100 % compensation is shared by shunt reactors at both line ends and at the center with the proportions of 1/4, 1/4, and 1/2. Saturation characteristics of shunt reactors were not modeled due to unavailability of the characteristics for different capacity of shunt reactors.

The charging capacity of overhead lines is also compensated to 100 % in order to find the statistical distributions of overvoltages in the same condition as cables. However, the distributions are studied also without shunt compensation since it is not common to compensate the charging capacity of the overhead lines of this length.

5.1.3.2 Cables

In order to derive the statistical distributions, 3,200 line energization simulations (4 line lengths × 4 feeding networks × 200 random switchings) were performed with 10 types of EHV cables. Cable types, physical and electrical parameters, and burial layouts were selected based on actual installations. Table 5-2 shows key parameters of 10 types of EHV cables.

All the 10 types of EHV cables are represented using the frequency-dependent model in the phase domain. It was assumed that their metallic sheaths are cross-bonded, which is the typical practice for a cable of this length. Fig. 5.7 illustrates the simulation model for line energizations. The highest overvoltages were observed at the open end of the line.

In order to assure a reasonable computational speed and numerical stability, the number of minor sections was reduced to 12. This means that the length of the minor section was increased to 8 km. This minor section length has not been achievable in underground cables, but it has been confirmed by test simulations that the errors introduced by this modification were below 5 %.
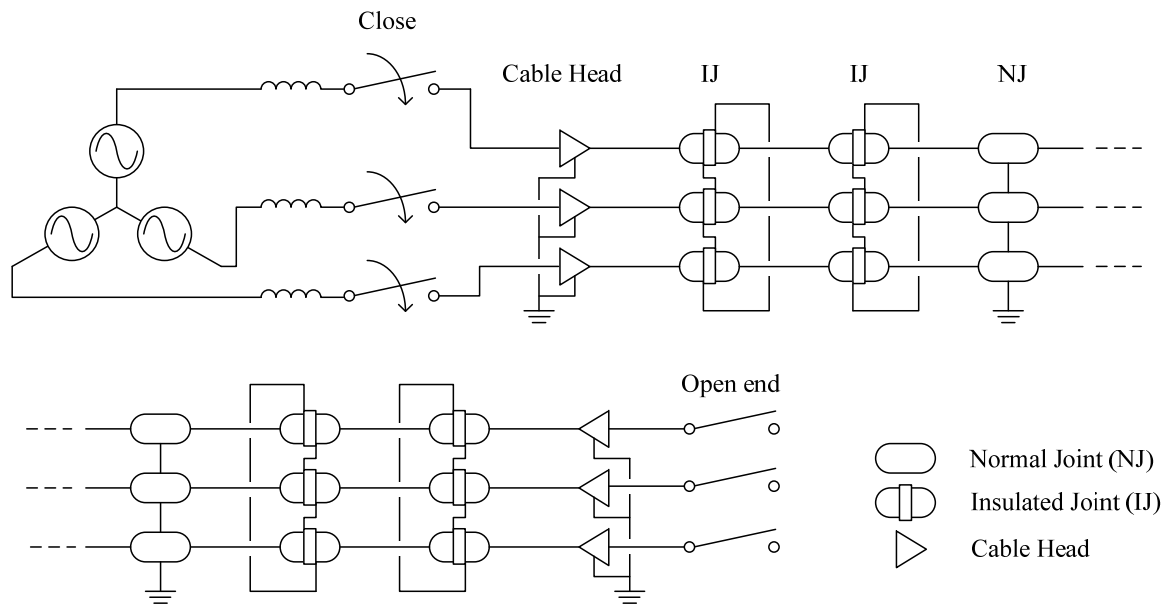
Fig. 5.7 Simulation model for cable line energizations.

Table 5-2 Key Parameters of 10 Types of Cables

	UGC1	UGC2	UGC3	UGC4	UGC5	UGC6	UGC7	UGC8	UGC9	UGC 10
Voltage [kV]	400	400	400	500	275	275	275	230	230	230
Core	Al	Cu	Cu	Cu	Al	Cu	Cu	Cu	Al	Cu
Size [mm2]	1600	1000	2500	2500	1600	2500	1400	630	1000	2000
Insulation	XLPE	SCFF	XLPE	XLPE	XLPE	XLPE	SCFF	SCFF	SCFF	XLPE
Sheath	Al	Pb	Al	Al	Al	Al	Al	Al	Al	Al
Layout	Flat	Flat	Flat	Tre-foil	Flat	Tre-foil	Tre-foil	Flat	Flat	Tre-foil
Phase separation [m]	0.3	0.3	0.5	0.17	0.5	0.17	0.5	0.3	0.3	0.14

(SCFF: Self contained fluid filled)

5.1.3.3 Overhead Lines

The statistical distributions of overhead lines are derived from energization simulations with 10 types of overhead lines. Physical and electrical parameters of the overhead lines and tower configurations were determined from actual installations. Table 5-3 shows key parameters of 10 types of overhead lines.

Table 5-3 Key Parameters of 10 Types of Overhead Lines

	OHL1	OHL2	OHL3	OHL4	OHL5	OHL6	OHL7	OHL8	OHL9	OHL 10
Voltage [kV]	400	400	400	500	275	275	275	500	400	400
Phase conductor	Mar-tin	Finch	Cur-lew	TACS R 810	TACS R 610	Zebra	LGJ 240	LGJ 400	Dove	Card-inal
# of conductors in a bundle	2	2	2	4	4	2	6	4	4	4
Conductor separation [cm]	40	40	45	50	50	40	37.5	45	40	40
# of ground wires	2	2	2	2	2	2	2	2	2	2
Tower type	Barrel	Barrel	Single	Pine	Pine	Single	Two	Two	Danu-be	Danu-be
Height of lower conductor [m]	20	20	22	46	43.5	20	30.8	30.8	31.75	31.75

(TACSR: ASCR with higher allowable temperature, Single: Single level delta tower, Two: Two level delta tower)

5.1.4   Simulation Results and Statistical Distributions

This section discusses simulation results of the line energizations and obtained statistical distributions. The effects of studied parameters, i.e., line length and feeding network, are also discussed.

The observed overvoltages are expressed in per unit, where 1 pu stands for the peak value of a phase-to-ground normal operating voltage.

5.1.4.1 Probability Distributions

Fig. 5.8 shows cumulative probabilities by which the maximum overvoltage can exceed each overvoltage level (horizontal axis). First, each probability distribution was found from the results of 32,000 line energization cases. Comparing cumulative probabilities of cables and overhead lines, the overhead lines clearly generate higher overvoltages. The maximum overvoltage observed with cables and overhead lines were respectively 2.54 pu and 2.91 pu.

In contrast, on the lower side, the differences are very small. For the overvoltage below 1.7 pu, the probabilities are virtually equal for the cables and the overhead lines. It leads to the small difference in the mean values shown in Table 5-4. The standard deviation for the cables is therefore smaller than that for the overhead lines.

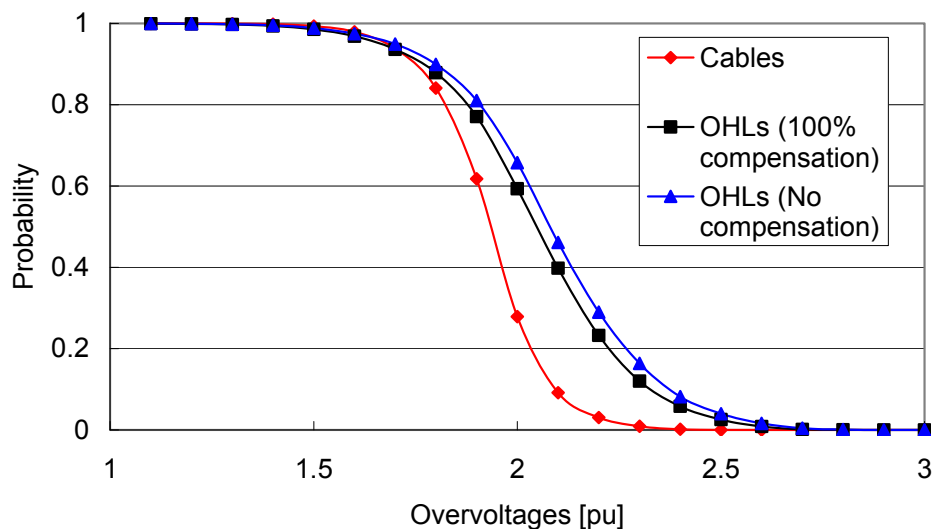**Fig. 5.8 Cumulative probability distributions.**

Table 5-4 Means and Standard Deviations of Probability Distributions

	Mean [pu]	σ [pu]
Cable	1.93	0.14
OHL (100 % compensation)	2.05	0.23
OHL (no compensation)	2.08	0.23

(σ: standard deviation)

As the charging capacity of the overhead lines is relatively small, there exist only minor differences between the overhead lines with 100 % compensation and those without compensation.

Second, probability distributions are found from each 200 random energization case. With 32,000 line energization cases, 160 probability distributions are obtained respectively for cables and overhead lines.

Probability distributions of random energization cases are often compared to the normal distribution [1]. For the parametric test, the skewness and kurtosis are obtained from 160 probability distributions. Table 5-5 shows average values of 160 skewness and kurtosis. The skewness (S) and kurtosis (K) are calculated as

$$S = \frac{1}{200} \sum_{i=1}^{200} \left(\frac{x_i - \bar{x}}{\sigma} \right)^3 \qquad \text{Eqn. 5.1}$$

$$K = \frac{1}{200} \sum_{i=1}^{200} \left(\frac{x_i - \bar{x}}{\sigma} \right)^4 \qquad \text{Eqn. 5.2}$$

where x_i is sample values, and $\bar{x}$ is the mean value.

Table 5-5 Average Skewness and Kurtosis of Probability Distributions

	Skewness	Kurtosis
Cable	-0.65	4.22
OHL (100 % compensation)	-0.52	3.62

Examples of probability distributions of cables and overhead lines are respectively shown in Fig. 5.9 and Fig. 5.10 with fitted normal distribution curves. The skewness and kurtosis of the overhead lines without compensation are not shown as the difference between with and without compensation is found to be negligible.

For both cables and overhead lines, the average skewness takes negative values, which means that their probability distributions have longer tail to the left side than to the right side. As the average skewness of the cables is smaller than that of the overhead lines, such a characteristic is more

noticeable in the probability distributions of the cables. The characteristic can also be observed in Fig. 5.9 and Fig. 5.10.

Table 5-5 also shows the average kurtosis for both cables and overhead lines. The kurtosis becomes equal to three when a probability distribution follows the normal distribution. The larger values of kurtosis mean probability distributions have more acute peaks than the normal distribution. The peaks of the probability distributions of the cables are more acute than those of the overhead lines. The characteristic can also be observed in Fig. 5.9 and Fig. 5.10. In conclusion, both skewness and kurtosis shows that the probability distributions of the overhead lines are closer to the normal distribution than those of the cables.
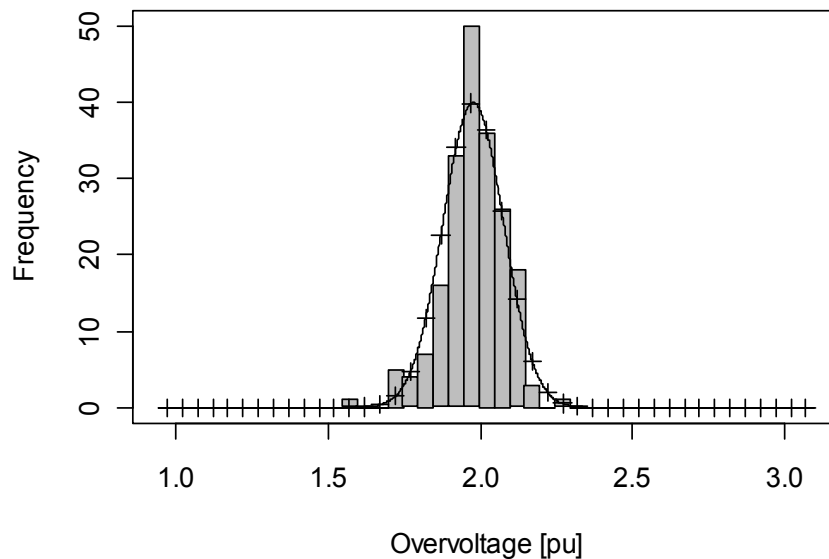
Mean: 1.98 pu, Standard dev.: 0.10 pu, Skewness: -0.68, Kurtosis: 4.44

Fig. 5.9 Example of probability distributions (UGC1, line length: 48 km, source impedance: 30mH).
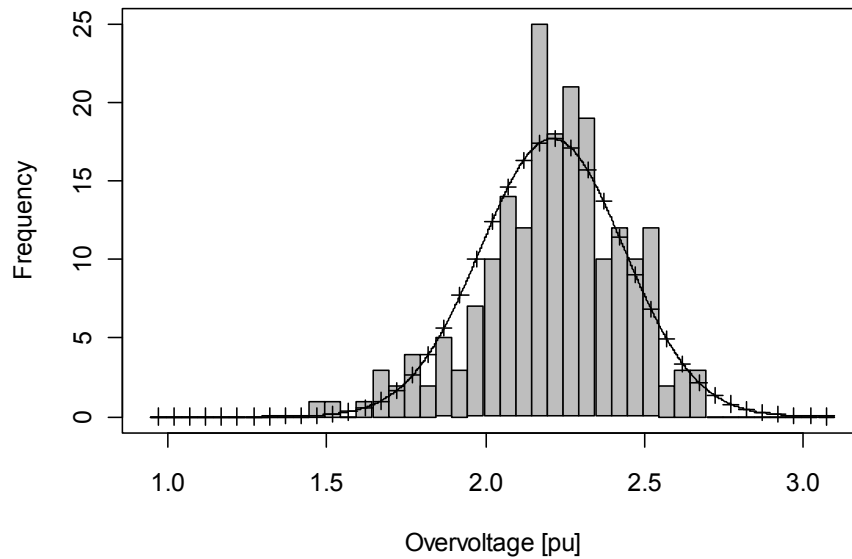
Mean: 2.21 pu, Standard dev.: 0.23 pu, Skewness: -0.54, Kurtosis: 3.35

Fig. 5.10 Example of probability distributions (OHL1 with 100 % compensation, line length: 48 km, source impedance: 30mH).

In addition to the parametric test, a Kolmogorov-Smirnov test was performed to the probability distributions obtained [17]. In Fig. 5.11, the horizontal axis is the significance level at which the hypothesis that the probability distributions follow the normal distribution is evaluated. The figure illustrates cumulative probabilities by which the probability distributions pass the Kolmogorov-Smirnov test at different significance levels. For example for cables, 16 probability distributions out of 160 (10 %) pass the Kolmogorov-Smirnov test at the 20 % significance level. The Kolmogorov-Smirnov test, as well as the parametric test, demonstrates that probability distributions of the overhead lines are closer to the normal distribution than those of the cables.
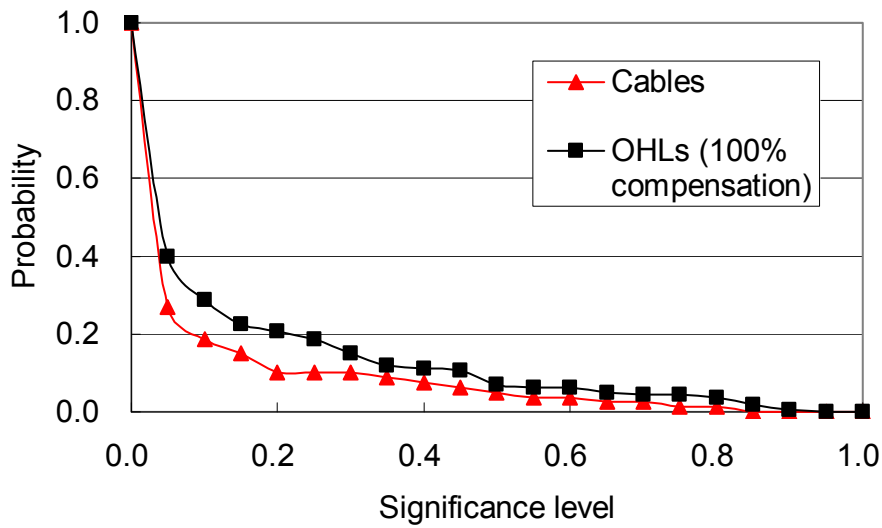
Fig. 5.11 Cumulative probabilities by which probability distributions pass the Kolmogorov-Smirnov test.

5.1.4.2   2 % Value

The 2 % values can be found as the fourth largest overvoltage in 200 random energization cases. With 32,000 line energization cases, one hundred sixty (160) 2 % values were obtained. Fig. 5.12 shows cumulative probabilities by which the 2 % value can exceed each overvoltage level.
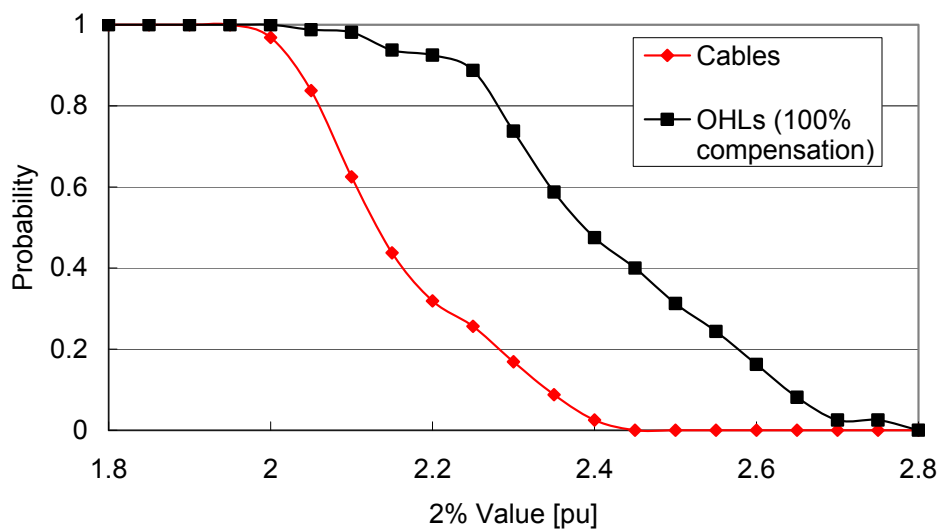
Fig. 5.12 Cumulative probability distributions of 2 % values.

The characteristics and differences of the probability distributions observed in Fig. 5.8 can also be observed in Fig. 5.12. However, as shown in Table 5-6, the difference of the mean value between cables and overhead lines becomes larger. On the contrary, the difference of the standard deviations becomes smaller.

Table 5-6 Means and Standard Deviations of Probability Distributions of 2 % Values

	Mean [pu]	σ [pu]
Cable	2.16	0.12
OHL (100 % compensation)	2.42	0.16

5.1.4.3 Comparison of Maximum Overvoltages with 2 % Values

CIGRE WG 13.02 reported for overhead lines that in 90 % of all line energization cases, maximum overvoltages were not more than 6.5 % higher than 2 % values. In addition, in 50 % of all the cases, maximum overvoltages were not more than 2.5 % higher than 2 % values.

The probabilities were also found from our simulation results for comparison. Table 5-7 summarizes the probabilities. The table shows that the differences between maximum overvoltages and 2 % values are larger in cables, compared with overhead lines, but the deviation between the cables and the overhead lines is minor. In the table, r_{2m} is defined as

$$r_{2m} = \frac{Maximum OV - 2\% \text{ value}}{2\% \text{ value}} \times 100$$

Eqn. 5.3

Table 5-7 Comparison of Maximum Overvoltages with 2 % Values

	WG 13.02	Cables	OHLs
$P(r_{2m} \leq 6.5)$	90 %	90 %	96 %
$P(r_{2m} \leq 2.5)$	50 %	45 %	59 %

(*P*: probability)

5.1.4.4 Effects of Line Length

Fig. 5.13 and Fig. 5.14 respectively show the effect of line length on the maximum overvoltages

and 2 % values in 200 line energizations. Different colors in the figures show different types of the line and different feeding networks (10 × 4 colors).

The overvoltages in the overhead lines have clear dependence on the line length. Regardless of line types or feeding networks, the highest overvoltages are observed when the line length is 72 km. The overvoltage level is raised with the increase of line length for short lines but is lowered after it reaches the highest with the line length 72 km.

In contrast, it is difficult to find any dependence of the overvoltages in cables on line length. The maximum overvoltages range around 2.0 – 2.6 pu regardless of line length and line types.

Fig. 5.13 Effects of line length – maximum overvoltages (top: cables, bottom: overhead lines with 100 % compensation).
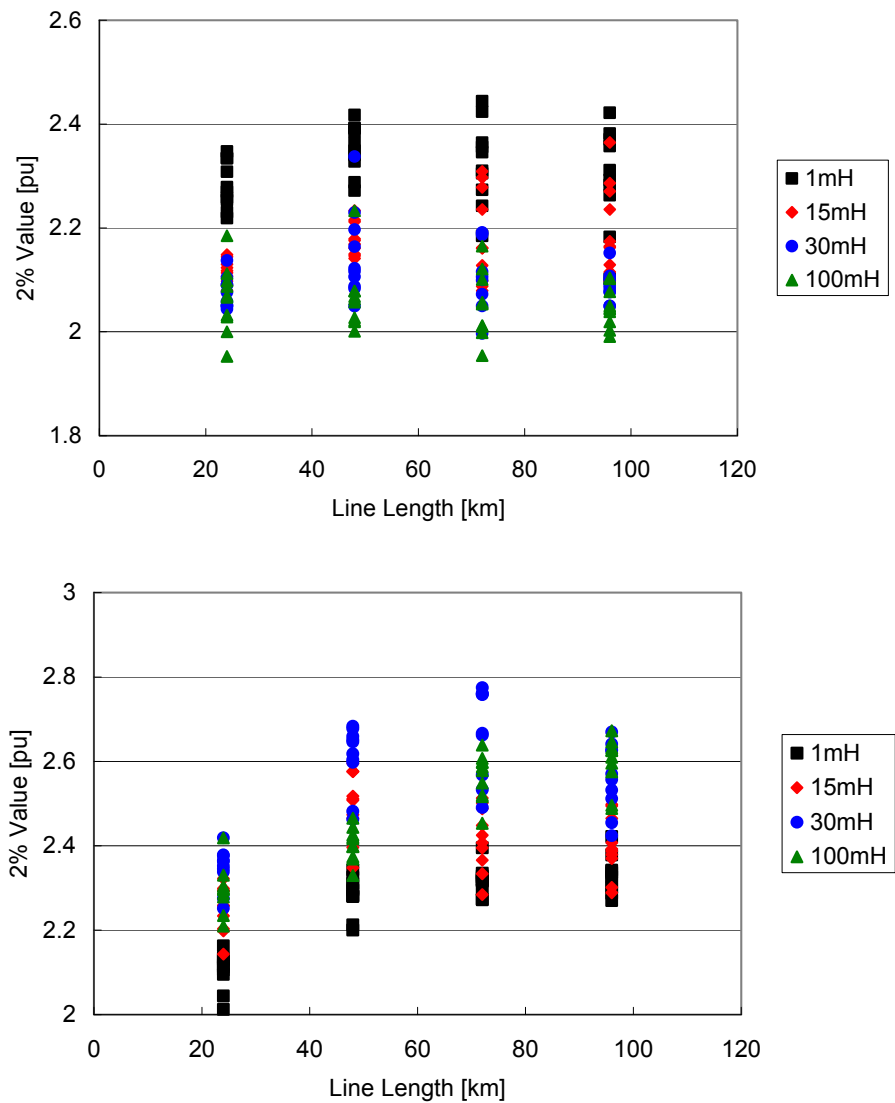
Fig. 5.14 Effects of line length – 2 % values (top: cables, bottom: overhead lines with 100 % compensation).

5.1.4.5 Effects of Feeding Network

Fig. 5.15 and Fig. 5.16 respectively show the effect of a feeding network on the maximum overvoltages and 2 % values in 200 line energizations. Different colors in the figures indicate different types of the line and different line lengths (10 × 4 colors).

It is observed in the figures that the overvoltages in the cables are dependent on a feeding network.

The overvoltage level becomes lower for a larger source impedance (weaker feeding network) regardless of line types. The dependence is opposite in the overhead lines when the source impedance is small. For the source impedance 1 to 30 mH, the overvoltages in the overhead lines become higher for a larger source impedance.
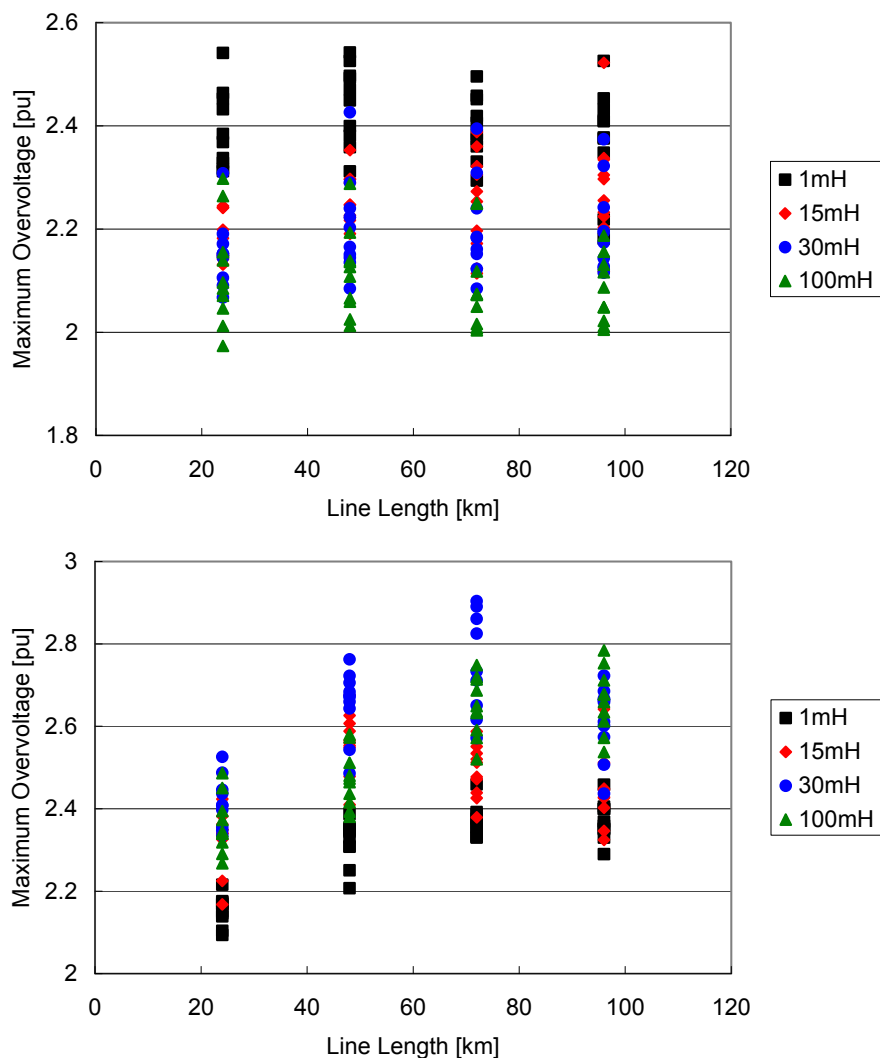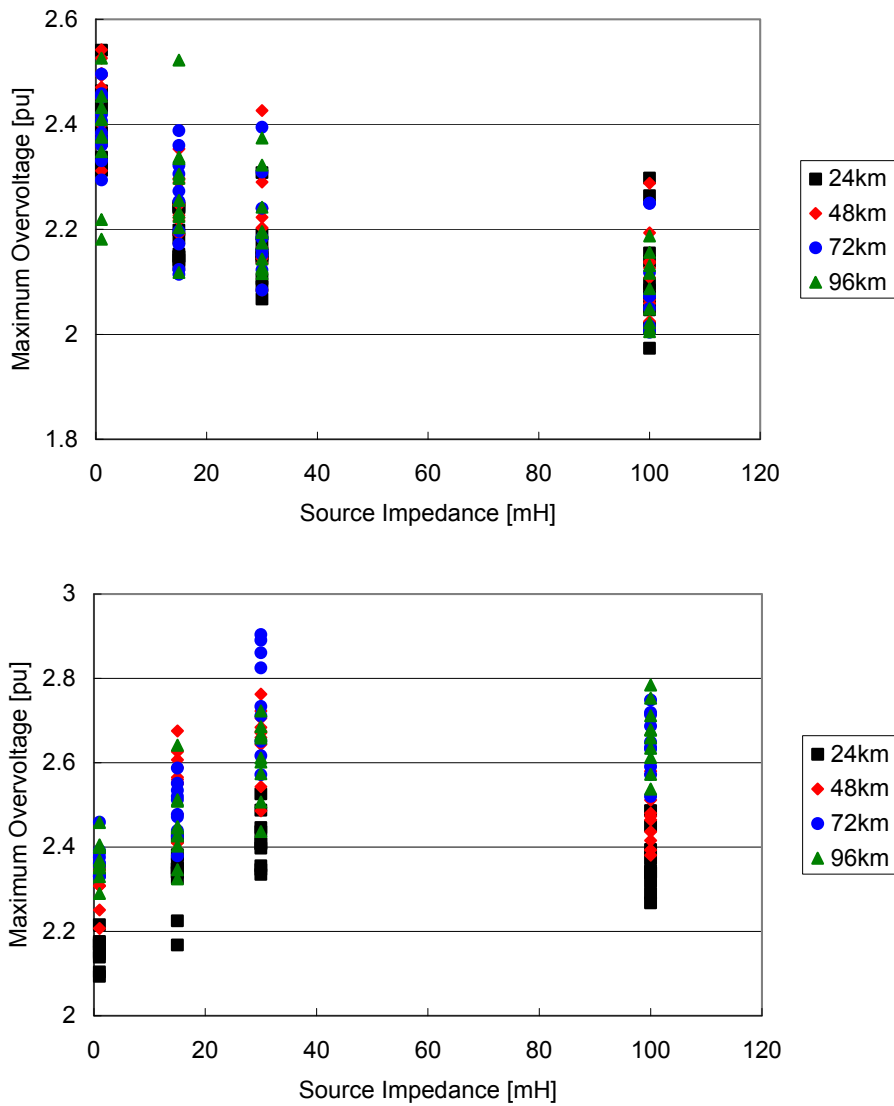

Fig. 5.15 Effects of feeding network – maximum overvoltages (top: cables, bottom: overhead lines with 100 % compensation).
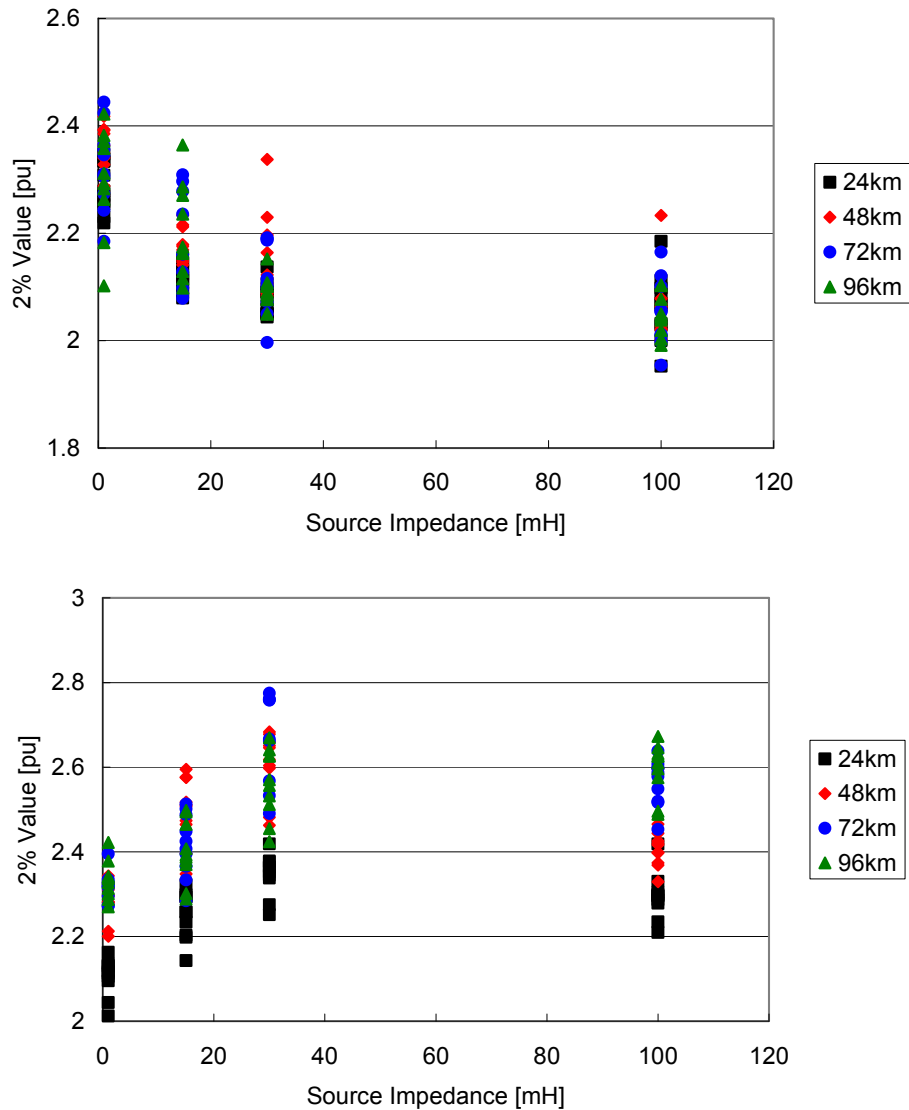
Fig. 5.16 Effects of feeding network – 2 % values (top: cables, bottom: overhead lines with 100 % compensation).

5.1.5   Summary

The statistical distributions of energization overvoltages of EHV cables have been derived from repeated simulations. Based on a comparison with the statistical distributions of overhead lines, it has been found out that line energization overvoltages in cables are lower than those in OHLs with respect to maximum, 2 %, and mean values. In addition, standard deviations are smaller for cables.

From the statistical distributions introduced in this thesis, a power system with cables receives

lower stress on its equipment compared with one with overhead lines. As a result, if only energization overvoltages are considered, it is possible to apply lower withstand voltages to the power system with the cables. However, careful examinations are necessary as possibility of a severe temporary overvoltage related to the cable systems has recently been reported [13] – [16].

The effects of line length and a feeding network have also been studied. The energization overvoltages of cables become lower for a weaker feeding network regardless of line types. In contrast, it is difficult to find any dependence of the overvoltages in cables on line length.

5.2 Overvoltage Caused by Line Energization from Complex Source

The previous section studied the cable / overhead line energization from an inductive source. In this section, the energization from a complex source is studied with the Kyndbyværket – Asnæsværket line.

According to the results of the past studies by CIGRE WG 13.02 and 13.05, it is obvious that the overvoltage level is lower when a line is energized from a complex source. It is estimated due to the fact that the overvoltage can propagate into adjacent lines when these lines are modeled in the simulations. In the previous section, the observed overvoltages were lower than SIWV. It is therefore expected that overvoltages observed in this section will be even lower than those in the previous section.

5.2.1   Study Conditions

As in the previous section, two kinds of randomness were considered in the statistical switching. The first randomness is the phase angle (point-of-wave) when the line circuit breakers receive the command to close themselves. A uniform distribution from 0 to 360 degrees was assumed for this randomness. The second randomness is the difference of close timings between three phases. A normal distribution with standard deviation 1 ms was assumed for the randomness.

Two different feeding networks were considered. One is the off-peak load condition (weak source) which is discussed in Section 3.1. In the other feeding network, a peak load condition (strong source) was considered by adding a dummy source to the Kyndbyværket or Asnæsværket 400 kV bus. The source impedance of the dummy source was set to 1 mH (extremely strong) so that the contrast with the off-peak load condition became clear.

Finally, the overvoltages were observed at the open end terminal. The profile of overvoltage along with the line length was studied for the most severe case.

5.2.2   Energization from ASV

This section studies the energization from the Asnæsværket side. The energization overvoltages on the Kyndbyværket side (open end terminal) were monitored.

Fig. 5.17 and Table 5-8 show the cumulative probability distributions and their characteristics. As

expected from the results in Section 5.1, the overvoltage level is much lower in the off-peak load condition with the complex source. The strong source causes more severe overvoltage as it fixes the voltage on the Asnæsværket side (sending end) and causes the total reflection. In this case, there is almost no difference between the complex source and the inductive source.
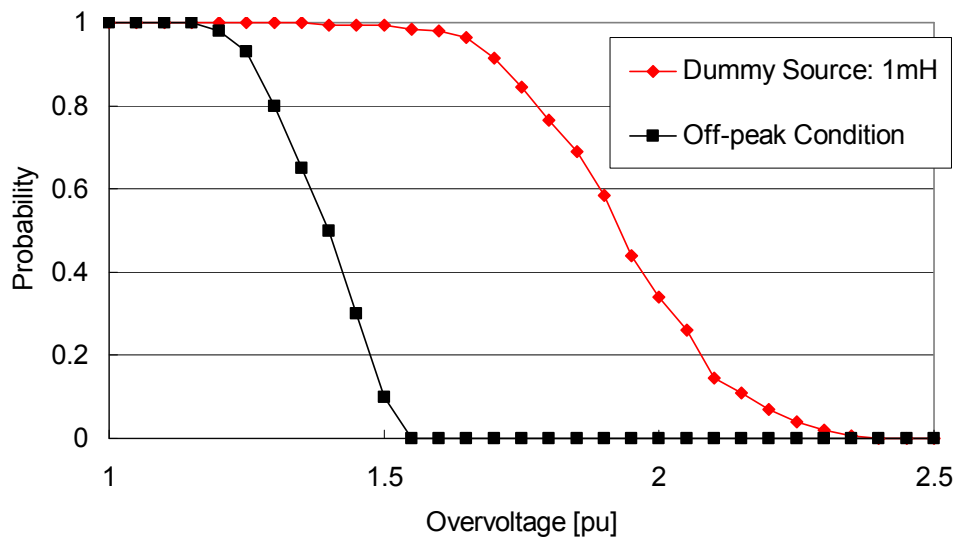
Fig. 5.17 Cumulative probability distributions for the KYV – ASV cable energization from the ASV side.

Table 5-8 Characteristics of Probability Distributions for the KYV – ASV Cable Energization from the ASV Side

	Dummy Source.: 1mH	Off-peak Condition
Max. OV [pu]	2.37	1.53
2% OV [pu]	2.31	1.52
Average OV [pu]	1.93	1.39
Standard dev. [pu]	0.1732	0.0888
Skewness	0.0328	-0.2813
Kurtosis	2.97	2.03

In the off-peak load condition, the most severe overvoltage was observed with the combination of the following switch timings:

        Phase A: 0.01831 s

        Phase B: 0.01972 s

        Phase C: 0.01967 s

Fig. 5.18 shows the profile of the overvoltage along with the line when the most severe overvoltage was observed. The overvoltage is highest around the Kyndbyværket side (open end terminal). Near the Asnæsværket side (sending end), the overvoltage is lower approximately by 0.08 pu. The overvoltage at Torslunde is slightly higher than its both sides since reflections occur at this point due to the separation of the sheath circuit. If the sheath circuits of the Asnæsværket side and the Kyndbyværket side are connected at Torslunde, there is no local peak at Torslunde.

Fig. 5.18 Profile of the overvoltage (energization from the ASV side).

As the maximum overvoltage was observed at the Kyndbyværket side (open end terminal), the waveforms of the energization overvoltage is shown in Fig. 5.19. As discussed in Chapter 4, the dominant frequency contained in the energization overvoltage is very low due to the long length of the cable line and the weak source. The wavefront of the first overvoltage 2.6 ms is approximately ten times larger than the standard waveshape of the slow-front overvoltage 250/2500 μs. The overvoltage is highly damped and the voltage waveforms go back to the normal sinusoidal waveforms within one cycle.
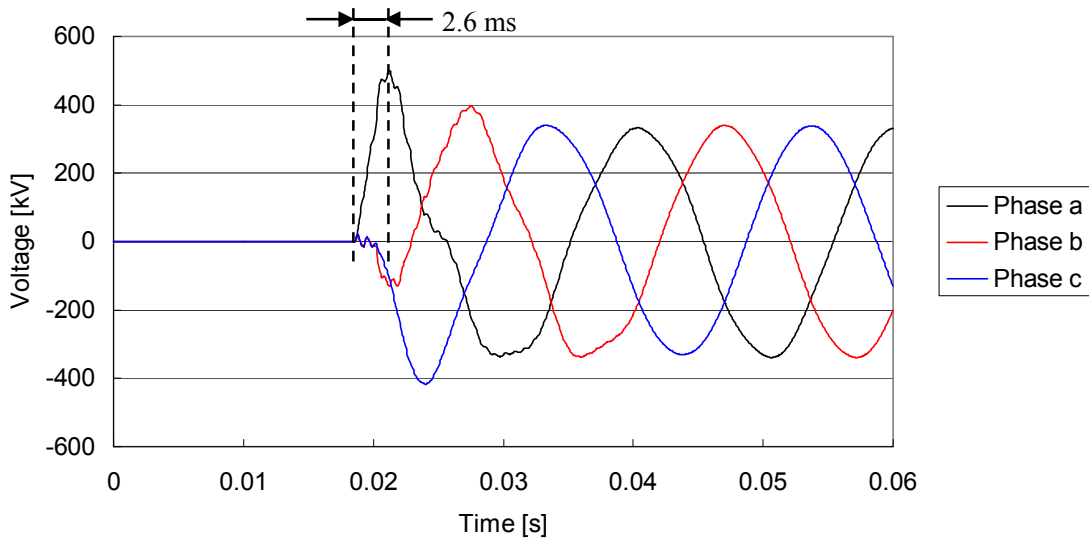
Fig. 5.19 Voltage waveform of the energization overvoltage at the KYV side (open terminal).

5.2.3   Energization from KYV

This section studies the energization from the Kyndbyværket side. The energization overvoltages on the Asnæsværket side (open end terminal) were monitored.

Fig. 5.20 and Table 5-9 show the cumulative probability distributions and their characteristics. The overvoltage level is even lower compared with the energization from the Kyndbyværket side. Besides that, the distributions and characteristics are very similar to those in case of the energization from the Asnæsværket side.
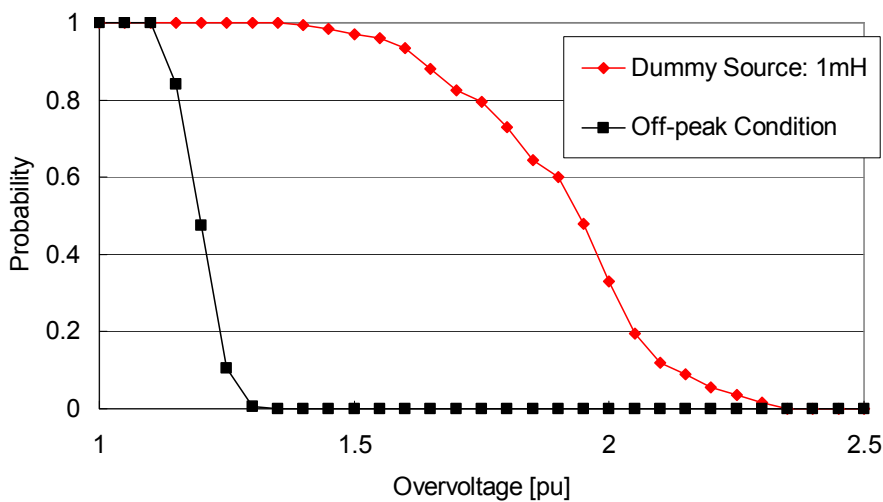
Fig. 5.20 Cumulative probability distributions for the KYV – ASV cable energization from the KYV side.

Table 5-9 Characteristics of Probability Distributions for the KYV – ASV Cable Energization from the KYV Side

	Dummy Source: 1mH	No Additional Source
Max. OV [pu]	2.33	1.31
2% OV [pu]	2.30	1.29
Average OV [pu]	1.91	1.20
Standard dev. [pu]	0.192	0.0413
Skewness	-0.352	0.141
Kurtosis	2.84	2.69

In the off-peak load condition, the most severe overvoltage was observed with the combination of the following switch timings:

Phase A: 0.02370 s

Phase B: 0.02337 s

Phase C: 0.02260 s

Fig. 5.21 shows the profile of the overvoltage along with the line when the most severe overvoltage was observed. Similarly to the energization from the Kyndbyværket side, the overvoltage is highest around the Asnæsværket side (open end terminal). Near the Kyndbyværket side (sending end), the overvoltage is lower approximately by 0.17 pu. The local peak at Torslunde cannot be observed in this case.
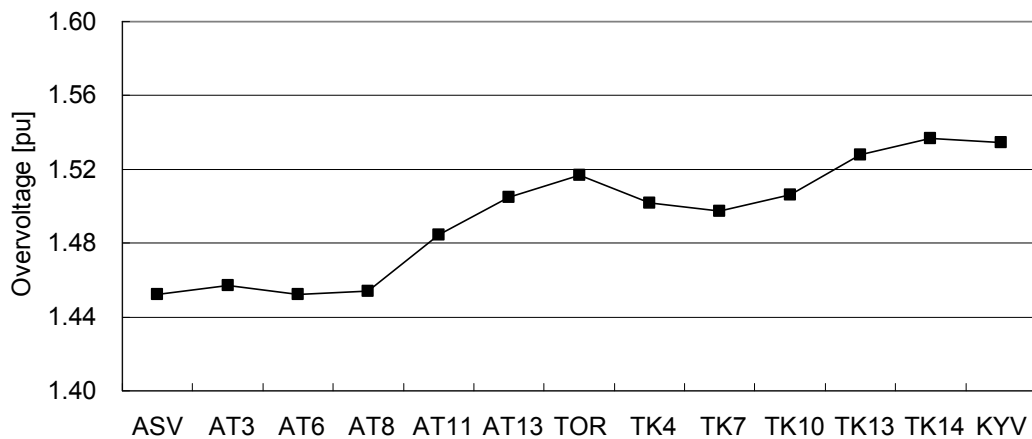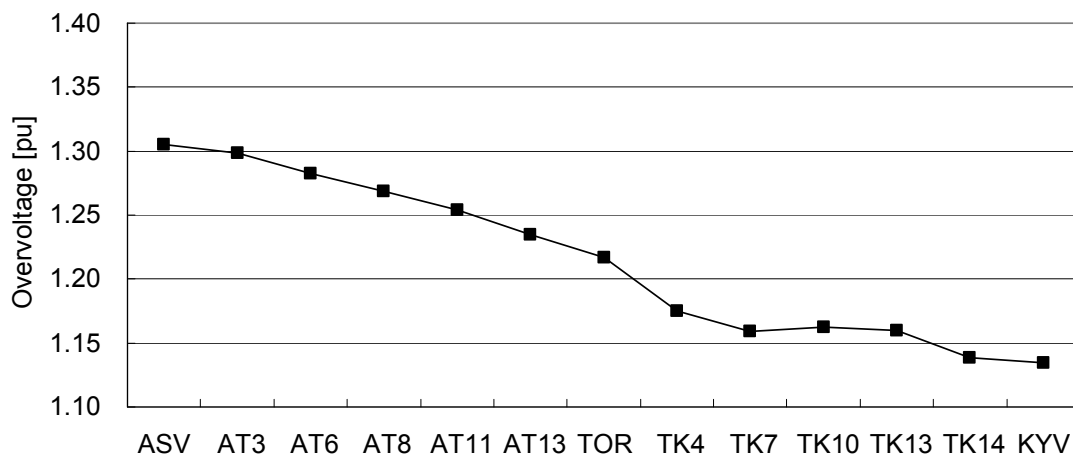

Fig. 5.21 Profile of the overvoltage (energization from the KYV side).

As the maximum overvoltage was observed at the Asnæsværket side (open end terminal), the waveforms of the energization overvoltage is shown in Fig. 5.22. As in the energization from the Asnæsværket side, the dominant frequency contained in the energization overvoltage is very low, and the overvoltage is highly damped.
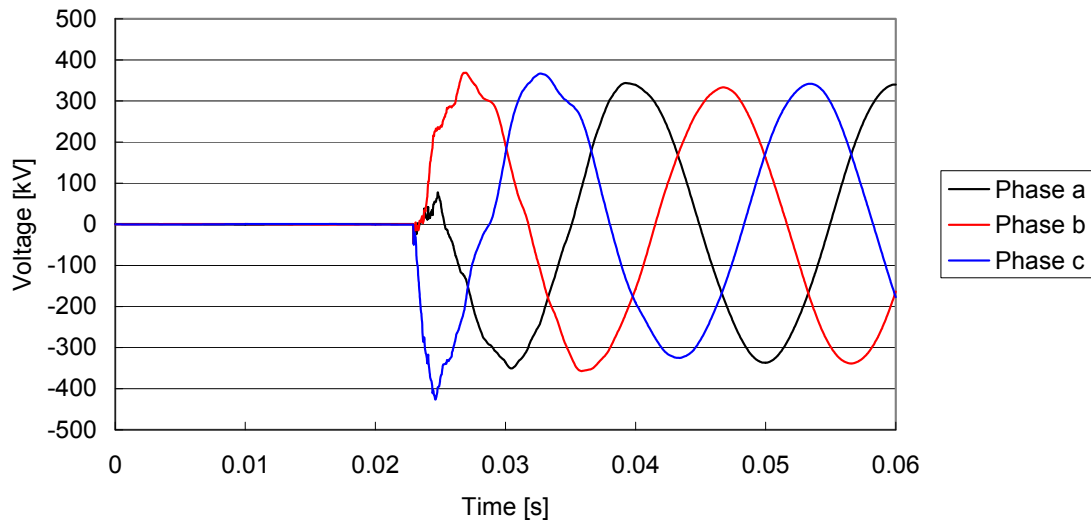
Fig. 5.22 Voltage waveform of the energization overvoltage at the ASV side (open terminal).

5.2.4   Effects of Synchronized Switching

As a countermeasure to the zero-missing phenomenon discussed in Section 6.3, the synchronized switching (point-on-wave switching) may be applied to the Kyndbyværket – Asnæsværket line. When each phase of the cable line is energized at its voltage peak by the synchronized switching, the DC component in the energization current can be minimized, resulting in the prevention of the zero-missing phenomenon.

The energization overvoltage analysis in this section, so far, considered two kinds of randomness in the statistical switching. However, due to the synchronized switching, the phase angle (point-of-wave) when the line circuit breakers receive the command to close themselves is no longer random. The randomness of the deviation from the voltage peak is modeled by the normal distribution with standard deviation 1 ms.

As the synchronized switching controls to energize the line at the voltage peak, it can lead to the higher energization overvoltages. It is therefore useful to find how the synchronized switching affects the probability distributions of the energization overvoltages.

Fig. 5.23 and Fig. 5.24 compare the cumulative probability distributions for the energization of the Kyndbyværket – Asnæsværket line with and without synchronized switching. The cable line was energized from the Asnæsværket side, and two feeding networks, off-peak load condition and peak load condition with a dummy source, were considered.

These figures show that the maximum overvoltages become lower with the synchronized switching. Standard deviations of the probability distributions become significantly lower by the synchronized switching, which helps to lower the maximum overvoltages. The average overvoltages can be lower or higher with the synchronized switching, depending on the feeding network.
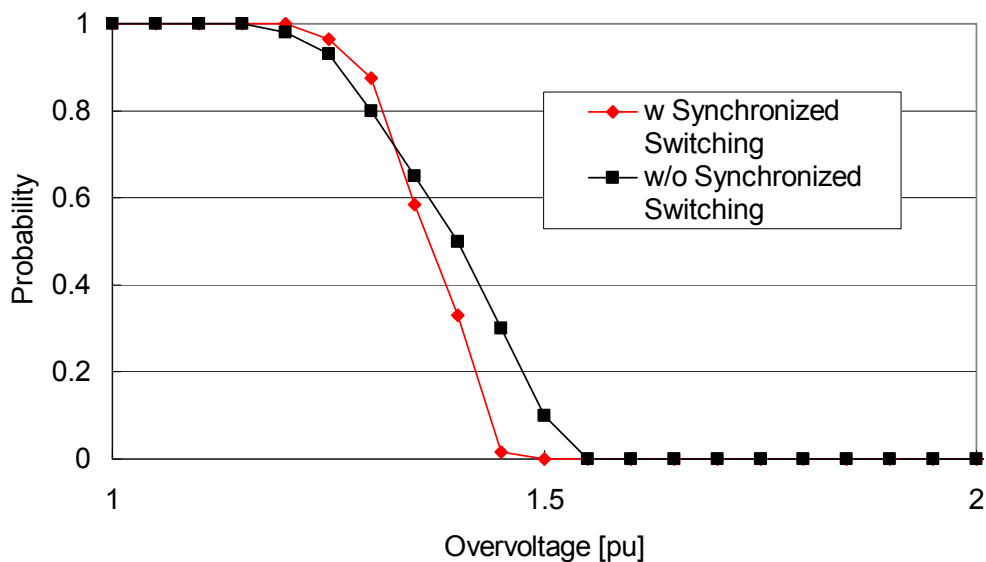

Fig. 5.23 Effect of synchronized switching on cumulative probability distributions (off-peak load condition).
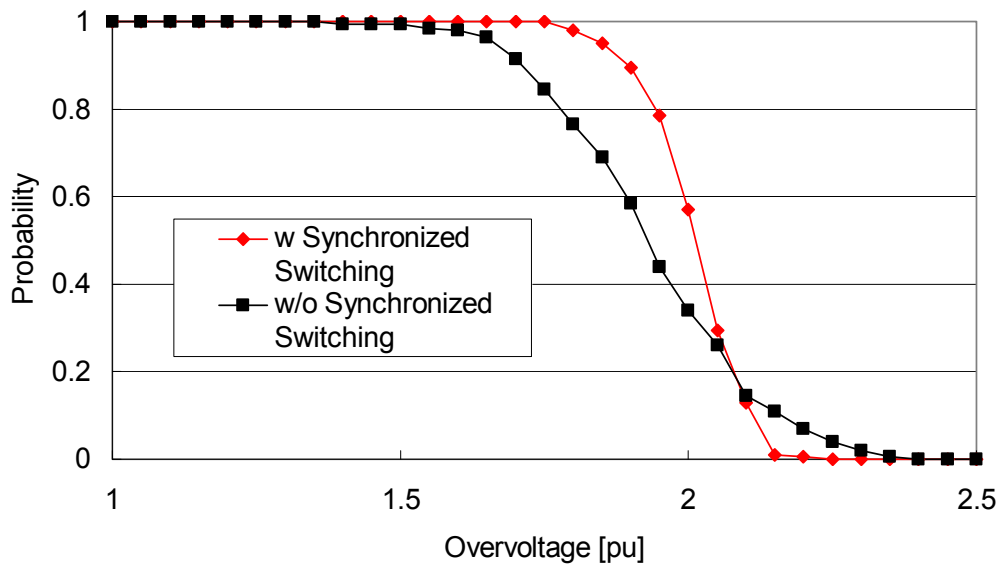
Fig. 5.24 Effect of synchronized switching on cumulative probability distributions (dummy source: 1 mH).

5.3 Analysis of Statistical Distribution of Energization Overvoltages

Sections 5.1 and 5.2 have identified characteristics of statistical distributions of energization overvoltages of EHV cables, compared with those of OHLs. They discussed possible causes that can lead to the characteristics, but the discussions are limited to qualitative analyses. Consequently, it is not clear which possible cause has the most dominant effect. This section identifies causes and physical meanings of the characteristics so that it becomes possible to use the obtained statistical distributions for the determination of insulation levels of cable systems.

Sections 5.1 and 5.2 studied 10 planned and existing EHV OHLs and cables, respectively. Four line lengths and four feeding networks (source impedances) were considered as parameters. The simulations were performed 200 times with random switches under each study condition. As a result, the study has found the following main characteristics of statistical distributions:

- Energization overvoltages for cables are lower than those for OHLs with respect to maximum, 2 %, and mean values. (Section 5.3.1)
- Energization overvoltages for cables do not show any dependence on the line length while those for OHLs peak with the line length 72 km. (Section 5.3.2)
- Energization overvoltages for cables become lower for a larger source impedance while those for OHLs peak with the source impedance 30 mH. (Section 5.3.3)

This section focuses on these three main characteristics in the identification of causes and physical meanings. The analysis in this section shows only one type of OHLs and cables because the same characteristics and contributing factors were found in all OHL and cable types.

5.3.1   Analysis on the Highest Overvoltages

First, we study why energization overvoltages for cables are lower than those for OHLs with respect to maximum, 2 %, and mean values. It is done by analysing voltage waveforms of energization overvoltages. Here, we define the maximum overvoltage as the largest overvoltage found in 200 random simulations, and the highest overvoltage as the largest overvoltage in one figure, or in other words, in one to four voltage waveforms.

Fig. 5.25 shows initial voltage waveforms of the energization overvoltage at the receiving end (*Vr*) and at the sending end (*Vs*) for one type of OHLs. The OHL was energized at the voltage peak of phase a (5 ms), and the voltage waveforms of phase a are shown in Fig. 5.25. The line length and the source impedance were fixed to 48 km and 30 mH, respectively.

Fig. 5.25 Initial voltage waveforms of the energization overvoltage for an OHL (line length: 48 km, source impedance: 30 mH).

For the OHL, the overvoltage of the inter-phase mode travels at the speed of light. It arrives at the receiving end 0.16 ms after it departs from the sending end (1st wave).

$$48\,\text{km} \div 300\ \text{m/μs} = 0.16\ \text{ms}$$

The inter-phase mode is reflected back to the sending end, but *Vr* rises towards around 2 pu as the overvoltage of the earth-return mode arrives. The propagation time of the earth-return mode can be obtained by performing frequency scan to the energized system or by performing Fourier transform to the voltage waveform. The result of the frequency scan shows the dominant frequency 980 Hz, which corresponds to the cycle time 1.02 ms. The result is reasonable as Fig. 5.25 shows the voltage peak of the earth-return mode with an interval of 1.02 ms.

The initial voltage rise time at the receiving end is difficult to find theoretically. The receiving end voltage starts to rise at 5.16 ms. Looking at the voltage amplitude of the earth-return mode, the voltage starts to rise from near the minimum. It suggests that it takes about 0.51 (= 1.02 / 2) ms to reach the maximum of the earth-return mode, but Fig. 5.25 shows the earth-return mode reaches its maximum in approximately 0.32 ms after it starts to rise.

This can be explained by the rate of voltage rise. When the voltage starts from the minimum, the rate of the voltage rise should increase in the first (1.02 / 4) ms and should decrease in the remaining (1.02 / 4) ms, assuming the receiving voltage follows the sinusoidal wave. However, in Fig. 5.25, the rate of voltage rise is largest when the receiving voltage starts to rise. This makes the voltage rise time to 2 pu shorter, and the earth-return mode reaches its maximum in approximately 5.48 (= 5.16 + 0.32) ms.

This reduction of the voltage rise time affects the magnitude of the highest overvoltage since 5.48 ms is exactly when the inter-phase mode comes back to the receiving end (2nd wave). As shown in Fig. 5.25, the inter-phase mode comes back to the receiving end with an interval of 0.32 ms as it travels at the speed of light. Since the peak of the earth-return mode (1st wave) and the peak of the inter-phase mode (2nd wave) reach their maximum almost at the same time around 5.48 ms, *Vr* goes above 2 pu and reaches to 2.3 pu.

The same analysis on the initial voltage waveforms is performed for one type of underground cables. Fig. 5.26 shows initial voltage waveforms of the energization overvoltage at the receiving end (*Vr*) and at the sending end (*Vs*). Study conditions, such as the switch timing (5 ms), line length (48 km), and source impedance (30 mH), are kept equal to the study on the OHL.
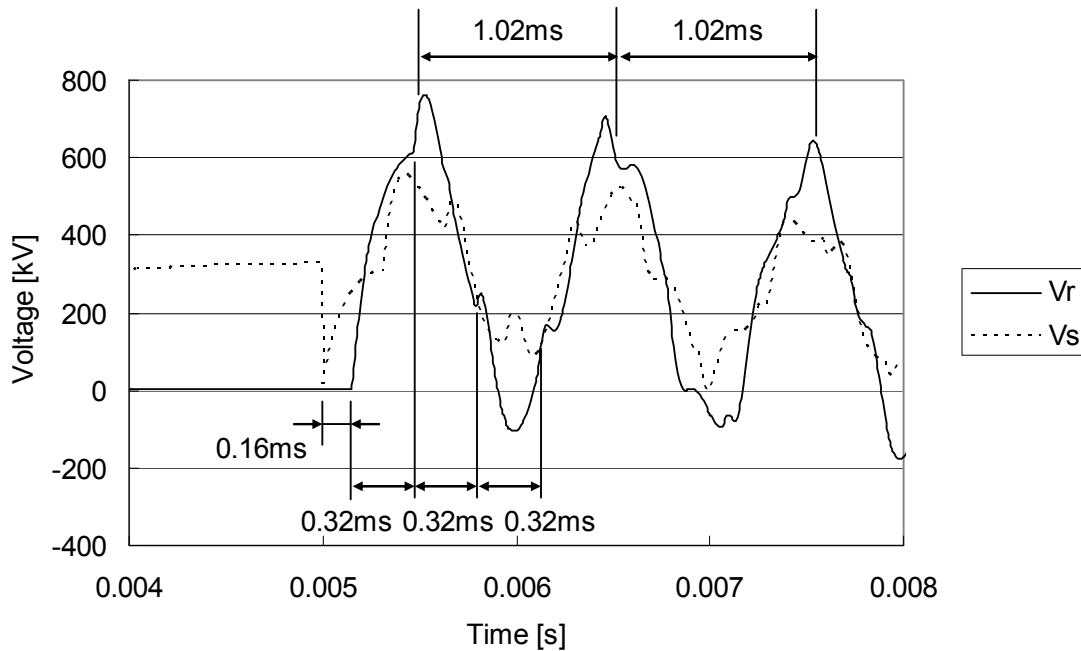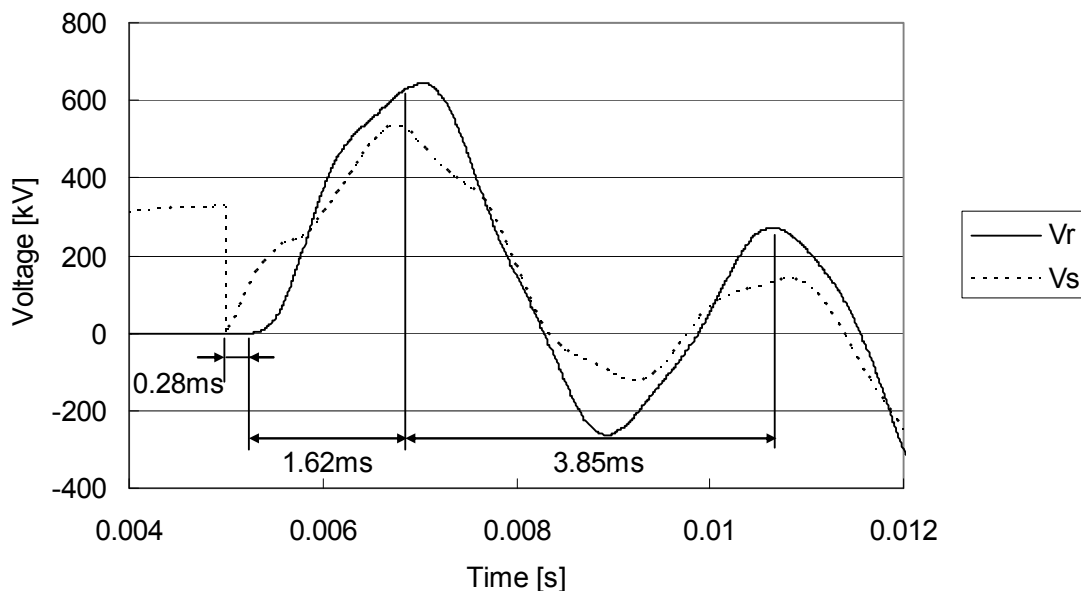

Fig. 5.26 Initial voltage waveforms of the energization overvoltage for a cable
(line length: 48 km, source impedance: 30 mH).

In case of the underground cable, the overvoltage of the coaxial mode first arrives at the receiving end (1st wave). When a cable is not cross-bonded, the coaxial mode travels at

$$\frac{300}{\sqrt{\varepsilon I1}} = \frac{300}{\sqrt{2.852}} = 178 \,\text{m}/\text{µs}$$ Eqn. 5.4

Here, $\varepsilon I1$ is the relative permittivity of the insulation in Table 3-2, which is corrected to account for semiconductive layers.

For a cross-bonded cable, it is known that the propagation velocity is reduced further, but it is not known how to analytically derive the reduced velocity. The propagation velocity is therefore derived from the propagation time. Fig. 5.26 shows the coaxial mode (1st wave) arrives at the receiving end 0.28 ms after it leaves the sending end. The propagation velocity is calculated as 171 m/µs (= 48 km / 0.28 ms). The reduction of 7 m/µs or 3.5 % is a typical value.

Similarly to the OHL, the coaxial mode is reflected back to the sending end, but *Vr* rises towards around 2 pu as the overvoltage of the inter-phase mode arrives. The propagation time of the inter-phase mode can be obtained by performing frequency scan to the energized system or by performing Fourier transform to the voltage waveform. The result of the frequency scan shows the dominant frequency 260 Hz, which corresponds to the cycle time 3.85 ms. The result is reasonable as Fig. 5.26 shows the voltage peak of the inter-phase mode with an interval of 3.85 ms.

The modes found in the energization overvoltage of the OHL and the cable are summarized in Table 5-10.

Table 5-10 Dominant Mode and Superimposed Mode of the Energization Overvoltage

	OHL	Underground cable
Dominant mode (cycle time)	Earth-return mode (1.02 ms)	Inter-phase mode (3.85 ms)
Superimposed mode (propagation time)	Inter-phase mode (0.16 ms)	Coaxial mode (0.28 ms)

Now, comparing the initial voltage waveforms of the OHL and the cable, the superimposition of two different modes found in the OHL cannot be observed clearly in the cable. There are some distortions of voltage waveforms on the inter-phase mode caused by the coaxial mode, but the distortions only have a small contribution on the highest overvoltage. This is because the overvoltage of the coaxial mode is smaller and more obtuse, compared with the inter-phase mode in the OHL.

Another factor affecting the difference in the highest overvoltage is the long cycle time of the inter-phase mode in the cable. About the time when the inter-phase mode reaches its maximum (1st wave), the 4th wave of the coaxial mode arrives at the receiving end. At this time, the coaxial mode is highly damped and is difficult to observe. Even in the OHL, the inter-phase mode can have an impact on the highest overvoltage only until its 2nd wave. It is highly damped and is difficult to observe after the 3rd wave.

5.3.2   Analysis on the Effects of Line Length

Second, we study why energization overvoltages for cables do not show any dependence on the line length while those for OHLs peak with the line length 72 km.

Fig. 5.37 shows initial voltage waveforms of energization overvoltages of the OHL at the receiving end (*Vr*). The switch timing is set to 5 ms as in the last section. The source impedance is set to 30 mH since the maximum overvoltage was observed with the source impedance 30 mH.
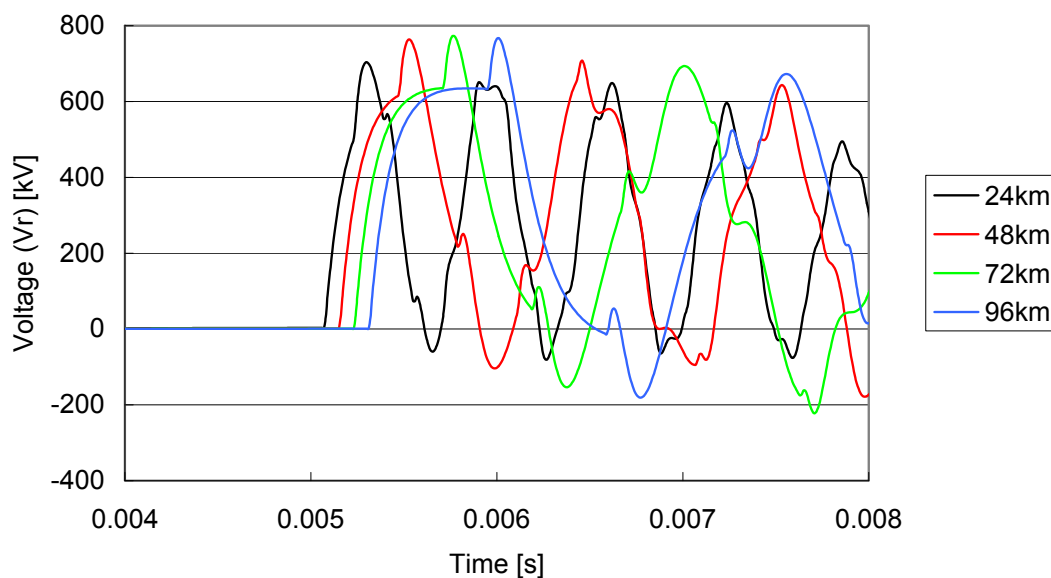

Fig. 5.27 Initial voltage waveforms of the energization overvoltage for the OHL (source impedance: 30 mH).

Fig. 5.27 demonstrates that highest overvoltages are caused by the superimposition of the earth-return mode (1st wave) and the inter-phase mode (2nd wave), regardless of the line length.

However, depending on the line length, the inter-phase mode (2nd wave) comes back to the receiving end at different points-on-wave of the earth-return mode (1st wave). For example, when the line length is 24 km, the inter-phase model (2nd wave) comes back to the receiving end before the earth-return mode (1st wave) reaches its maximum. As a result, the highest overvoltage becomes lower when the line length is 24 km. When the line length is 72 km, the inter-phase mode (2nd wave) comes back to the receiving end exactly when the earth-return mode (1st wave) reaches its maximum. This is why energization overvoltages of OHLs peak with the line length 72 km.

It has been shown that, for the source impedance 30 mH, the line length 72 km leads to the highest overvoltage. Considering how highest overvoltages are caused, different line lengths should lead to the highest overvoltage for different source impedances. For example, when the source impedance is 100 mH, the cycle time of the dominant overvoltage becomes larger. Therefore, a longer line length, which requires longer propagation time, should lead to the highest overvoltage.

Fig. 5.38 shows initial voltage waveforms of energization overvoltages of the cable when the source impedance is 100 mH. It demonstrates that the line length 96 km leads to the highest overvoltage as expected. This was, however, not observed in Section 5.1.4.4 since the source impedance 100 mH was not the study condition that leads to the maximum overvoltage. That is, the study condition 100 mH and 96 km caused a lower overvoltage than 30 mH and 96 km.
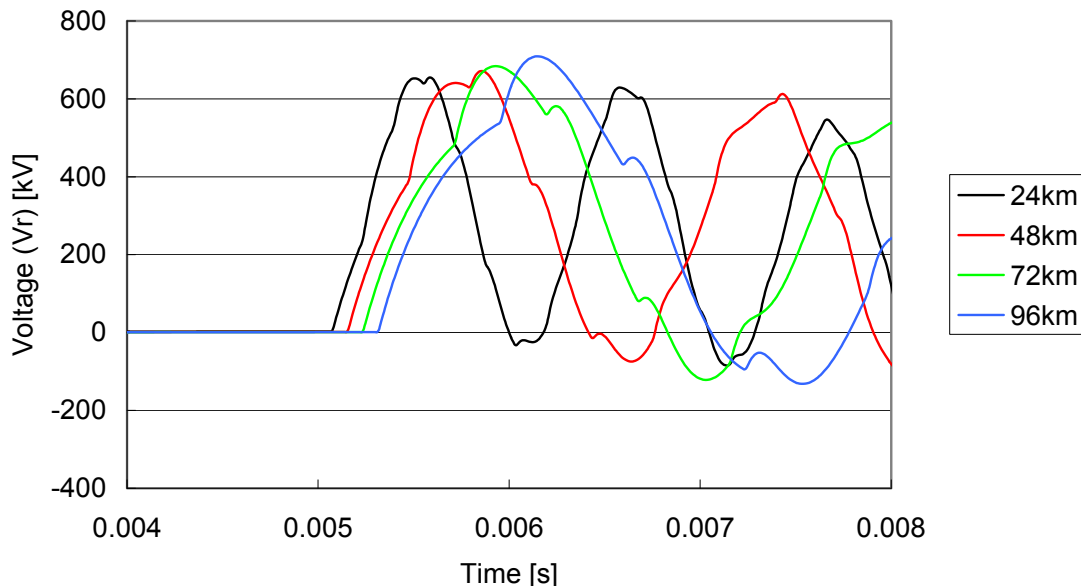

Fig. 5.28 Initial voltage waveforms of the energization overvoltage for the OHL (source impedance: 100 mH).

Fig. 5.29 shows initial voltage waveforms of energization overvoltages of the cable at the receiving end (*Vr*). The source impedance is set to 1 mH since the maximum overvoltage was observed with the source impedance 1 mH. As the source impedance is set so small, not only the rate of voltage rise but also the magnitude of the overvoltage becomes larger, compared with other source impedance values.

Another significant difference from other source impedance values is how the coaxial mode is reflected at the sending end. With the source impedance 1 mH, the reflection at the sending end is negative reflection, whereas the reflection at the sending end is positive reflection with other source impedance values. It is because the voltage level at the sending end is fixed to the source voltage when the source impedance is 1 mH.

The difference of the reflection can clearly observed in Fig. 5.29. So far, the superimposition of the two modes raised the highest overvoltage. On the contrary, in Fig. 5.29, the negative coaxial mode (2nd wave) makes dents on the peaks of the inter-phase mode (1st wave). The inter-phase mode (1st wave) is larger for shorter line lengths, but the negative coaxial mode (2nd wave) is also larger for shorter line lengths. As a result, the highest overvoltage is observed in case of the line length 48 km, and the effect of the line length on the highest overvoltage is reduced.

Fig. 5.29 Initial voltage waveforms of the energization overvoltage for the cable (source impedance: 1 mH).

Fig. 5.30 and Fig. 5.31 compare initial voltage waveforms of energization overvoltages of the cable for source impedances 30 mH and 100 mH.

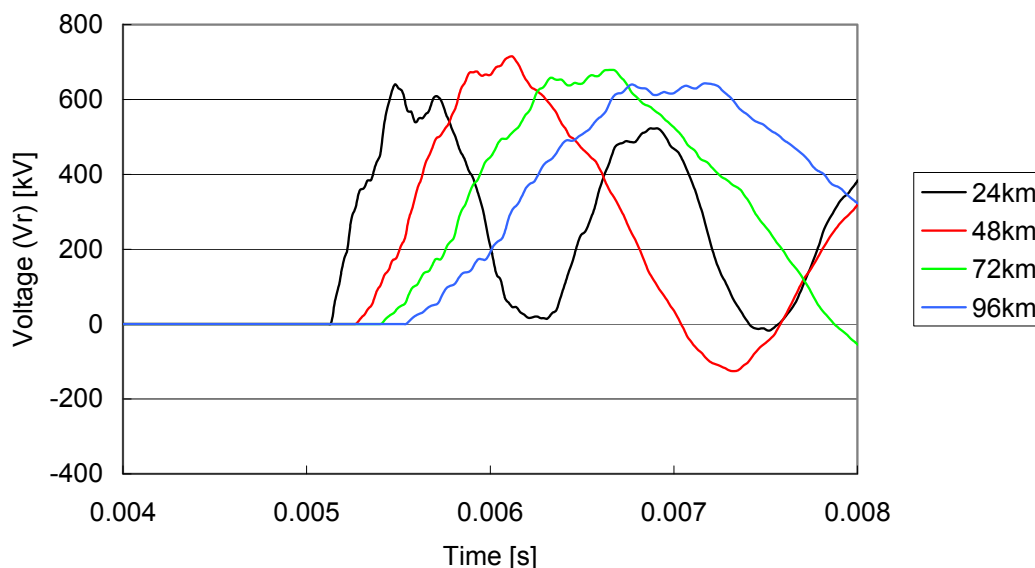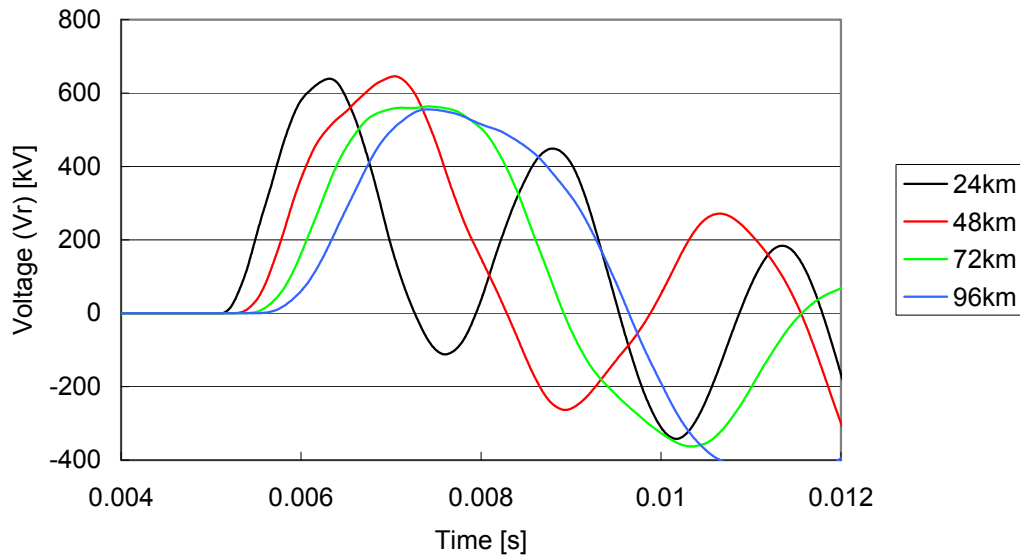**Fig. 5.30 Initial voltage waveforms of the energization overvoltage for the cable (source impedance: 30 mH).**
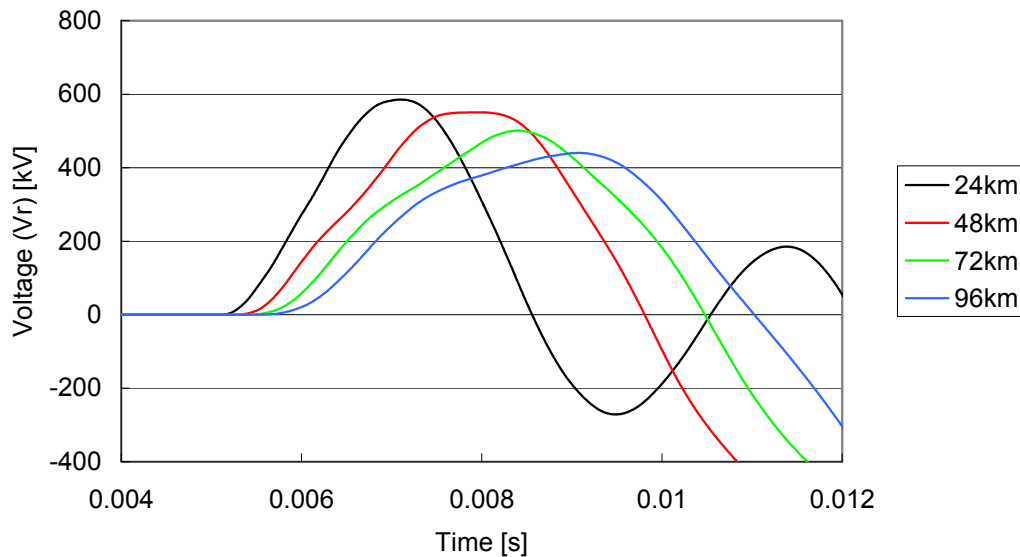
Fig. 5.31 Initial voltage waveforms of the energization overvoltage for the cable (source impedance: 100 mH).

With the source impedances 30 mH and 100 mH, shorter line lengths lead to higher overvoltages as expected. This characteristic was, however, not observed in Section 5.1.4.4 since the source impedance 30 mH or 100 mH was not the study condition that leads to the maximum overvoltage. The negative coaxial mode is not observed in these cases.

As we found in Section 5.3.1, the cycle time of the dominant mode of the cable is long (3.85 ms) with the line length 48 km and the source impedance 30 mH. It becomes even longer for longer line lengths or larger source impedances. As such, the horizontal axis of Fig. 5.30 and Fig. 5.31 is extended from 8 ms to 12 ms. The cable is energized at the voltage peak of phase a (5 ms), but the source voltage goes down to zero at 10 ms. This also contributes to lower overvoltages in case of longer line lengths or larger source impedances.

5.3.3   Analysis on the Effects of Feeding Network

Third, we study why energization overvoltages for cables become lower for a larger source impedance while those for OHLs peak with the source impedance 30 mH.

Fig. 5.32 shows initial voltage waveforms of energization overvoltages of the OHL at the receiving end (Vr). The switch timing is set to 5 ms as in the previous sections. The line length is set to 72 km since the maximum overvoltage was observed with the source impedance 72 km.
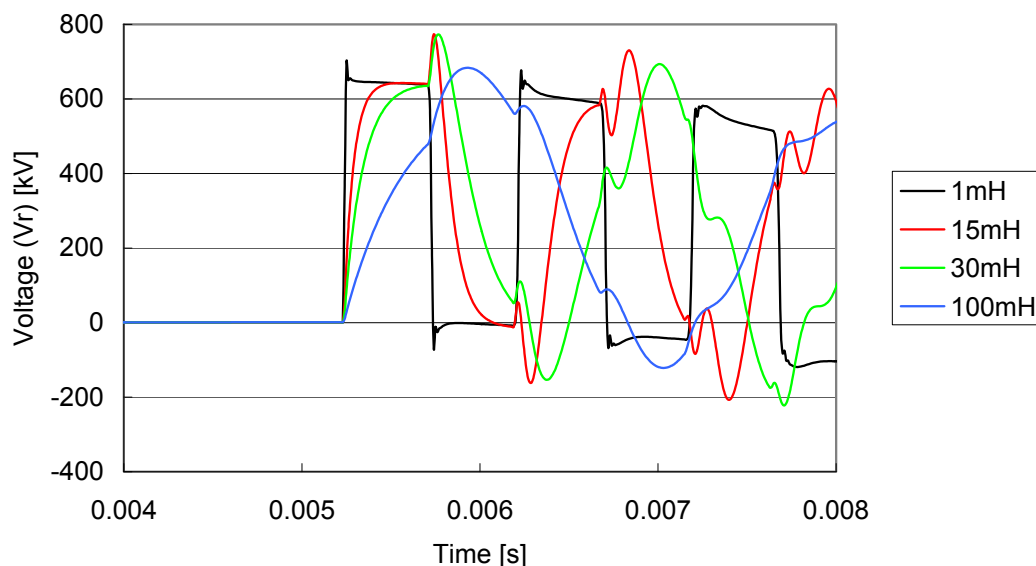
Fig. 5.32 Initial voltage waveforms of the energization overvoltage for the OHL (line length: 72 km).

As discussed in Section 5.3.2, the highest overvoltage of the OHL is determined by the timing when the earth-return mode reaches its maximum and the inter-phase mode arrives at the receiving end. Fig. 5.32 shows that source impedances 15 mH and 30 mH have the timing to cause high overvoltages. When the source impedance is 1 mH, the overvoltage of the inter-phase mode is smaller, which results in the lower overvoltage.

Fig. 5.33 and Fig. 5.34 show initial voltage waveforms of energization overvoltages of the cable for line lengths 24 km and 48 km. These two lengths were selected as we learned, in Section 5.3.2, that shorter line lengths lead to higher overvoltages except when the source impedance is 1 mH.

Fig. 5.33 demonstrates that smaller source impedances lead to larger overvoltages as we found in Section 5.1.4.5. This is not true only when the source impedance is 1 mH.
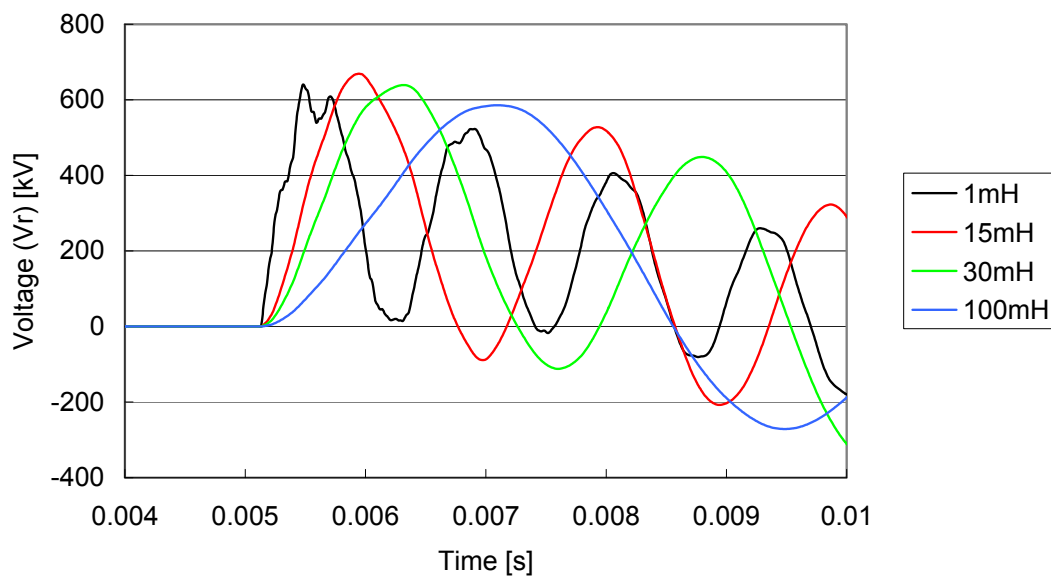
Fig. 5.33 Initial voltage waveforms of the energization overvoltage for the cable (line length: 24 km).

When the source impedance is 1 mH, the highest overvoltage is caused when the line length is 48 km as we learned in the last section. Looking at the source impedance 1 mH in Fig. 5.34 and other source impedances in Fig. 5.33, it is clear that smaller source impedances lead to larger overvoltages.
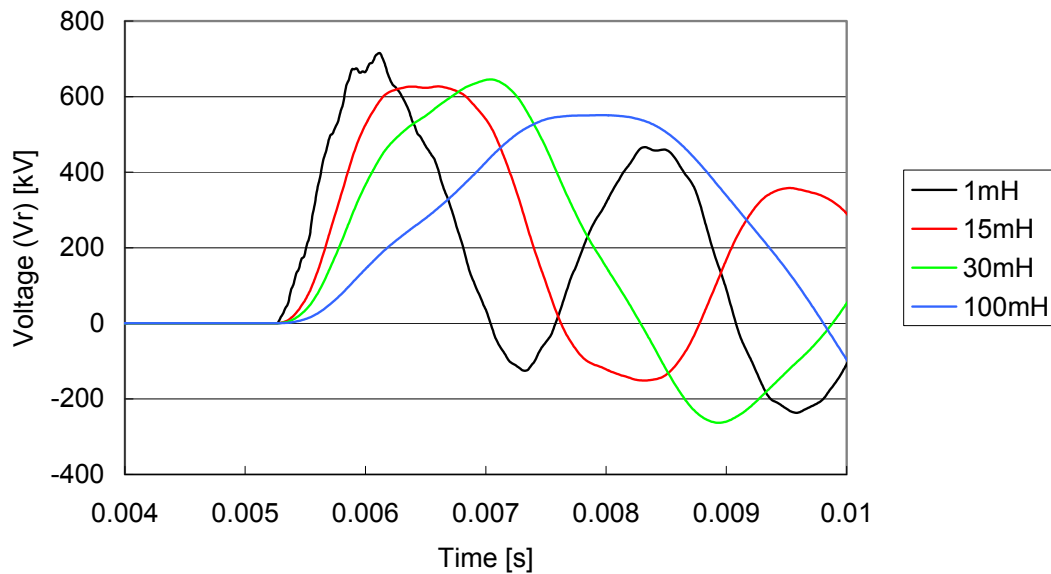
Fig. 5.34 Initial voltage waveforms of the energization overvoltage for the cable (line length: 48 km).

It is reasonable to have larger overvoltages with smaller source impedances as the rate of voltage rise becomes larger for smaller source impedances. The larger rate of voltage rise is apparent as the smaller source impedances lead to a higher dominant frequency contained in the energization overvoltage. For larger source impedances, due to their slow rates of voltage rise, the fundamental component already starts to decrease from the voltage peak by the time when the inter-phase mode reaches its maximum.

5.3.4   Summary

This section analyzed the characteristics of the energization overvoltage found in Sections 5.1 and 5.2. The analysis has found that these characteristics are not caused by random switching by accident, rather there are contributing factors and physical meanings behind the characteristics.

In summary, the analysis has identified contributing factors and has explained their physical meanings as follows:

•   Energization overvoltages for cables are lower than those for OHLs because the overvoltage of the coaxial mode in cables is smaller and more obtuse, compared with the inter-phase mode in OHLs. The long cycle time of the inter-phase mode in cables also affects this characteristic.

•   Energization overvoltages for cables do not show any dependence on the line length because

the maximum overvoltages are observed with the source impedance 1 mH. The negative coaxial mode makes dents on the peaks of the maximum overvoltage when the source impedance is 1 mH. With the other source impedances, shorter line lengths lead to higher overvoltages.

- Energization overvoltages for cables become lower for larger source impedances, which is reasonable from the theoretical analysis.

- Highest energization overvoltages for OHLs are caused by the superimposition of the inter-phase mode on the earth-return mode. The timing of the superimposition determines the magnitude of the highest overvoltage, and the line length and the source impedance affect this timing. The energization overvoltage for OHLs peak with the line length 72 km and the source impedance 30 mH because the combination provided the best timing for the superimposition within the studied conditions.

Since the contributing factors and physical meanings of the characteristics have been identified, it is now possible to use the obtained statistical distribution for the determination of insulation levels of cable systems. Especially, the obtained statistical distribution suggests a possible application of lower insulation levels to cable systems compared with OHLs. However, it may present a future challenge to define insulation levels for temporary overvoltages since a possibility of severe temporary overvoltages are reported in relation to cable systems [13][14][18][19].

5.4 Ground Fault and Fault Clearing Overvoltage

5.4.1   Study Conditions and Parameters

The idea of the statistical evaluation is also applied to the evaluation of the ground fault and fault clearing overvoltages since the fault location and the fault timing vary and cannot be controlled. Instead of considering them as random phenomena, it is a common practice to cover different fault locations and fault timings with fixed (pre-defined) steps.

Table 5-11 summarizes the study conditions and parameters for the ground fault and fault clearing overvoltages. The 10 fault locations were selected so that the separation between each fault location is limited to 3 – 6 km. In order to cover 10 fault locations and 19 fault timings, 190 simulations were performed. The 2 % value is the 3rd highest overvoltage in these simulations.

Table 5-11 Study Conditions and Parameters for the Ground Fault and Fault Clearing Overvoltage

Fault type	Single line to ground fault (core to sheath)
Fault location	Five points between ASV – TOR and TOR – KYV ASV – TOR: AT3, AT6, AT8, AT11 and AT13 TOR – KYV: TK4, TK7, TK10, TK13 and TK14
Fault timing	0° – 180° (10° step)
Fault clearing time	First current zero at least 40 ms after the fault occurrence
Fault clearing sequence	Line-CBs of all three phases are opened at the above fault clearing time. Sequential switching
Feeding source	Off-peak load condition + dummy source: 15 mH (strong source) and 100 mH (weak source)

As in the energization overvoltage analysis, two feeding networks were considered. One is the strong source case and the other one is the weak source case. Both feeding networks were modeled based on the off-peak load condition and by adding a dummy source to the Asnæsværket 400 kV bus. The source impedance of the dummy source impedance was set to 15 mH and 100 mH in the weak source and strong source case, respectively.

Since the ground fault and fault clearing overvoltages depend on the fault current, the fault current level needs to be set within a reasonable range. In a cable energization overvoltage analysis, the dummy source impedance was set to 1 mH in order to find the effect of a steep rise of an initial

overvoltage. However, this setting should be avoided in the ground fault and fault clearing overvoltage analysis as unreasonably large fault current will flow in the simulation with this setting. The dummy source impedance was therefore set to 15 mH in the strong source case.

The dummy source was also added to the off-peak load condition even in the weak source case, but the dummy source impedance was set to a large value (100 mH). Without the dummy source, ground fault and fault clearing overvoltages were almost unnoticeable since the fault current was too small.

In the ground fault and fault clearing overvoltage analysis, the highest overvoltage is not always observed at the open terminal. In addition, there is no open terminal for the ground fault overvoltage. As such, the overvoltages were monitored at AT3, AT6, AT8, AT11, AT13, TK4, TK7, TK10, TK13 and TK14 as well as at Asnæsværket, Torslunde and Kyndbyværket.

5.4.2   Results of the Analysis

Fig. 5.35 and Table 5-12 show the cumulative probability distributions of the ground fault and fault clearing overvoltages and their characteristics. The overvoltage level is as low as the energization overvoltage of the Kyndbyværket – Asnæsværket line in the off-peak load condition. The probability distributions are affected by the dummy source impedance, but the overvoltage level is low in both cases.
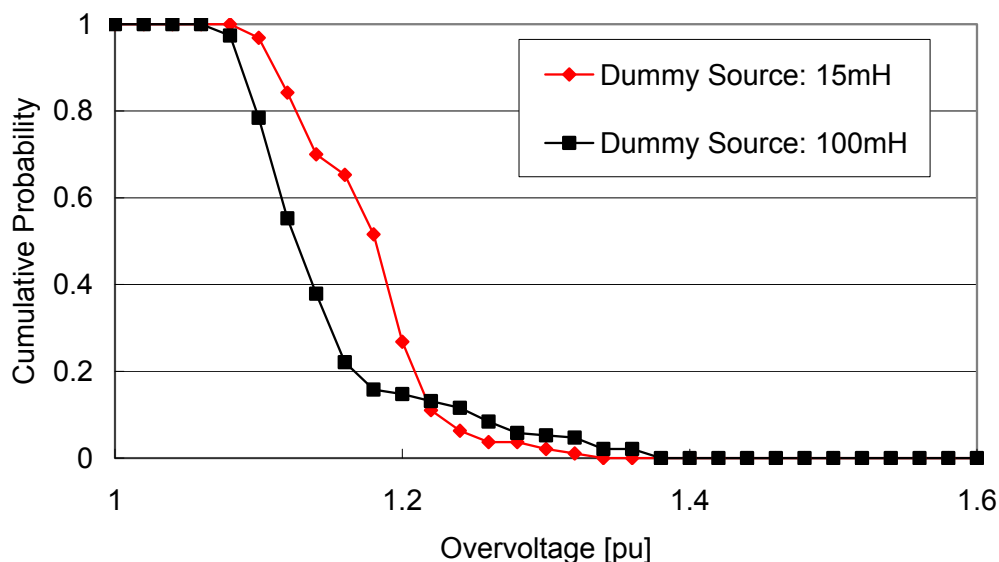
Fig. 5.35 Cumulative probability distributions for the ground fault and fault current overvoltage.

Table 5-12 Characteristics of Probability Distributions for the Ground Fault and Fault Clearing Overvoltage

	Dummy Source: 15mH	Dummy Source: 100mH
Max. OV [pu]	1.33	1.37
2% OV [pu]	1.30	1.36
Average OV [pu]	1.17	1.14
Standard dev. [pu]	0.0482	0.0647
Skewness	0.430	1.79
Kurtosis	3.52	5.76

With the dummy source impedance 15 mH and 100 mH, the maximum overvoltage was observed when the fault occurs at AT3 and at the phase angle 60° and 70°, respectively. In both cases, the maximum overvoltage was the ground fault overvoltages and was not the fault clearing overvoltages. Fig. 5.36 shows the profile of the maximum ground fault overvoltages along the length of the Kyndbyværket – Asnæsværket line. The figure shows that the maximum overvoltages were observed at the Asnæsværket 400 kV bus.
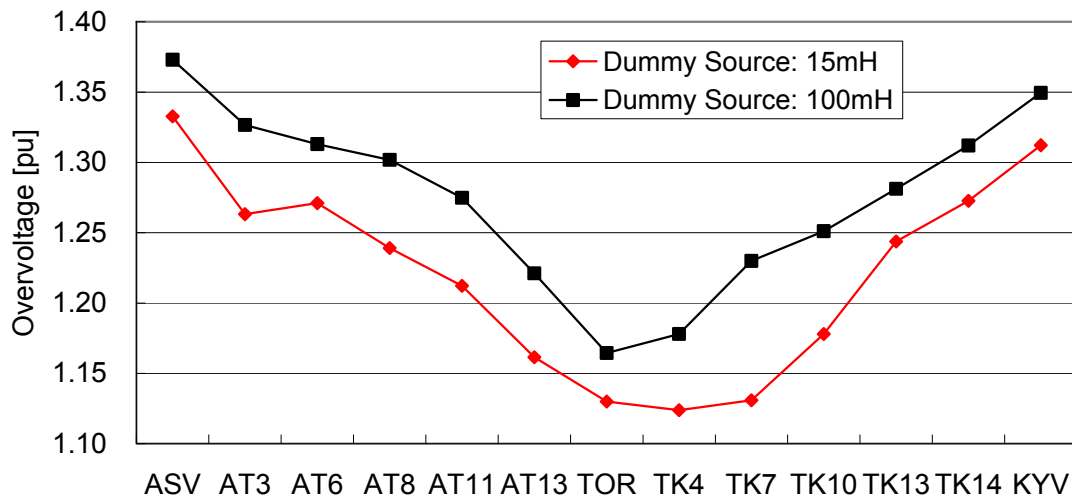
Fig. 5.36 Profile of the maximum ground fault overvoltages.

As the maximum overvoltage was observed at the Asnæsværket 400 kV bus, the voltage waveforms at the Asnæsværket 400 kV bus are given in Fig. 5.37 and Fig. 5.38. The figures show that both ground fault overvoltages and fault clearing overvoltages are highly damped.
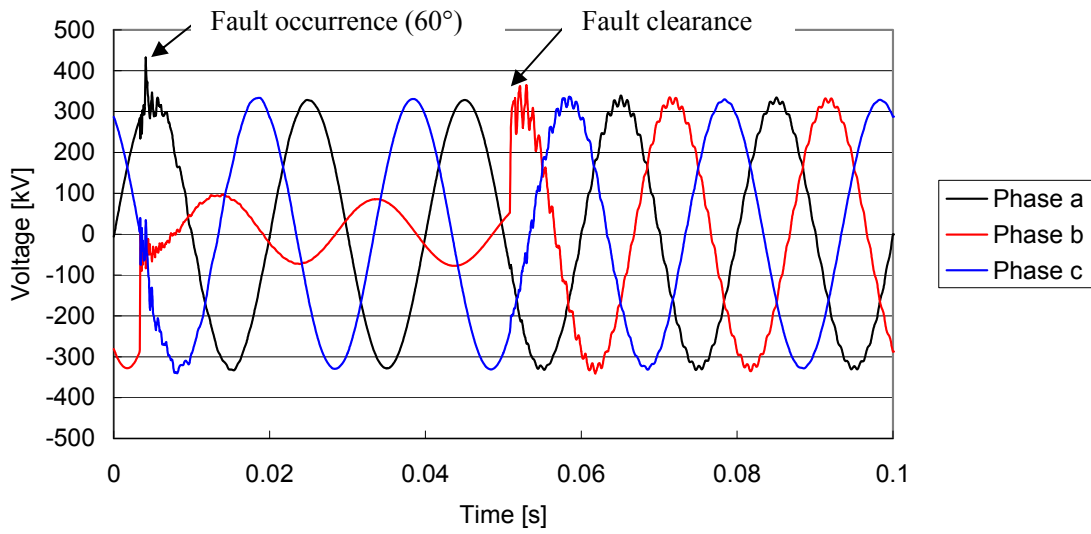
Fig. 5.37 Voltage waveforms of the maximum ground fault overvoltage at the ASV 400 kV bus (dummy source: 15 mH).
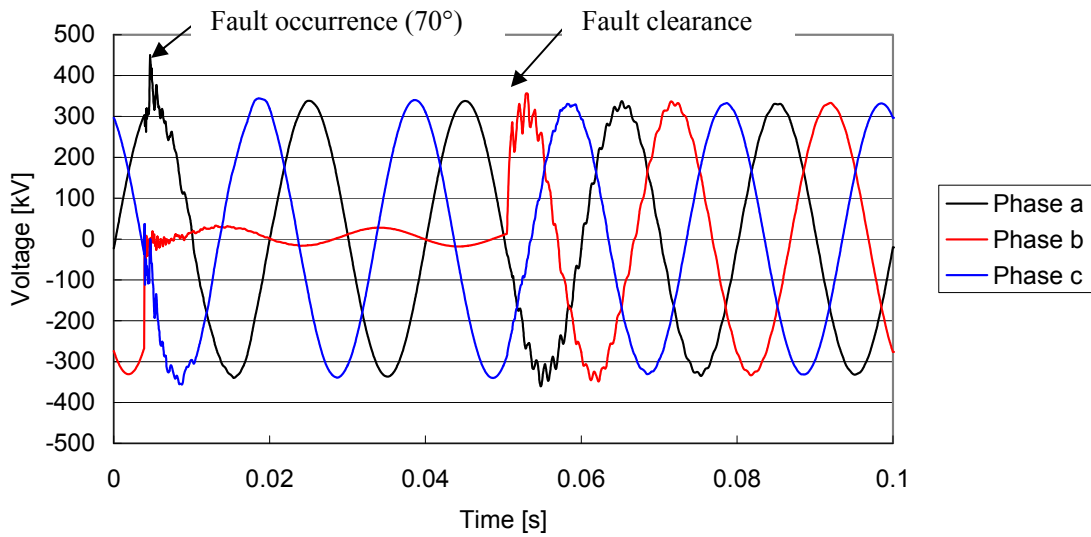
Fig. 5.38 Voltage waveforms of the maximum ground fault overvoltage at the ASV 400 kV bus (dummy source: 100 mH).

5.4.3 Results with the Sequential Switching

The sequential switching has been adopted as a countermeasure to the zero-missing phenomenon. With the sequential switching, the sequence for the fault clearing is different from the ordinal sequence simulated in the previous section. Detailed explanations on the sequential switching are given in Section 6.3.1.

According to the fault clearing sequence with the sequential switching, the ground fault and fault clearing overvoltage was analyzed with the following sequence:

Fault occurrence (phase a):   0.0 – 0.1 s

Fault clearing (phase a):   0.05 s

Shunt reactor tripping (phases b and c):   0.11 s (only on the Kyndbyværket side)

Line breaker tripping (phases b and c):   0.17 s

The time separations between above steps were set shorter than the actual setting. As long as the overvoltage caused by the previous step is well damped, the shorter time separations have no effect on the overvoltage caused by the next step.

In the previous section with the normal fault clearing sequence, ground faults in different phases were simulated. In this section with the sequential switching, ground faults occurs only in phase a. Since three phases are well balanced in the Kyndbyværket – Asnæsværket cable model, it is not expected that this has a major impact on the simulation results.

Fig. 5.39 and Table 5-13 show the cumulative probability distributions of the ground fault and fault clearing overvoltage and their characteristics. The maximum overvoltage level is lower than the overvoltage with the normal fault clearing sequence approximately by 0.1 pu. The average overvoltage is not affected by the sequential switching. The probability distributions are affected by the dummy source impedance, but the overvoltage level is low in both cases.
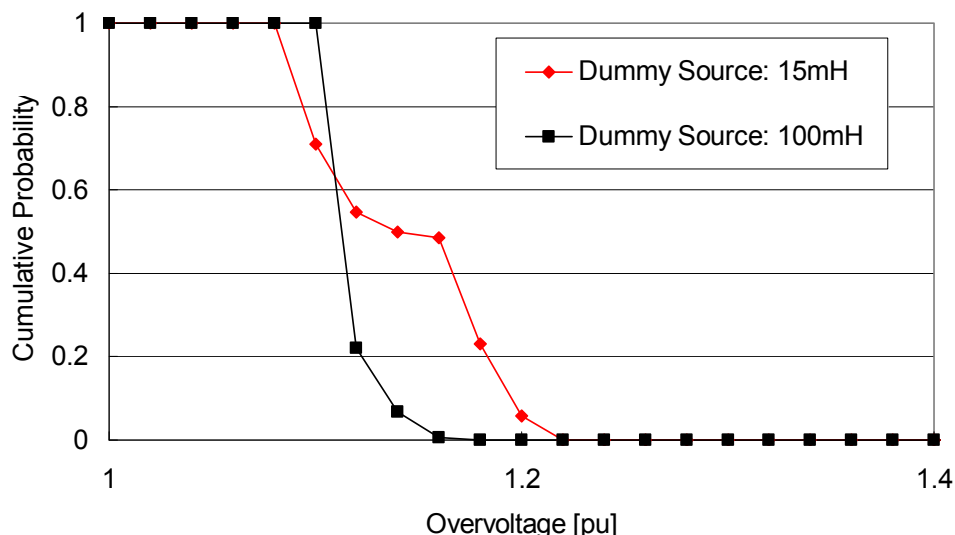
Fig. 5.39 Cumulative probability distributions for the ground fault and fault current overvoltage with the sequential switching.

Table 5-13 Characteristics of Probability Distributions for the Ground Fault and Fault Clearing Overvoltage with the Sequential Switching

	Dummy Source: 15mH	Dummy Source: 100mH
Max. OV [pu]	1.21	1.16
2% OV [pu]	1.21	1.15
Average OV [pu]	1.14	1.11
Standard dev. [pu]	0.0410	0.0145
Skewness	0.167	1.59
Kurtosis	1.42	4.47

With the dummy source impedance 15 mH and 100 mH, the maximum overvoltage was observed when the fault occurs at TK13 and TK17 respectively, and at the phase angle 130°. In both cases, the maximum overvoltages were the ground fault overvoltages and were not the fault clearing overvoltages. This means that the difference of the maximum overvoltage, compared to the one with the normal fault clearing, was not caused by the difference of the fault clearing sequence. The difference was caused by the faulted phase.

Fig. 5.40 shows the profile of the maximum ground fault overvoltages along the length of the Kyndbyværket – Asnæsværket line. The figure shows that the maximum overvoltages were observed at TK13 with the dummy source impedance 15 mH and at the Asnæsværket 400 kV bus with the dummy source impedance 100 mH.
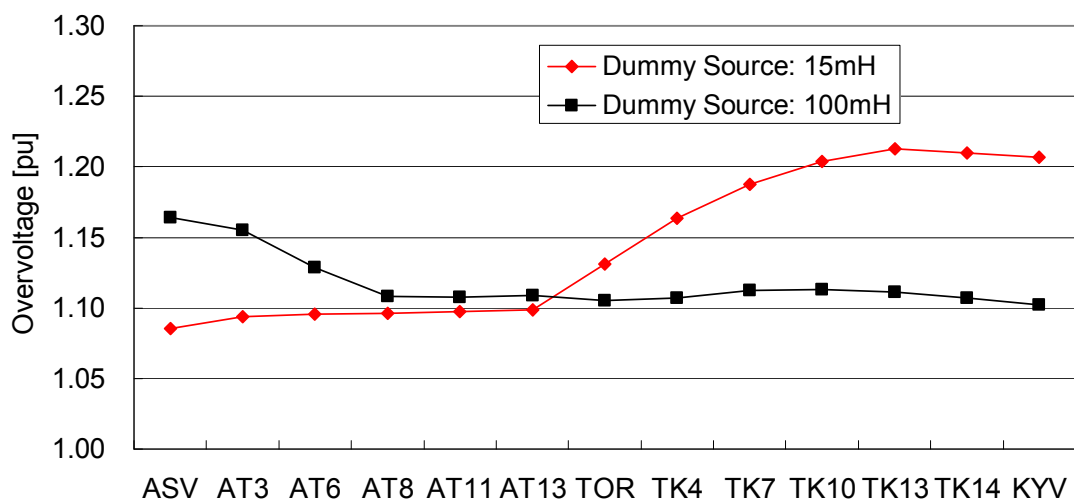
Fig. 5.40 Profile of the maximum ground fault overvoltages with the sequential switching.

As the maximum overvoltage was observed at TK13 with the dummy source impedance 15 mH, the voltage waveforms at TK13 are shown in Fig. 5.41. The line current at the Asnæsværket side is also shown in the figure for the better understanding of the sequential switching. The figures show that both ground fault overvoltages and fault clearing overvoltages are highly damped.

Fig. 5.41 Voltage and current waveforms of the maximum ground fault overvoltage at the ASV 400 kV bus with the sequential switching (dummy source: 15 mH).

As the maximum overvoltage was observed at Kyndbyværket 400 kV bus with the dummy source impedance 100 mH, the voltage waveforms at the bus are shown in Fig. 5.42
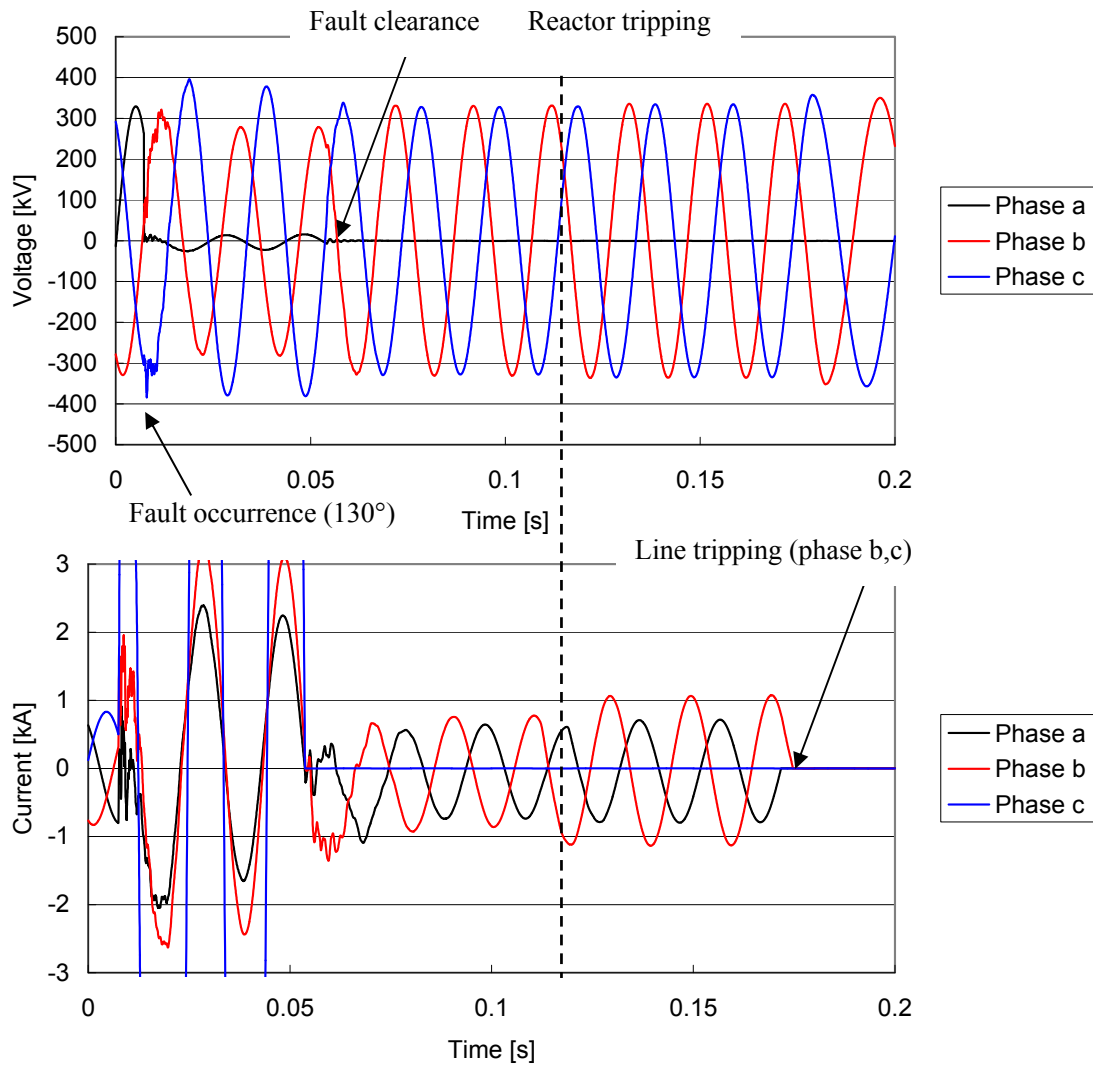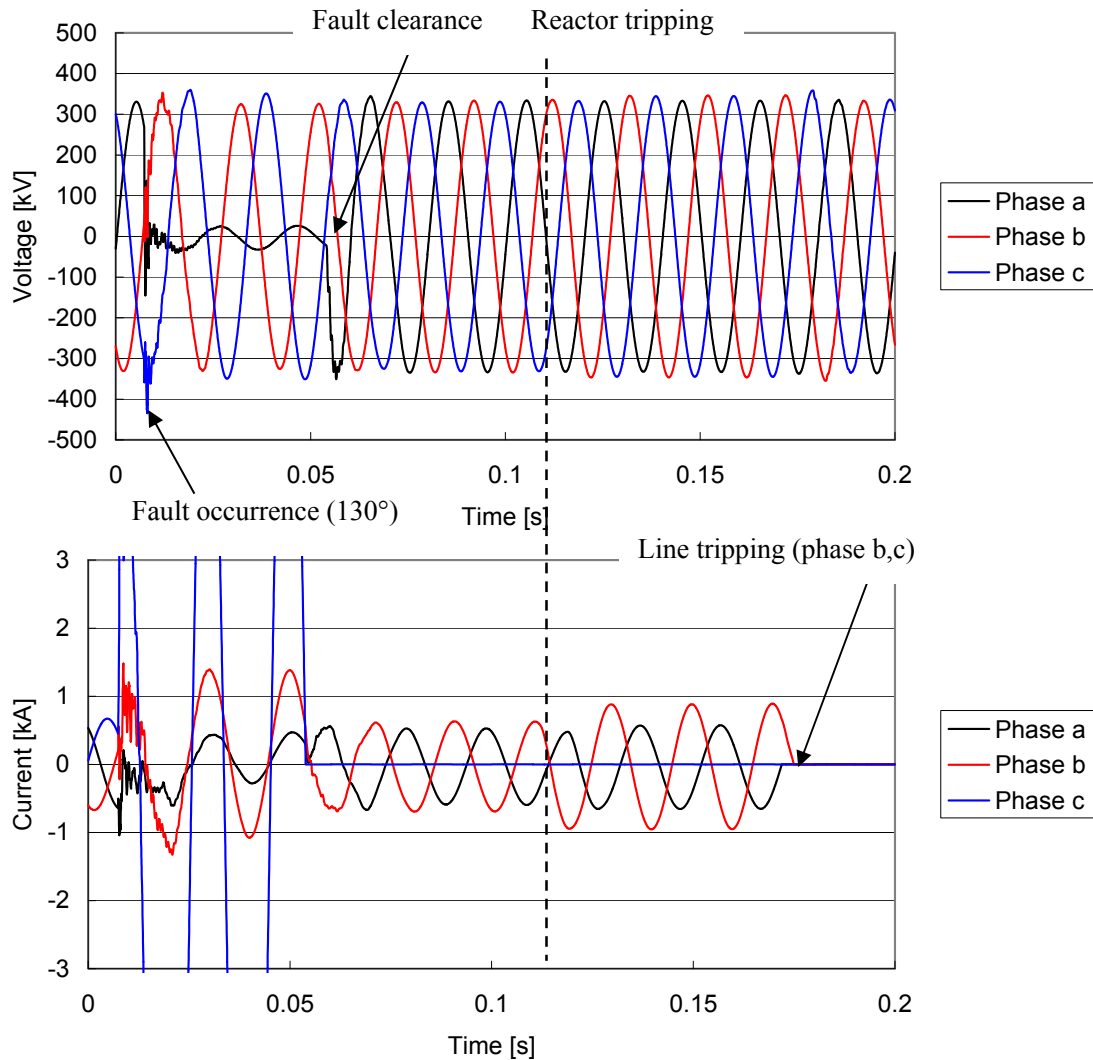

Fig. 5.42 Voltage and current waveforms of the maximum ground fault overvoltage at the ASV 400 kV bus with the sequential switching (dummy source: 100 mH).

5.5 Conclusion

This chapter studied the slow-front overvoltages of cable systems. In Section 5.1, the statistical distributions of line energization overvoltages were compared between overhead lines and cables. Through the comparison, it has been found that line energization overvoltages in cables are lower than those in overhead lines. More precisely, the maximum and mean values are lower, but the minimum values are almost equal. As a result, standard deviations are smaller for cables, and the statistical distributions of overhead lines are closer to the normal distribution than those of cables.

The statistical distributions show that, if one considers only line energization overvoltages, it is possible to apply lower withstand voltages for cable systems. However, there are issues related to temporary overvoltages in cable systems as discussed in the previous chapter. As such, careful examinations are necessary.

Section 5.2 studied the statistical distributions of energization overvoltages of the Kyndbyværket – Asnæsværket line. Even with an extremely severe condition, the maximum overvoltage found in the analysis was 2.37 pu, which was much lower than SIWV 1050 kV (3.2 pu).

The study has found that a strong source yields more severe results, which is in line with the simulation results with an inductive source. In addition, standard deviations were larger with the strong source. Additionally, it has been found that the maximum overvoltage becomes lower by the synchronized switching.

In all energizations, waveforms of the overvoltages looked very different from the ones typically observed with overhead lines. The observed wavefront was 2.6 ms, which is approximately ten times larger than the standard waveshape of the slow-front overvoltage 250/2500 μs. The difference was caused by the low dominant frequency contained in the energization overvoltages as discussed in Section 4.1.3.

Section 5.3 analyzed the characteristics of the energization overvoltage found in Sections 5.1 and 5.2. The section identified the contributing factors and physical meanings of the characteristics as summarized in Section 5.4.3 so that it would become possible to use the obtained statistical distributions for the determination of insulation levels of cable systems.

Section 5.4 studied the statistical distributions of ground fault and fault clearing overvoltages of the

Kyndbyværket – Asnæsværket line. The maximum overvoltage found in the analysis was 1.37 pu, which was much lower than SIWV 1050 kV (3.2 pu). The study has found that ground fault overvoltages are larger than fault clearing overvoltages. Effects of dummy source impedances were not significant.

The sequential switching may be applied to the Kyndbyværket – Asnæsværket line as a countermeasure of the zero-missing phenomenon. Since ground fault overvoltages were larger than fault clearing overvoltages, the sequential switching did not affect the severity of the overvoltages.

References

[1]   *Insulation Coordination for Power Systems*, Andrew R. Hileman, published by Marcel Dekker Inc., June 1999

[2]   CIGRE Working Group 13.02, "Switching Overvoltages in EHV and UHV Systems with Special Reference to Closing and Reclosing Transmission Lines," *Electra N°30*, pp. 70-122, 1973.

[3]   CIGRE Working Group 13.05, "The Calculation of Switching Surges," *Electra N°19*, pp. 67-78, 1971.

[4]   CIGRE Working Group 13.05, "The Calculation of Switching Surges – II. Network Representation for Energization and Re-energization Studies on Lines Fed by an Inductive Source," *Electra N°32*, pp. 17-42, 1974.

[5]   CIGRE Working Group 13.05, "The Calculation of Switching Surges – III. Transmission Line Representation for Energization and Re-energization Studies with Complex Feeding Networks," *Electra N°62*, pp. 45-78, 1979.

[6]   J. Sato, Y. Tsuchiya, A. Arai, N. Hotta, J. Shinavawa, N. Matsumoto, "Technical Development and View of Underground and Overhead Transmission Line," *SWCC Showa Review*, vol. 51, No. 1, 2001 (in Japanese)

[7]   L. Elgh, C.T. Jacobsen, B. Bjurstrom, G. Hjalmarsson, S.O. Olsson, "The 420 kV AC Submarine Cable Connection Denmark-Sweden," *CIGRE Session 1974*, 21-02.

[8]   I.A. Gubinsky, M.G. Khanukov, L.A. Kusnetsov, V.I. Masold, I.B. Peshkov, N.K. Sorochkin, "500 kV cable lines for hydro power stations," *CIGRE Session 1976*, 21-03.

[9]   W. Hahn, U. Muller, E.F. Peschke, " The first 380 kV bulk power transmission in Germany," *CIGRE Session 1976*, 21-08

[10] G. Gualtieri, G.M. Lanfranconi, W. Cavalli, "330-kV Oil-Filled Cables Laid in 1600-FT Vertical Shaft at Kafue Gorge Hydroelectric Plant," *IEEE Trans. on Power Apparatus and Systems*, vol. PAS-92, no. 6, Nov. 1973.

[11] Statistics of AC Underground Cables in Power Networks, *CIGRE Technical Brochure 338*, December 2007.

[12] Update of Service Experience of HV Underground and Cable Systems, *CIGRE Technical Brochure 379*, April 2009.

[13] *Assessment of the Technical Issues relating to Significant Amounts of EHV Underground Cable in the All-island Electricity Transmission System*, (available on the web) Tokyo Electric Power Company, November 2009, http://www.eirgrid.com/media/Tepco%20Report.pdf.

[14]   N. Momose, H. Suzuki, S. Tsuchiya, T. Watanabe, "Planning and Development of 500 kV Underground Transmission System in Tokyo Metropolitan Area," *CIGRE Session 1998*, 37-202.

[15]   M. Rebolini, L. Colla, F. Iliceto, "400 kV AC new submarine cable links between Sicily and the Italian mainland. Outline of project and special electrical studies," *CIGRE Session 2008*, C4-116.

[16]   L. Colla, S. Lauria, F. M. Gatta, "Temporary Overvoltages due to Harmonic Resonance in Long EHV Cables," *IPST 2007*, http://www.ipst.org/techpapers/2007/ipst_2007/papers_IPST2007/Session16/233.pdf.

[17]   Massey, F. J. "The Kolmogorov-Smirnov Test for Goodness of Fit," *Journal of the American Statistical Association*, vol. 46, no. 253, 1951, pp. 68–78.

[18]   T. Karasaki, T. Goto, A. Ametani, "An Abnormal Overvoltage due to Load Rejection on EHV Underground Transmission Lines", *International Conference on Power System Transients (IPST)*, September 1995.

[19]   L. Colla, M. Rebolini, F. Iliceto, "400 kV AC new submarine cable links between Sicily and the Italian mainland. Outline of project and special electrical studies", *CIGRE Session* C4-116, 2008.

Chapter 6 Other Studies

6.1 Protection of the EHV Cable System

6.1.1   Main Protection

Current differential relays are usually applied to the protection of EHV cable systems. When they are applied to a long EHV cable system, the following two issues need to be considered:

- The sum of currents at both ends does not become zero in the normal operating condition due to the cable charging current. The charging current needs to be compensated in the relay logic.

- Since shunt reactors are directly connected to cables, it is necessary to measure line currents excluding shunt reactor currents. CTs and current differential relays are connected so that the actual line current minus shunt reactor current is input into current differential relays.

For long HV underground cables, a charging current is relatively large which can affect the accuracy of current differential relays. In order to compensate the charging current, it is necessary to obtain charging current *Ic* by software computation using equations given in Fig. 6.1. Then, current *Id* is used for fault detection instead of *(Ia+ Ib)* [1].
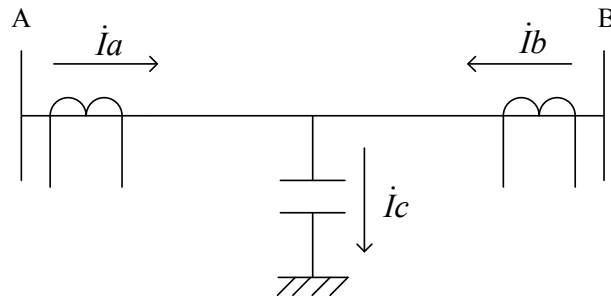
$$\dot{I}d = \dot{I}a + \dot{I}b - \dot{I}c$$

$$\dot{I}c = j\omega \begin{bmatrix} Caa + Cab + Cac & -Cab & -Cac \\ -Cab & Cbb + Cbc + Cba & -Cbc \\ -Cac & -Cbc & Ccc + Cca + Ccb \end{bmatrix} \cdot \dot{V}$$

Fig. 6.1 Compensation of a charging current in current differential relays.

6.1.2   Backup Protection – Ground Loop Impedance

Backup protection of EHV cable systems normally adopts a distance protection. The following items are often discussed with respect to the distance protection of long EHV cable systems:

- It is required to know accurate impedances of cable systems.

- Negative sequence distance protection is effective since it is not affected by the load current.

- Low order harmonics are contained in voltages and currents under disturbances, such as contingencies and network operations. Careful considerations are necessary to extract fundamental components from them.

Cable faults are normally single line to ground (SLG) faults. Short circuits are mostly man-caused and occur in very limited occasions. In a SLG fault, a cable core is short-circuited to the cable sheath, which is grounded at cable heads and normal joints. The return circuit for a SLG fault is later explained with Fig. 6.5.

Fig. 6.2 shows a circuit that expresses a SLG fault in a cable line. *Zl* is the cable impedance between the location of the impedance relay and the fault location.
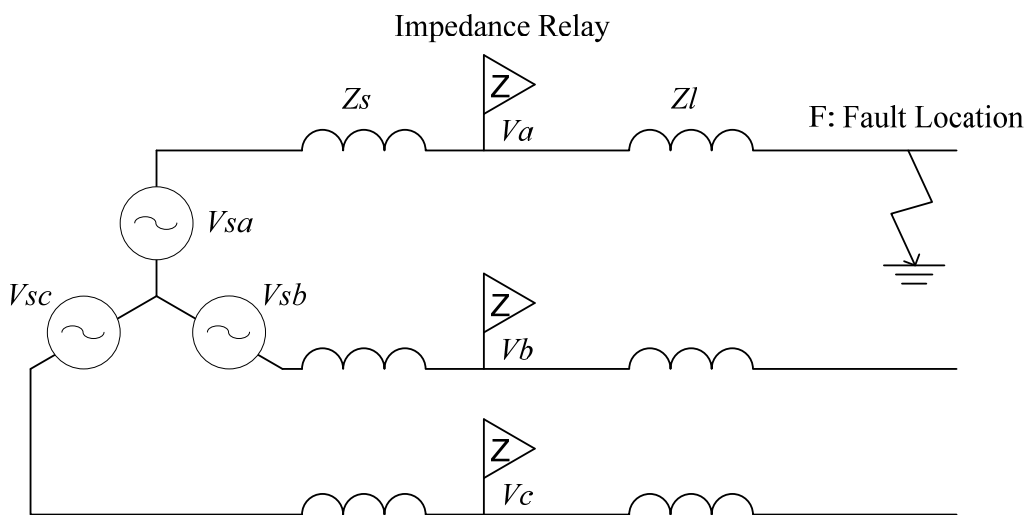
Fig. 6.2 SLG fault in a cable line.

The SLG fault in Fig. 6.2 can be expressed using symmetrical components as in Fig. 6.3.
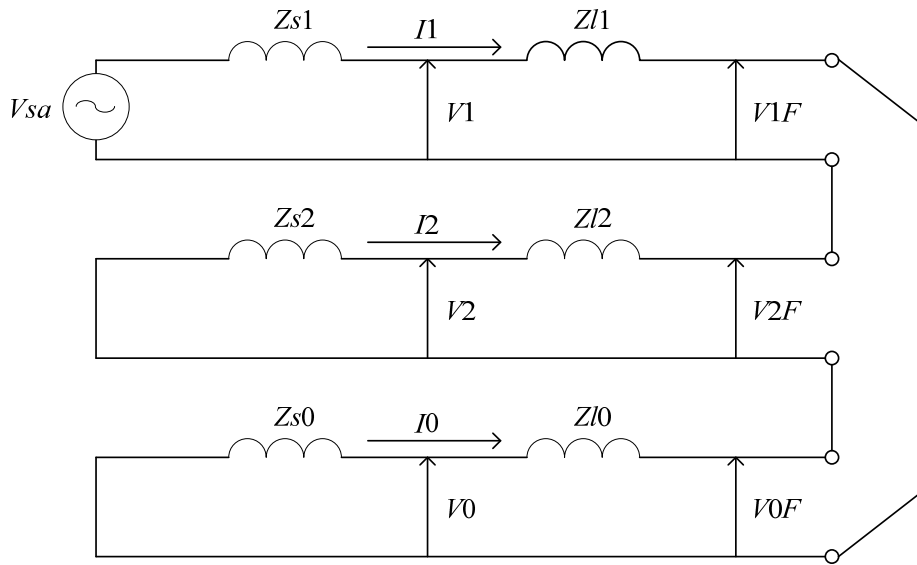
Fig. 6.3 Loop impedance in a single line to ground fault.

In Fig. 6.3,

$$Va = V1 + V2 + V0$$
$$= (Zl1 \times I1 + V1F) + (Zl2 \times I2 + V2F) + (Zl0 \times I0 + V0F)$$
$$= (Zl1 \times I1) + (Zl2 \times I2) + (Zl0 \times I0) + (V1F + V2F + V0F)$$
$$= (Zl1 \times I1) + (Zl1 \times I2) + (Zl0 \times I0)$$
$$= Zl1(I1 + I2 + I0) + (Zl0 - Zl1) \times I0$$
$$= Zl1\left(Ia + \frac{Zl0 - Zl1}{3Zl1} \times 3I0\right)$$

Eqn. 6.1

The ground loop impedance (positive sequence impedance) calculated by the ground impedance relay is

$$Zl1 = \frac{Va}{Ia + \dfrac{Zl0 - Zl1}{3Zl1} \times 3I0}$$
$$= \frac{Va}{Ia + k0 \times 3I0}$$

Eqn. 6.2

Here, the zero-sequence compensation $k0 = (Zl0 - Zl1)/3Zl1$.

Therefore, by considering the zero-sequence compensation, the ground impedance relay can accurately calculate the positive sequence impedance to the fault location. In a typical practice, the zero-sequence compensation $k0$ is calculated with the positive-sequence impedance $Zl1$ and zero-sequence impedance $Zl0$ for the total length of the line, assuming that both $Zl1$ and $Zl0$ have a linear relationship to the distance to the fault location.

Ground Loop Impedance of Cross-Bonded Cables

The ground loop impedance $Zl1$ of an overhead line is almost linear to the distance to the fault location as long as the line type and the tower configuration do not change too much. Using this characteristic, it is possible for the impedance relay to find the distance to the fault location.

For cross-bonded cables, it has been known that the ground loop impedance does not exhibit a linear relationship to the distance to the fault location [2], [3]. Fig. 6.4 shows the compensated loop impedance of a cable line. The ground loop impedance shows discontinuity at the cross-bonding points. This leads to the nonlinear relationship to the distance to the fault location and may result in unwanted operations or mis-operations of impedance relays.
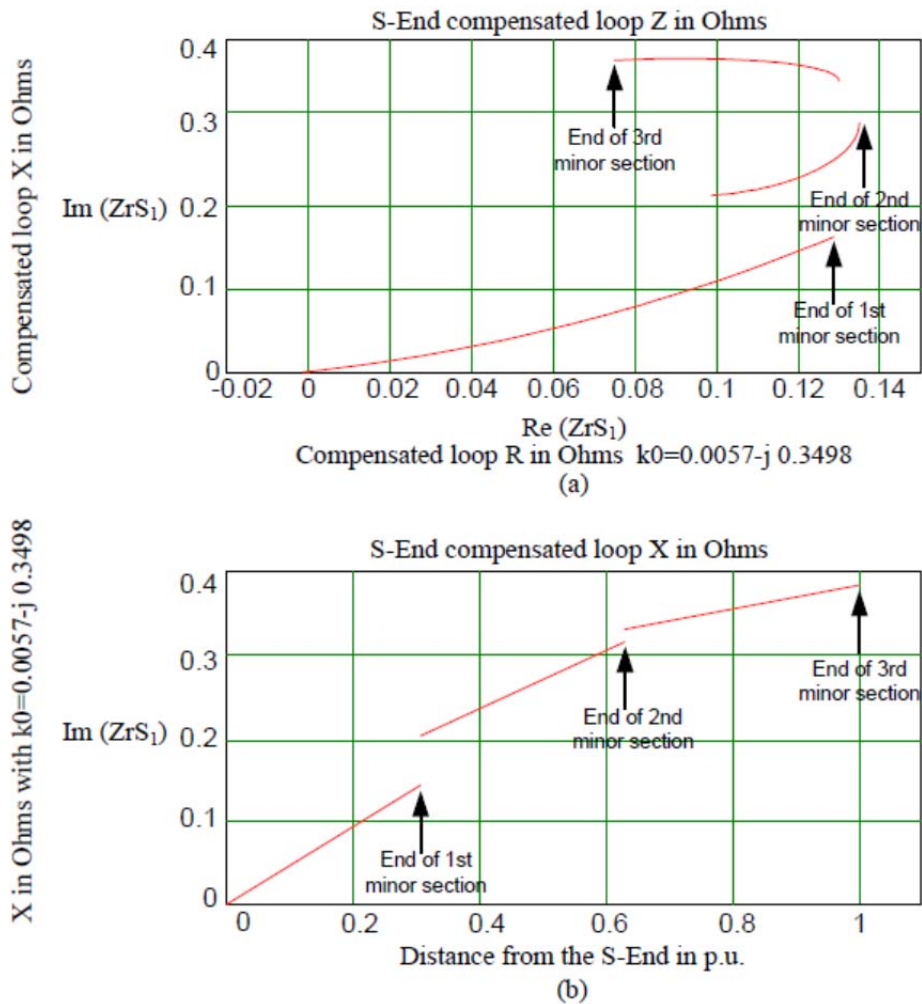
Fig. 6.4 Compensated loop impedance for cross-bonded cables. (Source: Protection of High-Voltage AC Cables [3]).

It has been found in the PhD project that an imbalance of impedances between phases caused the discontinuity of the ground loop impedance. Let us focus on one cross-bonding point. Because of the cross-bonding, a SLG fault before the cross-bonding point has a different return circuit (sheath) from a SLG fault on the same phase but after the cross-bonding point, as shown in Fig. 6.5. Therefore, if there is an imbalance of impedance between phases, the change of the return circuit can cause the discontinuity of the ground loop impedance.
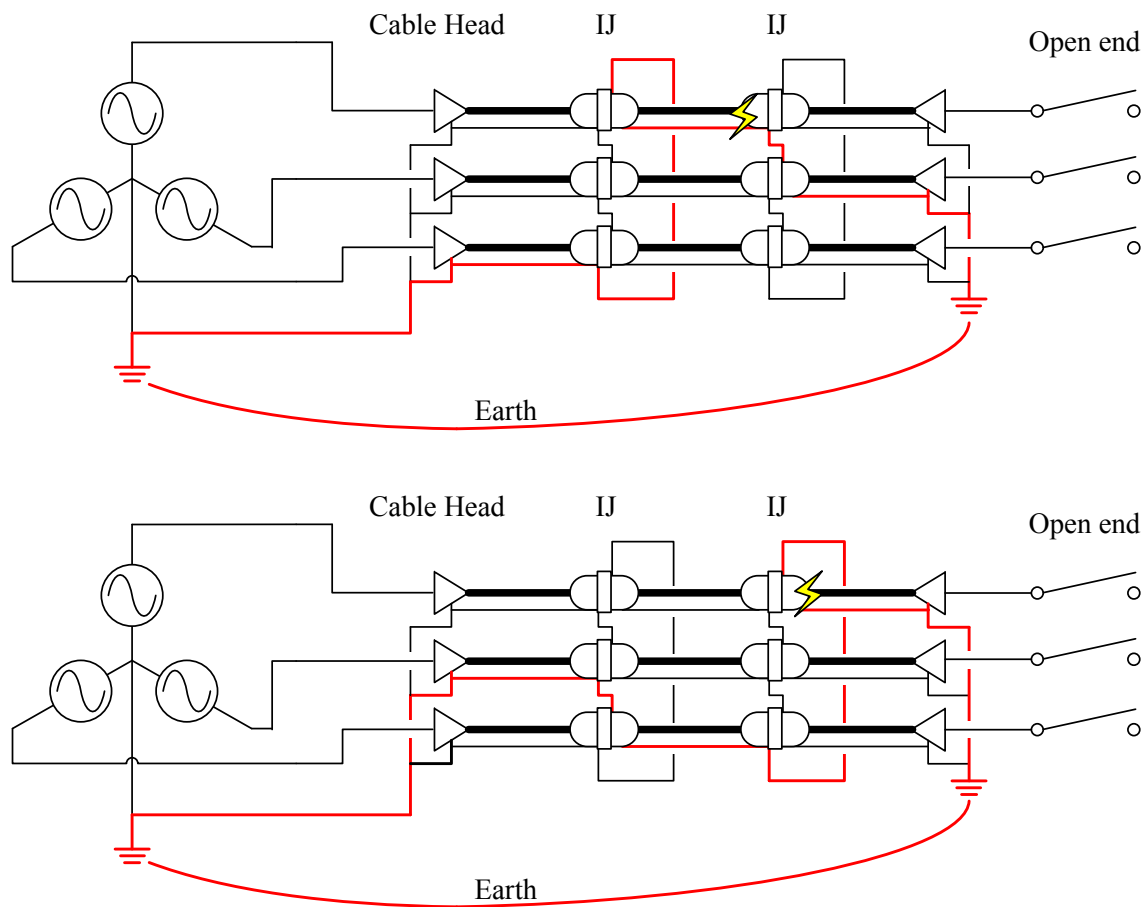
Fig. 6.5 Return circuit for a SLG fault before and after a cross-bonding point.

6.1.3   Cross-bonded Cable with One Major Section

In order to confirm the validity of the statement, the ground loop impedances were calculated for the following types of cross-bonded cables:

• Directly buried in a flat formation without transposition

• Directly buried in a flat formation with transposition

• Directly buried in a trefoil formation without transposition

• Directly buried in a trefoil formation with transposition

• Laid in a tunnel in a trefoil formation with transposition

Here, transposition means the transposition of the whole cable, which is different from cross-bonding.

As in the previous section, it was assumed that the cross-bonded cable had only one major section. The physical and electrical parameters of the Asnæsværket – Torslunde cable were used for the calculation. Assumed cable layouts are illustrated in Fig. 6.6.

(a) Directly buried in a flat formation   (b) Directly buried in a trefoil formation

(c) Laid in a trefoil formation in a tunnel
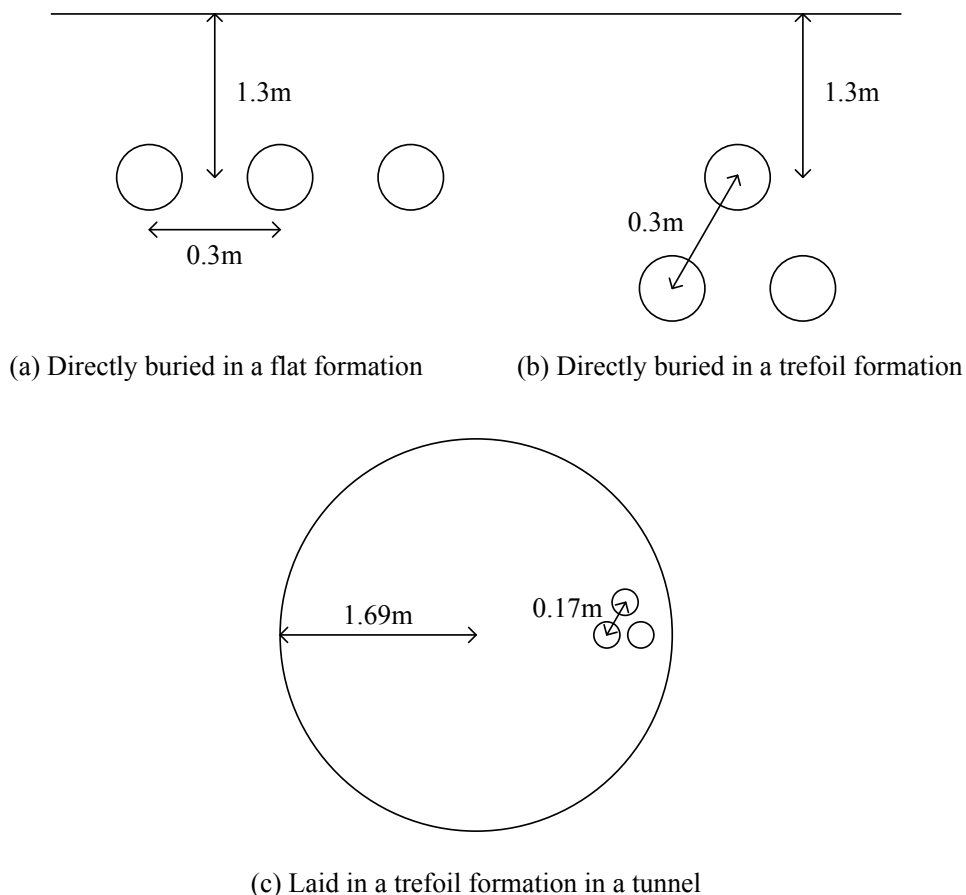
Fig. 6.6 Cable layouts.

The ground loop impedances were calculated using the steady-state calculation function of the ATP-EMTP. The cable parameters were thus calculated by the subroutine CABLE CONSTANTS with the target frequency 50 Hz within ATP-EMTP.

Fig. 6.7 shows the compensated ground loop impedances for different cable layouts and with/without transposition. It has been found that the transposition does not have any impact on the ground loop impedance when the cable is laid in a trefoil formation. Comparing the ground loop impedance, the discontinuity at the cross-bonding points is larger in the following order as shown in Table 6-1:

(1) Directly buried in a flat formation without transposition (Flat w/o Transp.)

(2) Directly buried in a flat formation with transposition (Flat w Transp.)

(3) Directly buried in a trefoil formation (Trefoil)

(4) Laid in a tunnel in a trefoil formation with transposition (Tunnel)

This order is reasonable considering the impedance balance between phases.

Table 6-1 Largest Discontinuity of Ground Loop Reactance at Cross-bonding Points

Cable layouts	(1) Flat w/o Transp.	(2) Flat w Transp.	(3) Trefoil	(4) Tunnel
Largest discontinuity	17.0 %	14.5 %	13.8 %	11.7 %

The difference of the discontinuity is significant especially at the second cross-bonding point where only minor discontinuity is observed for the cable laid in a trefoil formation in a tunnel. This is because the cable laid in a trefoil formation in a tunnel has the best impedance balance between phases due to the existence of the perfect ground (tunnel) close to the cable.

The calculated loop impedance shows the difficulty in protecting a short cross-bonded cable by the impedance relay without communication. When it is necessary, the rectangular characteristic is more suited than the mho characteristic.
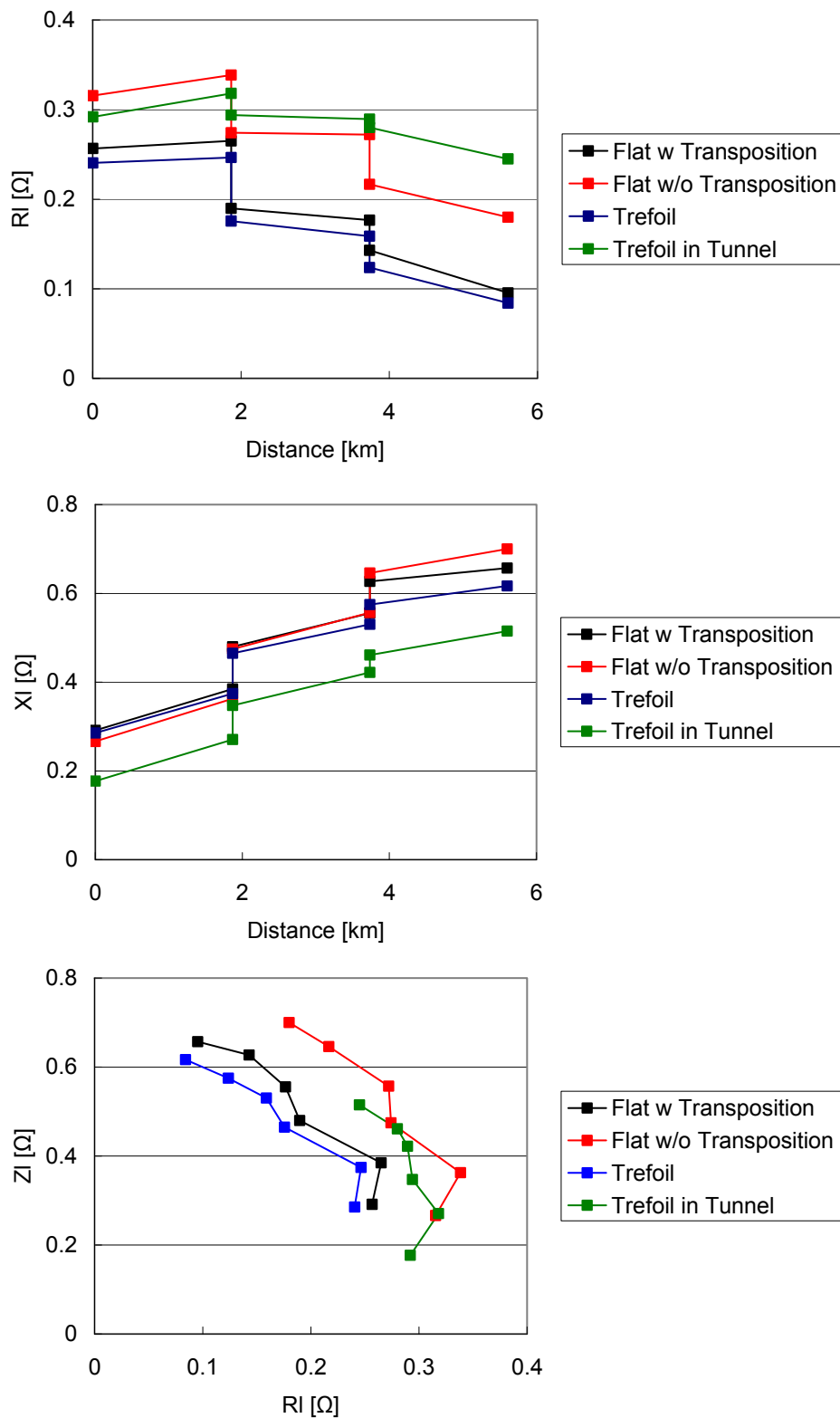
Fig. 6.7 Compensated ground loop impedance for cross-bonded cables with one major section.

6.1.4   ASV – TOR Cable Line

The ground loop impedance of a cross-bonded cable with one major section was previously discussed in literature even though its relationship with cable layouts or transposition has never been investigated [2], [3]. The ground loop impedance of a long cable has not been discussed, but the effect of the discontinuity is expected to become relatively small since the impedance of the total length becomes large.

This section studies the ground loop impedance calculated for the 400 kV 28 km Asnæsværket – Torslunde cable line. Effects of substation grounding resistance, cross-bonding, cable layouts and transposition are discussed.

6.1.4.1   Effects of Substation Grounding Resistance

As discussed in Section 6.1.2, the ground impedance relay calculates the ground loop impedance (positive-sequence impedance) using the zero-sequence compensation $k0 = (Zl0 - Zl1)/3Zl0$. Here, the zero-sequence compensation $k0$ is calculated with the positive-sequence impedance $Zl1$ and zero-sequence impedance $Zl0$ for the total length of the line. It is important to obtain $Zl1$ and $Zl0$ accurately in order to calculate $k0$ and the ground loop impedance with accuracy.

Fig. 6.8 illustrates the setup to obtain the zero-sequence impedance $Zl0$ of the Asnæsværket – Torslunde cable line. This section focuses on the grounding of phase conductors, enclosed by the dotted square in Fig. 6.8. From the theoretical formulas of sequence currents derived in Section 2.3, it is known that, whereas $Zl1$ is not affected by the substation grounding resistance, $Zl0$ is affected by the substation grounding resistance. The grounding of phase conductors therefore affects the accuracy of $Zl0$.

The upper figures of Fig. 6.9 describe the grounding of phase conductors in the setups for the field measurements in detail. Depending on the setups, the grounding of phase conductors can be close to or far from the grounding of cable heads.

The grounding of phase conductors is close to the grounding of cable heads in Phase conductor grounding (1). As shown in the lower left figure of Fig. 6.9, the sheath return current can go back to the source without going through the substation grounding resistance in this case. The cross-bonding is not shown in the figure for simplicity.

In contrast, the grounding of phase conductors is far from the grounding of cable heads in Phase conductor Grounding (2). As shown in the lower right figure of Fig. 6.9, the sheath/earth return current needs to go through the substation grounding resistance in this case.
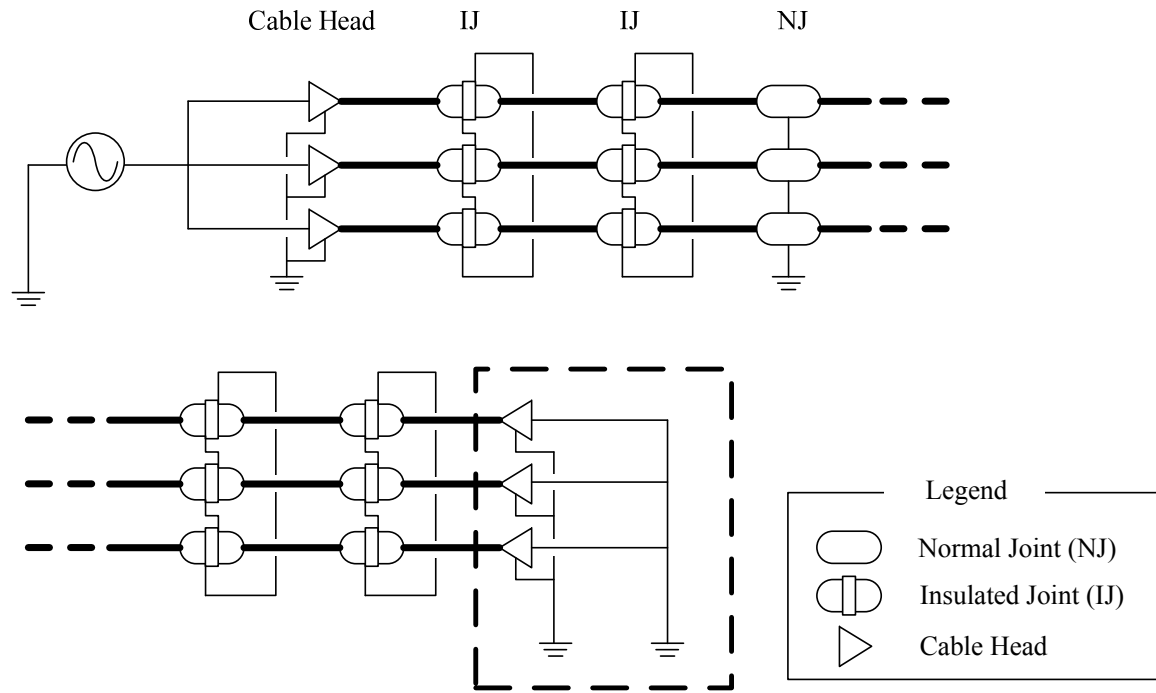
Fig. 6.8 Setup to obtain the zero-sequence impedance of the ASV-TOR cable line.

Phase conductor grounding (1)   Phase conductor grounding (2)
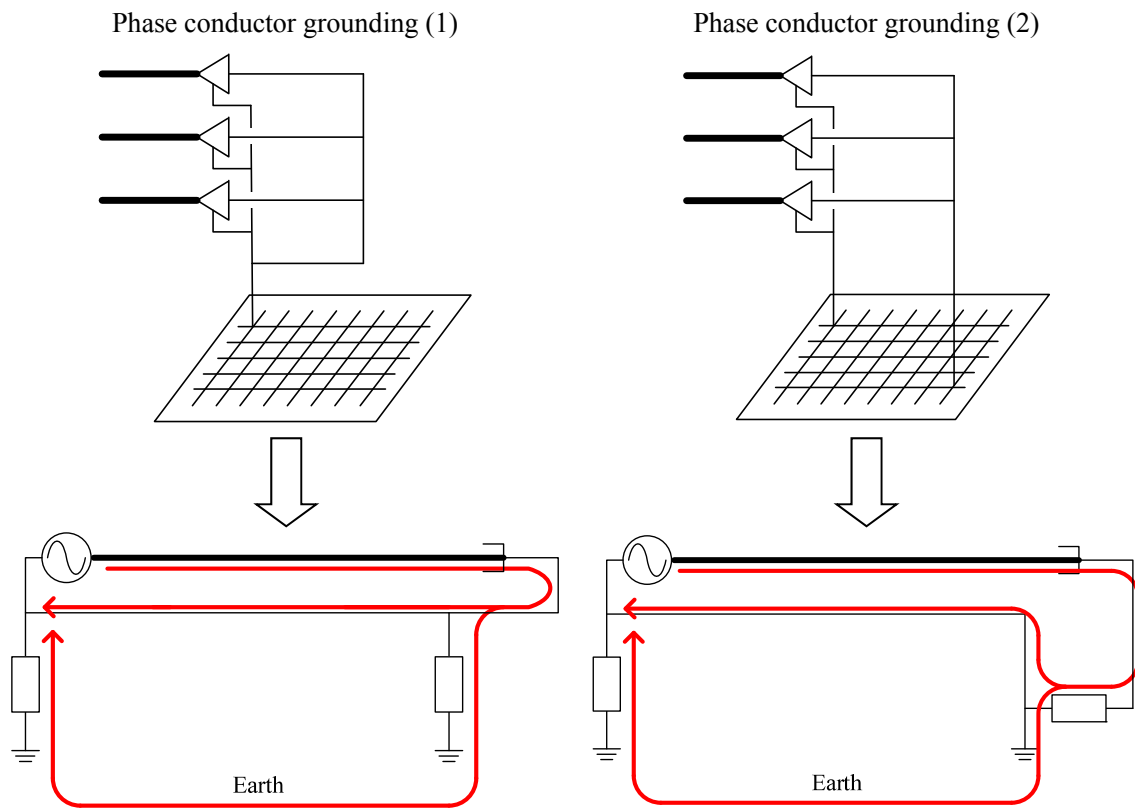
Fig. 6.9 Comparison of phase conductor groundings.

It is therefore expected that $Zl0$ obtained by the setup with Phase conductor grounding (1) has a smaller real part. Table 6-2 compares $Zl0$ and $k0$ with the substation grounding resistance 1 ohm. It is known that $Zl1$ is not affected by the phase conductor grounding or substation grounding resistances, but it is also shown in the table just to confirm it. The calculation results show that the phase conductor grounding has a significant effect on both $Zl0$ and $k0$. Since this difference will affect the calculated ground loop impedance, it is necessary to know which phase conductor grounding was selected for the field measurements of $Zl0$.

Table 6-2 Effects of Phase Conductor Grounding (1 ohm)

Phase conductor grounding	(1)	(2)
$Zl1$ [Ω]	0.487 + j5.07	
$Zl0$ [Ω]	4.82 + j 2.78	7.50 + j 3.42
$k0$	−0.122 − j 0.296	−0.0639 − j 0.467

Fig. 6.10 shows the sheath/earth return current in the SLG fault in a cable line. It is clear from the figure that the sheath return current can go back to the source without going through the substation grounding resistance. This means that Phase conductor grounding (1) is more appropriate for the field measurements of $Zl0$, considering that the value is used for the impedance relay setting. If the field measurements are conducted with Phase conductor grounding (2), the results need to be modified using EMTP simulations.

Fig. 6.10 considers the SLG fault in a cable line, for example, the Asnæsværket – Torslunde cable line. When a SLG fault occurs in another feeder from Asnæsværket, it will be arrested by the second zone or the third zone of the impedance relay located at the Torslunde side. In this case, the transformers at the Asnæsværket will provide the path for the return current. Therefore, the selection of the phase conductor grounding is not important in this case.
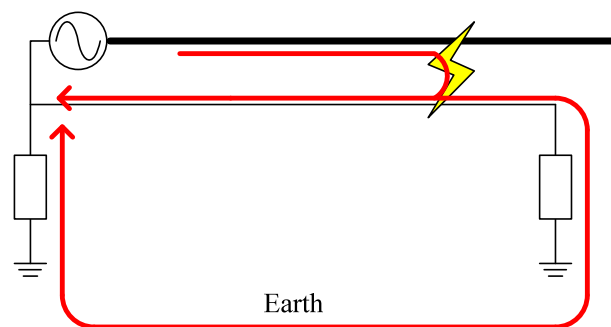
Fig. 6.10 Sheath/earth return current in the single line to ground fault.

One thing we need to keep in mind is that $Zl0$ calculated with Phase conductor grounding (2) may be preferred for other studies such as transient stability studies. Since Phase conductor grounding (2) leads to larger $Zl0$, it will result in a conservative assessment. We need to know which phase conductor grounding was selected when the field measurements of $Zl0$ are performed before we apply the value for the calculation of the ground loop impedance.

The discussion of this section, so far, assumed the substation grounding resistance 1 ohm. This value is an upper limit in a practice of many utilities. The choice of this value normally leads to a conservative evaluation in most studies. However, in reality, the substation grounding resistance of 0.1 ohm is often achieved.

Table 6-3 shows $Zl0$ and $k0$ calculated with Phase conductor grounding (1) and (2) with the substation grounding resistance 0.1 ohm. The calculation results show that the phase conductor grounding does not have a meaningful effect on $Zl0$ and $k0$ in terms of the impedance relay setting.

Table 6-3 Effects of Phase Conductor Grounding (0.1 ohm)

Phase conductor grounding	(1)	(2)
$Zl1$ [Ω]	0.487 + j5.07	
$Zl0$ [Ω]	2.57 + j 2.22	2.86 + j 2.25
$k0$	−0.173 – j 0.153	−0.169 – j 0.172

6.1.4.2   Effects of Cross-Bonding

In a typical practice, the zero-sequence compensation $k0$ is calculated with the positive-sequence impedance $Zl1$ and zero-sequence impedance $Zl0$ for the total length of the line. Assuming that both $Zl1$ and $Zl0$ have a linear relationship to the distance to the fault location, $k0$ takes a constant value regardless of the fault location.

However, for cross-bonded cables, $Zl0$ does not have a linear relationship to the distance to the fault location as shown in Section 6.1.3. As a result, the actual value of $k0 = (Zl0 - Zl1)/3Zl0$ changes depending on the fault location. Since $k0$ is normally input as a constant value for each zone setting, it causes an error in the calculation of the ground loop impedance.

This section studies how $Zl0$ and $k0$ changes according to the fault location with substation grounding resistances 1 ohm and 0.1 ohm. The actual values of $Zl0$ and $k0$ are calculated with the steady-state calculation function of ATP-EMTP. A SLG fault is placed at each joint in phase a, then Va / Ia gives $(2Zl1 + Zl0) / 3$ from the relay location to the fault location. As we know that $Zl1$ has a linear relationship to the distance to the fault location, $Zl1$ can be theoretically calculated from $Zl1$ of the total length in Table 6-2 and Table 6-3. This means that the actual values of $Zl0$ can be calculated as

$$Zl0 = 3\frac{Va}{Ia} - 2Zl1 \qquad\qquad \text{Eqn. 6.3}$$

Here, $Zl1$ and $Zl0$ are the positive-sequence and zero-sequence impedances from the relay location to the fault location. Note that they are not the sequence impedances for the total length.

Fig. 6.11 shows the comparison of the actual $Zl0$ calculated from Eqn. 6.3 and $Zl0$ obtained from the field measurements for the total length. When deriving $Zl0$ from the field measurements, it was assumed that $Zl0$ had the linear relationship to the distance to the fault location. Measurements (1) and (2) respectively mean the field measurements performed with Phase conductor groundings (1) and (2). Substation grounding resistance was set as 1 ohm.

From the figure, it is obvious that $Zl0$ does not have the linear relationship to the distance to the fault location. The discontinuities of $Zl0$ at cross-bonding points can be observed. As discussed in Section 6.1.4.1, Measurement (1) is closer to the actual $Zl0$. Measurements (1) and (2) are derived from the field measurements performed with the total length, there is no noticeable difference between the actual $Zl0$ and Measurement (1) at the end of the line.
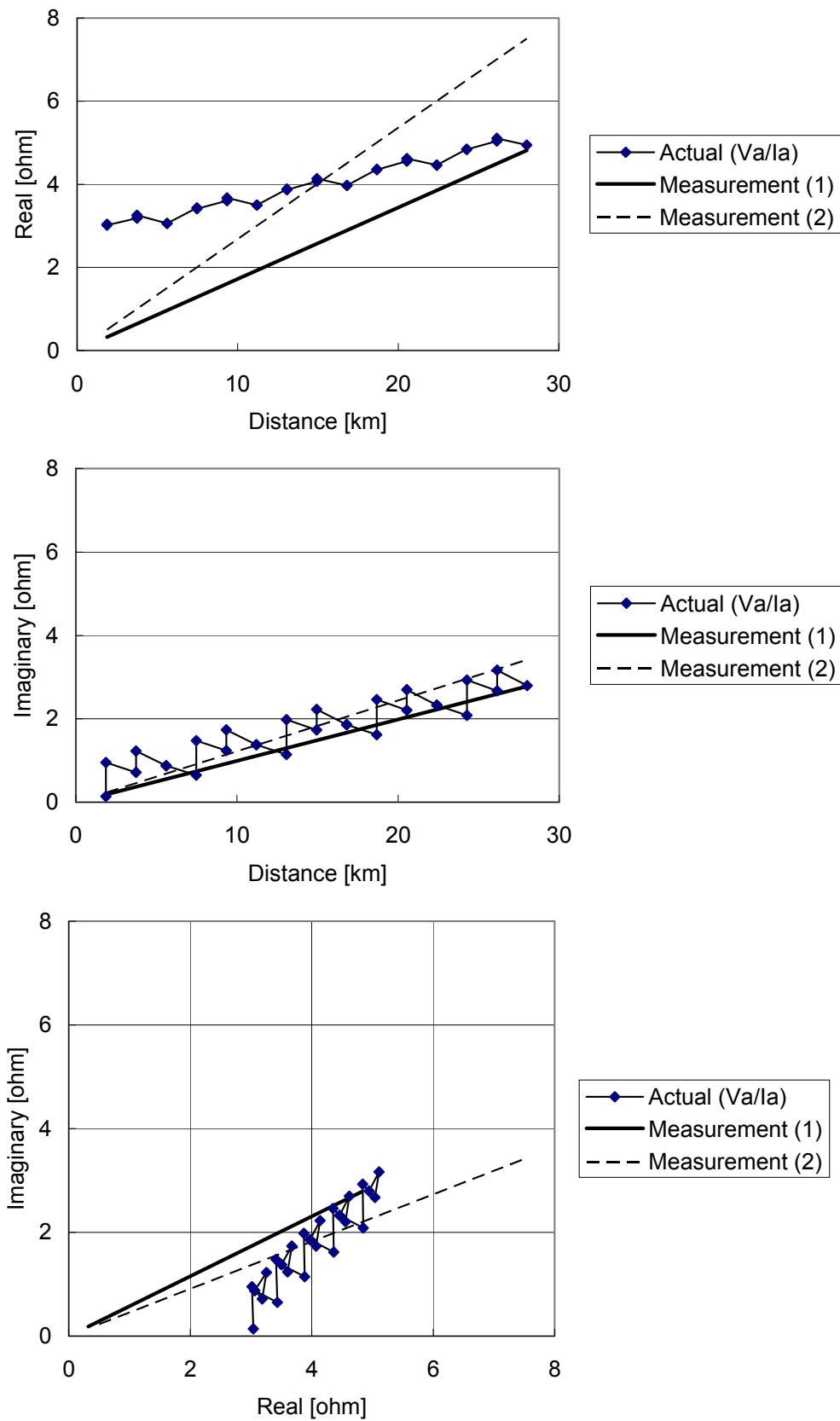
Fig. 6.11 Comparison of actual *Zl*0 and *Zl*0 obtained from field measurements (1 ohm).

Fig. 6.12 shows the comparison of the actual $k0$ calculated using EMTP simulations and $k0$ obtained from the field measurements for the total length. Since Measurements (1) and (2) assume the linear relationship between $Zl0$ and the distance to the fault location, $k0$ obtained from the field measurements becomes constant regardless of the fault location. It is clear from the results that $k0$ has a relatively large error when the fault occurs near the relay location.

Fig. 6.13 and Fig. 6.14 show the comparison of the actual $Zl0$ and $k0$ calculated using EMTP simulations and $Zl0$ and $k0$ obtained from the field measurements for the total length. The difference from Fig. 6.11 and Fig. 6.12 is the assumed substation grounding resistance, which was reduced from 1 ohm to 0.1 ohm. The discontinuities at cross-bonding points are observed in a similar fashion, but the error of $Zl0$ and $k0$ obtained from the field measurements become much smaller. Only the results with Measurement (1) are shown since Measurements (1) and (2) do not have a meaningful difference.

Fig. 6.12 Comparison of actual *k*0 and *k*0 obtained from field measurements (1 ohm).

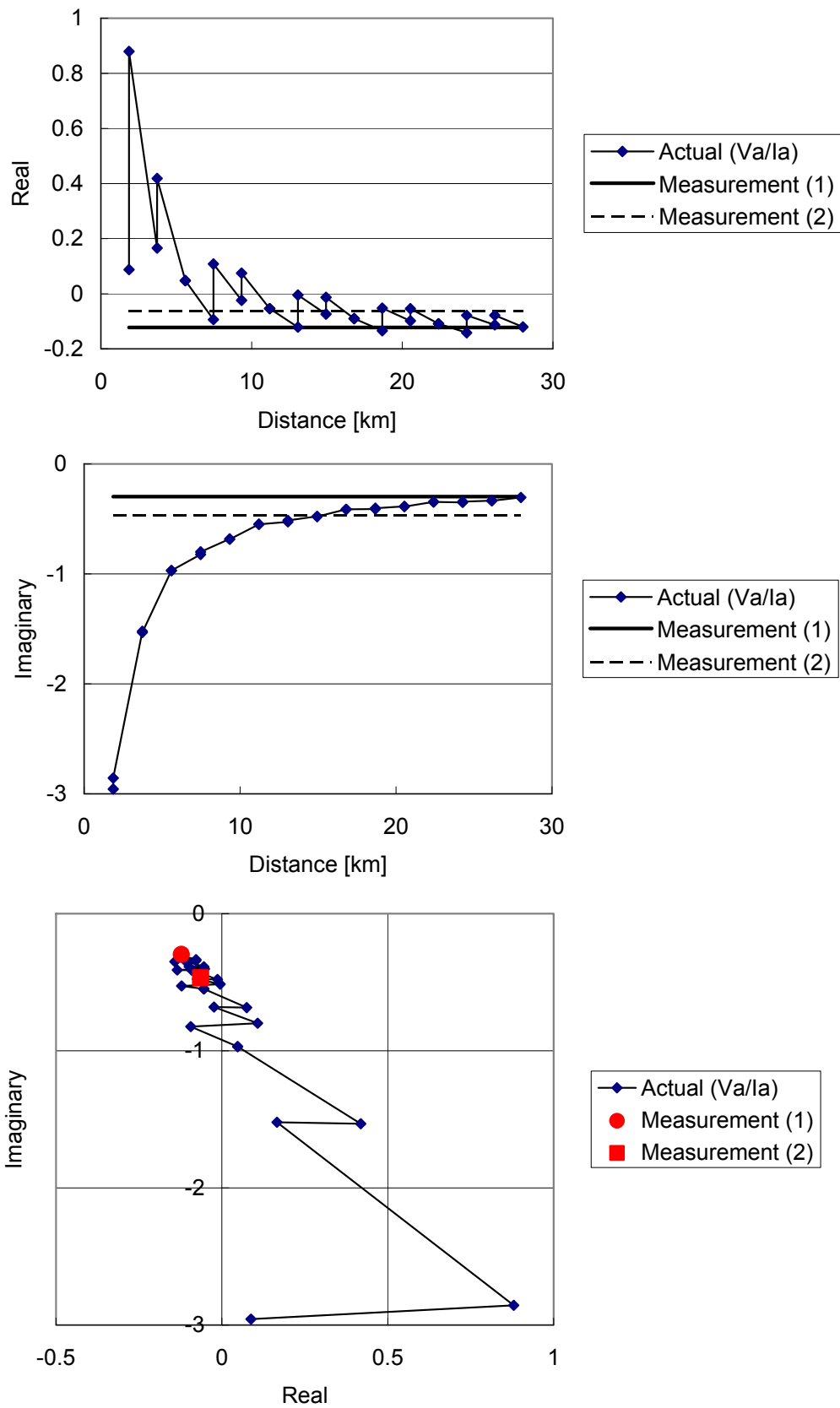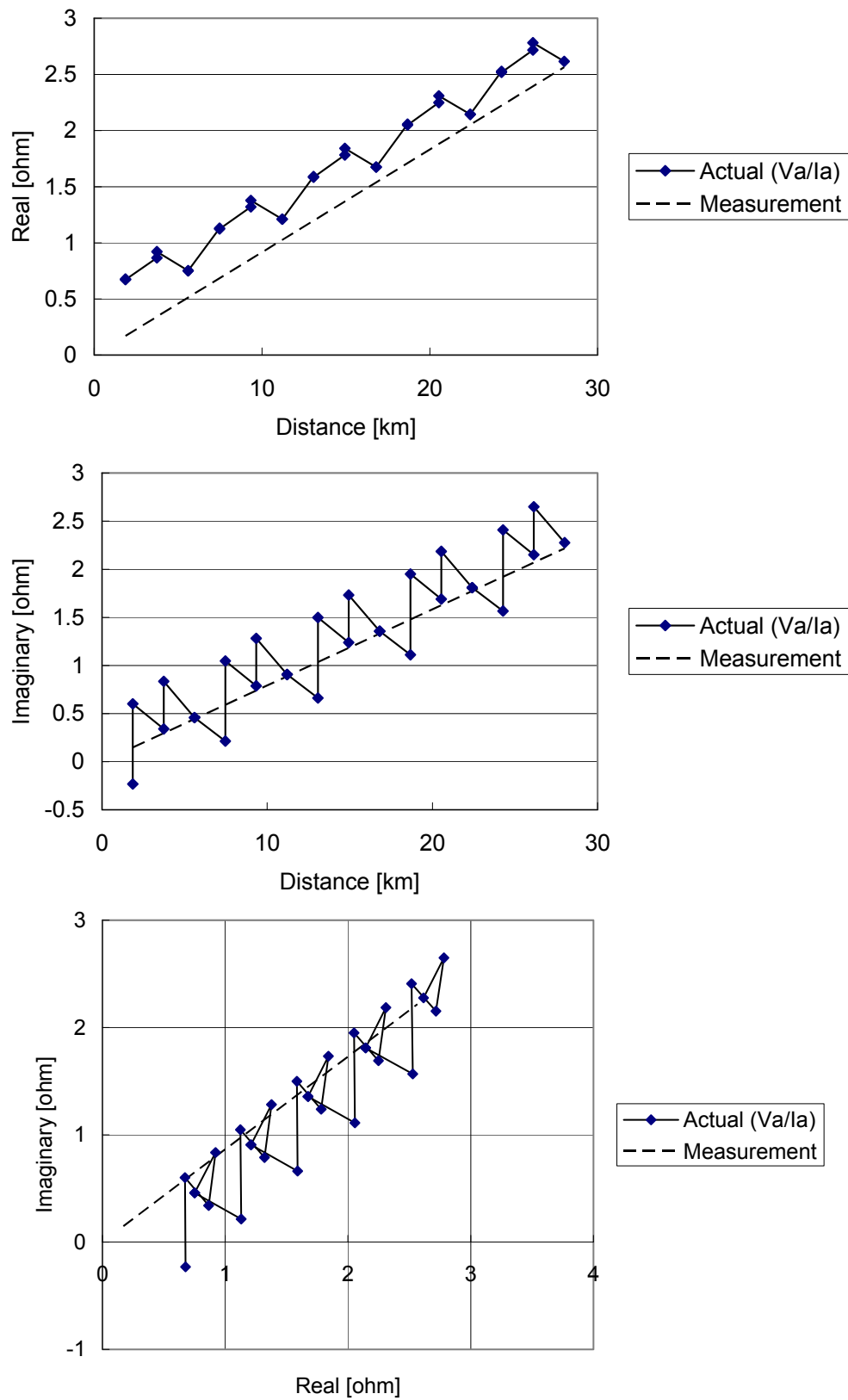**Fig. 6.13 Comparison of actual *Zl*0 and *Zl*0 obtained from field measurements (0.1 ohm).**
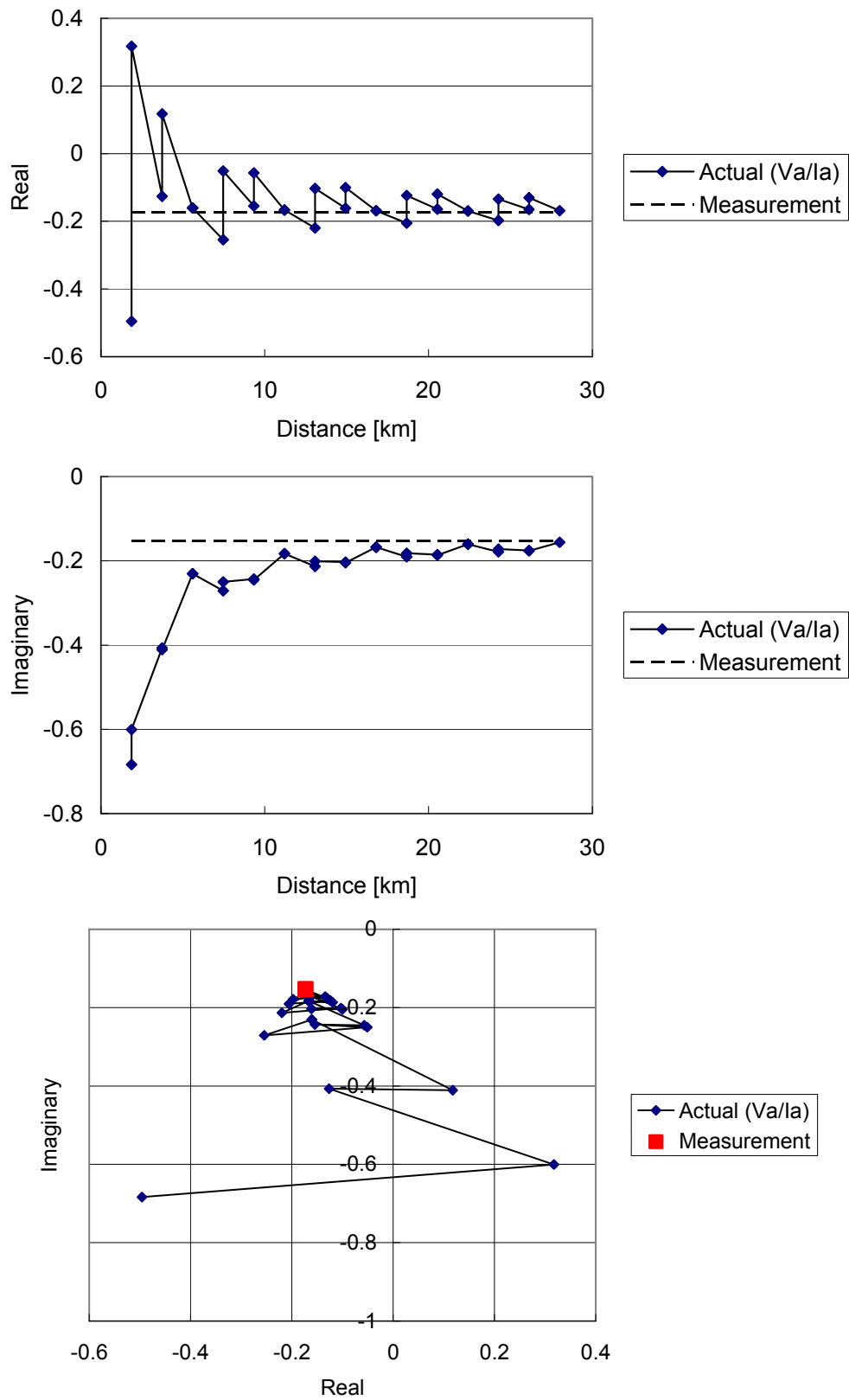
Fig. 6.14 Comparison of actual *k*0 and *k*0 obtained from field measurements (0.1 ohm).

6.1.4.3   Calculation of Ground Loop Impedance

In previous sections, we have found the effects of the substation grounding resistance and the cross-bonding. This section studies the impact of these effects on the ground loop impedance.

Fig. 6.15 illustrates the ground loop impedance calculated for the 400 kV 28 km Asnæsværket – Torslunde cable line. In the figure, *ZRy* is the actual uncompensated ($k = 0$) and compensated ($k = k0$) ground loop impedance calculated by the impedance relay, and *Zpos* is the positive sequence impedance obtained by field measurements for the total length. The substation grounding resistances were first assumed to be 1 ohm.

In Fig. 6.15, the ground loop impedance exhibits the discontinuity at cross-bonding points. The Asnæsværket – Torslunde cable line is assumed to be directly laid in a flat formation with transposition. The largest discontinuity of the compensated ground loop reactance at cross-bonding points is approximately 5.6 % of the reactance of the total length. The discontinuity at each cross-bonding point became much smaller, as expected, compared with the cross-bonded cable with one major section. The discontinuity is not observed at normal joints, which is reasonable.

Comparing the actual uncompensated ($k = 0$) and compensated ($k = k0$) ground loop impedance in the figure, an error in *k*0 has a larger impact on the ground loop impedance when the fault location is away from the relay location. It is because *k*0 has a larger impact when *I0* becomes larger compared with *Ia* as can be seen from Eqn. 6.2. As a result, the large error of *k*0 found in the last section when the fault occurs near the relay location will not lead to the unwanted operation or mis-operation of impedance relays.

If the first zone of the impedance relay covers 90 % of the total length, it may overreach to the bus on the other end and also to the next feeders due to the discontinuity of 5.6 %. The overreach is not favourable as it can result in an unwanted tripping of the Asnæsværket – Torslunde cable line in case of a fault in the bus on the other end or in the next feeders. It is more common to cover 80 % of the total length by the first zone. With this setting, the first zone will not overreach to the bus on the other end, even with the discontinuity of 5.6 % and a typical error around 5 % in the total impedance.
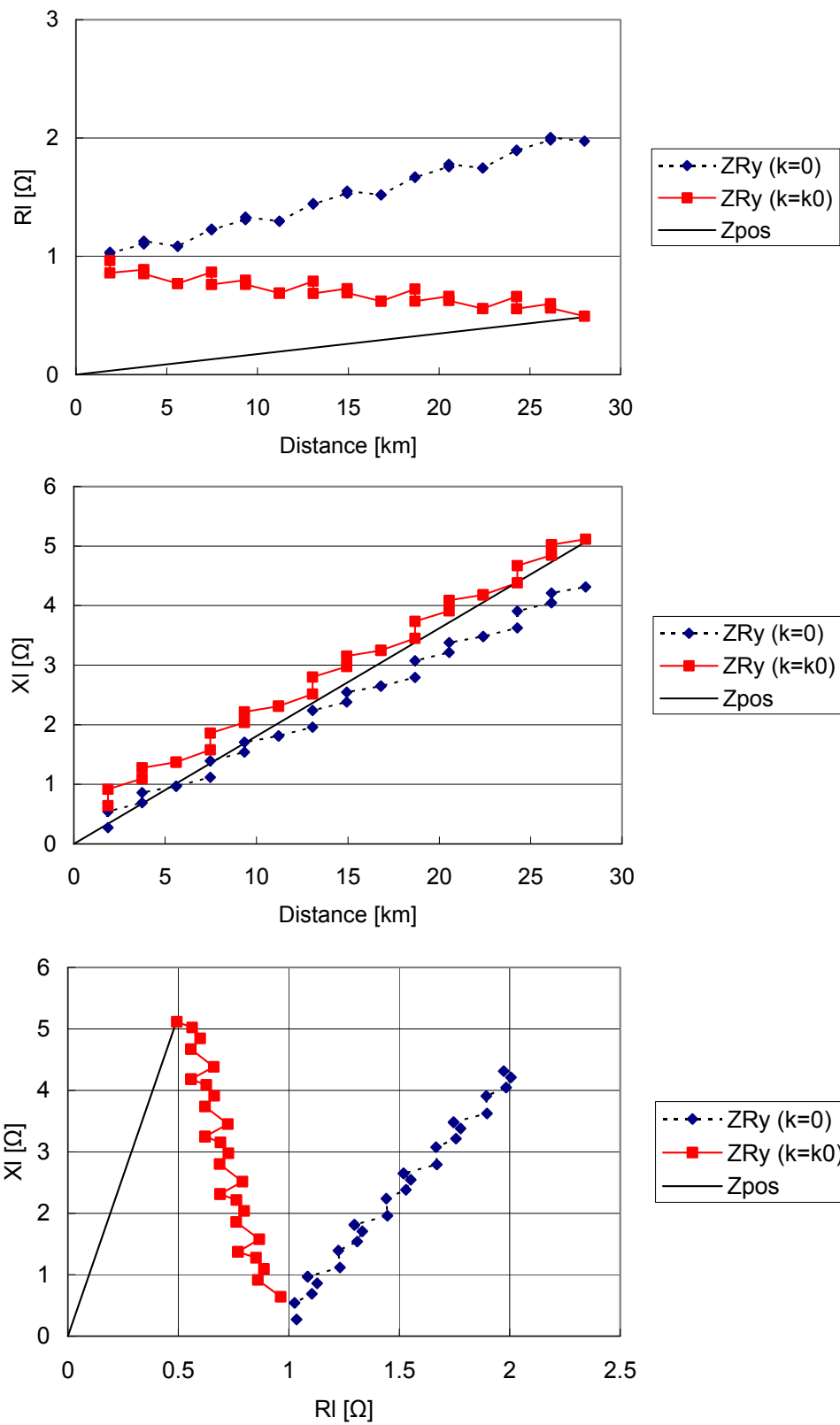
Fig. 6.15 Ground loop impedance for the ASV – TOR cable line (1 ohm).

Fig. 6.16 shows the ground loop impedance with the reduced substation grounding resistance (1 Ω to 0.1 Ω). It can be seen that *ZRy* becomes much closer to *Zpos*, especially for the resistance part *Rl*, which means that a better impedance relay setting is possible.

In contrast, with regard to the discontinuity, the largest discontinuity of the compensated ground loop reactance is increased to approximately 6.4 % of the reactance of the total length, by the reduction of the substation grounding resistance. This increase is reasonable since the substation grounding resistance is a balanced component for three phases. As a proportion of the balanced component in the total ground loop impedance is decreased, the imbalance of impedances between phases is increased. However, the first zone will not overreach to the bus on the other end with the discontinuity of 6.4 %, as long as it covers 80 % of the total length.

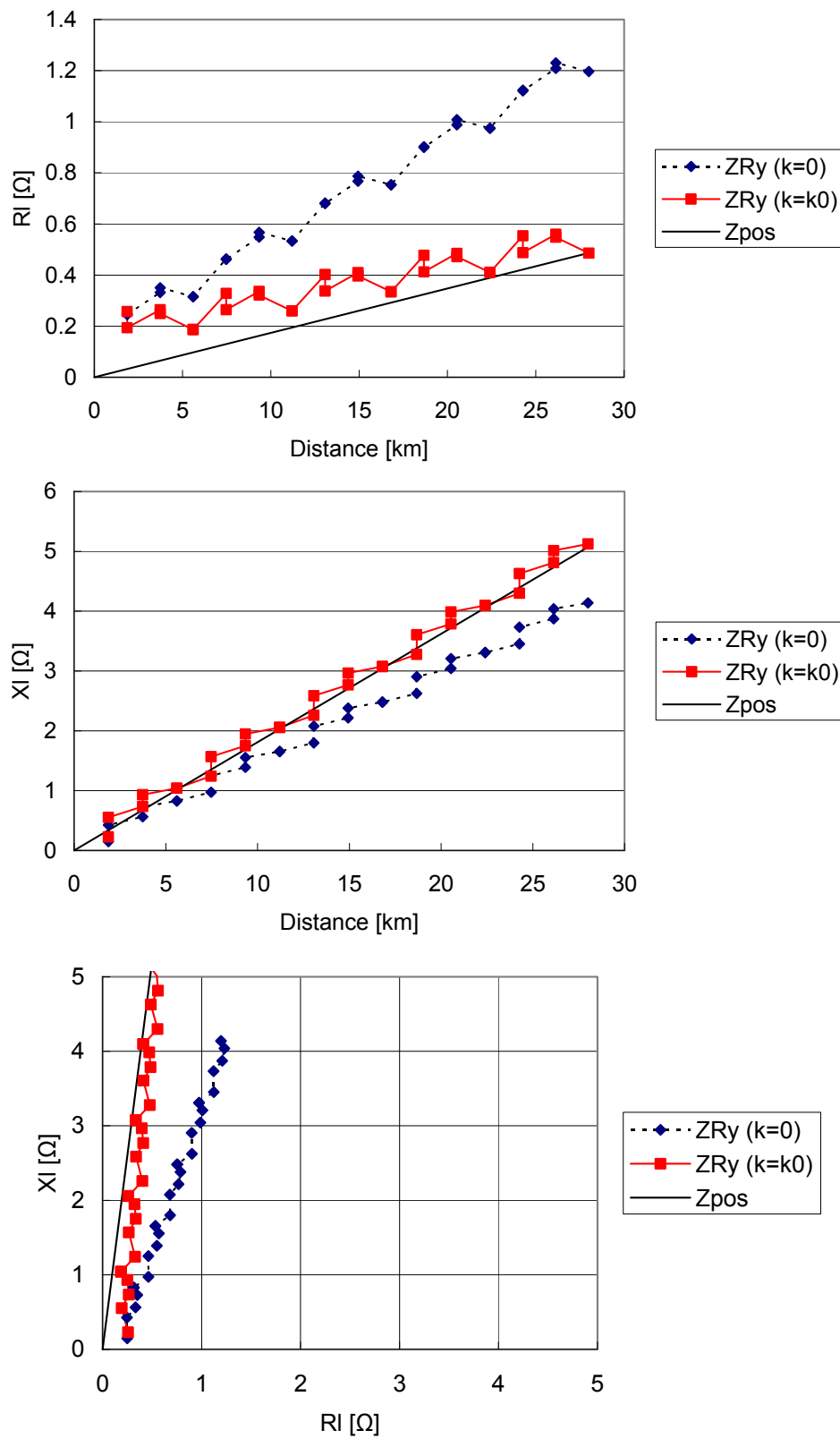**Fig. 6.16 Ground loop impedance for the ASV – TOR cable line (0.1 ohm).**

6.1.4.4   Effects of Cable Layouts and Transposition

Section 6.1.3 shows the effects of cable layouts and transposition with a cross-bonded cable with one major section. This section studies how the effects are changed with a long cable. In Section 6.1.4.3, the Kyndbyværket – Asnæsværket cable line was assumed to be directly buried in a flat formation with transposition. In this section, the ground loop impedances are compared with the following cable layouts as in Section 6.1.3:

(1)   Directly buried in a flat formation without transposition (Flat w/o Transp.)

(2)   Directly buried in a flat formation with transposition (Flat w Transp.)

(3)   Directly buried in a trefoil formation (Trefoil)

(4)   Laid in a tunnel in a trefoil formation with transposition (Tunnel)

Fig. 6.17 shows the comparison of the compensated ground loop impedance for different cable layouts. Substation grounding resistance was set to 0.1 Ω, and Phase conductor grounding (1) is assumed for the calculation of $k0$.

Table 6-4 shows proportions of the largest discontinuities of the compensated ground loop reactances against the reactances for the total length. The cross-bonded cable laid in a tunnel has a lower discontinuity compared with the other three cable layouts. As the discontinuities became smaller compared with the cross-bonded cable with one major section, the difference of the other three cable layouts became negligible.

Table 6-4 Largest Discontinuity of Ground Loop Reactance at Cross-bonding Points

Cable layouts	(1) Flat w/o Transp.	(2) Flat w Transp.	(3) Trefoil	(4) Tunnel
Largest discontinuity	6.0 %	6.4 %	6.4 %	4.6 %

The first zone will not overreach to the bus on the other end with this level of discontinuities, as long as it covers 80 % of the total length. The discontinuities are larger for the resistance part of the ground loop impedance compared with the reactance part. However, the discontinuities of the resistance part are not very important for the impedance relay setting as it is necessary to consider a fault resistance.
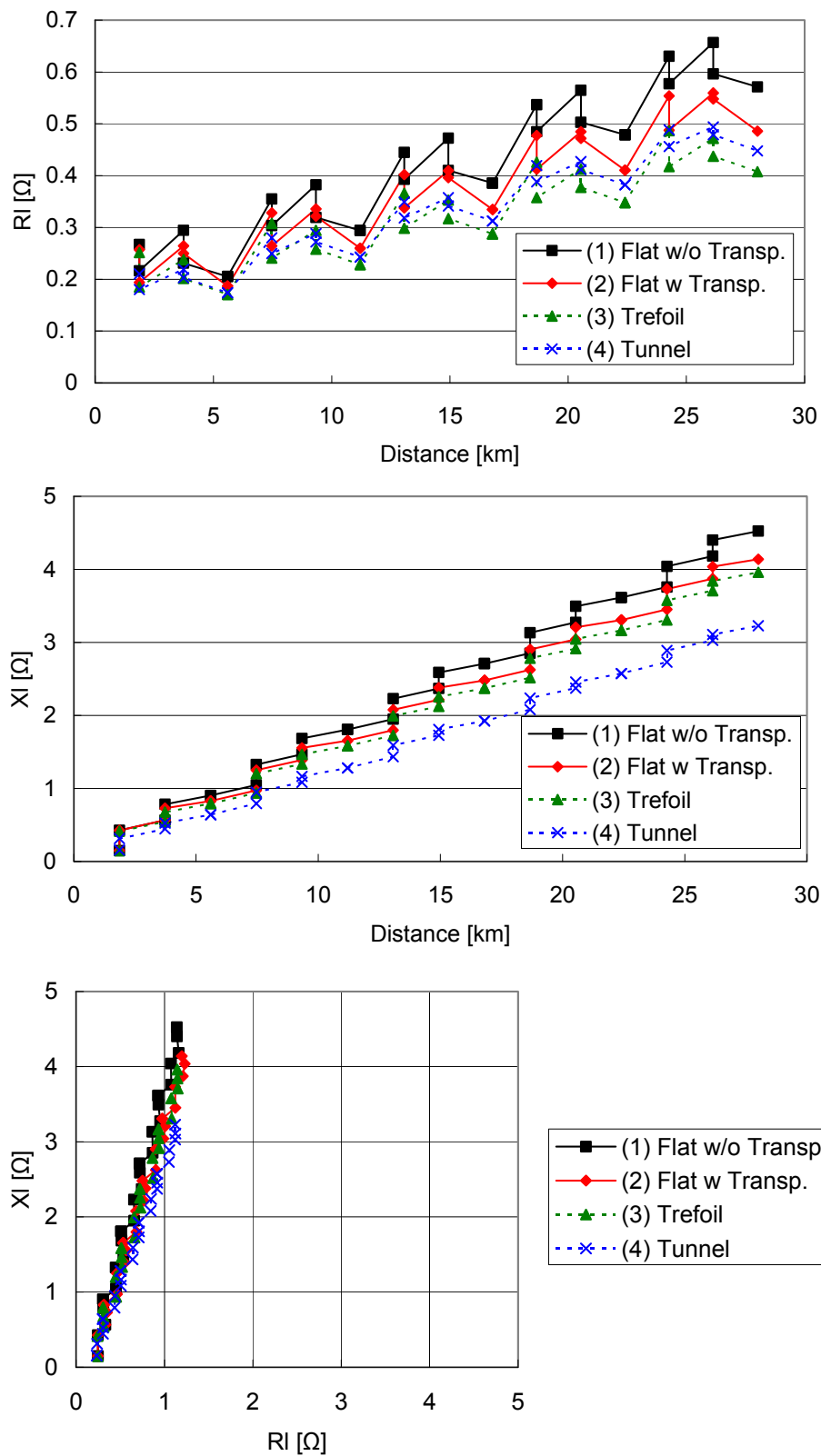
Fig. 6.17 Ground loop impedance for the ASV – TOR cable line with different cable layouts.

6.1.5   Summary

In conclusion, the analysis of the ground loop impedance has found the following items:

• It is difficult to protect a short cross-bonded cable by the impedance relay without communication as the discontinuities at cross-bonding points can go up to 17 % of the total reactance.

• It is possible to protect the Asnæsværket – Torslunde cable line (long cross-bonded cables) by the impedance relay without communication. The first zone will not overreach to the bus on the other end with the typical setting with the level of discontinuities found in the analysis.

• The substation grounding resistance affects the zero-sequence compensation $k0$. It is necessary to know the setup when the field measurements are performed.

• Since a constant value is assumed for the zero-sequence compensation $k0$, there is a large error in $k0$ when a SLG fault occurs near the relay location. However, it will not lead to the mis-operation or the unwanted operation of impedance relays since $k0$ has a smaller impact on the ground loop impedance near the relay location.

• Cable layouts and transposition affect the nonlinear characteristic of the ground loop impedance as the discontinuity is caused by an imbalance of impedances between phases.

• A cable laid in a flat formation has a larger discontinuity than a cable laid in a trefoil formation. However, it is difficult to see the difference in a long cross-bonded cable as the difference becomes small due to their homogenous nature [4][5].

6.2 Leading Current Interruption

When the leading current is interrupted at current zero, it occurs at a voltage peak assuming that the current waveform is leading the voltage waveform by 90 degrees. After the interruption, the voltage on the source side of the circuit breaker changes according to the system voltage, whereas the voltage on the other side is fixed at the peak voltage E as shown in Fig. 6.18. The most severe overvoltage occurs when a restrike occurs after half cycle when the voltage on the source side becomes $-E$. As the voltage difference between the source side and the other side is $2E$, the overvoltage can go as high as $-3E$. The restrike can be repeated to cause a very severe overvoltage.
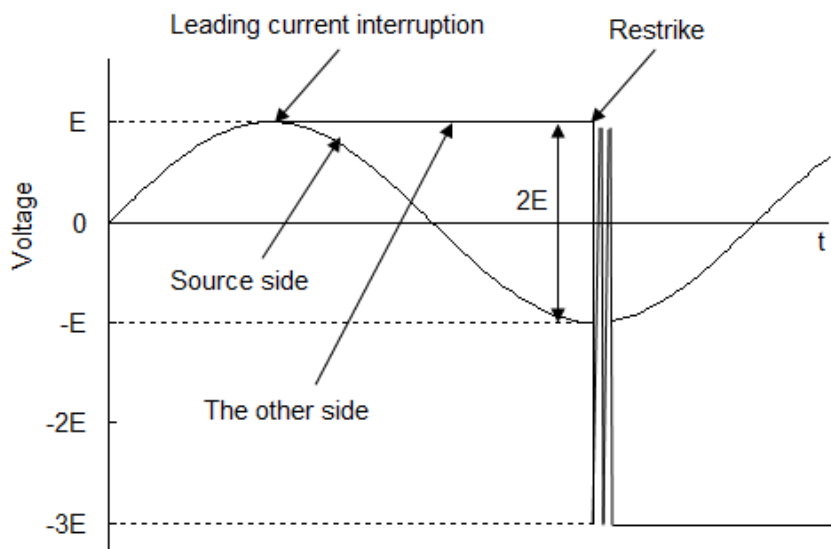
Fig. 6.18 Overvoltage caused by leading current interruption and restrike.

Considering the severe overvoltage that can be caused by the leading current interruption, the leading current interruption capability of circuit breakers is specified in IEC 62271-100. Table 6-5 shows the leading current interruption capability according to IEC 62271-100. It is necessary to make sure that leading currents interrupted by line breakers are below 400 A for the Kyndbyværket – Asnæsværket line.

Table 6-5 Leading Current Interruption Capability according to IEC 62271-100

Rated Voltage	Rated Capacitive Switching Currents* (Cable)
420 kV	400 A
550 kV	500 A

*: Preferred values, voltage factor: 1.4 pu

When the charging capacity of a long EHV cable line is not compensated by shunt reactors directly connected to the line, the leading current interruption capability requires a careful attention [1]. Considering typical capacitance 0.2 μF/km, the maximum line length for 400 kV cable line is limited approximately below 26 km. Here, it is assumed that the leading current is interrupted by one end, and the other end is open before the interruption.

Usually, a long EHV cable line, including the Kyndbyværket – Asnæsværket line, is compensated by shunt reactors directly connected to the line. When the compensation rate is high enough, the leading current interruption capability is not a concern. If the sequential switching is applied to a cable line as a countermeasure to the zero-missing phenomenon, however, the tripping of shunt reactors makes the compensation rate lower, sometimes even to 0 %. This is the only occasion that requires a careful attention and is discussed more in detail in Section 6.3.

6.3 Zero-missing Phenomenon

A DC offset current (Zero-missing current) appears when an EHV underground cable is energized with its shunt reactors [1][2][6][7][8][9]. In this condition, an AC component of a charging current has the opposite phase angle to the AC component of a current flowing into the shunt reactors. If the compensation rate of the cable is 100 %, the summation of these AC components becomes zero, and only the DC component remains. Since the DC component decays slowly with time, it can take more than 1 second, depending on the compensation rate, before a current that flows through the circuit breaker crosses the zero point. When the circuit breaker is to be operated to interrupt this current without the zero crossing, it may lead to a failure of this circuit breaker.

Fig. 6.19 shows an example of current waveforms when an EHV underground cable is energized with its shunt reactors. It can be seen that the AC component of the energization current is very small since the compensation rate is close to 100%. The simulation was run for 0.2 seconds, but the energization current did not cross the zero point during this duration.

Since the Zero-missing phenomenon is caused by a DC component of an energization current, it is severest when the cable is energized when the maximum DC component is contained in the current. In order to realize this condition in phase A, the cable was energized at the voltage zero point of phase a.
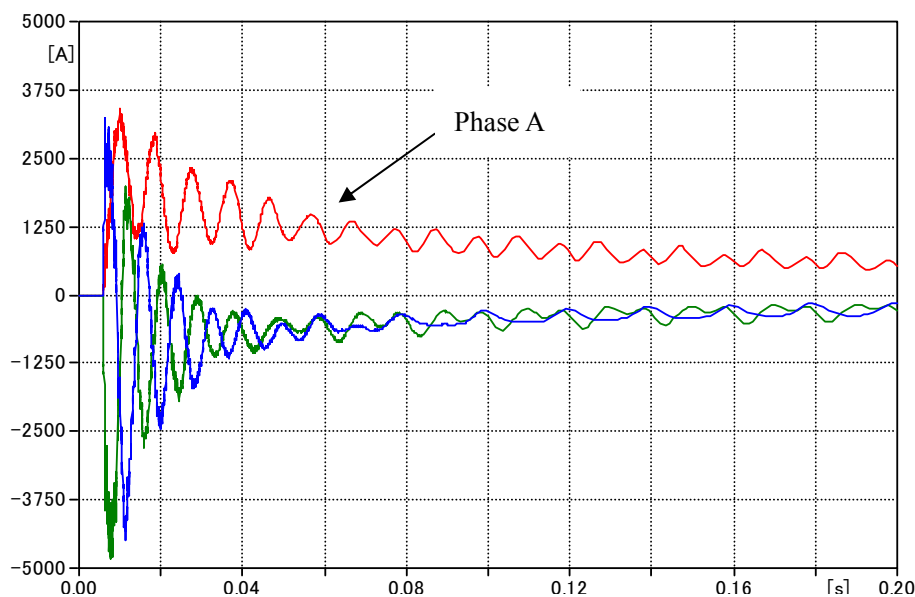

Fig. 6.19 Zero-missing current in the underground cable energization.

Table 6-6 summarizes countermeasures of the zero-missing phenomenon. All of these countermeasures, except for Countermeasure (4), have already been applied to the cable line in operation. Countermeasure (1), which in particular has a number of application records to long EHV cable lines, is discussed in detail later in this section.

Countermeasure (2) is also a proven technology. It is more often applied to the transformer energization in order to minimize inrush current. The effects of point-on-wave switching (synchronized switching) on the cable energization overvoltage are discussed in Section 5.2.4.

Countermeasure (3) can be implemented rather easier as long as a cable line is installed together with single phase circuit breakers and current differential relays. For this reason, this countermeasure is more suited to EHV cable lines than HV cable lines.

In this countermeasure, the faulted phase is opened instantly, but healthy phases are opened about 10 seconds later when the DC component is decayed enough. When this countermeasure is applied near a generator and especially when the cable line offers radial path to the generator, it is necessary to evaluate the negative-sequence current capability of the generator as this countermeasure causes an unbalanced operation for a prolonged duration.

Countermeasure (4) is applicable in theory [10][11], but the cost of the breaker will prohibit its application depending on the required size of pre-insertion resisters. Line breakers with pre-insertion resisters were, in the first place, proposed for overhead lines in order to lower the switching overvoltage. However, it could not become mainstream mainly due to its cost. A breakthrough, especially on heat dissipation, would be necessary to be applied as a countermeasure.

In Countermeasure (5), a resistance is connected in series to shunt reactors when a cable line is energized. The resistance needs to be sized so that the DC component decays fast enough. After the cable line is energized, the resistance is bypassed in order to reduce losses. Considering the additional cost for the resistance, this countermeasure is more suited to HV cable lines than EHV cable lines.

Countermeasure (6) cannot always be applied; especially, it is difficult to apply (6) to long EHV cables due to the steady-state overvoltage.

Table 6-6 Countermeasures of Zero-missing Phenomenon

	Countermeasures	Notes
(1)	Sequential switching	• requires higher leading current interruption capability • requires single phase circuit breaker and current differential relay
(2)	Point-on-wave switching (synchronized switching)	• may cause higher switching overvoltage • requires single-phase circuit breaker
(3)	Delayed opening of healthy phases	• requires single phase circuit breaker and current differential relay • may not be possible to apply near generators
(4)	Breaker with pre-insertion resistor	• may be necessary to develop a new circuit breaker (expensive)
(5)	Additional series resistance in shunt reactor for energization	• requires special control to bypass series resistance after energization
(6)	Energize shunt reactor after the cable	• causes higher steady-state overvoltage and voltage step

6.3.1　Sequential Switching

When a single line to ground fault occurs before the zero-missing current phenomenon disappears, the line breaker cannot interrupt the current, and it may result in the failure of the line breaker. Fig. 6.20 shows zero-missing current with a single line to ground fault in phase b.

In Fig. 6.20, a single line to ground fault is applied in phase b of an EHV underground cable before energization. The figure shows that the current in the faulted phase contains a large AC component due to the fault current. The line breaker of the faulted phase can interrupt this current since this fault current superimposed on the cable energization current crosses the zero point due to its large AC component.
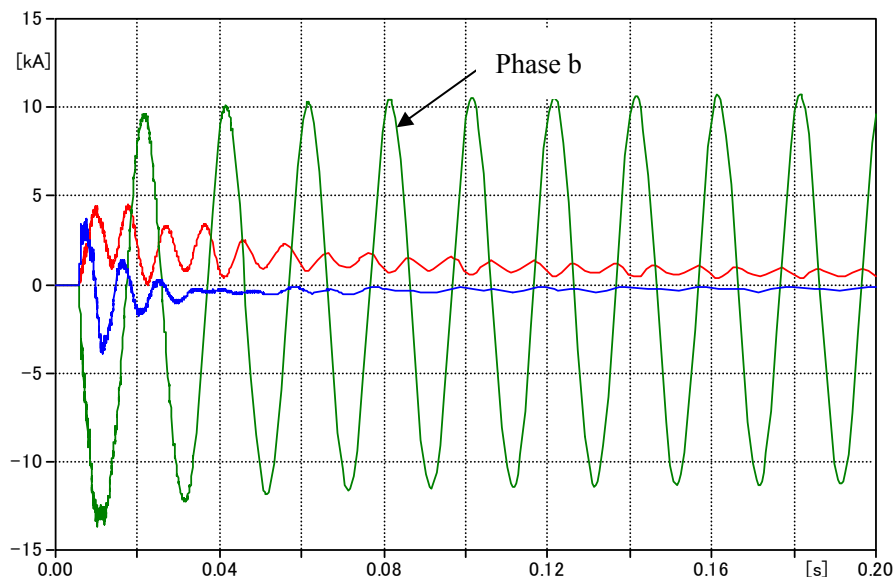
Fig. 6.20 Zero-missing phenomenon with a single line to ground fault.

Fig. 6.21 shows the time sequence of sequential switching when the cable line is energized from Substation A. The line breaker of phase b is opened, in Step 1, 60 ms after the fault, and the fault is cleared by this CB tripping. Since the fault is already cleared by the opening of phase b line breaker, there is no problem to take some time before opening line breakers of other healthy phases.

In Step 2, shunt reactors are tripped before the line breakers of healthy phases. It is necessary to trip shunt reactors of only healthy phases. At this time, it is not necessary and not recommended to trip shunt reactors of the faulted phase since the current through shunt-reactor breakers of the faulted phase does not cross the zero point.

It is now possible to open the line breakers of the healthy phases in Step 3. Fig. 6.22 shows that the current in healthy phases contains the AC component and crosses the zero point after tripping the shunt reactors.

Since shunt reactors are tripped before line breakers of healthy phases, it is required to confirm that the leading current in the line breakers does not exceed its breaking capability in Table 6-5. For a very long cable, as the Kyndbyværket – Asnæsværket line, it is highly recommended to trip half of the shunt reactors before the line breakers of healthy phases in order to reduce the leading current in the line breakers of healthy phases.
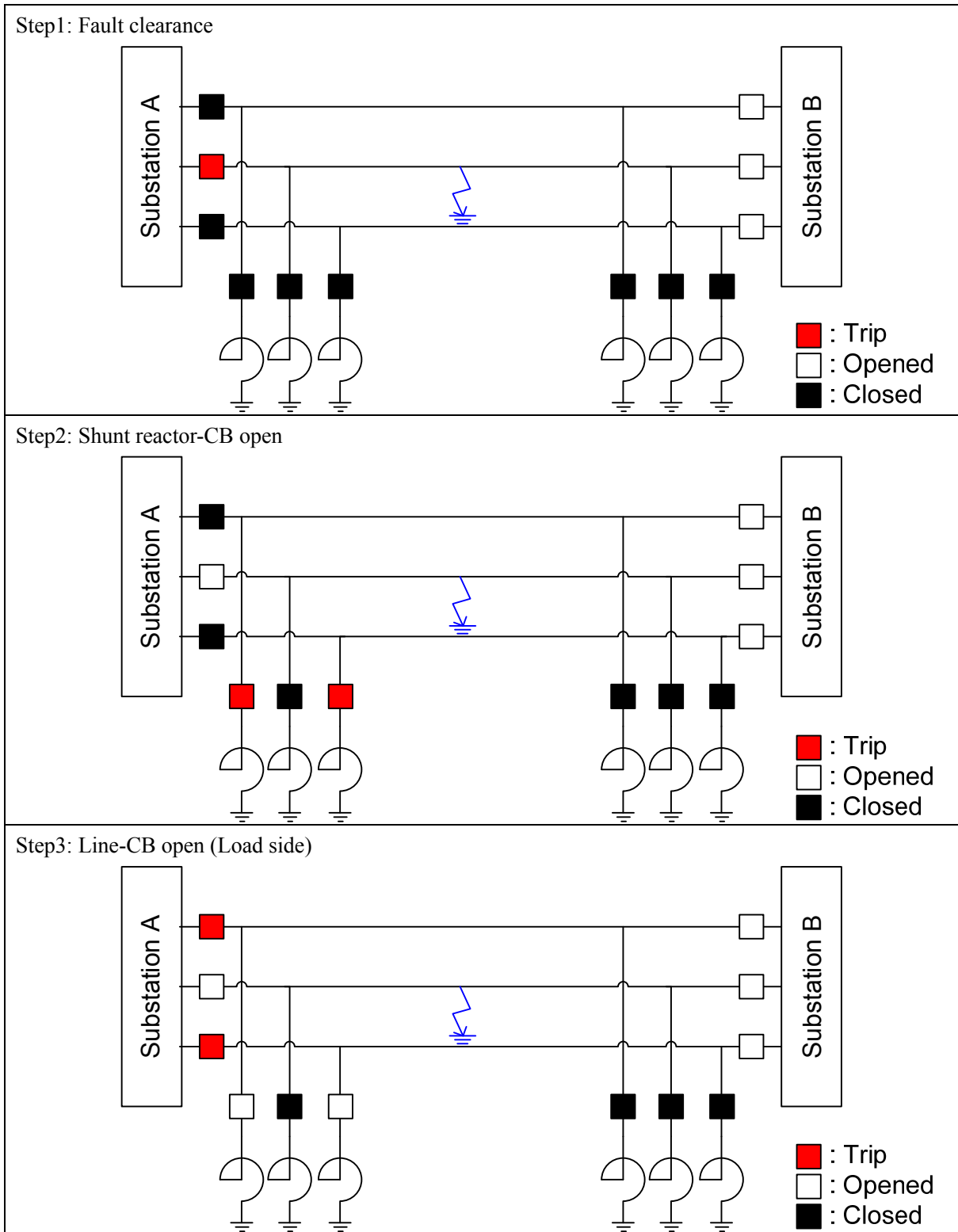
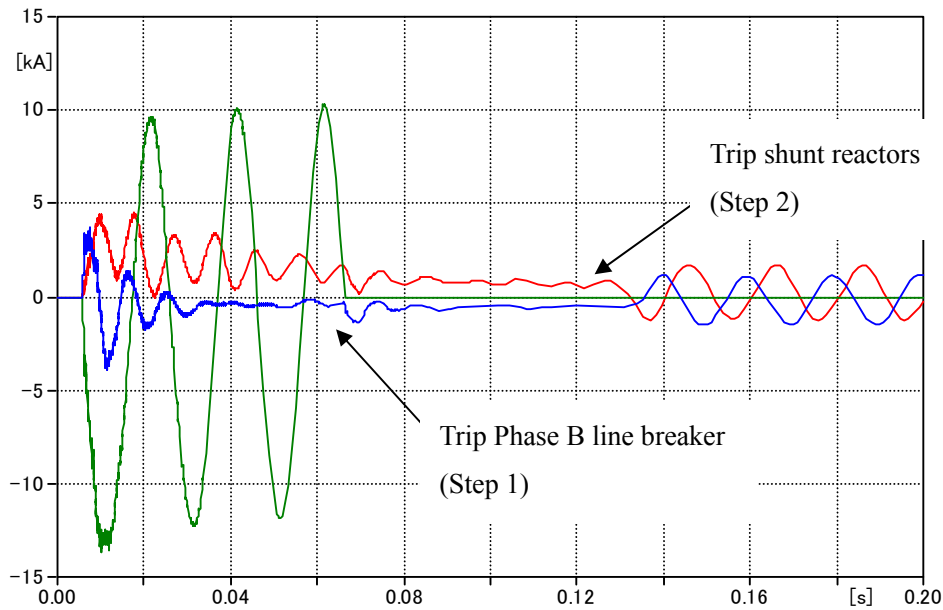**Fig. 6.21 Time Sequence of sequential switching.**

Fig. 6.22 Zero-missing phenomenon with sequential switching.

In the recommended compensation pattern (Pattern 1), a 300 MVar shunt reactor is installed each at Kyndbyværket and Asnæsværket. If one of these shunt reactors is tripped in Step 2, the uncompensated charging current will be 427.8 A at 400 kV as calculated in Table 2-11. As discussed in Section 6.2, this leading current slightly exceeds the specification defined in IEC 62271-100. However, the leading current interruption capability 400 A is defined at the voltage 1.4 pu, and circuit breakers have higher capability at a lower voltage level.

A simulation was conducted in order to find the voltage level when the leading current is interrupted. In the simulation, the Kyndbyværket – Asnæsværket line is energized from the Kyndbyværket side in the initial condition. The cable line was energized only from one end as it is the severe condition. If the cable line is energized from both ends, the line breaker at each end interrupts only half of the leading current. The ground fault was not simulated since the results in Section 5.4 show that the ground fault overvoltage disappears before the fault clearing. The simulation therefore started from the fault clearing of phase a

Fig. 6.23 shows the current in the line breaker of the Kyndbyværket – Asnæsværket line at the Kyndbyværket side. The initial current is almost zero because of the high compensation rate 100.7 % in the recommended compensation pattern. After Step 2 of the sequential switching in Fig. 6.21, the current in the line breaker increases to around 470 – 480 A due to the uncompensated charging capacity. The leading current is larger than the value in Table 2-11 (427.8 A) because of

the voltage rise caused by the shunt reactor tripping (Step 2).
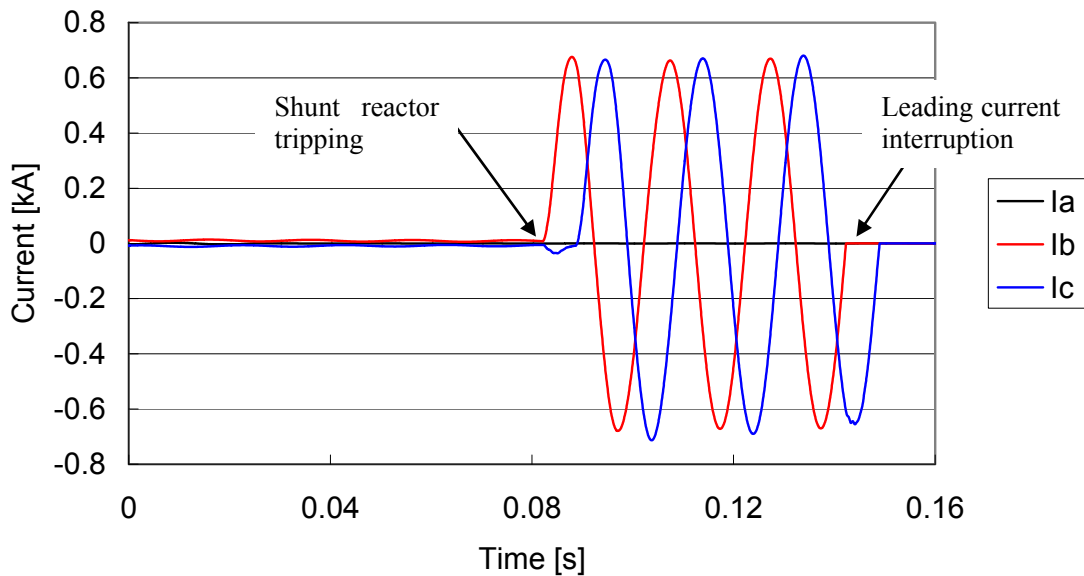
Fig. 6.23 Leading current interruption with sequential switching.

Fig. 6.24 shows the overvoltage caused by the shunt reactor tripping. The overvoltage goes up to around 1.1 pu after the shunt reactor tripping. As the overvoltage is much lower than 1.4 pu, it is highly likely that the line breaker can interrupt the leading current around 470 – 480 A without a problem. It is recommended to test the leading current interruption capability at the voltage 1.15 pu or 1.2 pu in order to confirm it.
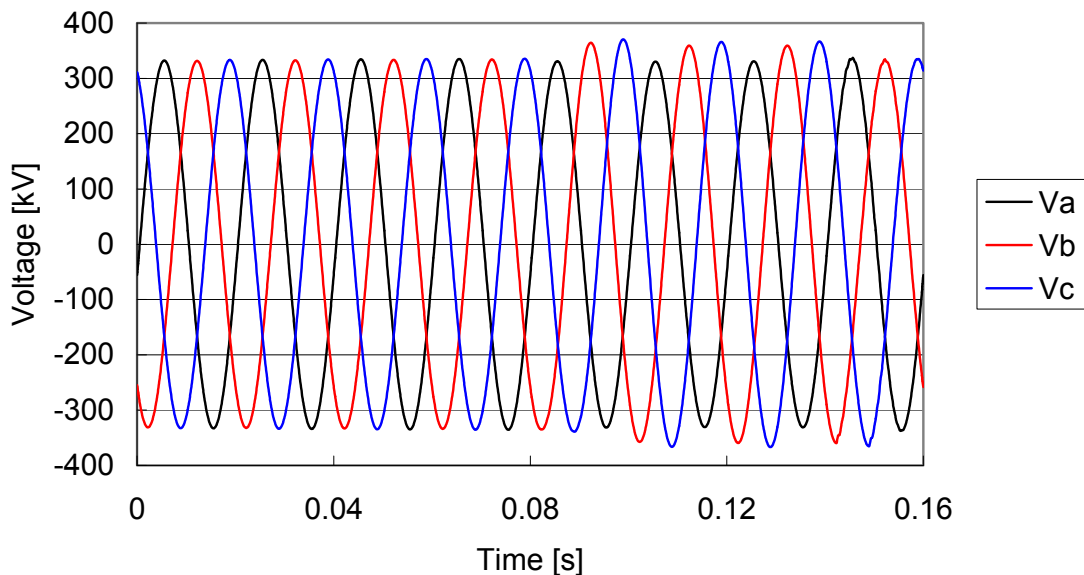
Fig. 6.24 Overvoltage with sequential switching.

6.3.2   Summary

This PhD project recommends to apply Countermeasure (1) (sequential switching) to the Kyndbyværket – Asnæsværket line after confirming the leading current interruption capability of line breakers.

Countermeasure (1) has a lot of application records for EHV cable lines and is also the most reliable countermeasure in terms of the duplication. Since the failure of the scheme may lead to the failure of a line breaker, it is necessary to ensure that a single failure will not lead to the failure of the scheme. The followings describe how the duplication is ensured in Countermeasure (1):

- Considering the failure of the main relay (current differential), both Main 1 and Main 2 protection trigger the sequential switching.
- In case of the breaker failure of a shunt reactor, the sequential switching trips the shunt reactor on the other end.

The duplication can be achieved as the Kyndbyværket – Asnæsværket line has shunt reactors on the both ends. For shorter cable lines which have only one shunt reactor, the duplication is not achieved. In order to standardize the countermeasure for the zero-missing phenomenon including these shorter cable lines, it is effective to apply both Countermeasures (1) and (2).

6.4 Cable Discharge

If a shunt reactor is directly connected to a cable line, the cable line is discharged through the shunt reactor when disconnected from the network. In this case, the time constant of the discharge process is determined by Q factor of the shunt reactor. Since Q factor ranges around 500 for EHV shunt reactors, the time constant of the discharge process is around 8 minutes.

If a cable line is disconnected from the network and energized again within a couple of minutes, there remains a residual charge in the cable line, and the residual charge can be highly dependent on the time separation between the disconnection and the re-energization. Under this condition, the re-energization overvoltage can exceed SIWV when the residual voltage has an opposite sign to the source voltage at the time of re-energization.

This is usually an issue for overhead lines since auto-reclose is applied to overhead lines. For cable lines, it is not common to apply auto-reclose. If it is applied to the cable lines, they may experience higher overvoltages because of their higher residual voltage. System operators are required to know that they need to wait for about 10 minutes (maybe more to be conservative) before re-energizing a cable line though it would not be a typical operation to re-energize a cable line.

If a shunt reactor is not directly connected to the cable line, the cable line is discharged through inductive VTs. In this case, the discharge process will be completed within several milliseconds. The inductive VTs need to have enough discharge capability if a cable line can be operated without a shunt reactor or all the shunt reactors are tripped by sequential switching. It takes several hours for the inductive VTs to dissipate heat after dissipating the cable charge. If the inductive VTs are required to dissipate the cable charge twice within several hours, the required discharge capability will be doubled.

6.5 Overvoltage Caused by Restrike

When a circuit breaker of a shunt reactor is opened, it can interrupt a current into the shunt reactor [1][9]. The interrupted current is usually very small, but it can cause a high slow-front overvoltage expressed by $L\dfrac{di}{dt}$. Due to this high slow-front overvoltage, a restrike can occur between the contacts of the opening circuit breaker, generally with a higher probability compared with circuit breakers used for other equipment.

In addition, this slow-front overvoltage imposes a severe initial condition for the overvoltage caused by the restrike. An example of the initial condition is shown in Fig. 6.25. In this example, the shunt reactor CB was opened when a current through the CB was 10 A, which was a very severe assumption contingent on the unit size of the shunt reactor.
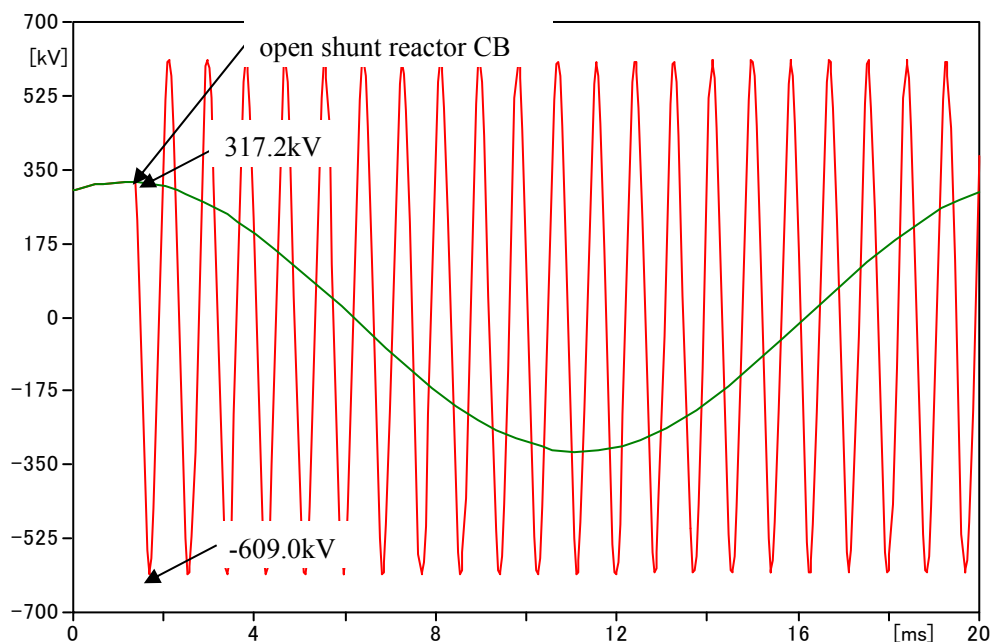

Fig. 6.25 Results of the current chopping analysis.

After opening the circuit breaker, it can be seen that the voltage on the shunt reactor side (red line) becomes very high as explained above. The voltage on the system side (green line) is kept at 1pu.

Fig. 6.26 shows an example of the analysis of the overvoltage caused by the restrike. For the simulation, arc impedance is modeled by a series circuit of resistance 2Ω and inductance 0.5μH [12]. The overvoltage is higher than LIWV without surge arresters for shunt reactors.
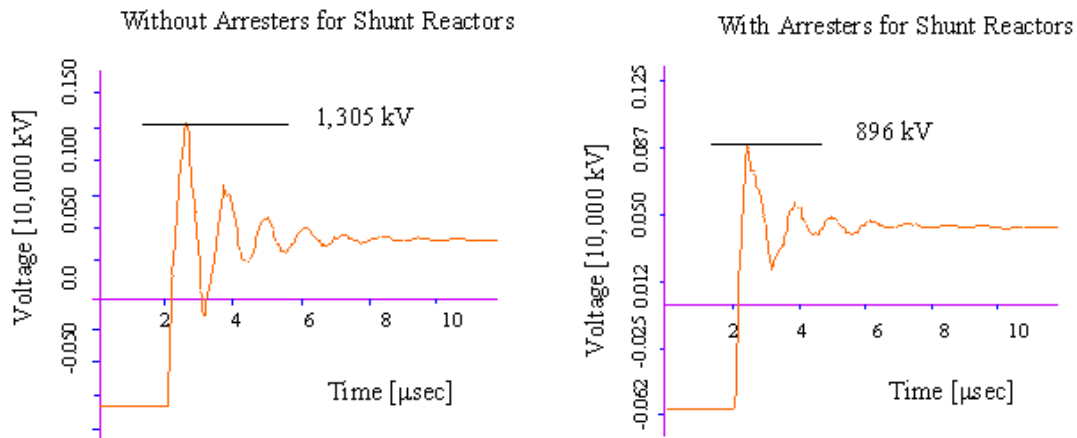
Fig. 6.26 Overvoltage caused by the restrike.

It is highly recommended to apply point-of-wave switching to the circuit breakers of shunt reactors. The point-of-wave switching should adjust the CB open command timing so that the distance between the contacts of the CB is at the maximum when shunt reactor current reaches the zero point. Since the zero-crossing point of shunt reactor current is different for each phase, this control requires a separate control for the CBs of different phases.

Even if the overvoltage level is lower than the withstand voltage, the restrike itself is an unfavorable phenomenon as it can damage the CB contacts and nozzles. By applying the point-of-wave switching, the restrike phenomenon itself can be avoided. A comparison between the two countermeasures, the surge arrester and point-of-wave switching, is compared in Table 6-7.

Table 6-7 Comparisons of Countermeasures for the Overvoltage Caused by the Restrike

	Advantage	Disadvantage
Surge arrester	No worry about malfunction	Damage to CB contacts and nozzles cannot be avoided.
Point-of-wave switching	Restrike itself can be avoided.	Malfunction of the controller may lead to equipment failures.

References

[1] T. Ohno, "Operation and Protection of HV Cable Systems in TEPCO", *Global Facts, Trends and Visions in Power Industry, Swiss Chapter of IEEE PES*, April 2010.
Presentation available on the web:
http://www.ieee.ch/assets/Uploads/pes/downloads/1004/10042ohnoexperiencetepco.pdf.

[2] V. Leitloff, X. Bourgeat, and G. Duboc, "Setting Constraints for Distance Protection on Underground Cables", in *Proc. 2001 7th IEE International Conference on Developments in Power System Protection*.

[3] D. A. Tziouvaras, "Protection of High-Voltage AC Cables", available on the web:
http://www2.selinc.com/techpprs/6221_ProtectionACCables_DT_20060131.pdf.

[4] N. Nagaoka and A. Ametani, "Transient Calculations on Crossbonded Cables," *IEEE Trans. on Power Apparatus and Systems*, vol. PAS-102, no. 4, 1983.

[5] A. Ametani, Y. Miyamoto, and N. Nagaoka, "An Investigation of a Wave Propagation Characteristic on a Crossbonded Cable," *IEEJ Trans. PE*, vol. 123, no. 3, pp. 395-401, 2003 (in Japanese).

[6] B. Kulicke, H. H. Schramm, "Clearance of Short-circuits with Delayed Current Zeros in the Itaipu 550 kV-Substation", *IEEE Trans. on Power Apparatus and Systems*, vol. PAS-99, no. 4, July/Aug 1980.

[7] T. Michigami, S. Imai, O. Takahashi, "Theoretical Background for Zero-miss Phenomenon in the Cable Network and Field Measurements", *IEEJ General Meeting 1459*, 1997 (in Japanese).

[8] H. Hamada, Y. Nakata, T. Maekawa, "Measurement of Delayed Current Zeros Phenomena in 500 kV Cable System", *IEEJ General Meeting 2001* (in Japanese).

[9] "*Joint Feasibility Study on the 400 kV Cable Line Endrup-Idomlund*", Final Report, Tokyo Electric Power Company, April 2008.

[10] F. Faria da Silva, C. L. Bak, U. S. Gudmundsdottir, W. Wiechowski, M.R.Knardrupgard, "Use of a preinsertion resistor to minimize zero-missing phenomenon and switching overvoltages", *IEEE-PES General Meeting 2009*.

[11] F. Faria da Silva, "Analysis and simulation of electromagnetic transients in HVAC cable transmission grids", PhD Thesis, Aalborg University, 2011.

[12] S. Ogawa, E. Haginomori, S. Nishiwaki, T. Yoshida, K. Terasaka, "Estimation of Restriking Transient Overvoltage on Disconnecting Switch for GIS," *IEEE Trans. on Power Systems*, vol. PWRD-1, no. 2, April 1986.

Chapter 7 Conclusion

The objectives of this PhD project have been to shed light on the phenomena peculiar to long cable lines. Through the studies on the 400 kV 60 km Kyndbyværket – Asnæsværket line, the thesis has addressed major problems and potential countermeasures related to the installation of long cable lines. The PhD project has tackled all the problems formulated in Chapter 1 and has yielded important findings which will be useful for studies on future cable lines.

7.1 Summary

7.1.1   Insulation Coordination Study

First of all, the PhD project performed the insulation coordination study for the 400 kV 60 km Kyndbyværket – Asnæsværket line in order to address the technical feasibility of the cable line and identify major problems and possible countermeasures.

The reactive power compensation analysis in Chapter 2 found the best compensation pattern, which requires installing one 300 MVar shunt reactor each at Kyndbyværket and Asnæsværket. The compensation rate becomes 100.7 % in this compensation pattern. It is confirmed that the steady-state overvoltage will not be a problem even considering a Ferranti phenomenon. However, if the cable line has to be in-service even when one shunt reactor is out of service, it is recommended to install two 150 MVar shunt reactors each at Kyndbyværket and Asnæsværket.

The temporary overvoltage analysis in Chapter 4 covered the resonance overvoltage and the overvoltage caused by the system islanding. Table 7-1 summarizes the results of the analysis. With respect to the initial overvoltage (first impulse), the highest overvoltage 805.0 kV was caused by the overvoltage caused by the system islanding, but it is much lower than the SIWV (1050 kV) defined in IEC 60071-1. The high overvoltage 517.8 kV was observed after the first peak in the parallel resonance overvoltage. It is highly recommended that the applied surge arresters have a withstand voltage higher than or equal to 1.60 pu for 1 second.

Table 7-1 Summary of the Temporary Overvoltage Analysis

		Highest Overvoltage (peak)	Withstand Voltage (peak)
Series Resonance	1st peak	285.5 kV	230 or 275 kV × √2 *[1]
	3rd peak	228.7 kV	
Parallel Resonance	1st peak	702.6 kV (2.15 pu)	1050 kV (3.21 pu, SIWV)
	1 sec	517.8 kV (1.59 pu)	551.5 kV (1.69 pu, Arrester)
Overvoltage Caused by the System Islanding	1st peak	805.0 kV (2.46 pu)	1050 kV (3.21 pu, SIWV)
	10 sec	400.0 kV (1.22 pu)	523.3 kV (1.60 pu, Arrester)

*[1]: Standard short-duration power-frequency withstand voltage defined in IEC 60071-1

The slow-front overvoltage analysis in Chapter 5 covered the line energization overvoltage and the ground fault and fault clearing overvoltage. The line energization overvoltage is much higher than the ground fault and fault clearing overvoltage. Both overvoltages are lower than the SIWV (1050 kV) defined in IEC 60071-1 and will not be a problem in the operation of the Kyndbyværket – Asnæsværket line.

Table 7-2 Summary of the Slow-front Overvoltage Analysis

	Highest Overvoltage (peak)	Withstand Voltage (peak)
Line Energization	775.2 kV (2.37 pu)	1050 kV (3.21 pu, SIWV)
Ground Fault and Fault Clearing	448.4 kV (1.37 pu)	1050 kV (3.21 pu, SIWV)

7.1.2   Required Specifications for the Related Equipment

The insulation coordination study and other studies have identified required or recommended specifications for the related equipment. Table 7-3 summarizes these required or recommended specifications.

Table 7-3 Required / Recommended Specifications for the Related Equipment

	Required / Recommended Specifications
Cable (IEC 62067)	Required: Power frequency withstand voltage 440 kV – 15 min, SIWV 1050 kV, LIWV 1425 kV
Surge Arrester (IEC 60099)	Required: Withstand voltage 1.60 pu – 1 sec Recommended: Line discharge class 3
Line Breaker (IEC 62271-100)	Required: Leading current interruption capability 400 A – 1.4 pu, 480 A – 1.15 pu (voltage)
Shunt Reactor Breaker (IEC 62271-100)	Required: Point-on-wave switching for opening if ASV or KYV 400 kV bus is GIS.
Protection Relay	Required: Current differential relay (main) Distance relay (backup) Sequential switching for the fault clearance Recommended: Distance relay that can apply different zero-sequence compensation $k0$ for different zones
VT (Line)	Discharge capability is not necessary as shunt reactors are always directly connected to the ASV – KYV line.

7.2 New Contributions

The PhD project produced the five papers listed in Table 7-4. The findings and contributions of these papers were used for the study on the Kyndbyværket – Asnæsværket line and will be useful for studies on future cable lines.

Table 7-4 Papers Produced by the PhD Project

Title	Co-authors	Outlet	Status
Derivation of Theoretical Formulas of Sequence Currents on Underground Cable System	Teruo Ohno, Akihiro Ametani, Claus Leth Bak	IPST 2011	Published
Derivation of Theoretical Formulas of the Frequency Component Contained in the Overvoltage related to Long EHV Cables	Teruo Ohno, Claus Leth Bak, Wojciech Wiechowski, Thomas Sørensen, Akihiro Ametani	IEEE Transactions on Power Delivery	Published
Statistical Distribution of Energization Overvoltages of EHV Cables	Teruo Ohno, Claus Leth Bak, Wojciech Wiechowski, Thomas Sørensen, Akihiro Ametani	IEEE Transactions on Power Delivery	Under 2nd review
Ground Loop Impedance of Long EHV Cable Lines	Teruo Ohno, Claus Leth Bak, Thomas Sørensen	Western Protective Relay Conference	Published
Analysis of the Statistical Distribution of Energization Overvoltages of EHV Cables and OHLs	Teruo Ohno, Claus Leth Bak, Wojciech Wiechowski, Thomas Sørensen, Akihiro Ametani	IPST 2013	Abstract submitted

Although the findings and contributions of these papers have already been discussed in detail in this thesis, the important points are summarized here for convenience:

(1) Derivation of theoretical formulas of sequence currents on underground cable system (Section 2.3.2)

The PhD project derived theoretical formulas of sequence currents of a cross-bonded cable and a solidly-bonded cable. The derived formulas consider the cable as a cable system; they can thus consider sheath bonding and sheath grounding resistance. The verified accuracy of the proposed formulas shows sequence impedance / current can now be obtained before the

installation without making measurements for a majority of cables. This gives an important advantage in setting up transient overvoltage studies as well as planning studies.

(2) Derivation of theoretical formulas of the frequency component contained in the overvoltage related to long EHV cables (Section 4.1.3.1)

The PhD project derived the simple theoretical formulas for estimating the propagation velocity and dominant frequency from impedance and admittance calculations. The comparison between the proposed formulas and the simulation results was performed using the Kyndbyværket – Asnæsværket line. From the comparison, the derived formulas were found to be sufficiently accurate to be used for the efficient analysis of resonance overvoltages.

(3) Statistical distribution of energization overvoltages of EHV cables (Sections 5.1 and 5.2)

The PhD project derived the statistical distributions of energization overvoltages of EHV cables from a number of simulations. Through the comparison with the statistical distributions of energization overvoltages of overhead lines, it has been found that line energization overvoltages on the cables are lower than those on the overhead lines with respect to maximum, 2 %, and mean values. In addition, standard deviations are smaller for the cables.

(4) Ground loop impedance of long EHV cable lines (Section 6.1)

Through the calculation of the ground loop impedance for cable lines, The PhD project has found that, for long EHV cable lines, the reliable operation of the ground distance relay is possible with a typical relay setting, despite the discontinuity at cross-bonding points. Effects of parameters, such as substation grounding, cable layouts and transposition, are also found through the analysis.

(5) Analysis of the statistical distribution of energization overvoltages of EHV cables and OHLs (Section 5.3)

The PhD project has identified the causes and physical meanings of the characteristics of the statistical distribution of energization overvoltages of EHV cables. From the theoretical analysis of voltage waveforms, the main characteristics of the statistical distribution are found to be caused not by random switching by accident, rather there are contributing factors and physical meanings behind the characteristics.

7.3 Future Work

This section lists future works related to the installation and operation of long EHV cables. These items may require serious considerations even though they are not studied in the PhD project:

- Evaluation of high-impact low-probability (HILP) events

  Since a severe temporary overvoltage occurs only in specific conditions, it can be considered as a low-probability event. When it occurs, however, it can cause a major damage to related equipment, which poses a high-impact on the safe operation of the power system.

  It will be helpful for future construction and operation of EHV cable lines to establish a procedure to evaluate risks associated with HILP events.

- Burden that can be placed on the system operation

  Severe temporary overvoltages are similar to extreme contingencies, such as N-2 contingencies, as they both are HILP events. One difference is that severe temporary overvoltages can be avoided not only by equipment specifications but also by applying operational constraints since they occur only in specific conditions. However, if operational constraints are too strict or too complicated, it will place a burden on the system operation. The decisions should be made also based on the skills of system operators.

- Should cable test voltages be re-considered?

  In order to test the insulation performance of cables, lightning impulse voltages, switching impulse voltages and power frequency test voltages are applied to cables according to international and national standards. IEC 62067 defines the test methods and requirements for XLPE cables and accessories for rated voltages above 150 kV up to 500 kV. According to IEC 62067, the test voltage 440 kV is applied to 400 kV cables for 15 minutes, as power frequency voltage test, after the lightning impulse voltage test.

  Considering the level of temporary overvoltages found in the PhD project, the level of applied power frequency voltage in IEC 62067 appears to be low, and the duration is long. However, it requires discussions to decide if cable test voltages in IEC 62067 should be re-considered, since it is a common practice to test the insulation performance of equipment at lower voltages with longer duration. In addition, the mismatch is not an immediate issue as the overvoltage is normally evaluated against the insulation performance and the energy absorption capability of surge arresters.

7-7

- Effects on harmonics

  As we have seen in the parallel resonance overvoltage analysis, the introduction of long cable lines with shunt reactors significantly lower parallel resonance frequencies of power systems. The system total impedances at 5th and 7th harmonic frequencies are often increased by this shift of resonance frequencies. Since the increase of impedances will results in the increase of the total voltage harmonic distortion, it should be evaluated in the areas where harmonics are of concern.